Tungsten oxide nanostructures and their electrochromic performance

Submitted by **Kunyapat Thummavichai** to the University of Exeter

As a thesis for the degree of

Doctor of Philosophy in Engineering

In April 2018

This thesis is available for Library use on the understanding that it is copyright material and that no quotation from the thesis may be published without proper acknowledgement.

I certify that all material in this thesis which is not my own work has been identified and that no material has previously been submitted and approved for the award of a degree by this or any other University.

Signature: ……..

Abstract

The electrochromic behaviour of tungsten oxide (WO_x) bulk forms has attracted huge research interest for decades owing to advantages of fast response time, good reversibility and high colouration efficiency compared with other electrochromic materials. Nanomaterials have certainly brought in new opportunities and opened the door for better, higher and smarter devices fabrication. This thesis will first investigate, explore, and understand the electrochromic performance of WO_x in the nanoscale, and identify ways to enhance its performance via effective doping electrolyte selection and heat treatment. Moreover, the thesis will evaluate the prototype device performance based on our new understandings obtained in this project. The main findings are as follows:

- Successfully synthesised crystalline WO_x-based nanomaterials using a simple solvothermal technique, and achieved a series of La-, Ce- and Na-doped nanomaterials. The results show that the dopants caused distortion of the parental WO_x frameworks and increased the oxygen vacancy inside the structure, which is beneficial for the chromic properties.
- The best electrochromic performance was obtained from Ce/W = 1 : 15 samples which presented 44.3% for optical contrast colouration efficiency of 67.3 $cm^2\ C^{-1}$.
- Conducted in-situ phase transition investigations using both WO_3 nanoparticles and $W_{18}O_{49}$ nanowires, and found out that temperature was affecting the relaxation of W-O framework and phase transition. Based on the investigation, the 187.6 cm^{-1} band has identified as a fingerprint band for the phase transition from γ- to β- of the WO_3 nanoparticle at 275 °C. $W_{18}O_{49}$ nanowires exhibit better thermal stability than the WO_3 nanoparticles.
- Intensive electrochemical investigations of La- and Ce-doped WO_x structures were exhibit better diffusion kinetics, stability and colouration efficiency compare with plain WO_x. These improvements are contributed to the improved oxygen vacancy (V_o). D_{Li}^+ of the Ce-doped samples were

much higher than that of the plain $W_{18}O_{49}$ nanowires, by 177%, 102% and 84% for the 1:15, 1:10 and 1:5 samples respectively. D_{Li}^{+} values of all La-doped samples were over 100% higher than those of the plain $W_{18}O_{49}$. The La-doped thin films increased the stability by 9%, 4% for intercalation, and 25% and 23% for de-intercalation, for La/W = 1:15 and 1:10 samples respectively, against the plain $W_{18}O_{49}$.

- Provided experimental evidence to explain the degradation of chromic thin films, which is related to the Li^{+} trapping and loss of V_o in the WO_x the structures.
- The 350 °C annealed $W_{18}O_{49}$ thin film sample showed better diffusion kinetics by 25% for intercalation and 30% for de-intercalation compared with the un-annealed $W_{18}O_{49}$ samples. Stabilities also showed 31% improvement for the de-intercalation, against the un-annealed $W_{18}O_{49}$ sample.
- Fabricated electrochromic device prototypes, and investigated the influence of various electrolytes, an optimal combination of $LiClO_4$/PPC/PC polymer electrolyte has been developed, to improve the performance in ion kinetics and switching time of $W_{18}O_{49}$.

These results have shown that WO_x nanomaterials via further effective modification including doping with rare-earth elements or proper heat treatment are promising and practical candidate for the creation of fast, reliable and highly efficient electrochromic devices/smart windows for various applications.

Publications

Journal papers

1. **K. Thummavichai**, N. Wang, F. Xu, G. Rance, Y. D. Xia, Y. Q. Zhu, In-situ X-ray diffraction and Raman Spectroscopy phase transition investigations of ultrathin $W_{18}O_{49}$ nanowires, *Royal Society Open Science* (2018), 4, 1-10. DOI: 10.1098/rsos.171932.
2. **K. Thummavichai**, F. Xu, N. Neate, N. Wang, A. D. Sanctis, S. Russo, S. Zhang, Y. D. Xia and Y. Q. Zhu, Ce-Doped bundled ultrafine diameter tungsten oxide nanowires with enhanced electrochromic performance, *Nanoscale* (2018), 10, 4718-4726, DOI: 10.1039/C7NR08385H.
3. **K. Thummavichai**, N. Wang, L. Lem, M. Phillips, C. Ton-That, H. Chang, C. Hu, F. Xu, Y. Xia, Y. Zhu, Lanthanide-doped $W_{18}O_{49}$ nanowires: Synthesis, structure and optical properties, *Materials Letters* (2017), 214, 232-235, DOI: org/10.1016/j.matlet.2017.12.022 5.
4. **K. Thummavichai**, L. Trimby, N. Wang, C. David Wright, Y. Xia, Y. Zhu, Low temperature annealing improves the electrochromic and degradation behavior of tungsten oxide (WO_x) thin films, *Journal of Physics and Chemical C* (2017), 121, 20498-20506, DOI: 10.1021/acs.jpcc.7b06300.
5. **K. Thummavichai**, N. Wang, Y. Xia, Y. Zhu, Effect of Low Temperature Treatment of Tungsten Oxide (WO_x) Thin Films on the Electrochromic and Degradation Behavior, *IEEE Nanotechnology Materials and Devices Conference* (2016).
6. **K. Thummavichai**, Y. D. Xia, Y. Q. Zhu, Recent progress in chromogenic research of tunsten oxides towards energy-related application. *Progress in Material Sciences* (2017), 88, 281-324, DOI: 10.1016/j.pmatsci.2017.04.003.
7. N. Wang, Z. Yang, Y. Wang, **K. Thummavichai**, Y. Xia, O. Ghita, Y. Zhu, Interface and properties of inorganic fullerene tungsten sulphide nanoparticle reinforced poly (ether ether ketone) nanocomposites, *Results in Physics* (2017), 7, 2417-2424, DOI: org/10.1016/j.rinp.2017.07.018. 2.

8. N. Wang, Z. Yang, **K. Thummavichai**, F. Xu, C. Hu, H. Chen, Y. Xia, Y. Zhu, Novel graphitic carbon coated IF-WS2 reinforced poly (ether ether ketone) nanocomposites (2017), RSC Advances, 7, 35265-35273, DOI: 10.1039/C7RA06205B.
9. N. Wang, Z. Yang, F. Xu, **K. Thummavichai**, H. Chen, Y. Xia, Y. Zhu, A generic method to synthesise graphitic carbon coated nanoparticles in large scale and their derivative polymer nanocomposites, *Scientific Report* (2017), 7, 1-9, DOI: 10.1038/s41598-017-12200-1.
10. J. Ruan, **K. Thummavichai**, Y. Lu, Y. Q. Zhu, H. Yan, Phase transition and optical absorption evolution of WO_3 nanoparticles induced by pressure, Materials Research Express (Accepted Manuscript online 29 June 2018), DOI: 10.1088/2053-1591/aad00f.

Conference presentation and poster

1. **K. Thummavichai**, Y. Xia, Y. Q. Zhu. Ce-doped bundled tungsten oxide nanowires for enhanced electrochromic performance *BIT's 3rd Annual World Congress of Smart Materials-2017*, March 2017, Bangkok, Thailand.
2. **K. Thummavichai**, Y. Xia, Y. Q. Zhu. Low Temperature Treatment of Tungsten Oxide (WO_x)Thin Films on the Electrochromic, *IEEE 11th Nanotechnology Materials and Devices Conference NMDC,* 9 - 12 October 2016, Toulouse, France.
3. **K. Thummavichai**, Y. Xia, Y. Q. Zhu. Effect of Low Temperature Treatment of Tungsten Oxide (WO_x)Thin Films on the Electrochromic and Degradation Behavior, *The 23rd Joint Annual Conference of CSCST-SCI*, September 2016, University of Nottingham, UK.
4. **K. Thummavichai**, Y. Xia, Y. Q. Zhu. Solvothermal synthesis and characterization of bundles tungsten oxide nanowire doping different among of sodium metal (Na_xWO_y),*12th International Conference on Material Chemistry (MC12)*, 20 - 23 July 2015, University of York, UK.
5. **K. Thummavichai**, Y. Xia, Y. Q. Zhu. Solvothermal synthesis and characterization of bundles tungsten oxide nanowire, *The 21st Joint Annual Conference of CSCST-SCI*, October 2014, University of Surrey, UK.

Table of Contents

Acknowleadgement

Frist and foremost, I am extramely grateful to my superviour, Yanqiu Zhu who gave me this PhD opportunity, expertly assisted me through my graduate education and shared the excitement of my project discoveries at the University of Exeter. I have been extremely lucky to have a supervisor who cares so much about my work and responses to my queries and questions so promptly. His continuous support and guidance are immeasurable and without it I would not be where I am today. His kindness, enthusiasm and the substance of genius really taught me so many things. I have grown and deverloped, not only academically as a professional scientist but also socially as a person in my career. I also thank Dr. Yongda Xia for the advices and provided to my research and pubilications.

My appreciation also extent to my lovely laboratory colleagues: Drs. Binling Chen, Bahareh Yazdani Damavandi, Sakineh Chabi, Zhuxian Yang, Yuan Wang, Oluwafunmilola Ola, Ms Zheng Huang, Mr Yu Chen, Mr Zahid Hussain, Mr Pablo Martinez Pancorbo, and especially Dr. Nannan Wang whose help and support during my ups and downs offered warmth and positive atmosphere.

I am also thankful to the staff at the enginenring department Drs. Yat-Tarng (Tommy) Shyng and Hong Chang for their efficient characterisation assistance. In addition, a thank you to colleagues at The University of Nottingham, especially to Dr. Fang Xu and her team.

Thank Prof. Russo Saverio, Dr. Adolfo De Sanctis and Mr. Peter Karlsen from the Physic Department at the University of Exeter, for their collaboration and support in some experiments and result analyses.

Thanks also go to both of my close friends: Drs. Meiying Chen, Polina Nikolaou, Ana Cinta Gonzalez, Ms Janire Escolar Ulibarri, Mr Harry Liu and Mr Hao Dong who blessed me with joy when the laboratory light switched off and helped me survive these years.

Finally, a big thank you to my lovely parents, for their encouragement and emotional support, as always.

List of Figures

List of Tables

List of Abbreviations

Ag	Silver
AgCl	Silver choride
$BMIMBF_4$	1-n-Butyl-3-Methylimidazdium Tetrafluoroborate
CA	Chronoampermetry
CC	Chrocoulometry
CE	Coloration Efficiency
$CeCl_3.7H_2O$	Cerium chloride heptahydrate
C_2H_6O	Ethanol
CL	Cathodoluminescence
CV	Cyclic voltammogram
CVD	Chemical vapor deposition
$D_{Li}+$	Diffusion coefficient of Lithium ion
EDS	Energy-dispersive X-ray spectroscopy
FLY	Fluorescnce yield
FWHM	Full width at half maximum
HRTEM	High-resolutionTransmission electron microscopy
ILs	Ionic liquids
ITO	Indium tin oxide
IVCT	Inter-valence change transfer
JCPDS	Joint Committee on Powder Diffraction Standards
$LaCl_3.7H_2O$	Lanthanium chloride heptahydrate
$LiClO_4$	Lithium perchlorate
NaCl	Sodium chloride
PC	Propylene carbonate
PET	Polyethylene terphthalate
PPC	Polypropylene carbonate

Pt	Platium
PVD	Physical vapor deposition
Q_d	Transported charge per unit area
rpm	Revolutions per minute
SAED	Seleted area electron diffraction
SEM	Scanning electron microscopy
Si wafer	Silicon wafer
t_b	Bleaching time
t_c	Colouration time
TEM	Transmission electron microscopy
TEY	Total electron yield
V_O	Oxygen vancacy
WCl_6	Tungsten hexachloride
WO_x	Tungsten oxide
XANES	X-ray absorption near edge spectroscopy
XPS	X-ray photoelectron spectroscopy
XRD	X-ray diffraction
ΔOD	Change in optical density
ΔT	Optical contrast

Chapter 1 Introduction

As a semiconducting material, tungsten oxides (WO_x) have emerged as an important candidate for future nanotechnology developments due to their unique and wealthy compositional, structural and property characteristics. Their excellent chromogenic performances, huge range of compositional combinations and vast crystalline structures from amorphous to different crystallised forms have made them unique and particularly attractive. The chromogenic behaviour of WO_x is determined by their optical properties (absorbance, transmittance and reflectance), which allows them to switch between a coloured and a bleached state in response to various external conditions applied.

Amongst many traditional chromogenic materials, WO_x ($2 \leq x \leq 3$) have been intensively studied because of their proven potentials for outstanding performance. It has been reported that WO_x have better electronic conductivity (10-10^{-6} S/cm) and faster Lithium-ion (Li^+) insertion than many other oxides [1]. They offer excellent cyclic stability, high Coloration Efficiency (CE), good memory and high contrast ratios, compared with other transition metal oxides [2]. CE is determined as the ratio of change (between transparent and coloured state) of Optical Density (OD) parameter to the inserted charges per unit, which can be expressed as: $CE = \frac{\Delta(OD)}{\Delta Q}$ [3]. A greater CE means better transmittance variation per unit charge [4]. Four types of WO_x have been reported as attractive coloration media with high stability: pure stoichiometric WO_3 (yellow), non-stoichiometric $W_{20}O_{58}/WO_{2.9}$ (dark blue), $W_{18}O_{49}/WO_{2.72}$ (violet), and WO_2 (chocolate brown) [5].

The main principle of the coloration process for WO_x is the result of the insertion/extraction of electrons and charges balancing small ions such as H^+, Li^+, K^+ and Na^+. These ions located at the W sites alter the inter-valence of the tungsten ion transition from W^{6+} to W^{5+}. Another principle is the small polaron absorption. The abundant crystalline structures, and especially the almost countless compositional combinations in WO_x, which are all associated with

their chromogenic behaviour, making them very unique. Meanwhile, such characteristics bring in immense complexities in research, in order to achieve deeper understandings and draw a full picture towards applications.

An essential issue is the stability and degradation of electrochromic materials that affects the ultimate performance of chromic devices however, this issue has not been properly dealt with in the past, and fundamental understanding remains as a huge challenge. A few reports have claimed that the cause of degradation in WO_x electrochromic devices was a result of Li^+ accumulation or trapping at the initial stage of colouring and bleaching cycles [6-8].

Among different ways reported for improving the chromic performance, materials synthesised in the forms of nanoparticle/nanostructure with significantly decreased size and properly tuned morphologies have recently attracted the research attention. Nanostructured materials have enhanced surface-to-volume ratios, which allow for more surface areas to be involved in reactions [9]. The decrease of the grain sizes could shorten the length of ion diffusion paths and make the ion diffusion more effective than those in bulk forms, therefore nanostructures are beneficial for improving the responding time of chromic devices [10]. Similarly, an interesting strategy to increase the surface area is to control the porosity of WO_x structures [11, 12]. Moreover, the electrochromic property of WO_x can also be improved by combining with suitable metal, metal oxide or alkali metal compounds, etc.

Different crystalline or modified structures of WO_x could be related to the amount of O content and bonding relaxation inside the structure. O content played an important role in generating the W^{5+} state with ion insertions during the colouration and bleaching reactions of the WO_x chromic materials. It has been reported that optical properties and CE of a WO_x chromic material are strongly influenced by the O content in the WO_x films, for both the sub- and over- stoichiometric WO_x structures [13-15].

A simple low temperature annealing treatment is another solution that has been used for modifying the structure of chromic materials. Reports have pointed out

that the annealing treatment affected the structure homogeneity, eliminated the defects and improved the crystallinity of transition metal films [16-20], which in turn could affect the Li^+ trapping behaviour. Therefore, such investigations were directly related to the degradation issue and could benefit the efficiency improvement for chromic device and gas sensor applications [21, 22].

To achieve enhanced chromic performance, it should not only focus on the development of materials and structures, but also pay attention to external factors, such as types of electrolyte, thicknesses of both courter and working electrodes, suitable values of applied potentials, etc. which are very important for determining the overall chromic performance.

This thesis has been presented as seven main Chapters. Chapter 1 introduces the motivation and organization of the thesis. Chapter 2 presents the WO_x structures and their chromic properties, based on literature review. Chapter 3 provides the general WO_x nanostructure syntheses and thin film preparations, and techniques used for characterisation and property assessments in this thesis. Chapter 4 shows the preparation details of the plain WO_x nanowires and the differently doped WO_x nanostructures by using a solvothermal technique. The morphology and structure characterizations of each synthesised material are also presented. Moreover, an understanding of the phase transition loop for both the plain WO_x nanowires and nanoparticles will be reported. Chapter 5 presents the electrochromic property of WO_x nanowires and nanoparticles based on electrochemistry measurements. Also, the enhancements of WO_x electrochromic performance via different techniques including low temperature annealing treatment of the WO_x thin films, relaxation of WO_x nanowires by rare-earth dopants, and different types of gel electrolytes will be investigated. Chapter 6 presents the optical properties and coloration efficiencies of the plain and doped WO_x nanowires in nanodevice prototypes. Chapter 7 draws the conclusion, presents all key findings from this thesis, and recommends some future work to continue research in related areas.

Aim and objectives of the project

The aim of this thesis is to improve the electrochromic properties of WO_x based thin films by (1) doping WO_x with Rare-earth elements (Ce and/or La) and (2) annealing heat treatment at the low temperature. The objectives of the study are:

1. To investigate the structural effect of different dopants on WO_x and their electrochromic performance.
2. To investigate the effects of temperature on the WO_x thin films and their electrochromic performance.
3. To optimise the best electrochromic performance of both doping and heat treatment techniques.
4. To understand the coloration and bleaching mechanism of WO_x based electrochromic device.
5. To investigate the effect of electrolytes on WO_x electrochromic device.
6. To investigate the cause of degradation on the electrochromic device.

Chapter 2 Literature review

Intensive investigations have been carried out over the last several decades on tungsten oxides (WO_x), due to their interesting chromic properties and wealthy nature of structures which opens great potentials for numerous applications, such as in optical device, reliable and highly sensitive gas sensors [23, 24], photocatalysis [25], and solar cells [26, 27], in ion lithium batteries [28] and in field emission [29], flat-panel display, optical memory for advanced devices. In this Chapter, the background information associated with the electronic and crystalline structures, the synthesis methodologies, electrochemical properties and the potential applications of WO_x, as well as the technical challenges towards engineering applications, will be presented and discussed based on most recent literatures.

2.1 Structure of WO_x

2.1.1 Crystalline structure of WO_x

Stoichiometry WO_3 is a wide band gap semiconductor, with a band gap ranging from 2.6 - 3.0 eV. It exists as a perovskite-like structure (AMO_3, where A represents a mono or divalent cation, and M is the main metal in the compound), which builds up a three-dimensional network by corner and edge sharing of the WO_6-octahedra [30]. Each W atom, lying off-centre, is surrounded by a regular octahedron of six nearest O atoms, as shown in Fig. 2.1a. The WO_6-octahedra organized in various sharing (edges, corners and planes) at different tilting angles and distortions result in a variety of WO_x phases [31]. Basically, the WO_3 crystalline structures are categorized based on the temperature, tetragonal (α-WO_3) at temperature above 740 ºC, orthorhombic (β-WO_3) from 330 to 740 ºC, monoclinic I (γ-WO_3) from 17 to 330 ºC, triclinic (δ-WO_3) from -43 to 17 ºC, and monoclinic II (ε-WO_3) below -43 ºC (Fig. 2.1b) [10, 32].

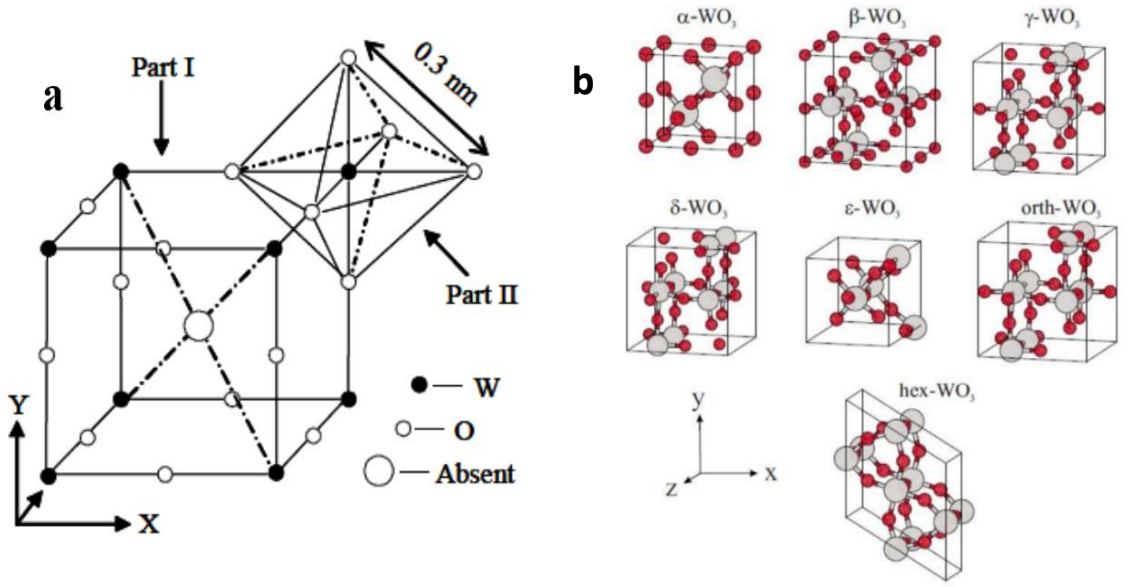

Fig. 2.1 (a) Geometry of the perovskite lattice cell (Part I) and the octahedral symmetries (Part II) in a perovskite structure [33], (b) unit cells of different phases of (WO_x) [34].

WO_3 is also known for its non-stoichiometry structures (WO_{3-x}, where $0 < x \leq 1$), although WO_{3+x} exists with less occurrence. The wide existence of these non-stoichiometric structures is owing to the WO_x lattice that can withstand a considerable number of O deficiency, therefore resulting in the formation of different oxidation states for W [35]. Many examples of WO_{3-x} have been reported thus far, such as $WO_{2.63}$ ($W_{32}O_{84}$), $WO_{2.67}$ (W_3O_8), $WO_{2.72}$ ($W_{18}O_{49}$), $WO_{2.77}$ ($W_{17}O_{47}$), $WO_{2.8}$ (W_5O_{14}), $WO_{2.83}$ (W_5O_{14}), $WO_{2.9}$ ($W_{20}O_{58}$), $WO_{2.92}$($W_{25}O_{73}$), and so on [36]. Some of these structures are presented in Fig. 2.2. Of which, the $WO_{2.72}$ has attracted the most research attention, due to this is the only non-stoichiometric oxide that can be easily isolated in pure form, and it contains W ions of mixed valency.

These perovskite structures allow to intercalate mono- or di-valent cations on the vacancies or channels within a network of WO_6 octahedra (the absent channel in Fig 2.1a), to form the so-called “tungsten bronzes”. Tungsten bronze is a group of compounds made up of WO_x and commonly alkali metals (Fig. 2.3) [37], with a general formula A_xWO_3, where A is the cation atoms from group I alkali, consisting of H [38-40], Rb [41], Na [42, 43], Li [44, 45], P[46], K [47] and Cs [48, 49]; and x varies from zero to unity. Fig. 2.3a shows the crystal structure

changes of A_xWO_3 with increased x values with different alkali metals of varied sizes, and with different x concentrations.

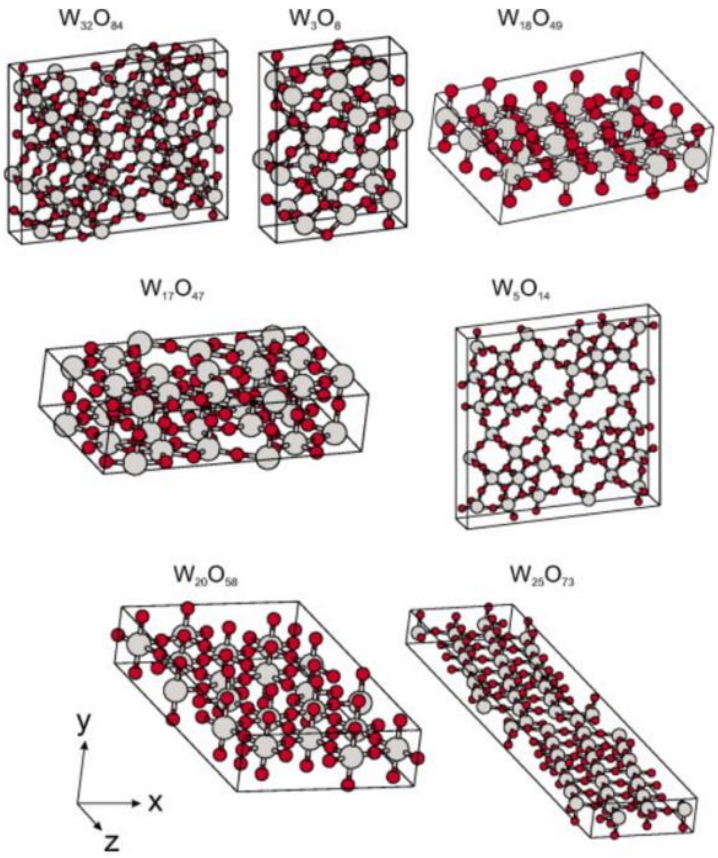

Fig. 2.2 Unit cells of different non-stoichiometric WO_{3-X}. The larger grey balls stand for W atoms, while the smaller red balls represent O atoms [36].

As the tunnel cations are embedded within the cross-linked WO_6 octahedral framework along the c-axis, a hexagonal tungsten bronze (HTB) results in, which is typically known for its characteristically one-dimensional (1D) tunnel structures [50]. The existence of this structure is dependent upon the size of the cation ions and their concentration x. Moreover, this HTB structure is more favourable to exhibit superconductivity, magnetism and electrochromic properties than other bronze structures, due to its intercalation chemistry and open-tunnel features. A large tunnel cavity of the HTB structure can easily intercalate with larger cations, exhibiting smaller lattice distortions thus higher stability. It can also promote greater possibilities for diffusion, therefore resulting in higher electrochromic performance compared with cubic structures [51-53]. It

has been pointed out that when $x \leq 0.33$, the (Cs, Rb, and K)$_x$WO$_3$ formed hexagonal structures, because they were fully intercalated inside the hexagonal tunnels [53]; whereas the HTB structure became unstable at low alkali concentration ($x < 0.10$) [54].

Roussel *et al*. studied the tilt phenomenon of the WO_6 octahedra inside a slab of WO_3-type structure via monophosphate tungsten bronzes, $A_x(PO_2)_4(WO_3)_{2m}$, in which m is a thickness function [46]. They reported that this could be formed either with pentagonal tunnels or with hexagonal tunnels. Another diphosphate tungsten bronze $A_x(P_2O_4)_2(WO_3)_{2m}$, was mainly reported existing as the hexagonal tunnels. Guo *et al*. researched the near infrared (NIR) shielding performance of both Rb_xWO_3 and Cs_xWO_3 nanoparticles [41, 55], and they reported the HTB and demonstrated their potentials as a solar filter in applications for both nanomaterials. Laonova *et al*. demonstrated that the hexagonal $Rb_{0.3}WO_3$ could also act as the reference electrode in a solid-state potentiometric sensor system for detecting CO_2 and H_2S operating in natural conditions [56].

Among many alkali-metals, Na was widely used for WO_x bronzes investigations aiming to understand their behaviours, electrical conductivities, optical and other physical properties associated with different structures of the bronze [42, 57-61]. The crystalline structure of Na_xWO_3 is dependent on Na concentrations (x values) [62]. When x varies from zero to unity, corresponding to different structures, the materials show interesting colour changes from yellowish-green to grey, blue, deep violet, red and finally to gold (Fig. 2.4) [37]. Na_xWO_3 bronzes are n-type semiconducting when $x < 0.25$, and become metallic at $x > 0.25$ [59]. So far, studies of Na_xWO_3 structures are limited only to the cubic, nanobelts and nanorods [63], and $Na_2W_4O_{13}$ nanofibers [64]; the triclinic $Na_{0.5}WO_{3.25}$ nanoplates [65]; the cubic and tetragonal Na_xWO_3 nanobundles [43]; the hexagonal $NaWO_3$ nanorods [50]; the triclinic $Na_5W_{14}O_{44}$ nanowires [66], and the Na_xWO_3 nanowhiskers [62].

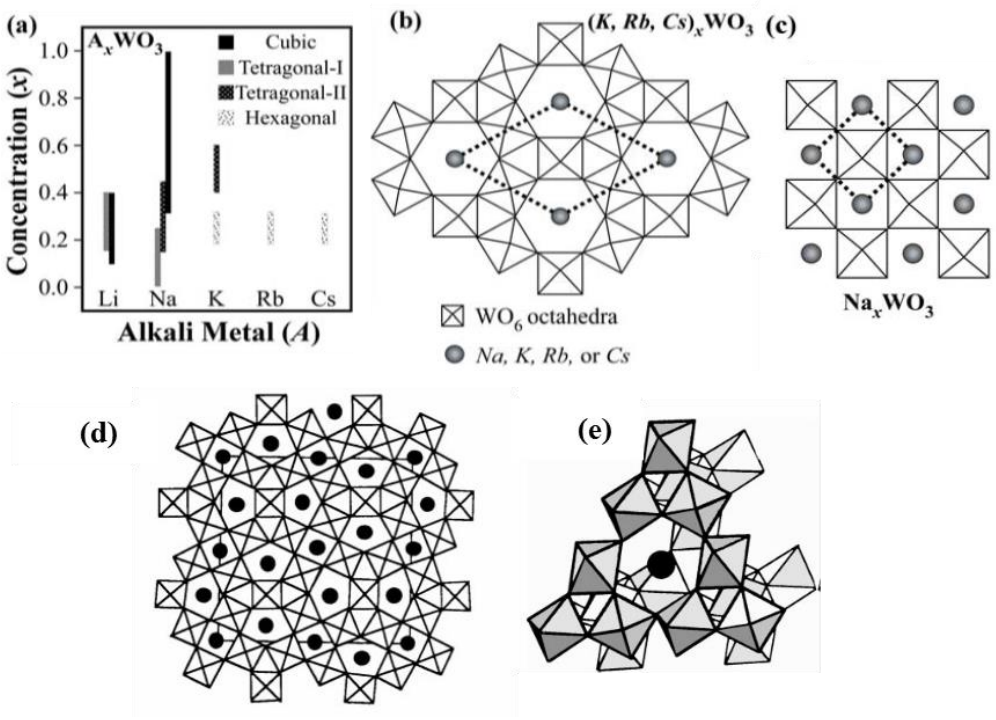

Fig. 2.3 (a) Relationship between crystal structures and compositions for the "alkali-metal tungsten bronzes"; (b) Hexagonal, (c) cubic crystal, (d) tetragonal, and (e) pyrochlore structure of the alkali metal tungsten bronzes [37].

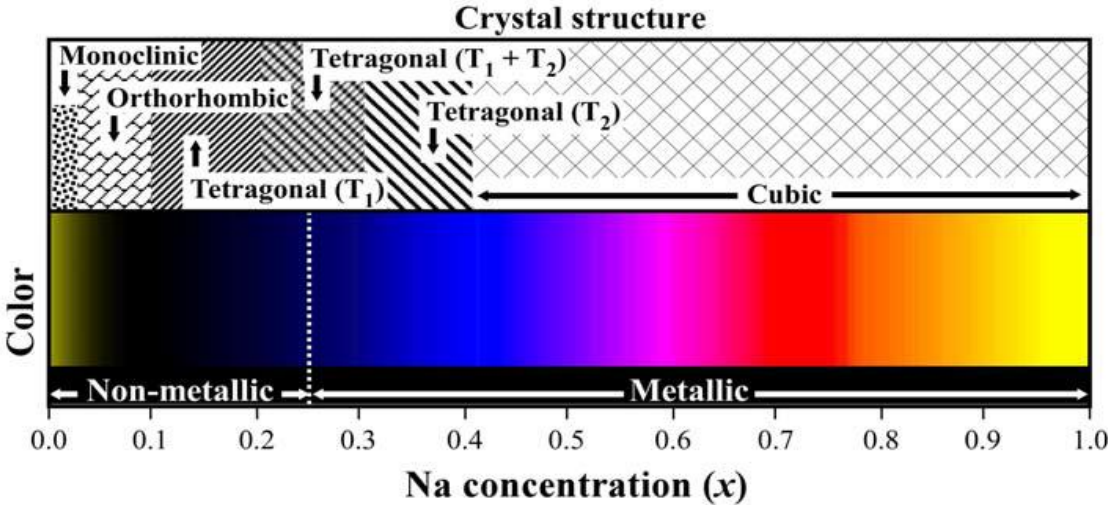

Fig. 2.4 Diagram view of phase diagram correlating the optical properties of Na_xWO_3 with different Na concentration x [37].

Regarding the interaction of WO_3 with H (H_xWO_3), three groups of phases have been categorised as following: cubic with 0.50 < x < 0.6; tetragonal A with 0.33 < x < 0.5; and tetragonal B with 0.15 < x < 0.23 [67]. It is believed that the H

ions form the O-H bonds and modify the host structure of WO_x [68]. The WO_6 octahedra are distorted [R(W-O) = 1.73 – 2.19 Å], compared with the original perovskite structure [R(Re-O) = 1.875 Å], besides the W ions being displaced off-centre, which results in a symmetrisation and decrease of the W-O-W angle in the H_xWO_3 structure from 180 to 170º. Yoon and Manthiram reported the improved performance of interaction of WO_x with H ($H_xWO_{3-\delta}$) for Ni catalyst-based anodes in solid oxide fuel cells, and they documented an over 200 h of stable operation with methane fuel at 650-700 ºC [40]. The H_xWO_3 has also enhanced and promoted the electrocatalytic activity of platinum (Pt) for methanol oxidation [40].

Potassium tungsten bronze (K_xWO_3) with a formula $K_{0.3}WO_{3.15}$ also forms the HTB structure [69]. A few papers have been reported the hexagonal Rb tungsten bronze with different compositions, such as $Rb_{0.3}WO_3$ [56], and Rb_xWO_3 (x = 0.2, 0.214, 0.23 and 0.22) [41]. Likewise, HTBs of alkaline earth metals such as Ca, Sr and Ba have also been prepared under high pressures. Rare earth compounds such as Pr_2O_3 can be used to synthesise Pr_xWO_3 with $0.04 \leq x \leq 0.1$ [54]. Bi_2O_3-doped WO_x can be synthesised as Bi_2WO_6 and $Bi_2W_2O_9$ that both occur as an orthorhombic phase [70].

Other HTB phases have also been reported in both the $WO_3 \cdot 1/3H_2O$ hydrate crystallite where hexagonal layers of WO_6 octahedra are shifted by a/2 from one layer to another layer, and the dehydrated $WO_3 \cdot 1/3H_2O$ crystallites by annealing at temperatures above 250 °C where the structures are stacked directly on top of each layer [71]. The crystal structure of WO_3 hydrates is believed to be of a cubic pyrochlore-type (p-WO_3). Three types of oxygen including intra (O_1), inter-layer (O_2), and inter-layer (O_3) of inter-layer water molecules, which results in four different W-O distances in the first coordination shell. The inter-layer oxygen (O_2) has a very short distance of 1.68 Å, the intra-layer oxygen (O_1) has two medium distances (1.82 and 1.93 Å) and inter-layer water molecule (O_3) has a long site (2.33 Å) [68]. Furthermore, the tilting angle that exists between four neighbouring octahedra within the layer is about 160º.

An amorphous WO_3 (*a*-WO_3) is believed to be a spatial network of tightly bounded clusters that are built from the hydrated WO_6 octahedra sharing with their corners or edges. The network is coordinated by three-, four-, and six-membered rings of WO_6 octahedra sharing with corners [72], however the six-membered coordination is still unsettled. Furthermore, a two-membered coordination was rarely found [73].

2.1.2 Electronic band structure of WO_x

The main features of the electronic band of WO_x refer to the valence band (VB) of crystalline WO_x which is dominated by O 2p-like states; whilst the conduction band (CB) is dominated by W 5d-like states (Fig. 2.5) [74, 75]. The conduction band mainly consists of t_{2g} orbitals ($5d_{xy}$, $5d_{yz}$, and $5d_{xz}$ derived), whereas e_g orbitals ($d_x2_{-y}2$, d_z2) are located at much higher energies. WO_{3-x} ($x < 1$) is presented as a small band of filled states. If the WO_3 structure contains O vacancies (V_o), which is also common in an almost sub-stoichiometric phase, W might form a new oxidation state from 5^+ to 4^+. A position energy levels with the d-symmetry in the CB, whose formation depends on whether or not the vacancy is created in the direction of the -W-O-W- chain [76].

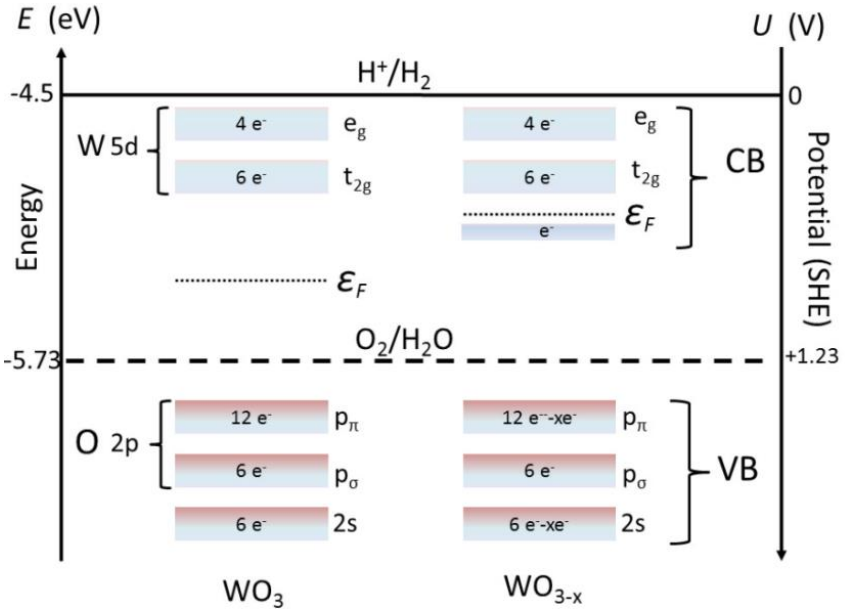

Fig. 2.5 The electronic band states in WO_3 and WO_{3-x} on the y-axis. To the left is the energy (eV) and to the right is the potential, according to the standard hydrogen potential (SHE) in vacuum [76].

To understand the band structures, electronic and optical properties originating from phase transitions of WO_x and associated bronzes, both computer simulations and experimental investigations have been documented. On the theoretical side, Cora *et al.*, reported the electronic, lattice, chemical bonding and mechanical properties of ReO_3, WO_3 and $NaWO_3$ bronze, using the full-potential linear muffin-tin orbital (FP-LMTO) code with in local-density approximation (LDA) function [77]. They found that the CB of WO_3 was empty, while it was half-filled in ReO_3 and $NaWO_3$, by assuming the energy levels A and B in the CB, and I in the VB, in which all these levels were denoted along the Γ-X direction in the DFT-LDA study. The different energies between bands (ΔE) were determined about 0.40, 1.35 and 1.85 eV in ReO_3, WO_3 and $NaWO_3$, respectively. It was also reported that donor atoms (such as Li, Na and H) could introduce extra energy levels inside the WO_x band structure, which made the Fermi level shifted closely to the CB site, whilst reduced the bandgap [78]. Berggren *et al.* also suggested that the Fermi level shifting was related to the W/O ratios in the structure of *a*-WO_x films [79, 80]. Moreover, they also reported that the *a*-WO_x film deposited at high temperatures exhibited smaller E_g, compared with those prepared at lower temperatures [81]. Many exchange-correlation potential approximation techniques, such as the generalized gradient approximation (GGA) [53, 82-84], Hedin-Lundqvist [85], Perdew-Becke-Ernzerhof [75, 86], G_0W_0 [78, 87] etc. as well as other different theoretical methods such as the projected augmented wave (PAW) [75, 88, 89], plane-wave pseudo potential density functional [86], density functional perturbation theory (DFPT) [78], were involved in this sort of study.

On the experimental side of the investigation, the electronic structure of WO_x has been analysed by using X-ray photoelectron (XPS), emission (XES), and absorption (XAS) spectroscopy by Khyzhun *et al*. [90]. Niklasson used an electrochemical method, [91] called intercalation spectroscopy [chronopotentionmetry (CP), gel-vanotatic intermittent titration (GITT) and electrochemical impedance spectroscopy (EIS)], to study the electronic density-of-states of Li intercalation in WO_x. The results of electronic density of stage (EDOS) from different electrochemical methods were used to compare with the computed DOS of the monoclinic WO_3. Other experimental methods including

the high-energy electron-energy loss spectroscopy (EELS) [92], and angle-resolved photoelectron spectroscopy [93] etc. were also utilised to study the electronic and atomic structures of a wide range of WO_x-based materials.

2.2 Synthesis of nanostructured WO_x thin films

Several methods have been pursued over recent years for the synthesis of WO_x nanostructures either as thin films or powder. These methods include thermal treatment [94, 95], sol-gel, Chemical Vapor Deposition (CVD) [96], sputtering [97], template-assited growth, thermal evaporation, pulsed laser deposition, hydrothermal [98], solvothermal [99, 100], etc. Among them, the simple hydrothermal and solverthermal methods appear to be the most effective technique which allows to control the size and shape of the final powder products by easily adjusting the process parameters, such as types of solvents, reactions, surfactants, amounts of persusor, reaction time and temperatures. Different morphologies of WO_x have been sucessful synthesised by this technique, such as the cauliflower-like structures [101], nanorods [29, 102, 103], nanoparticles [104, 105], nanobundles [25], nanoplates [106], and the snowflake-like structures [28]. This technique has also been widely used for composite WO_x-based nanostructure fabrication, such as Nb- [107], Mo- [108, 109], Ce- [110], Al- [111], Cs- [112], and Na-doped WO_3 [50].

The hydrothermal or solvothermal technique is to use W-containing precurcors, such as $Na_2WO_4{\cdot}2H_2O$ [28, 113], WCl_6 [113, 114], in solvents that are ususlly a mixture of alcohol or/and water with/without acids and surfactants. Genarally, different types of agent can be utilised to adjust the pH value of the percusor solution, these includes HCl [115], H_2SO_4, and Na_2SO_4 [103]. From literlature, it has been confirmed that different stuctures of WO_x can be controlled by different hydrothermal reaction time [28, 116], and raction temperatures [106]. Many works have been reported that the pH value of the persulor might be a key to control the morphology and crystallinity of the final WO_x structure [25, 102, 116]. Yang *et al*. comfirmed that the different structure of $W_{18}O_{49}$ can be achieved by using different solvents, such as ethanol, n-propanal, tert-butanol and butylalcohol [100] (Fig. 2.6). Zhou *et al*. also successfully produced different

sizes and morphologies of $W_{18}O_{49}$, as bundles of nanofibres and as 3D hierarchical spheres, by controlling various amounts of WCl_6 used in the synthesis [117].

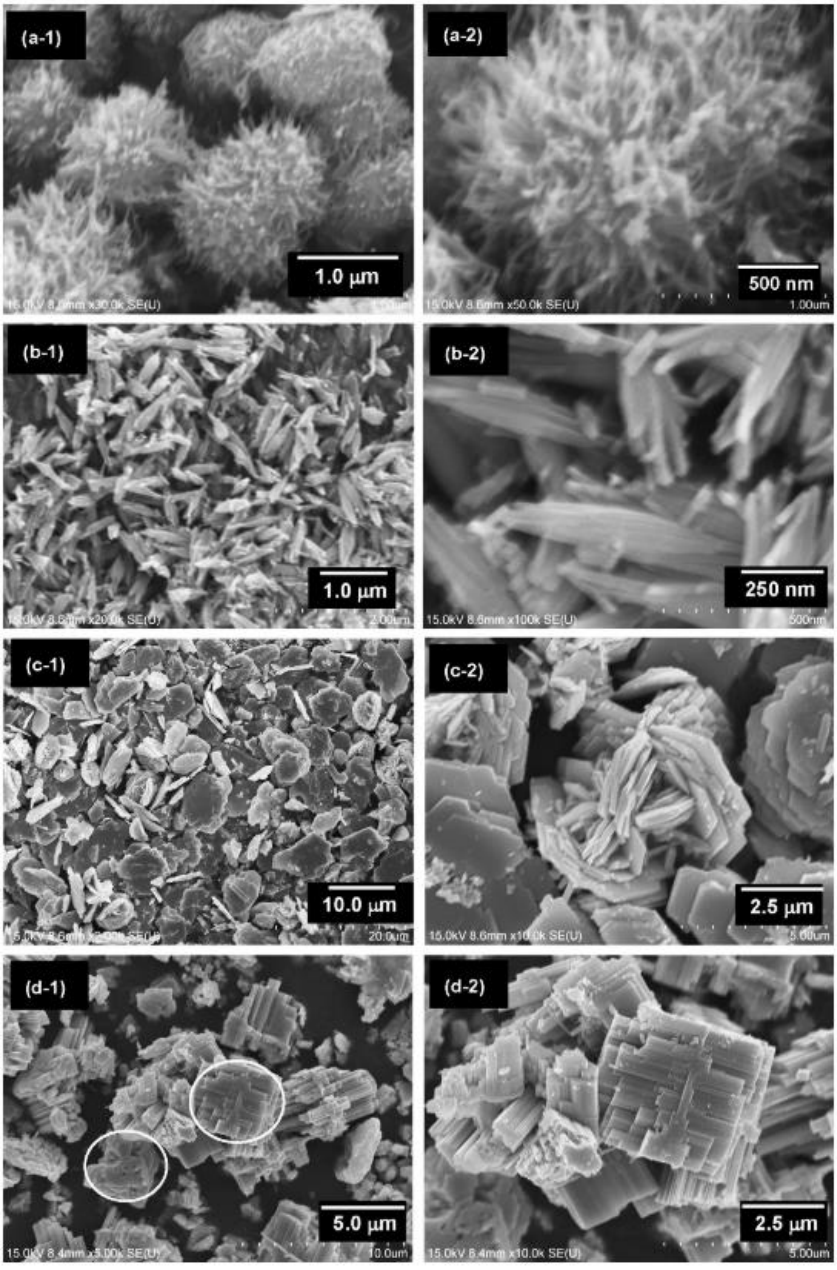

Fig. 2.6 Low and high magnification SEM images of different WO_x products (urchin like nanowire spheres, spindle-shaped nanowire bundles, mixed plates and microrods) via the solventhermal method with diffferent solvents: (a) ethanol. (b) 1-propanol, (c) 8.57 vol.% water-ethanol mixed solution, and (d) 85.7 vol.% water-ethanol mixed solution [118].

$W_{18}O_{49}$ nanorods can also be synthesised by pyrolysing $(NH_4)_xWO_{3+x/2}$ [119]. An electrochemical anodization was used to synthesise WO_3 nanotubes by reacting a W foil in a mixture of Na_2SO_4 and NH_4F electrolyte [120]. The thermal docomposition of $WO(OMe)_4$ at 700 ºC in a closed Swagelo cell under N_2 atmosphere was used to prepare $W_{18}O_{49}$ nanorods [121]. In addition, annealling treatment can convert the $W_{18}O_{49}$ to WO_3 nanostructures [121]. Zumer *et al*. used NiI_2 as the growth promoter in a chemical transport reaction to prepare W_5O_{14} nanowires [122].

Table 2.1 A summary of synthesis methods for WO_x thin films.

Group	Sub-group	Method
Physical Vapour deposition (PVD),	Evaporation	Thermal evaporation [123-127] Electron beam evaporation Pulsed-Laser evaporation [128, 129]
	Sputtering	RF Magnetron sputtering [130-133] Reactive sputtering [87, 134, 135] Ion beam sputtering
Chemical vapour deposition (CVD)		Low-pressure CVD (LPCVD) Plasma-enhanced CVD (PECVD) at low temperature Hot-wire chemical vapour deposition (HWCVD) [3],[9] Electrophoresis [136]
Sol-gel deposition		Dip-coating [137] Spin coating [138-140] Inkjet printing technology [104, 141] Langmuir-blodgett [142, 143] Spray pyrolysis Electrochemical deposition (ECD) [144, 145]

WO_x-based thin films have played a very important part in the construction of chromic devices. Therefore, various thin film production processes have been established, which effectively promoted the chromic device development. There

are mainly three deposition techniques, notably Physical Vapour Deposition (PVD), CVD and sol-gel synthesis, each with many variations. The physical method depends on the evaporation or ejection of materials from a source by using high-energy particle bombardment, to a transparent substrate where the film nucleation and growth take place. The chemical method involves specific chemical reactions of either a volatile compound to be deposited with other gases, or the decomposition and condensation of a compound from a gas phase onto the substrate, to produce a solid deposit. The sol-gel technique starts from a uniform colloidal solution and after being dried, a deposit will be created. Many deposition techniques, as presented in Table 2.1, have been successfully used for the synthesis of thin films of WO_x.

The evaporation process can be realised by means of resistive heating, RF heating, etc., under high vacuum (10^{-6} to 10^{-9} Torr) [146], to allow for the vapour to reach the substrate without reacting with or scattering against other gas-phase atoms in a chamber [147]. Variations of the evaporation techniques based on the power sources include electron beam-, thermal-, laser-, and ion beam evaporation. The deposition rate is controlled by the amount of heat supplied to the material, which could reach thousands of atomic layers per second. Ultra-high purity films (ranging from 5 - 20 nm) can be produced by improving the vacuum state (up to 10^{-6} Torr) in the deposition chamber [146].

For the sputtering technique, both RF and direct current (DC) sputtering have been applied to create WO_x-based thin films, either from a compressed powder of WO_x or a simple metallic W target. The composition and deposition rate (one atomic layer per second) of the film can be easily controlled by tuning the constituents of the inert sputtering gas (such as Ar and O_2) at low pressure (< 4×10^{-2} Torr) [148]. Substrate type, substrate temperature (100 - 400 °C) [149], and the applied power (50 - 400 W) [150-152], all have an effect on the deposition rate (which increases with sputtering power in the range of 2 - 3 nm/s), film thickness (range from 50 nm up to 500 nm), composition, morphology and structure of the resulting sputtered films [153].

Low pressure CVD (LPCVD) process can produce layers with excellent uniformity of thickness. The operation only requires pressures ranging from 0.25 to 2 Torr at high temperature of 600 ºC with slow deposition rates. However, a modified Plasma-Enhanced CVD (PECVD) process can be operated at much lower temperatures (below 300 ºC, even close to ambient temperature) [154], while is only able to deposit on one side of a wafer (1 to 4 wafers) at a time. For both side deposition and large amounts of sample it is better to use the LPCVD technique.

The WO_x also can be formed from a colloidal through a poly-condensation process, either by the acidification of an aqueous salt or by the hydrolysis of an organometallic compound, which is called the sol-gel technique. To obtain a stable metal oxide film, post deposition annealing is necessary [155]. Example colloidal solutions that are suitable for this technique include WCl_6 (precursor) mixed with anhydrous ethanol [144, 156], additionally with an aqueous solution of peroxotungstic acid (PTA) [157], or 0.1 M $Na_2WO_4 \cdot 2H_2O$ solution mixed with HCl [158]. Moreover, the involvement of block copolymer templates such as polystyrene (PS) [140], and P_{123} [144], could result in porous structured thin films.

Another interesting technique is the Langmuir-blodgett (L-B) process. A single layer of molecule, which is organised at the water/air interface as a monolayer before being transferred onto a substrate, can form a thin film on a substrate with a thickness of the constituent molecules. The L-B process offers a level of control over the orientation and placement of molecules on mono- and multilayer [159]. Multiple layers can be created simply by repeating the processes. During the drawing stage of L-B process, the surface tension should be high enough to generate a sufficient cohesion force in the monolayer, to obtain homogeneous multilayers later. The range of tension in the surface layer has been well-documented, and is usually in the range from 10 to 40 mN/m [160].

Electrochemical deposition of metal and alloy species involves the reduction of ions from aqueous, organic or molten salt electrolyses by applying a potential [161]. The low-temperature deposition (<100 ºC) process avoids the corrosion and oxidation of the metallic substrates [162]. Commonly used precursors such as W metal powder [163], WCl_6 [164, 165], and sodium tungstate (peroxotungstic acid) [157, 166], have been reported for the preparation of WO_3 thin films by using this technique.

Spin coating is one of the most common techniques to create transition metal thin films on flat substrates, due to its ability to quickly and easily produce highly uniform films ranging from a few nm to μm in thickness. A typical process involves depositing a small drop of liquid suspension at the centre of the substrate and then spinning at high speed (generally ranging from 1000 up to 10000 rpm) so that the fluid will be spread over the entire substrate leaving a thin layer of fluid on the surface. Final thickness of thin film and other properties generally depend on the nature of the liquid solution (such as drying rate, viscosity, surface tension etc.) and parameter of the spin process (such as spin time, acceleration and especially rotation speed etc.). However, typical drawback of this technique is its lack of material efficiency, as only 2 - 5% of the material remains on the substrate whilst the other 95 - 98% will be flung off into the coating bowl and disposed [167]. Tasaki *et al.* prepared a uniform thin film of Sm-based perovskite-type oxide by using a spin speed of 4000 rpm (Fig. 2.7). The thin film was tested for application as acetylene sensor. Paipiyak *et al.* obtained 400 nm thick Ti-doped WO_3 thin film on an F-doped tin oxide substrate by using 2000 rpm spin rate, and then used the resulting film for optical and electrochromic applications [168]. Others metal oxide thin films such as In_2O_3 [169], ZnO [170], CeO_2 [171], Cu_2O [172] etc. were also successful prepared by using the spin coating technique.

It is obvious that various conventional thin film deposition techniques could be selected to suit for nanoscale thin film fabrication. Thin films consisting of different compositions, morphologies, crystalline structures can be deposited using these techniques, which can be further tuned by using post-deposition drying and sintering, even doping process. Some of these technologies offer a

high level of control in dopant, size, and surface finish at low cost, simply from W and its salt precursors.

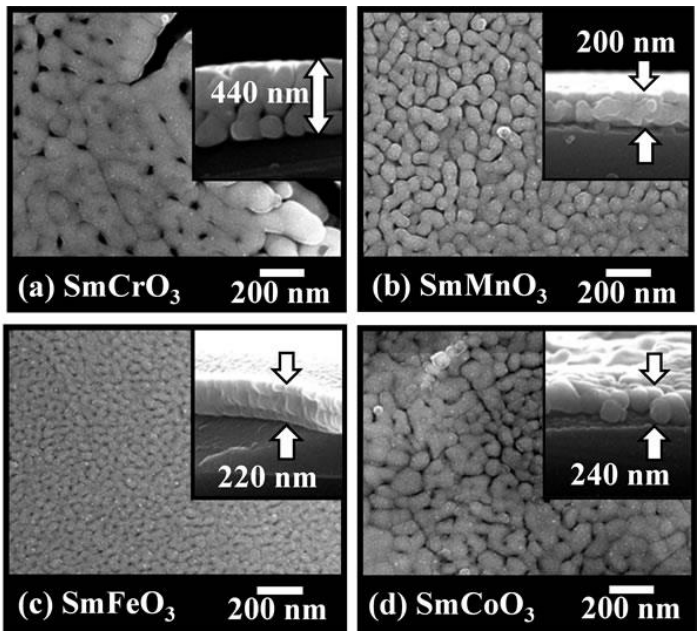

Fig. 2.7 SEM images of uniform perovskite oxide thin films spin-coated on an Al_2O_3 substrate [173].

2.3 Eletrochromic properties of WO_x

Chromic materials change reversibly their optical properties (colour ↔ transparent) in response to changes in environment, such as temperature, light, voltage, gas, etc. Hence, the chromic properties of WO_x can be defined as electrochromic, gasochromic, thermochromic, photochromic. It has been reported that WO_x has better electronic conductivity (10 - 10^{-6} S/cm) and faster Li^+ insertion than many other oxides [1, 101]. Specifically, WO_x exhibits excellent cyclic stability, high CE, good memory and high contrast ratio, when compared with other transition metal oxides, therefore research into this material has attracted a wide attention.

The first interesting electrochromic property of WO_3 thin films was reported by Deb in 1973 [174]. The behaviour of an electrochromic material is an ability to reversibly change, which could be continuously switched between two or more different optical states, upon different potential or current being applied. It is

widely believed that the optical modulation in materials is directly related to the double injection/extraction of electrons and ions in the materials.

Three types of electrochromic material are classified, as follows [175]:

a) Cathodically colouring material presents colour in the reduced state, and bleaches the colour in the oxidised state. This can be explained by Eq. 2.1:

$$\underbrace{xM^{+} + xe^{-} + WO_3}_{\text{Bleaching}} \leftrightarrow \underbrace{M_xWO_3}_{\text{Colouration}} \qquad \text{Eq. 2.1}$$

M is either an alkali metal or H, etc.

b) Anodically colouring materials. For this type, it is bleached in the reduced state and the colouration occurs in the oxidized state. Following Eq. 2.2:

$$\underbrace{Ni(OH)^2}_{\text{Bleaching}} \leftrightarrow \underbrace{NiOOH + H^{+} + e^{-}}_{\text{Colouration}} \qquad \text{Eq. 2.2}$$

c) Materials are coloured in both states; and the mechanism is similar to both types a) and b).

2.3.1 Electrochromic Mechanism of WO_x

For more than several decades, various models have been proposed to explain the electrochromic mechanism of different WO_x phases and structures. The first colour-centre model (O vacancy as the colour centre with one trapped electron) for a colouration of *a*-WO_3 thin film has been proposed by Deb [174]. The energy levels related to 0, +1 and +2 charge states of V_o lie inside the VC, in the band gap, and in the CB of the semiconductor respectively, thus absorbing at different wavelengths. As a result of the optically encouraged variation of the V_o charge state, a change in the absorption property and coloration of the material would occur. On the contrary, Ryan *et al.* have described that the effect of the V_o was dependent upon the availability of both the O p and W d electrons [176], which are different for various phases of the WO_3. Accordingly, they believed that the polaron of the WO_3 was dependent upon both the distribution of V_o and the crystal structures. Lusis *et al.* have proposed that the injected electrons were localised on the W site and the absorption was caused by

charge transfers between WO_x ions. Faughnan *et al.* first introduced the inter-valence charge-transfer (IVCT) model for a-WO_3 thin films. This model considered that inter-valence transfer of W between W^{5+} and W^{6+} (as shown in Eq. 2.3) caused the band absorption in the electrochromic of WO_3.

$$hv + W^{5+}(A) + W^{6+}(B) \rightarrow W^{6+}(A) + W^{5+}(B) \qquad \text{Eq. 2.3}$$

A and B denote the sites where the W^{5+} state has been identified as colour centres in the electrochromism of WO_3. This means that the colouration (or absorption band) was formed in the film with increasing of the W^{5+} state. Schirmer *et al.* explained the underlying physic of the Faughnan model as a small radius polaron absorption [177, 178]. According to this model, inserted electrons are localised in W^{5+} sites and polarise their surrounding lattice to form small polarons. Indicant photons are absorbed by these small polarons which hop from one site to another. The IVCT and polaron absorption processes are similar in that they both constitute electronic transitions between states in the CB [179]. Both the IVCT and the small polaron in WO_3 have a maximum absorption in the near infrared spectral region and in the visible range. The results with optical spectra of a coloured a-WO_3 film absorption from Gabrusenoks *et al.* are also supportive of the IVCT model, rather than the polaron model [180].

Both IVCT and polaron models are consistent with many experiment observations, however they cannot explain when films with higher O deficiency exhibit a better coloration efficiency and colourless in their as-deposited form. Moreover, the M^+ content in the film increases with increasing colouration, as predicted in Eq. 2.1. Gerard *et al.* reported that H^+ content in the film did not increase with increasing colouration [181]. A new chromic model for *a*-WO_{3-y}·*n*H_2O films has been proposed by Bechiniger, in an effort to unify existing models [182]. The model explained that the as-deposition WO_x had W mainly consisted of the W^{6+} and W^{4+} states. This chromic mechanism was based on the small polaron transition between the charge inducing the W^{5+} state and the original W^{4+} state, instead of the W^{5+} and W^{6+} states. If the film mainly consists of W^{6+} and W^{4+} states, it will result in transparent, because there is no polaron

available in the film [182]. This model has been widely accepted by many studies and applied to explain the colouration of *a*-WO_x [125, 128, 183, 184].

As the absorption is of wavelength dependence and is an important source of colour production, the CE of the absorption band becomes higher with the energy side and its maximum position shifts to the lower energy side [185]. Generally, the *a*-WO_3 has a higher colouring efficiency than that of a crystalline WO_3. The CE would increase with increasing sub-stoichiometry. It has been reported that sub-stoichiometric films in WO_x ($2.75 \leq x \leq 3.0$) were very transparent due to the abundant W^{4+} and W^{6+} states in the band and reached a coloured phase when the non-stoichiometry was substantial ($x < \sim 2.75$). Even though the mechanism of colouration in WO_x has been studied for many decades, there are still many phenomena that cannot be well-explained. The huge specific surface areas and large aspect ratios of new nanowires and nanorods may have a significant effect on the V_o states and colour centres of WO_x, correlated with their morphology, crystalline structure and diameters. These emerging characteristics demand intensive investigations in the future.

2.3.2 Electrochromic properties for the chromic material analysis

Many phases of WO_3 have been investigated to understand their structural influence on the electrochromic behaviour. By using either (two- or three-) electrode cells or prototypes of a small device, the electrochromic properties can be investigated by electrochemical analyses [which measures the cyclic voltammogram (CV), chronoamperometry (CA) and chrocoulometry (CC)], combined with results from different types of spectrophotometer. These investigations can not only provide much deeper understandings about the mechanisms of electrochromic phenomenon, but also offer insight on practical solutions to improve efficiencies of a device.

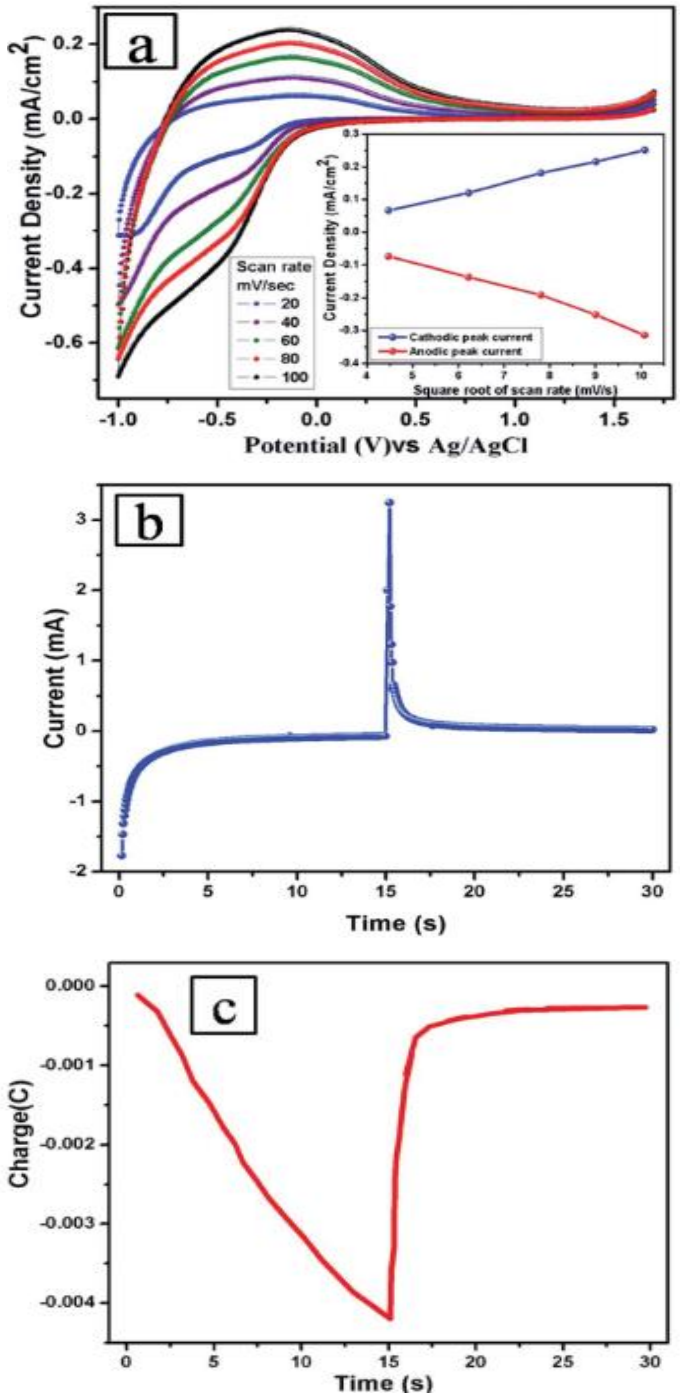

Fig. 2.8 (a) CVs of a WO_3 thin film recorded at different scan rates of 20, 40, 60, 80 and 100 mV, the potential was swept from 1.6 to -1.0 V (inset shows the linear behaviour of the anodic and cathodic peak current densities as a function of the square root of the scan rate). (b) current transient (I-t) plot of the colouration and bleaching of the WO_3 thin film at a pulse potential of ±1 V for 15 s. (c) CC trace of the WO_3 thin film [186].

The cathodic/anodic (redox reaction) behaviour of a WO_3 thin film was investigated via CV, as shown in Fig. 2.8a. An anodic normally presents in the

negative region of the current (reduction reaction). As the co-intercalation of Li^+ and electrons into the lattice of the WO_3 thin film to form Li_xWO_3, the film becomes blue. On the contrary, the cathodic presents as the oxidation reaction (in the positive current region). The de-intercalation of Li^+ and electrons which exist in Li_xWO_3 will be oxidised back to the original WO_3. The effective diffusion coefficient (D) of Li^+ can be estimated using the slope of the peak current *vs* $v^{1/2}$ graph, according to the well-known Randles-Sevick equation, Eq. 2.4 [2, 187]:

$$D = \frac{i_p}{2.69 \times 10^5 \times n^{3/2} \times A \times C_0 \times v^{1/2}} \qquad \text{Eq. 2.4}$$

where i_p is the peak current density, n is the number of electrons transferred in unit reaction (n = 1 in this case), A is the surface area of the electrode film, C_0 the concentration of the diffusion species Li^+ (mol/cm^3), and v the scan rate (V/s).

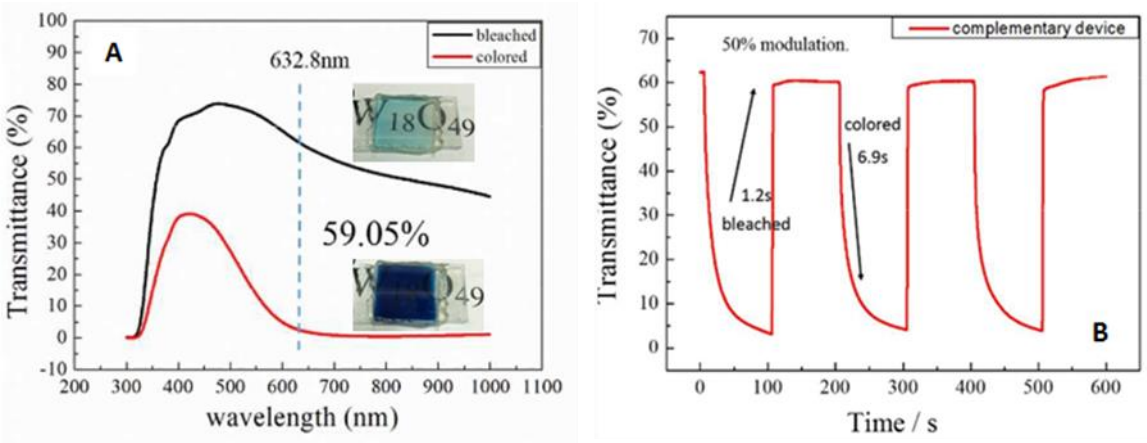

Fig. 2.9 (A) Transmittance spectra of a $W_{18}O_{49}$/Prussian blue device in its coloured and bleached states on an applied potential of ±3 V. (B) In-situ transmittance–time response of the $W_{18}O_{49}$/Prussian blue device at ±3 V, at 632.8 nm [188].

The optical contrast (ΔT) of electrochromic materials has been calculated using Eq. 2.5 [15].

$$\Delta T = T_{bleached} - T_{coloured,} \qquad \text{Eq. 2.5}$$

where $T_{bleached}$ (%) is the transmittance of the sample in bleached state, and $T_{coloured}$ (%) is the transmittance of the sample in coloured state. As shown in

Fig. 2.9(A), the ΔT of $W_{18}O_{49}$ at 632.8 nm was calculated to be 59.06% in the visible range between the bleached state at +3 V and the coloured state at -3 V.

The switching time response characteristics [including the colouration (t_c) and bleaching (t_b) time] of an electrochromic material can be determined according to 90% change in the ΔT, as presented in Fig. 2.9(B). However, this parameter can also be determined as the time needed for the excess current being reduced to 10% of its absolute maximum value from the CA measurement (Fig. 2.8b) [189]. In most cases, bleaching kinetics was faster than the colouration kinetics, because the films had higher resistances during the colouration kinetics from the WO_3 to Li_xWO_3 transition [186]. Another important parameter for chromic materials is the CE, which is expressed as cm^2/C, and defined as:

$$CE(\lambda) = (\Delta OD)/Q_d \qquad \text{Eq. 2.6}$$

where (ΔOD) is the change in optical density at a fixed wavelength, and Q_d is the total amount of charge density injected [can be obtained from chrocoulometry (CC) scan (Fig. 2.8c)]. The CE value might range from 40 to 100 cm^2/C, and the response of coloration and bleaching switching time might vary from milliseconds to a few seconds. Furthermore, the number of bleaching and coloration cycle life relies on the electrolyte used, and can reach 10^6 cycles [190]. The optical density change (ΔOD) of a film can be calculated following Eq. 2.7:

$$(\Delta OD)(\lambda) = \log[T_b(\lambda)/T_c(\lambda)] \qquad \text{Eq. 2.7}$$

where $T_c(\lambda)$ is the coloured transmittance, and $T_b(\lambda)$ is the bleached transmittance [13]. Both CE and OD are based on quantities of the wavelength. ΔOD is also correlated with the transported charge, q (per unit area), as determined in Eq. 2.6 above.

2.3.3 Electrochromic device from WO_x nanostructures

One of the typical applications of the colouration device is as a smart coating in windows of residential and commercial buildings, to reduce energy

consumption, whilst enhancing privacy when needed. Windows are a critical component for a modern building envelope, and are an important element for the effort to improve energy efficiency of buildings. Smart windows allow the efficient use of sunlight by managing the reflection and absorption to realise ideal thermal flows, thus regulating temperatures inside the room.

A typical electrochromic window assembly is illustrated in Fig. 2.10, and its multiple stacking structure consists of an active electrochromic electrode (working electrode) layer, a counter electrode layer, an electrolyte layer (a pure ion conductor) inserting between the two electrodes, and two transparent conducting layers serving as electrical leads and the supporting substrates (glass). Switching on the device by applying a voltage between the two opposite conducting layers drives the cations to migrate from the counter electrode through the electrolyte into the working electrode, so that the device changes its oxidation state and its optical properties (*i.e*. shown as coloured state). In an opposite way (bleached state), the cations such as Li^+ or W^{5+} are resided in the electrolyte and the counter electrode, respectively.

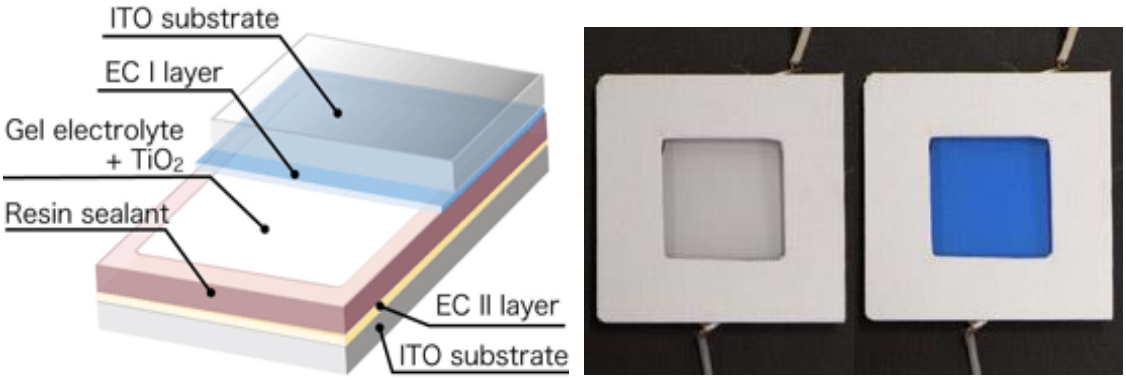

Fig. 2.10 A basic assembly of an electrochromic device consisting of 5 layers: ITO or FTO glass (transparent conductor coated on plane glass)//courter electrode//electrolyte//electrochromic material//ITO or FTO glass [191].

A sealing is required around the perimeter of the device. The sealing is quite important for the device, and it should be free of leakage and has a low diffusion rate for oxygen and humidity, as these are the primary causes of device degradation. To produce devices in a real manufacturing production line, a

simple process like the bar-coating method can be adopted which can cover large areas and create uniform devices [191].

The courter electrode serves for two purposes. The auxiliary electrode Prussian is originally used to carry out investigations on chromic devices. In 1998, Ho *et al.* prepared WO_3-Prussian devices by using solid polymer electrolytes (sodium vinylsulfonic acid and 1-vinyl-2pyrrolidinone) [192]. The CE of the device reached 73.5 cm^2/C at 550 nm at the beginning, however degradation at both the coloured and bleached states was observed, with about 57% loss of charge over a 2 months period for the colouration, and much less stable for the bleaching. The degradation in the coloured state may be caused by the oxidation of the H_xWO_3 electrode; whilst the bleached state degradation might be associated with the hindrance by H_2O in the counter electrode. By replacing the polymer electrolytes with electrochemically oxidiseable and reducible materials for their higher charge carrying capabilities was also discussed in the work [156].

The ion size in the electrolyte plays an essential role in the coloration and its kinetics. As mentioned earlier, the diffusion coefficient (D) of ions during the coloured and bleached process of a WO_3 film exhibited values in the range of 8.82×10^{-13} to 9.59×10^{-11} cm^2/s for K^+ injection/de-injection, and of 7.35×10^{-12} to 1.44×10^{-9} cm^2/s for Li^+ [193]. Lee *et al*. reported that by using H^+ intercalation, a stronger and more reversible coloration in the WO_3 film was observed, compared with the bigger ions like Li^+ and K^+, whilst the Li^+ has shown better performance in the reversible colouration than that of K^+ due to its smaller molecular weight [194]. Therefore, a fast ion diffusion is expected for a small cluster size and low density WO_3 film.

Using a complex multi-layered strategy to further improve the performance has recently emerged. Multiple thin films of different types of oxide metal (NiO_x/Ta_2O_5/amorphous non-stoichiometric WO_{3-x}) were prepared by reactive DC magnetron sputtering and electron beam evaporation techniques. An impressive CE of 82.4 cm^2/C, 6 s and 5 s coloured and bleached time, respectively, and a transmittance variation of 60% have been documented

[195]. Further, the incorporation of WO_3 with Pt to form different types of Pt-coated WO_3 thin films was also discussed recently [196].

2.3.4 Performance improvements

Among different ways reported to improve the device performance, the creation of WO_3 structures into nanoscale to increase their effective surface areas, and the doping with metal, metal oxide or alkali metal compounds etc. is simple and effective. These electrochromic performances include the CE, colouration and bleaching speed (responding time), cyclic stability, long cycle life, optical memory factors, and energy saving functions in operation [12, 197]. In general, a larger area to volume ratio offers a faster kinetics *via* an increased area for reactions and a higher speed of adsorption, thus leading to increases in the sensitivity of the device and decreases in the response time of an electrochromic system [12, 142, 198, 199]. Vijay *et al.* reported that the electrochromic behaviours of a WO_3 nanocrystalline film performed better than a WO_3 bulk form [186]. Li *et al*. found out that different sizes of WO_x nanoparticles indeed led to different electrochromic performances, and by increasing the particle size from 17, 22 to 94 nm, the CE values decreases from 38, 30 to 20.3 cm^2/C, respectively [200]. An improvement of coloration and bleaching characteristics of WO_x porous structures synthesised *via* a simple heat treatment (annealing-treatment) or by an effective sol-gel chemical technique, using tri-block copolymer Pluronic 123 (P123) [201], polyethylene-glycol (PEG) [202], hybrid organically modified silicates (ORMOSIL) [11, 203], as templating agent to form the desired porosities, has been reported. Badilescu, Ashrit and Yang *et al*. generated a high density of pores within the W framework (as shown in Fig 2.11) by using polystyrene (PS) as the template to form a compact network of pores, compared with WO_3 films without using template [156, 204]. Their results showed that films with PS could obtain higher CE values than those without using PS as the template. Annealing treatment also creates shrinkage, crystallization and densification of the oxide materials, and as a result more W^{6+} will be created within the structures [14, 157, 158, 205]

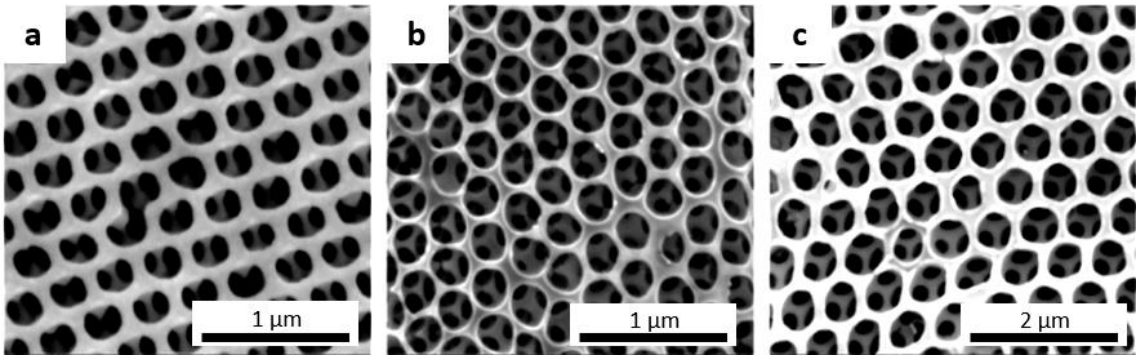

Fig. 2.11 SEM graphs of hexagonal macroporous WO_3 films fabricated using different sizes of the PS template; (a) 325, (b) 410, and (b) 620 nm in diameters.

The electrochromic property of WO_x can be enhanced by combining with suitable amount of metal oxides or metal ions which can lower the oxidizing ability or generate higher electronegativity than W ions, such as VO_x [174, 206], TiO_x [207, 208], Ta_2O_5 [209], and MoO_x [210]. Lekshmi *et al*. reported that the number of charge carriers increases with the increase in the level of Na doping [211]. Lin *et al*. presented that the Ta-doped WO_x can improve the optical modulation by 12.5% at wavelength of 800 nm, and importantly can reduce the colouration time by 5 s, with an increased Li^+ diffusion coefficient of 0.8×10^{-10} cm^2/s [212]. Au-doped macroporous WO_x films were created, and an impressive enhancement of the coloration efficiency to 70 cm^2/C was reported, against a standard porous film of 48 cm^2/C [213].

It has been recorded that the CE value could be increased by altering the amount of O contents of both the over- and sub-stoichiometric WO_x, as the O content plays an important role in generating the W^{5+} states with ion insertions [14, 135, 182, 214-216]. Kim *et al.* prepared thin films at different O_2 flow ratios, various from 0.55 to 0.7 [15], and the result showed that the deposition rate of WO_{3-x} decreased with increasing the O_2 flow rates. Moreover, a highest ΔD and charge density were obtained at high O_2 flow ratios. Liao *et al.* investigated the optical and electrochromic properties of WO_{3-x} nanowire films (W/O ratio ranging from 2.78 - 2.86) after annealing treatment at 200 - 600 ºC [205], and the $WO_{2.86}$ annealed at 500 ºC showed the best CE of 61.3 cm^2/C, against 36 cm^2/C for the as-deposited sample. At the meanwhile, the transmission modulation of 500 ºC annealed sample was also enhanced by 20% at 700 nm,

compared with the as-deposited sample. The annealed and the as-deposited samples both remained reasonably good coloration/bleaching kinetics, at 3 s/1.5 s and 1.5 s/0.5 s, respectively. $WO_{3.2}$ polycrystalline films obtained 22 cm^2/C of CE value with fast response times less than 1 s of coloured state and about 40 s to reach fully bleached state [13]. In addition, three different over-stoichiometric structures, at O/W ratios of 3.3, 3.5 and 3.7, have been demonstrated to exhibit CE values of 213 cm^2/C, 111 cm^2/C and 55 cm^2/C, respectively [14].

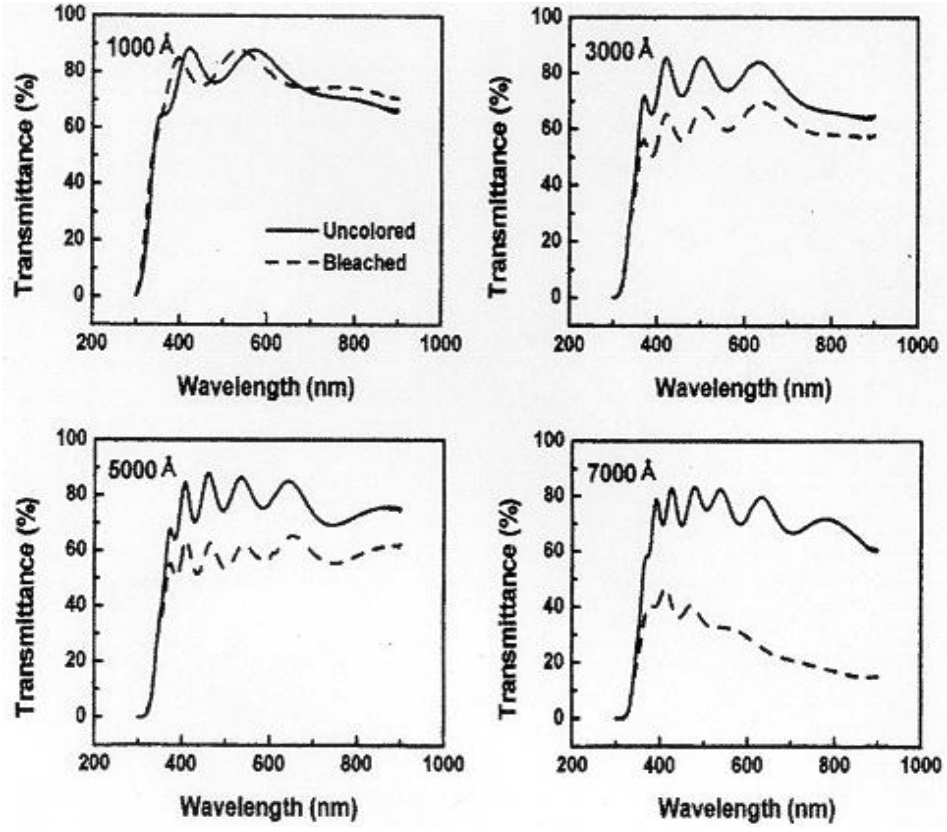

Fig. 2.12 Transmittance of WO_3 films prepared with different thicknesses after coloured and bleached state for 130 cycles [217].

Lee *et al.* determined the variation in the amount of injected charges based on different thickness of the WO_3 thin film (Fig. 2.12) [217]. In a thick film, a high amount of injected charges may be required to provide a high rate of reaction, which could result in unbalanced interference positions before and after the coloured and bleached cycles. The increases of interference position are believed to be the reason for a decreased redox current, originating from changes in the composition and electron structure of the film.

Apart from film thickness, an electrolyte plays an important role in the electrochromic device, as it relates to the mobility of the available ions during the electrochromic switching process (ionic conductivity). The main elements of all typical electrolytes consist of various ion conductors which are combined with different cations (such as H^+, Li^+, Na^+, and K^+,) and anions (such as PO_4^{3-}, SO_4^{2-}, $CH_3CO_2^-$, ClO_4^- and Cl^-), mixing with suitable aqueous and non-aqueous solvents such as acetonitrile, dimethylformamid (DMF), ethylene carbonate (EC), and especially propylene carbonate (PC) [218-224]. The ionic conductivity of electrolytes must be greater than 10^{-4} S/cm at room temperature, to minimize the ionic drop across the device [225]. Although solid polymer electrolytes are reported to have impressive ionic conductivity ranging from 10^{-9} to 10^{-5} S/cm at room temperature, it is still not high enough for practical applications. A liquid electrolyte generally offers a very high value of ionic conductivity, up to 10^{-1} S/cm [226]. A good solvent must possess: (1) high dielectric constant, (2) wide range of operating temperatures, (3) low vapour pressure, and (4) good electrochemical stabilities.

The gel electrolyte can be formed by adding ionically conducting materials into high molecular weight polymers to form a solution, followed by a partial solvent removal. Some commonly used electrolyte polymers are poly(methyl methacrylate) (PMMA), poly(ethylene oxide)(PEO) [227], polyvinylacetate (PVA), polyacrylonitrile (PAN), polyethalene glycol (PEG), and others [228]. Alternative ionic liquid (ILs) electrolyte solvents have reported recently. It has presented slower switching time and lower conductivities of 0.1 to 18 mS/cm (540 or 730 mS/cm for aqueous electrolytes), however presented higher thermal and chemical stabilities, volatility, lower melting points, higher contrasts, and higher safety than those of conventional electrolytes [224, 229]. Room temperature ionic liquids (RTILs) could be considered as molten salts with a considerably low melting point of below 100 °C and an almost negligible vapour pressure [230]. RTILs are usually quaternary ammonium salts such as tetraalkylammonium or cyclic amine-based varieties, both saturated (piperidinium, pyrrolidinium) and aromatic (pyridinium, imidazolium). The first

RTILs comprised chloroaluminate anions which were improved later by having 1-ethyl-3- methylimidazolium (EMIM) cations and tetrafluoroborate (BF_4) anions [229], therefore they are resistant to moisture traces. Zanarini *et al*. prepared WO_3/V_2O_5 electrochromic device using a methacrylate-based polymer matrix (BEMA and PEGMA) with a RTIL or EC/DEC, LiTFSI and D1173 at a ratio of 20:10:57:10:3 wt% gel polymer electrolytes [141]. The switching time of RTIL-electrochromic device was slower (16.7 s for $T_{coloured}$ and 4.8 s for $T_{bleached}$) than those using EC/DEC as the solvent (1.9 s for $T_{bleached}$ and 4.8 s for $T_{coloured}$), however the RTIL-based device showed a higher contrast (33%) than the EC/DEC-based device (20%).

2.3.5 Other applications of WO_x

Apart from being utilised in outstanding electrochromic device, WO_x has also exhibited other promising applications, such as gas or humility sensor [231], solar cell [232], optical-modulation devices [233, 234], light emitting [235, 236], catalyst [237, 238], lithium-ion battery [239, 240], etc. Different WO_x and WO_x-based structures have been studied on various target gases such as ammonia [241], ethanol and NO_2 [242], H_2S [243], H_2 [244] etc. Zhu *et al*. prepared a self-heating gas sensor prototype, based on $Pt/W_{18}O_{49}$ nanowires network (Fig 2.13). The prototype is highly sensitive to H_2 gases (lower than 50 ppm) by using low power of 30-60 mW at 6 V. Also, the prototype has low responding on C_3H_8, CO, CH_4 and ethanol gases. The degradation of Pt/WO_3 films are caused by the water from atmospheric humidity and air poisoning, which located in the films [245-247]. Doping WO_3 with metal oxides, such as Bi_2O_3[248] or La_2O_3 [249], resulted in improved gas sensing properties for VOC (such as toluene xylene and benzene) and for low amount of NO gases. Other Cr- [250], Cu- [251], Au- or Al- [252], Fe- [198, 253], Pd- [254] doped WO_3 were also used to study as ozone, CO, ethanol, H_2S, NO_2 or CO detectors. The sensitivity of Au- and Pd-doped WO_3 film sensor can be obtained about 4.1 and 1.4 times higher than that of the plain WO_3 film sensor [254].

Fast and deep colouration gasochromic properties can be obtained by using combining WO_3/V_2O_5 thin films [255]. *a*-TiO_2 and mixture of *a*-TiO_2/*m*-WO_3 also

shown good gasochromic activity under H_2 exposure [256]. Chen *et al.* proposed less than 10 ms of coloured switching time by using Pt/WO_3 [257]. The reason of coloration contrast degradation in gasochromic properties was also explained as an indicator of air poisoning and/or aging as same in gas sensor application [258]. Coating the WO_x gasochromic thin films with polydimathylsiloxane (PDMS) as a protective layer can help to prevent air poisoning. Fewer studies on photochromic property of WO_x have been reported. As-prepared amorphous Nb-, Ta-, Ti- and Zr-doped WO_3 with heat treatment ranging from 100 to 450 °C showed good results of photochromic responding.

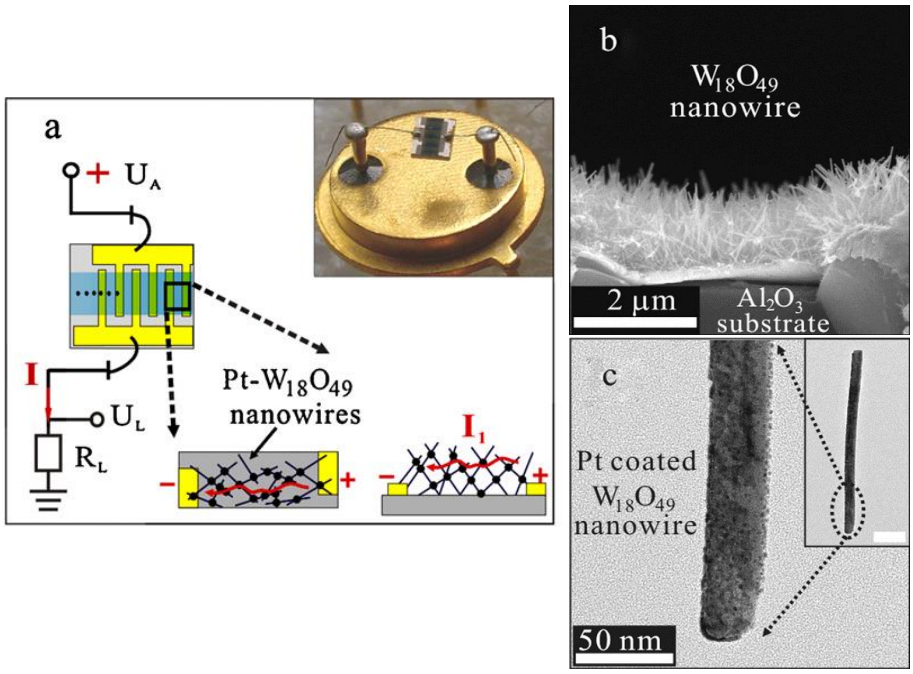

Fig. 2.13 (a) Schematic arrangement of electrical measurement for the gas sensor experiment (inset: prototype sensor), (b) SEM image of the $W_{18}O_{49}$ network in cross-section view, and (c) TEM image of $W_{18}O_{49}$ nanowires coated with Pt particles [259].

The best transmittance values of 59.35% and 73.49% from Zr-WO_3 2 layered films and 3 layered films were obtained [260]. Shen *et al.* improved the photochromic property by doping Al particle into WO_3 structure [111]. The photochromic effect of WO_3 is generally limited to the high energy near-UV range. Bechinger *et al*. however have tried to study and overcome this limitation by using a thin CdS layer as the photocatalyst deposited underneath a WO_x thin film [261]. A study of WO_3-MoO_3 composite film has claimed that the samples

exhibited coloration under the visible light (2.15 eV that matches with the peak of eye-sensitivity curve between 1.7 and 3.3 eV), whilst the absorption peaks for pure MoO_3 or WO_3 out of eyes responsive range are 1.56 and 1.4 eV, respectively [262, 263]. Double layer-coated film of $Cs_{0.33}WO_3$ tungsten bronze nanoparticles was reported to exhibit 80% and 10% transmittance at 550 nm (in the visible region) and 1000 nm (near-infrared region), respectively, yielding a haze value of 1% or less [264]. More complex glass transition systems such as $NaPO_3$-BaF_2-WO_3 [265], $SbPO_4$-WO_3 [266], and Na_2O-WO_3-$SbPO_4$ [267], have also been prepared successfully to display interesting photochromic performance, with large absorption band extending from the near infrared to the visible range.

According to thermochromic glazing study, a high T_c of 95 °C would be ideally suitable for a coating on solar thermal collectors [268]; whereas a low T_c at around 35 °C would be desirable for use as coating on thermochromic window [269]. Coatings of W-doped VO_2 ($V_{1-x}W_xO_2$) thin films as the glazing of a solar collector have been prepared by using the thermal evaporation technique which aims to protect solar thermal systems from overheating without involving any mechanical devices. At only a 0.17 at% of W-doping, the T_c can be lowered from 68 °C for pure VO_2 to 49.5 °C [269]. Indeed, to achieve high absorption (α) (*i.e.* low reflection) surface in the solar spectrum range (0.3-2.5 μm), and low thermal emittance (ε) (*i.e*. high reflectance) in the infrared spectrum range (2.5-30 μm) to minimize heat re-radiation losses at suitable transition temperatures, are the main objectives of recent energy-related studies [270]. Jin's group have confirmed such reduction in $V_{1-x}W_xO_2$ films, and obtained a reduction efficiency associated with the W content, as low as 24 °C at a few percent of WO_x doping. They have achieved a comfortable temperature range by adopting x as 0.05 to 0.06 (about W/V ratio is 5 to 6%) [271, 272].

Because the band gap of WO_x is situated within the solar spectrum range, WO_x are one of the solar energy transformation materials. Using WO_3 as an anode interfacial layer between top electrode and photoactive layer in polymer solar cells (PSCs) with TiO_2 nanocrystalline as electron selective layer can obtain an impressive enhancement in power conversion efficiency compared with that

without the WO_3 layer [273]. Tan *et al*. also used WO_3 as a buffer layer in both origin light-emission diodes and PSCs of substitute PEDOT:PSS [274]. By adding high mobility (9.4×10^{-3} $cm^2/V{\cdot}s$) and high light transmittance, the WO_3 layer could be ascribed to increase the hole collection and charge transportation efficiencies in PSCs applications. 6.36% under the illumination of AM 1.5G and 100 mW/cm^2 of power conversion efficiency was obtained. Highly promising for future WO_3-buffer light-emission diodes (LEDs) for the next generation of lighting and display applications have also been reported by a few studies [236, 275-277].

In recent years, there have been growing interests in WO_x-based catalyst due to their unique acidity performance that improves the activity and selectivity, thermal and chemical stability, which relate them to versatile applications, such as green oxidation process [278], synthesis of malonic acid ester [238], metathesis and isomerization of alkenes [279-281], dehydration of alcohol [282], hydrodesulfurization [283, 284] and hydrocracking of heavy fractions [285] in the petroleum area. In addition, WO_3 has also played a role in flexible energy storage development. Original WO_3 thin films were used as a negative electrode material for solid state Li-ions batteries [286]. Flexible WO_x-C nanofiber electrode were also investigated as an anode for Li-ions batteries, resulting in high stability, large capacity and good rate performance [240]. $WO_3{\cdot}2H_2O$ has recently been demonstrated as a new candidate for developing pseudocapacitive electrode in layered transition metal oxide for high-power energy storage [287].

2.4 Summary

This chapter provides an overview of the recent research on the structures and properties of the broad family of WO_x nanomaterials, including the latest developments of utilising their different forms in various chromic applications, and the main technical challenges, with specific interest on energy-related device constructions. Based on the background understanding of WO_x, the main objectives of this thesis have been defined, as follows:

- To synthesise pure WO_x and doped-WO_x structures, including Na, La and Ce-doped WO_x, using the sol-gel technique.
- To investigate the structure and morphology of the original WO_x nanomaterials, compared with the modified WO_x, using different stuctural characterisation techniques, such as XRD, SEM, TEM, Raman, XPS etc.
- To understand the phase transition of both WO_x nanoparticles and nanowires, using in-situ techniques.
- To observe and analyes the electrochromic properties of all WO_x-based thin films, and obtain different parameters including the Diffusion Coefficienct (D), Colouration Coefficienct, stability, switching time, etc.
- To further improve the electrochormic properties of resulting WO_x nanomaterials, using low temperature annealling technique for the WO_x thin films, linking the structural feature with the electrochemitry characterisations.
- To investigate and optimise the effects of different type of gel electrolytes on the electrochromic performance.
- To understand the mechanism of colouration and bleaching process of WO_x thin films using XPS analysis.
- To explore the feasibility of preparing electrochromic device on soft substrate, and investigate its electrochromic performance.

Chapter 3 Experimental methodology

3.1 Introduction

This Chapter presents the general information of characterization techniques used in this thesis. Detailed structure and properties investigations will be further described in each relevant Chapter. In this thesis, WO_x and doped WO_x compounds were synthesised using a solvothermal technique. The structure and morphology were characterised by a series of techniques, including X-ray diffraction (XRD), Scanning Electron Microscopy (SEM), Transmission Electron Microscopy (TEM), Raman spectroscopy and X-ray Photoelectron Spectroscopy (XPS), etc. The electrochromic properties were mainly evaluated by using a 3-electrode electrochemistry potentiostat and UV-Vis spectroscopy.

3.2 Materials and synthesis technique

3.2.1 Materials

All chemical compounds and solvents for the synthesis of the WO_x-based products in this thesis are purchased from Sigma Aldrich, including Tungsten Hexacholoride (WCl_6, 99.9%), Cerium(III) Chloride Heptahydrate ($CeCl_3{\cdot}7H_2O$, 99.999% trace metal basic), Lanthanum(III) Chloride Heptahydrate ($LaCl_3{\cdot}7H_2O$, 99.999% trace metal basic, Sodium Chloride (NaCl, 99%, AR grade), Tungsten Oxide nanoparticles (WO_3, <100 nm particle size) and Cyclohexanol (99% purity). For the thin film preparation process, ethanol (C_2H_6O, absolute, extra pure, SLR, Fisher Chemical) and Indium Tin Oxide coated polished glasses (ITO, 10-15 ohm/sq, Japan AGC Polished grade, 75 mm × 25 mm × 1.1 mm, Kintec Company) were used as the solvent and substrate, respectively. The gel electrolyte consisted of Lithium Perchlorate ($LiClO_4$, Battery grade, dry 99% trace metal basis), Propylene Carbonate (PC, anhydrous, 99.7%), Poly Propylene Carbonate (PPC, average M_n ~50000) and 1-n-Butyl-3-Methylimidazolium Tetrafluoroborate (BMIMBF 4, 98+%) ionic liquid.

All were purchased from Sigma Aldrich, except the ionic liquid which was purchased from Alfa Aesar.

The materials used for device preparation were Gene flame spacer (125 uL, 1.7 × 2.8 cm^2 purchased from thermos Fisher Scientific), a UV-light sensitive gel nail polish (from Eleacc) and a UV light bulb (model F20T12, 20 watts). Moreover, a Platinum target (Pt, Annular, 82 mm OB, 60 mm ID, 0.1 mm thick, Quorutach) was used to prepare the thin film as the counter electrode of the device, by using the sputtering technique. Finally, an adjustable DC regulated linear beach power supply (0 - 18V, 0 - 2A, Circuit Specialists) was used as the power source for the chromic testing.

3.2.2 Synthesis technique

Among various techniques for the synthesis of WO_x nanocrystalline structures, solvothermal is one of the well-known and efficient processes. This method has advantages such as good energy efficient, high product purity, easy processing and product geometry control, etc. Therefore, it has been widely used to prepare a variety of materials, in diverse geometries including powders, single crystals, nanocrystallines, and thin films of different metals, ceramics and polymers, in the form of rod, wire, sphere, *etc*. By controlling the solvent supersaturation, chemical concentration, and reaction kinetics, the composition and geometry of the products can be controlled to some extent. The disadvantage of the solvothermal technique is the low yield at batch process, which can be overcome by high-throughput continuous the solvothermal/hydrothermal reactions.

Solvothermal technique is very similar to the hydrothermal route. In both cases, reactions are proceeded in a sealed reactor, known as an autoclave or high-pressure bomb. The only difference is that the precursor solution is usually not aqueous for a solvothermal process. The solvothermal synthesis involves heating the solvents and metal coordination compounds in the presence of an organic capping agent at high temperatures. The process usually comprises three stages: (1) heating of the solution during dissociation of the metal precursor (usually occurs above 523 K); (2) aging of the solution at a desired

temperature for particle nucleation and growth. This is a critical stage that determines the final particle size and surface properties of the products; and (3) particle separation and collection from the unreacted materials and the solvent [288].

The solvothermal reactor generally consists of two main parts, outer high-quality stainless-steel jacket to hold the high pressures, and inner Teflon or other alloys (such as platinum, gold or silver) liner chamber to protect the autoclave body from the highly corrosive solvent at high temperatures and pressures. In this thesis, an acid digestion bomb (Model No 4748 from Parr Instrument Co. UK) was used. It has a 125 ml removable PTFE cup in the stainless-steel body, with six cap screws in the screw cap to seal the flanged PTFE cup. The bomb should be operated within the limited maximum pressures and temperature, which is 1900 psi and 250 °C respectively for this model, for safety reason. For all samples synthesised in this project, the precursor solution was fixed at 50 ml for this autoclave and reacted at 200 °C.

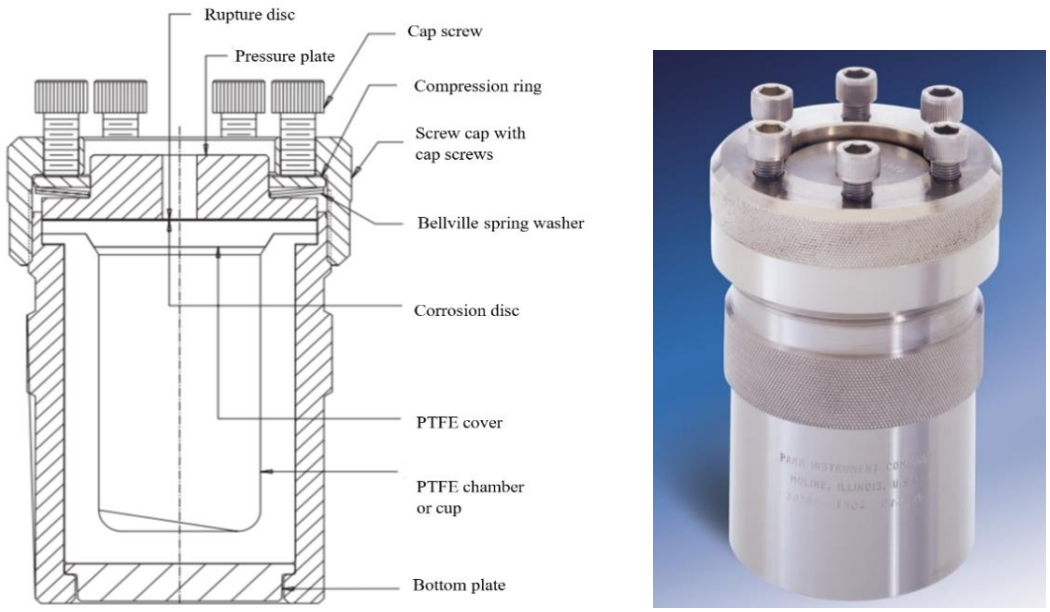

Fig. 3.1 A schematic and a picture of the solvothermal reactor used in this work.

3.2.3 WO_x thin film preparation

Thin films of WO_x nanowires on a conductive substrate were prepared for further electrochemical and chromic property assessments, by using a common spin coating technique. In a typical preparation, 0.1 g of each WO_x-based powder was dispersed in 2 ml of ethanol in a beaker, which was well-mixed by using an ultrasonic bath treated for 1 h, to create a uniform suspension. The uniform suspension was then immediately dropped onto an ITO conducting glass substrate. The substrate of 3.75 × 2.5 cm in size was sitting inside the spin coater. An operation protocol was developed as following: the machine was set up at 1200 rpm for 5 s in the first step, and then continued to spin at 1500 rpm for further 5 s. Each sample was re-coated for 6 rounds to obtain a good and uniform coverage of a desired film thickness, and then dried at 80 °C in an oven for several hours. The thickness of the films, which was around 400 nm on average for all samples, was measured using the Profilometry technique.

3.2.4 Electrochromic device preparation

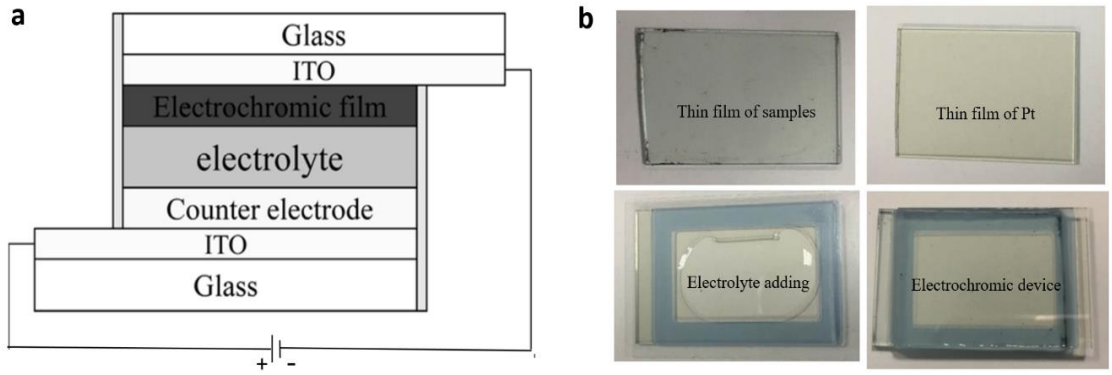

Fig. 3.2 A schematic (a), and the actual prototype (b) of a chromic device

A schematic assembly of a complementary prototype electrochromic device is shown in Fig. 3.2. The configuration of different layers is illustrated. Firstly, we need to prepare the electrochromic reactive WO_x layer. The WO_x thin films on ITO substrate are prepared as described in the above section. Secondly, we need to prepare for a counter layer with excellent stability and conductivity, to pair with the WO_x-ITO substrate in the device. In this case, a thin film of Pt coated ITO glass substrate was used, which was prepared by using a sputtering technique, to achieve a thickness of about 6 nm. Thirdly, a fixed space for the

electrolyte between the above two substrate layers was required. For reproducibility and manufacturing considerations, a gene frame spacer was chosen which allowed for the two substrates to host the gel electrolyte. Fourthly, a proper seal of the electrolyte was very important for the performance and service life of the device, as any leaking or degradation would be problematic. After numerous attempts to use various adhesives, a UV-light sensitive nail polish gel was chosen to seal around the edges of the device after all layers were sandwiched together, due to the low cost, effective seal and easy to handle features. Finally, after drying under a UV light for about 1 h, a prototype device was fabricated (Fig. 3.2b).

3.2.5 Gel electrolyte preparation

A certain amount of $LiClO_4$ was dissolved into PC or/and ionic liquid solvent to achieve a Li^+ concentration of 0.5 M. The mixture was well-mixed under magnetic stirring at room temperature for 6 h, and then different w/v% of PPC was added into the homogenous solution and continuously stirred for overnight to obtain the gel electrolyte. The exact amount of PPC w/v% will be shown in the experimental results in following Chapters.

3.3 Structural and morphological characterization techniques

To understand the structure and morphology of our materials, we used various techniques as described earlier to characterise them. A brief introduction of the working principles of each technique, including X-ray diffraction (XRD), Scanning Electron Microscopy (SEM), Transmission Electron Microscopy (TEM), Raman spectroscopy, X-ray Photoelectron Spectroscopy (XPS), Electrochemical potential stage and UV- vis spectroscopy will be presented below.

3.3.1 XRD

XRD shows the fine structural feature of a crystalline material, either in bulk or powder or thin film forms. When a sample is irradiated by the X-ray beam

(incident X-ray) from the generator and produces constructive interference (which occurs only at specific wavelengths, crystal lattice planar spacing and angle of the incidence) after reflection, the resulting diffraction will be recorded with a detector as the intensity of the diffracted beam. The relationship between incident X-ray beam and diffracted X-ray can be explained following Bragg's Law: $n\lambda = 2d\sin\theta$, where n is any integer, *d* is the spacing between the adjacent crystal planes, θ is the angle between the incident X-ray beam and the scattering plane, and λ is the wavelength of the incident X-ray [289, 290]. Schematically, Bragg's Law is shown in Fig. 3.3.

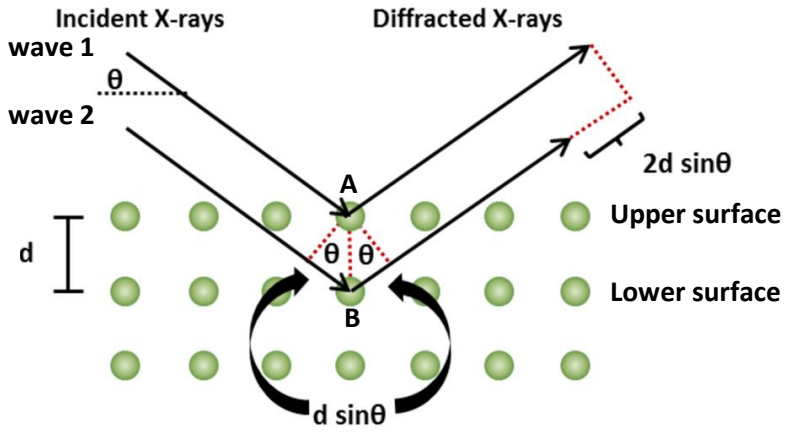

Fig. 3.3 An illustration of the reflection of an X-ray beam from two parallel crystalline planes separated by a distance *d*. The reflection from the wave 2 travels further than wave 1, by a distance of $2d\sin\theta$ [291].

The Bragg equation allows to determine the distance between the crystal lattice planes of the atoms that produce the constructive interference (d_{hkl}), by using the position of the diffraction peak and wavelength of the X-ray source. Moreover, the Bragg diffraction peak is also related to the average crystallite sizes. By using Scherrer's formula, $L = \frac{k\lambda}{\beta cos\theta}$ (where *k* is constant, λ is wavelength of the X-ray source, β is Full width at half maxima, and θ is the half of the diffraction angle (Bragg angle) [292], one can work out the average crystallite sizes. During testing, the machine generates data consisting of a record of photon intensity and detector angle 2θ. Plotting 2θ versus intensities will result in a diffraction pattern with various peak positions and intensities.

These positions and intensities can be used to identify crystalline phase and lattice constants, by comparing with the standard reference patterns from data base.

In the present work, a D8 advanced X-ray diffractometer (XRD, Bruker, UK) with a Cu radiation generated at 40 kV and 40 mA was used as a primary technique for identifying and quantifying the nanowires we produced. The scan is normally from 2θ = 10-70, at a step size 0.03° with a dwell time of 1 s. We used the EVA program to assist the results comparison and analysis. To prepare the sample for XRD measurement, 0.2 g dry powder of the sample was simple placed and flattened on a glass substrate. Due to the limited amount of sample, we did not use the standard sample holder to prepare specimens for XRD testing.

3.3.2 SEM

In the SEM system, a highly concentrated electron beam from the cathode at the top of the device passes through a magnetic lens and directly hits the top surface of a specimen that is normally located in a vacuum chamber. A variety of electron signals from the surface of the specimen, such as X-rays, primary back scattered electrons and secondary electrons, etc. will be generated. These signals are collected by different detectors and sent to a cathode ray tube which allows to translate to a 2-diametional image on a screen. A schematic of an SEM is presented in Fig. 3.3. In general, two main detectors are normally utilised in an SEM, which are used to detect the primary back scattered and the secondary electrons. The back scattered electrons are a reflection of primary electrons from the source after hitting the specimen surface; whilst the secondary electrons are own electrons of the specimen that released after being excited by the source electron. In this thesis, a HITACHI S3200N SEM equipped with a tungsten filament was used to analyse the morphological features of all samples, operated at 20 kV.

To prepare the sample for SEM investigation, a low concentration suspension of each sample in acetone will be prepared and dropped onto a Si wafer. After drying for overnight at 80 °C, a thin film will be obtained on the Si wafer. The

wafer is then stuck onto an Al SEM sample holder using a double-sided conductive carbon tape, and the sample is ready for observation. In case of poor conductivity of the samples, a sputter coater can be used to provide an ultra-thin coating layer of Au (about 1-2 nm) on the sample, to provide a better conductive path between the sample and sample holder, and to eliminate charging which results in blur images.

3.3.3 TEM

TEM is a technique used to observe the features of very small specimen and able to provide higher magnification and higher resolution image compared with SEM. As shown in Fig. 3.4, TEM uses an accelerated electron beam, the same as in a SEM system, which passes through a region of very thin specimen, focusing by a condenser lens inside a vacuum chamber [293, 294]. Part of the beam (un-scattered electrons) will be transmitted and magnified by other lenses, thus projecting the final high-resolution image onto a fluorescent screen at the bottom of the machine, or directly forming images in a digital camera. The sample thickness is normally less than 100 nm, to allow for electron transparency.

TEM also allows to focus the beam onto one specific point of the sample, to obtain a selected area electron diffraction (SAED) pattern which in principle is the same as the X-ray diffraction. Diffraction patterns are formed at the back focal plane and the resulting image where the electron scattered at the same direction by the sample is collected into a single point. Compared with XRD, SAED can obtain much finer localised details about phase structure, crystal orientation, and lattice spacing of the sample, from micron down to nanoscale.

In this work, a JEM-2100 TEM will be used to acquire the HRTEM and SAED images of the samples. It has a 0.25 nm point resolution and a 0.14 nm lattice resolution when it is operated at 200 kV. TEM samples are prepared on a 3 mm holy-carbon coated Cu TEM grid. A low concentration sample suspended in acetone will be prepared, probe-sonicated, and dropped onto the TEM grid. After drying for overnight at 80 °C in an oven to eliminate potential solvent

contamination to the high-vacuum chamber inside the TEM column, the sample will be ready for investigation. In addition, an Energy-Dispersive X-ray spectroscopy (EDX, Oxford Instrument System, liquid nitrogen-free SD detector,

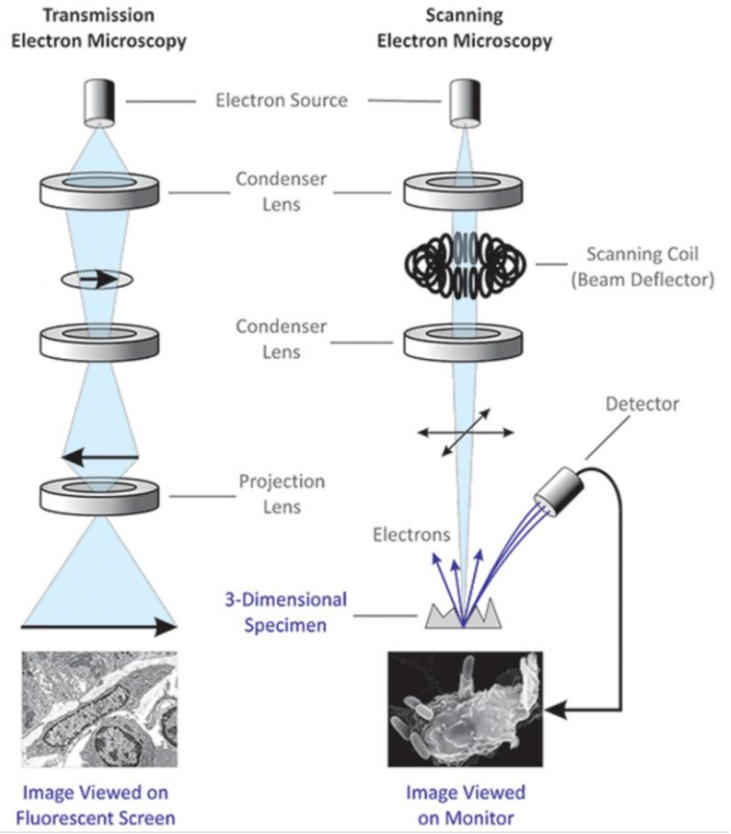

80 mm^2, 138 eV), attached to the TEM, will also be used to analyse the chemical elemental information of the samples. Both point analyses and elemental mapping are used.

Fig. 3.4 Schematic comparison of the principles between TEM and SEM [295].

3.3.4 XPS

XPS is used for surface compositional analyses that can provide elemental information, including empirical formula, chemical states and electronic state of a material's surface (approximately up to 1-10 nm in depth). An XPS spectrum is obtained by exciting the surface of a sample using an X-ray beam, which causes photoelectrons to be emitted from the first few atomic layers of the sample surface. A photoelectron spectrum is recorded by counting the ejected electrons over a range of electron kinetic energies. Peaks appear in the

spectrum from atoms emitting electrons of a specific characteristic energy, thus the atomic composition of the sample or the chemical states of a certain element can thus be determined.

We used XPS to determine the different of surface chemical states of different elements and estimated the relative composition of these constituents in the surface region for all samples. Due to the ultrathin nature of the nanowires, 2-5 nm, and the potential depth the X-ray beam can penetrate, we believe that the surface information obtained from the XPS examination will be a reliable reflection of the states of the nanowires. In this study, a Kratos AXIS ULTRA spectrometer with a mono-chromated Al KR X-ray source (1486.6 eV) operated at 15 kV anode potential and 10 mA emission current will be used for the assessments, operated under high vacuum condition.

3.4.5 Raman spectroscopy

Raman spectroscopy arises from molecular vibration which causes changes in polarizability of the molecule. This technique can be used for sample identification and quantitation, because different molecules have different sets of vibrational spectra or frequencies. When a light source (energy) is irradiated onto a molecule, the molecule will absorb and re-emit photons, which causes vibration and rotation of the chemical bond inside the molecule. The Raman scattered light is therefore generated and detected as the Raman spectrum. Raman scattering includes both stokes and anti-stokes modes, occurring when there is an energy transfer between photon and the molecule. The stokes is a process in which the photon has lost energy to the molecule; whereas the anti-stokes is a process in which the photon has gained energy from the molecule. The peak appearing in the Raman spectrum can thus be devised from a specific molecule or lattice vibration mode. Peak positions show the specific vibration mode of each molecular functional group included in the material.

For the present study, a Renishaw RM1000 Raman machine with a laser power of 49 mW will be utilised to track the changes in the molecule structure of samples. A 532 nm laser at 10% of power output will be used to excite and scan

the wavelength range from 100 to1000 nm. The sample will be prepared into a thin film via drop-coating onto a glass slide or Si wafer substrate.

3.6 Property characterization

3.6.1 Electrochemical potential state

For electrochemistry measurements, a standard three-electrode cell was used to carry out the investigations, with Pt, WO_x thin films and a non-polarizable Ag/AgCl as the courter, working and reference electrodes, respectively. In this system, (1) the counter electrode is used to ensure that current does not run thought the reference electrode, as such flow would change the potential of the reference electrode. (2) The working electrode is the indication electrode where reduction and oxidation being investigated will take place. (3) The reference electrode is used to detect the potential across the working electrode and electrolyte (should be non-polariable).

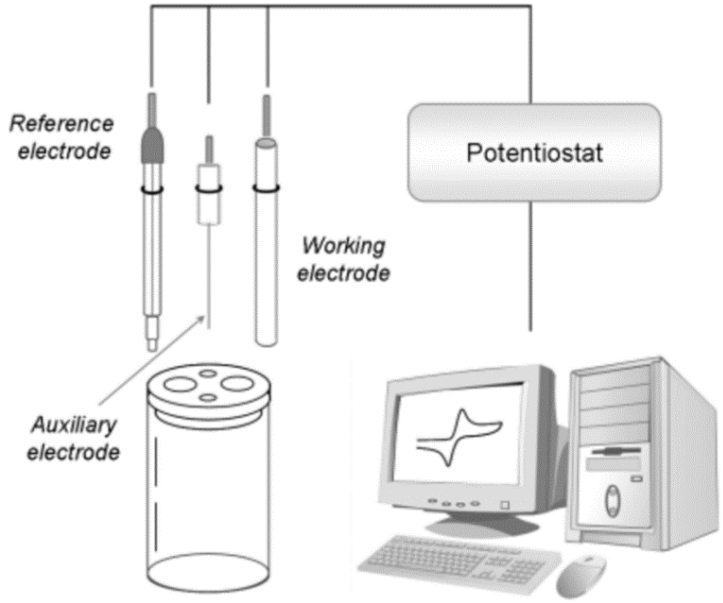

Fig. 3.5 A schematic electrochemical cell with a three-electrode system [296].

All three electrodes are placed into an electrolyte where a chemical reaction generates or uses electric current. The electrolyte is usually a solution of water or other organic solvents in which salt ions are dissolved. A diagram of

the three-electrode electrochemical cell is shown in Fig. 3.5. This widely used three-electrode cell along with a potentiostat allows to accurately gain essential understandings of the electrochemical process.

In this thesis, the cell was connected to a computer controlled CHI760D potentiostat (CHI, UK). $LiClO_4$ dissolved in propylene carbonate (PC) was utilised as the base conductive salt and solvent, respectively. The concentration of the $LiClO_4$ was 0.5 M. We conducted Cyclic voltammogram (CV), Chronoamperometric (CA) and Chronocoulometric (CC) scans in this thesis to acquire different data for analyses. The CV can provide the current measurements for the working electrode when the applied scanning potentials are varied. Subjecting to a sweep potential applied to the electrochemical cell, a plot of applied potential *vs* current can be obtained, called a voltammogram [297]. The shape and peak locations can provide key insight into the electrochemical reactions of the device during the electrochromic processes, such as oxidation and reduction or redox potentials. The CA scan involves a step potential applied to the working electrode. This measurement can result in currents from the faradaic process occurring at the electrode, and they are recorded as a function of time. The CC technique measures the charge *vs* time response to an applied potential step waveform [298].

3.6.2 UV- vis spectroscopy

A basic structure of the UV-Vis spectroscopy is shown in Fig. 3.6, which consists of a light source, lens, monochromator, wavelength selector (slit), sample and detector. When a light beam passes thought and reflects with the lens inside the system, the light is separated into all different wavelengths of the light by a prism inside the monochromator. However, only one specific wavelength will be allowed to pass through. When this specific light beam hits a molecule, the electron inside the molecule will be absorbed and emit energy (jumping up and down between the ground state and a higher energy state), which is recorded as the light intensity. The changes in intensity of those lights are measured by the electronic detector, and the resulting transmittance or absorbance will form the spectra for the bleached and coloured states.

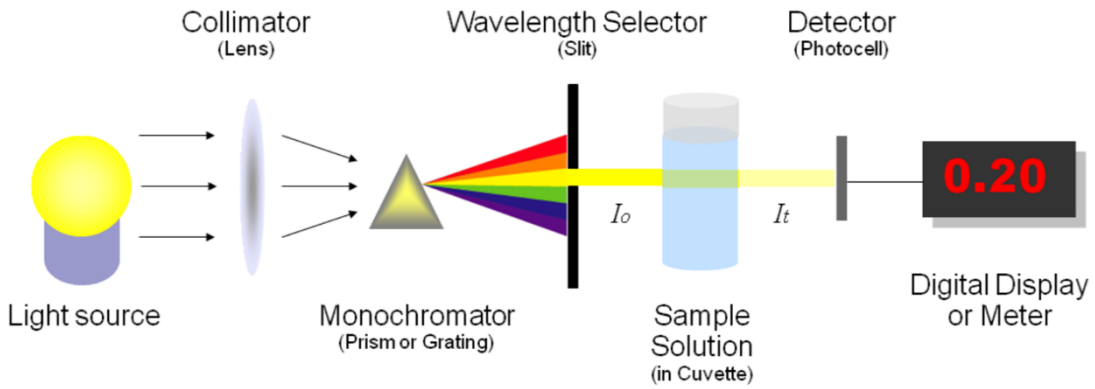

Fig. 3.6 A basic structure of UV-Vis spectroscopy [299].

A MSV-5300 UV-Visible Microspectrometer Series (from JASCO Germany GmbH) was used to investigate the electrochromic device in this thesis. The measurement was conducted in the UV-Vis to NIR region, ranging from 200 to 1600 nm. The resulting transmittance spectra in both bleached and coloured states of a device were recoded and used for further optical calculation. For the colouration changes, a voltage from power supply was applied to the prepared device, which was a negative voltage ranging from -1.5 to -2.5 V to achieve the coloured stage, whilst a positive voltage ranging from +2.0 to +3.5 V was applied to achieve the bleaching.

Chapter 4 Synthesis and characterisation of plain and Na-, Ce- and La-doped WO_x ultrathin bundled nanostructures

4.1 Introduction

The general information of precursors, synthesis methods and characterisation techniques has been introduced in the last Chapter. This Chapter will be extended further and present more detailed specific experimental parameters, step by step preparation of all products and their resulting structures, which can be separated into 4 parts. Firstly, the syntheses of all materials including the plain $W_{18}O_{49}$, Na-, Ce- and La-doped WO_x nanostructure are presented. Secondly, the morphology and structure analyses of all products will be discussed. Thirdly, we will also appraise the use of in-situ diffraction and Raman spectroscopy techniques, complemented with ex-situ electron microscopy analyses, to investigate the geometry and phase change behaviour of bundled ultrathin diameter $W_{18}O_{49}$ nanowires against the commercial WO_3 nanoparticles. To understand the fundamental aspects of $W_{18}O_{49}$ and WO_3 phase transformations could unlock the mechanisms of those WO_x phase transitions, leading to an effective guidance towards the future design and development of WO_x-based devices where temperature is involved during operation. Finally, we will investigate the cathodoluminescence property of the plain $W_{18}O_{49}$ nanowires, compared with the Ce- and La-doped WO_x nanostructures. This Chapter will present thorough morphology, structure, phase change and optical properties characterisations of these nanomaterials.

4.2 Synthesis of the $W_{18}O_{49}$, Ce-WO_x, La-WO and Na-WO_x nanostructures

4.2.1 $W_{18}O_{49}$ nanowires

WCl_6 and cyclohexanol were used as the precursor and solvent respectively to synthesise the $W_{18}O_{49}$ nanowires *via* the solvothermal method. The precursor solution was prepared by dissolving 0.059 g of WCl_6 in 50 ml of 0.003 M cyclohexanol to form a mixed solution. The mixed solution was then treated in an ultrasonic bath for 45 min and the homogenous solution was then transferred

into the Teflon-lined stainless-steel autoclave. The solvothermal reaction was conducted at 200 °C for 6 h in an oven.

4.2.2 Na-doped WO_x nanostructures

The mixture of 0.059 g WCl_6 and 49 ml cyclohexanol was well dissolved by using ultrasonic bath for 1 h, as previously described. 10 ml pre-solution stock of NaCl in ethanol was prepared with different concentrations (including 7.5×10^{-4}, 3.75×10^{-4}, 2.5×10^{-4}, 1.875×10^{-4}, 1.5×10^{-4} M), to achieve the actual Na:W molar ratios of 1:4, 1:8, 1:12, 1:16 and 1:20, respectively. 1 ml of each pre-solution was added into the 49 ml well-mixed WCl_6 and cyclohexanol solution, which was subject to an ultrasonic bath for another 10 min to achieve the final well-mixed 50 ml solution. The final solution was transferred to the Teflon-lined stainless-steel autoclave, and then reacted under 200 °C for 6 h.

4.2.3 Ce- and La-doped WO_x nanostructures

To prepare the Ce-doped WO_x samples, $CeCl_3 \cdot 7H_2O$ was first dissolved in 10 ml of ethanol to obtain a stock pre-solution then treated under ultrasonic bath for 1 h. The 0.059 g WCl_6 were mixed with 49 ml of cyclohexanol under the ultrasonic bath treatment condition for 30 min. 1 ml of the pre-solution was dropped into the 49 ml well-mixed WCl_6-cyclohexanol solution, followed by ultrasonic treatment for another 10 min. The final uniform solution was then transferred to the Teflon-lined stainless-steel autoclave. The reaction vessel was then sealed and heated at 200 °C for 10 h. The actual Ce:W molar ratios of $CeCl_3 \cdot 7H_2O$ and WCl_6 were 1:15, 1:10 and 1:5, respectively. The base solution concentration of WCl_6 was 0.003 M, for all doped samples. Similar process was used for the La-doped WO_x sample preparation, and during which $LaCl_3 \cdot 7H_2O$ was used as the precursor for preparing the 10 ml stock pre-solution.

All the final products were centrifugal collected, after being washed with deionized water, ethanol and acetone for several times, and then dried at 80 °C for 12 h prior to further testing.

4.3 Morphological and structural characteristics of the $W_{18}O_{49}$, Ce-WO_x, La-WO_x and Na-WO_x nanostructures

4.3.1 Morphological characteristics of plain WO_x and doped WO_x nanostructures

4.3.1.1 $W_{18}O_{49}$ nanowires

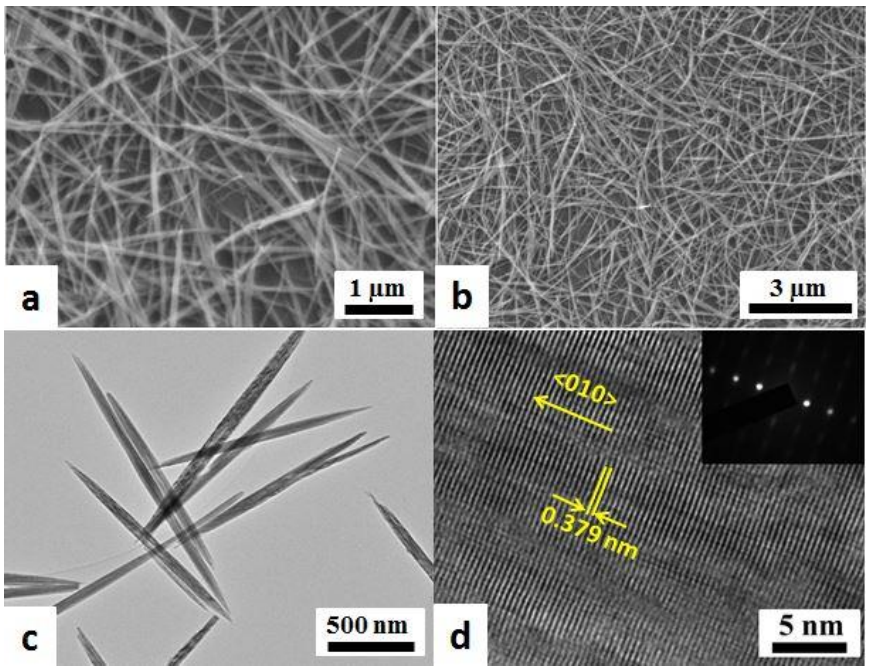

Fig. 4.1 (a and b) SEM images of the pristine $W_{18}O_{49}$ nanowire bundles at low and high magnifications. (c and d) Low and high magnification TEM images of the $W_{18}O_{49}$ nanowire bundles. Inset in (d) is the corresponding SAED pattern.

Fig. 4.1a and b show that each bundle is about 50 nm in diameter and up to 3 μm in length under SEM (Fig. 4.1a and b). TEM observations confirmed that these as-prepared $W_{18}O_{49}$ nanowires consisted of ultrathin nanowires of only *ca*. 2-5 nm in diameters and up to 2 μm in length, which were self-assembled into larger bundles as seen under the SEM due to resolution limit (Fig. 4.1c and d) [300]. In fact, further SAED pattern and corresponding HRTEM lattice images have shown that these nanowires are all single crystalline, with the same growth axis (i.e. the nanowire axis) along the <010> direction, perpendicular to the parental (010) which has a spacing of 0.379 nm in the SAED pattern and corresponding HRTEM lattice images. This is a typical character of the bundled

1-D nanostructured materials. This result, combined with the XRD result that will be discussed in the next section, shows that the bundled nanowires are $W_{18}O_{49}$.

4.3.1.2 Na-doped WO_x

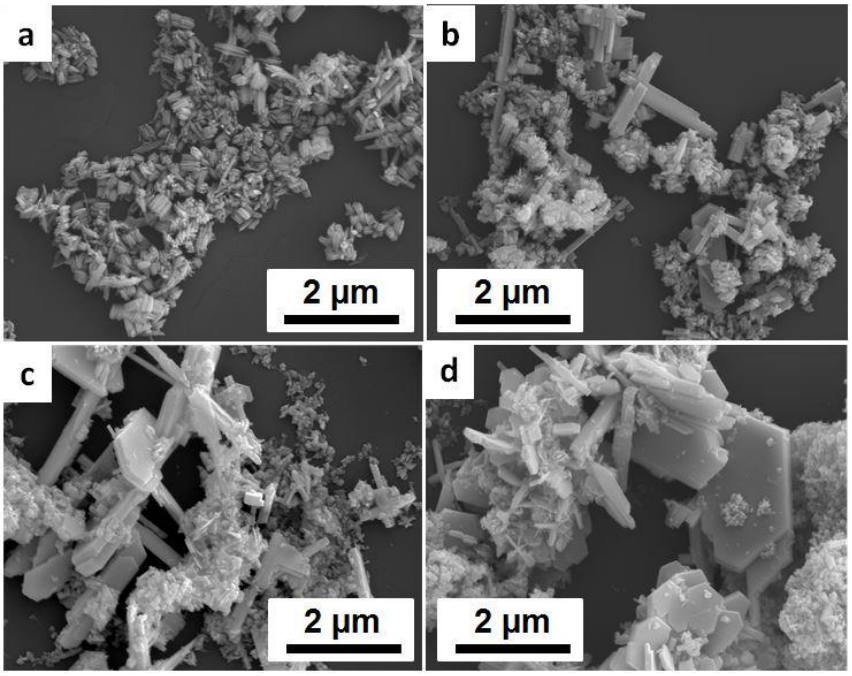

Fig. 4.2 SEM images of the Na-doped WO_x with different Na/W molar ratios. (a) 1:16, (b) 1:12, (c) 1:8, and (d) 1:4.

The Na-doped structures are shown in Fig. 4.2. In Fig. 4.2a, the nanowires are tied together exhibiting a block of bundles. The length of bundles ranges from 150 to 300 nm, and the diameter ranges from 100 to 200 nm, on average. It is clear that the length and diameter of the Na-doped nanowire bundles are shorter and wider than those of the plain $W_{18}O_{49}$, respectively (Fig. 4.1a and b). Increasing to higher concentrations (1:12, 1:8 and 1:4), the resulting samples are presented as mixtures of nanorod, nanoplates and agglomerated bundled structures, as shown in Fig. 4.2b-d, respectively. The size or diameter of nanoplates is even bigger with increased Na concentrations, as shown in Fig. 4.2c (1:8) and Fig. 4.2d (1:4). We suspect that the different morphology could be a result of different amounts of Na doped within the structural framework, which will be discussed later. At low Na concentration, TEM results show that the bundles contain numerous small diameter nanowires of 2 - 5 nm on average, akin to the plain $W_{18}O_{49}$ structures (Fig. 4.1c), but much shorter.

The HRTEM studies (Fig. 4.3b) further confirmed the same growth axis of the doped nanowires in the bundle, as seen in the plain $W_{18}O_{49}$, along the <010> direction with a (010) spacing of 0.38 nm. At high Na concentration, the d space value and SAED patterns of the huge crystals are different, as shown in Fig. 4.3c-h. The d value becomes 0.385 nm, suggesting a lattice of WO_3.

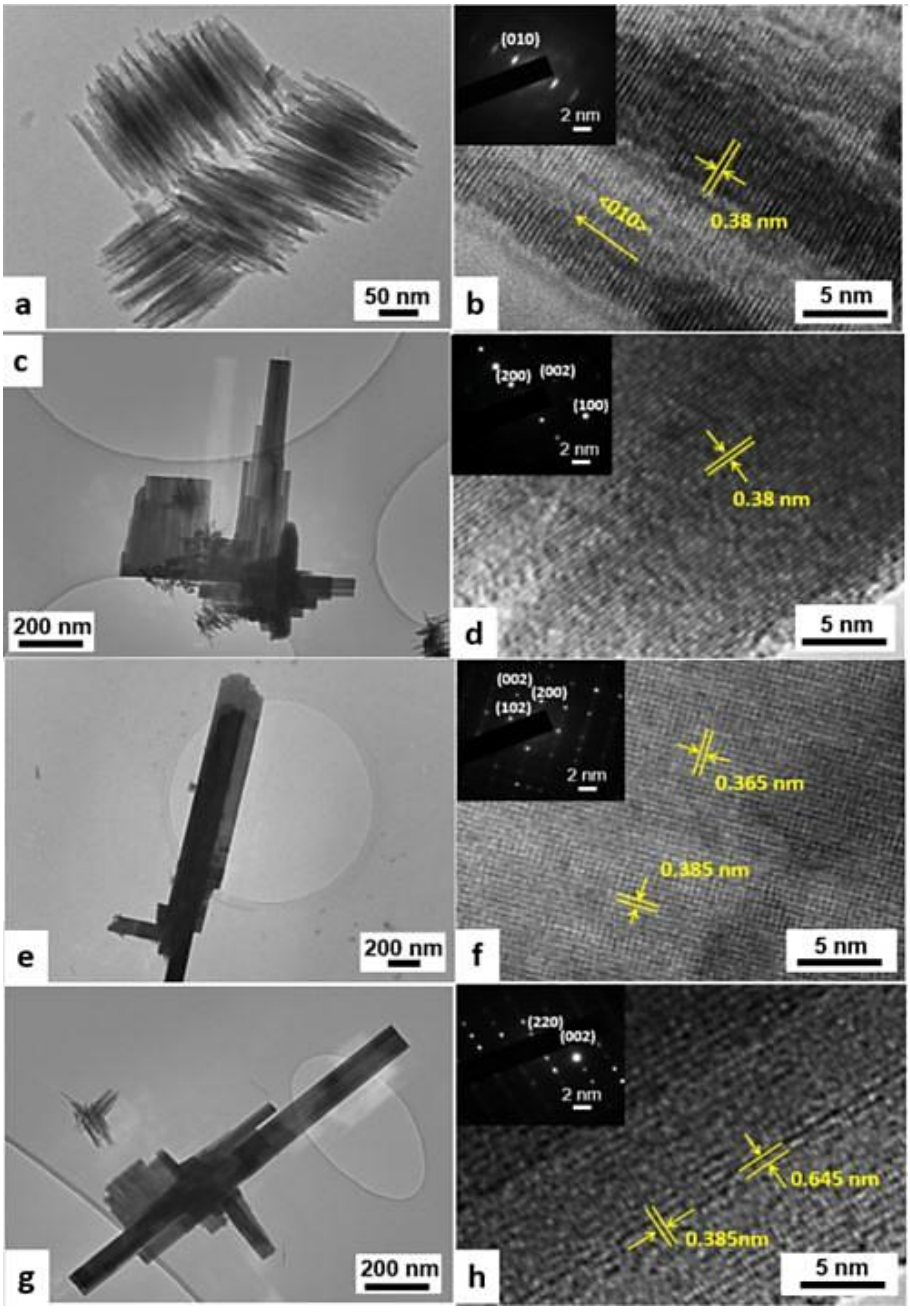

Fig. 4.3 TEM and HRTEM images of Na-doped WO_x nanostructures with different Na/W molar ratios. a and b, 1:16; c and d, 1:12; e and f, 1:8; and g and h, 1:4, respectively. Inset shows the SAED patterns of each sample.

4.3.1.3 Ce-doped WO_x

The SEM images in Fig. 4.4a-c show that the lengths of the bundles and the morphology of original WO_x were strongly influenced by the addition of Ce, varying with the Ce concentrations utilised during the synthesis stage. At a Ce doping ratio of Ce/W =1:15, the nanowires became shorter in length and thicker in diameter, compared with the plain $W_{18}O_{49}$ (Fig. 4.1a and b). This feature became more obvious at higher Ce concentrations (Ce/W = 1:10), and eventually very short agglomerates were visible at Ce/W = 1:5.

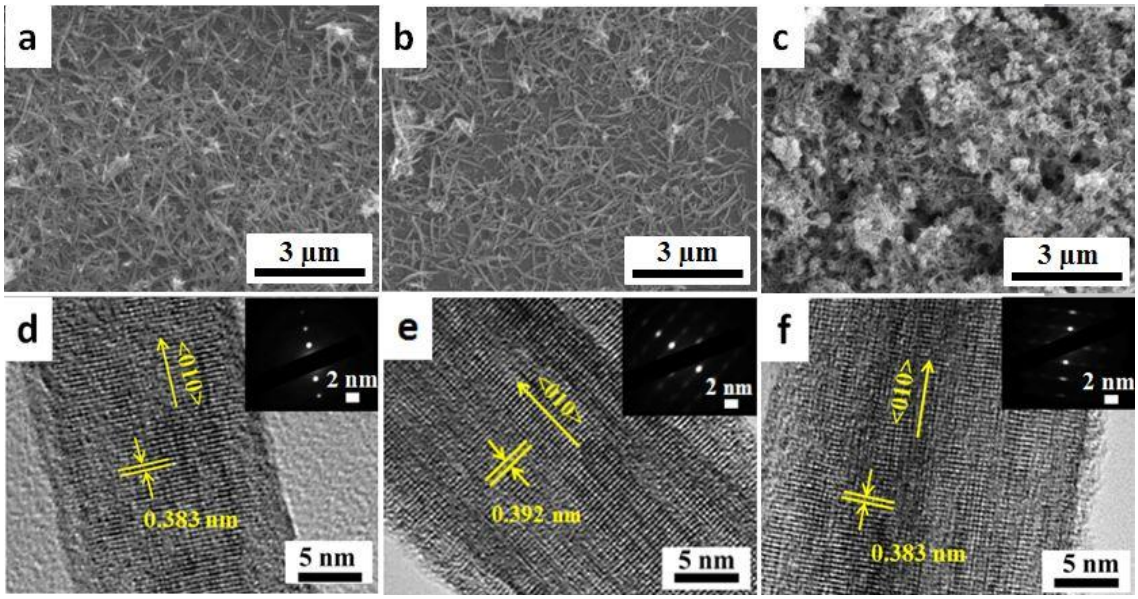

Fig. 4.4 SEM and HRTEM images the Ce-doped WO_x nanostructures with different Ce/W molar ratios. a and d, 1:15; b and e 1:10; c and f, 1:5 respectively. Inset shows the SAED patterns of each sample.

A slightly increased (010) lattice spacing, by 1.1, 3.4 and 4.8%, for the differently doped nanowires at 1:15, 1:10 and 1:5 respectively, against the plain $W_{18}O_{49}$ nanowires, has been recorded. The enlargement tendency appeared to be correlated with the increased Ce/W molar ratios (marked in Fig. 4.4d-f). It is obvious that all doped samples examined showed single crystalline characteristics, resembling the plain $W_{18}O_{49}$, however the insertion of Ce into the structures has indeed resulted in a minor lattice distortion, hence the evident of increased d values.

4.3.1.4 La-doped WO_x

Fig. 4.5a-c shows the morphology of the La-doped WO_x samples. The bundles are about 60 nm to 1 μm in length, which is shorter than the original $W_{18}O_{49}$ (Fig. 4.1a and b). This result confirms that the morphology of the original $W_{18}O_{49}$ was also influenced by the addition of La, varying with the La concentrations utilised during the synthesis stage, similar to the Ce-doped WO_x samples. However, the morphology difference of various doping concentrations was not obvious, in terms of the bundle lengths and sizes.

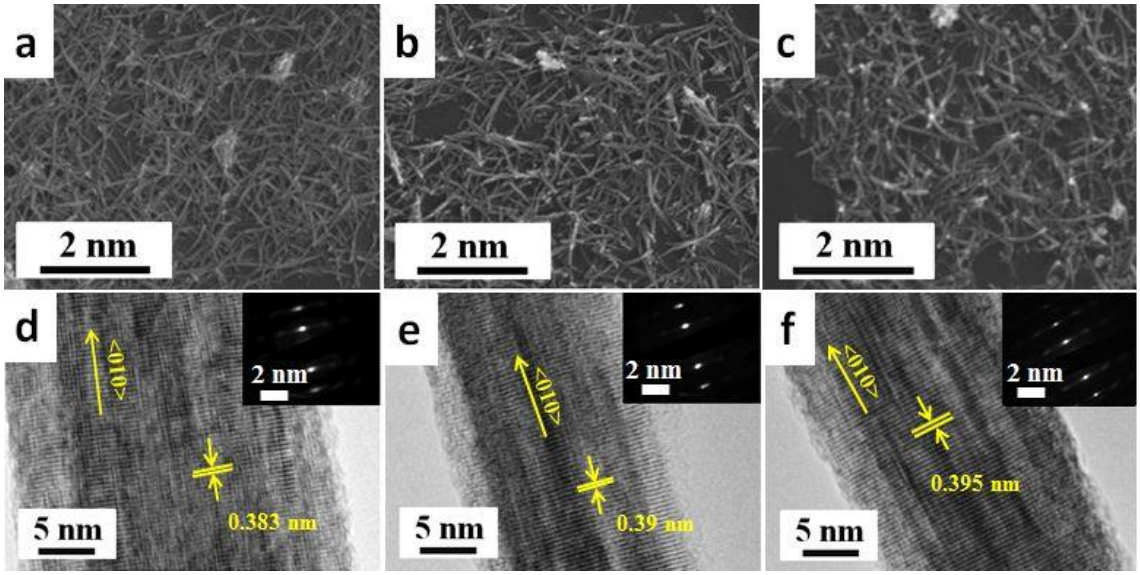

Fig. 4.5 SEM (top) and TEM (bottom) images of the La-doped WO_x nanostructures, with different La/W molar ratios of: (a) 1:15, (b) 1:10 and (c) 1:5, respectively. HRTEM images of differently doped nanowires and corresponding SAED patterns in the inset: (d) La/W = 1:15; (e) La/W = 1:10; and (f) La/W = 1:5.

The (010) plane d-values of La-doped samples were increased by 1.1, 2.9 and 4.2% for the differently La-doped nanowires at 1:15, 1:10 and 1:5, respectively (Fig. 4.5d-f), compared with the plain $W_{18}O_{49}$ (Fig. 4.1d), which exhibits a similar trend to the Ce dopant. SAED patterns of the sample also show that the La-doped nanowires grew along the <010> direction. Interestingly, the lattice distance of the Ce-doped samples is larger than that of the La-doped samples, although the ionic radius of Ce (1.034 Å) is smaller than La (1.061 Å). This

minor distortion in lattice due to La insertion into the structures could be related to the actual amounts of dopant located within the frameworks.

4.3.2 Structural and compositional characteristics of plain WO_x and doped WO_x nanostructures

4.3.2.1 $W_{18}O_{49}$ nanowires

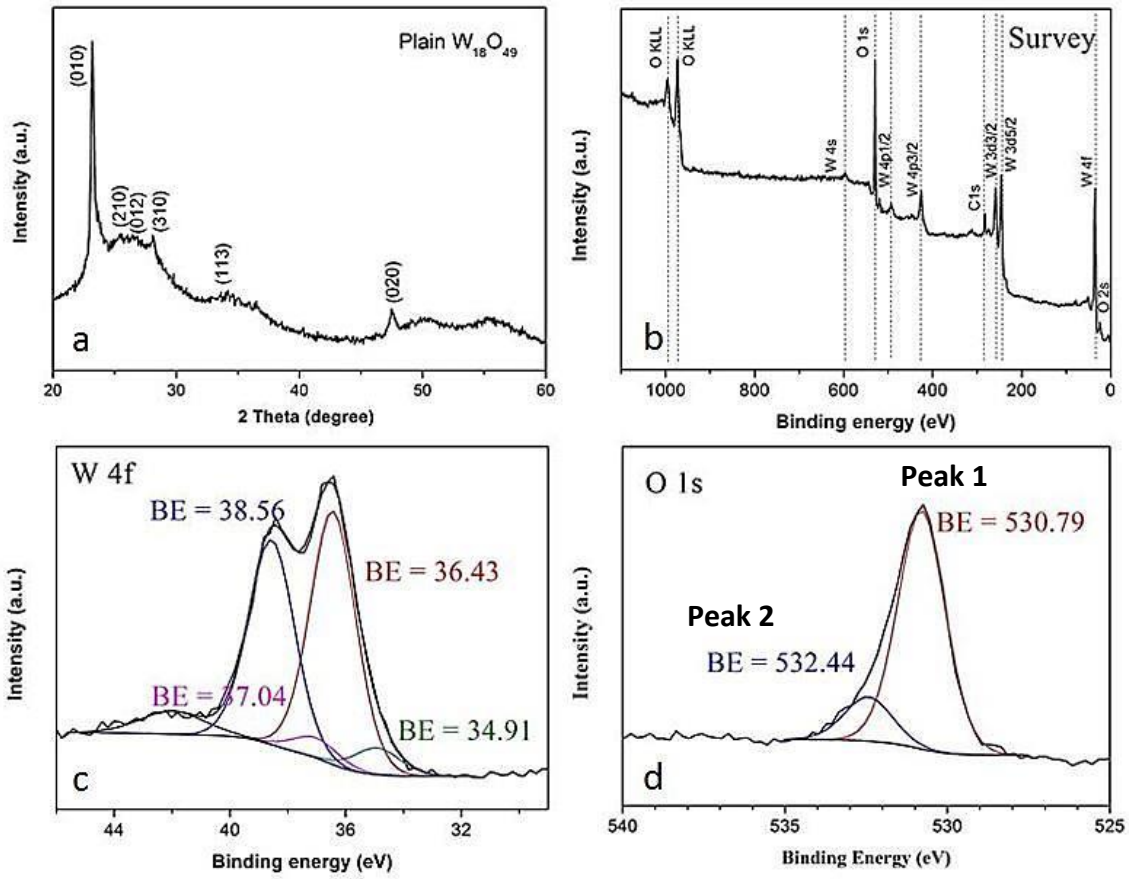

Fig. 4.6 (a) XRD pattern, (b) XPS survey spectra, (c) and (d) high resolution XPS scans of the W 4f and O 1s peaks of the bundled $W_{18}O_{49}$ nanowires, respectively.

The XRD patterns of the synthesised WO_x match well with JCPDS No: 01-073-2177, confirming the dominant base crystalline feature of the $W_{18}O_{49}$ monoclinic phase, with lattice constants of a = 0.1832, b = 0.379, c = 1.404 nm, and β = 115.03°. Two main diffraction peaks at 2θ at about 23.2° and 47.5° can be assigned to the (010) and (020), respectively (Fig. 4.6a). The strongest intensity of the (010) plane is indicative of that the nanowires are preferably grown along

the <010> direction, and thus very weak intensities of other planes in the profiles, such as (210), (012), (310) and (113), which is a typical feature of the 1-dimensional nanowires. The detailed 2θ information of the JCPDS for this phase is listed in Appendix A. The d value of plane (010) from the XRD pattern is 0.379 nm, which matches well with the d value from the SAED pattern of $W_{18}O_{49}$ nanowire bundles (as shown in Fig. 4.1d).

The survey spectra of plain $W_{18}O_{49}$ nanowires are presented in Fig. 4.6b. The atomic concentration percentages of O 1s and W 4f are 74.4 and 25.6, respectively. The chemical state of core-level W 4f for the plain $W_{18}O_{49}$ nanowires could be fitted into two spin-orbit doublets (Fig. 4.6c), which are assigned to two different oxidation states of the W atoms, including W^{6+} and W^{5+}. The main doublets for W $4f_{5/2}$ and W $4f_{7/2}$ with binding energy at 38.56 and 36.43 eV respectively are associated with the W atoms in the W^{6+} oxidation state. The other doublet with binding energies of W $4f_{5/2}$ at 37.04 eV and W $4f_{7/2}$ at 34.91 eV could be identified as the W^{5+} oxidation state. O 1s spectra (Fig. 4.6d) also show two main peaks, of which the lower binding energy peak (530.8 eV) is corresponding to the oxygen in the lattice and O^{2-} (peak 1) and the higher binding energy peak (532.4 eV) is associated with O^{2-}, O^{-}, and OH^{-} in the oxygen-deficient regions (peak 2) [301].

4.3.2.2 Na-doped WO_x

The XRD pattern of the low Na concentration samples (1:16) matches with JCPDS No: 01-073-2177, remaining as the crystalline feature of the plain $W_{18}O_{49}$ monoclinic phase. Two main diffraction peaks at 2θ at about 23.2° and 47.5° can be assigned to the (010) and (020), respectively. The strongest intensity of the (010) plane suggests that the nanowires are preferably grown along the <010> direction, which also agrees with the results from the HRTEM imaging and SAED patterns (Fig. 4.3b). The higher amounts of Na dopant (1:12, 1:8 and 1:4) not only cause the change in morphology, but also modified their structures slightly. The XRD patterns of 1:12, 1:18 and 1:14 samples match with two possible standard patterns of PDF 00-046-0174 and 01-850-2459 which are from the Na_xWO_3 and WO_3 hexagonal phases, respectively.

The lattice constants of hexagonal phase Na_xWO_3 include *a* = 7.411 and *c* = 7.619 nm. For the WO_3 hexagonal phase, the lattice constants are 7.324 and 7.663 nm for *a* and *c* respectively. The measured 2θ values of the 1:12, 1:8 and 1:4 samples include 13.9°, 23.3°, 28.2°, 33. 36.7°, 33.7°, 47.5°, 49.8° and 55.5°, which can be assigned to the plane (100), (002), (200), (112), (202), (004), (220) and (222), respectively. Moreover, two small peaks at 2θ at about 13.86° and 36.86° were obtained in the XRD pattern of the 1:16 sample, which are assigned to planes (100) and (202), as same as those presented in high Na concentration samples. It may be possible that a small amount of nanoplates and nanorods also occur in the 1:16 samples.

Table 4.1 A summary of the (002)/(200) ratios and FWHM for (002) and (200) at various Na doping concentrations.

Samples	**Height**		**Intensity Ratio (002)/(200) peak**	**FWHM**	
	Plane (002)	Plane (200)		Plane (002)	Plane (200)
Na/W = 1:16	-	-	-	-	-
Na/W = 1:12	20650	12791	1.61	0.31	0.63
Na/W = 1:8	15389	13922	1.11	0.46	0.58
Na/W = 1:4	13549	15262	0.88	0.53	0.50

Note: FWHM = Full width half maximum of the peak (unit = Theta degree)

Remarkably, the intensity ratios of (002)/(200) are decreased with the increase of Na concentrations. This correlation suggests that the incorporation of Na ions into the WO_x has changed the original plane stacking characteristics, either reduced the number of (002) planes, i.e. larger nanorods and nanoplates, or enhanced the other planes growth. Meanwhile, the Full-width at half-maximum (FWHM) of the (002) plane also shows greater values, whilst the (200) plane presents smaller values with increased Na:W molar ratios, i.e. corresponding to smaller size on (002) growth direction and larger size on (200) growth direction. The ratios are summarised in Table 4.1. This analysis matches very well with the SEM observations that nanorods and nanoplates become bigger at higher Na concentrations.

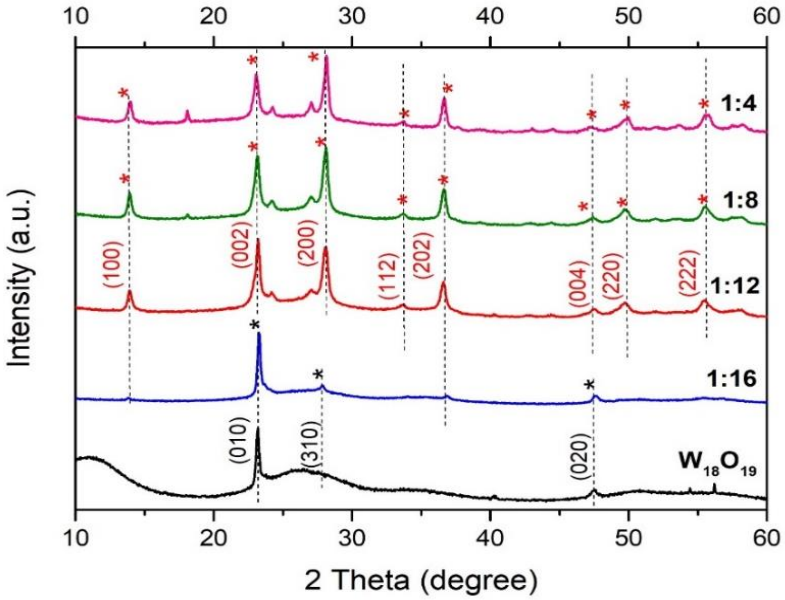

Fig. 4.7 XRD patterns of the Na-doped WO_x samples with different Na:W molar ratios.

The surface compositions of Na-doped WO_x nanostructures of Na:W molar ratios at 1:16, 1:12, 1:8 and 1:4 have been analysed by using XPS. The XPS survey spectrum clearly shows that the element of W, O and Na exists in the samples, as shown in Fig. 4.8a. The high-resolution scan of Na 1s region presents that the peak is located at about 1072 eV (Fig 4.8b). The W 4f and O 1s peak positions shift toward the lower binding energy with the increases of Na ions doped into the structure, compared with the plain $W_{18}O_{49}$ (Fig. 4.8c and d, respectively). The details of the peak location of each region are presented in Fig. 4.8. The spin-orbit doublets of W 4f and O 1s could be separated as the same to the plain $W_{18}O_{49}$, which has been explained in the previous section. The variation of W, O and Na content for each sample, the ratios of W^{5+}/W^{6+} and O 1s peak 1/peak 2, which are approximate to the ratios of the fitted peak areas, are summarised in Table 4.2.

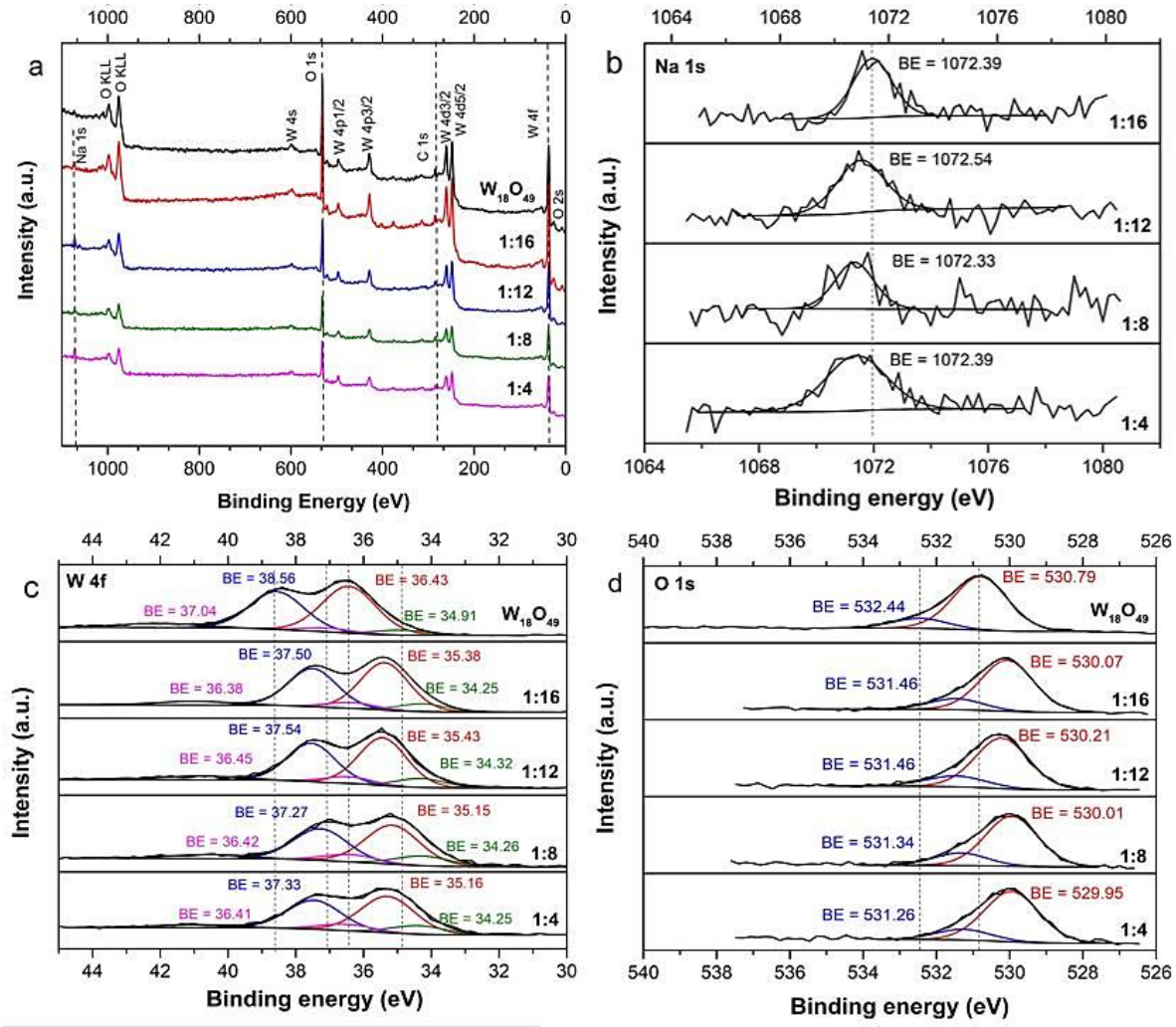

Fig. 4.8 (a) XPS survey spectra, and high-resolution scans of (b) Na 1s, (c) W 4f, and (d) O 1s of un-doped and Na-doped WO_x samples.

Table 4.2 XPS surface characterisation results of the Na-doped samples.

Samples	**Surface composition (atomic ratio)**				
	W^{5+}/W^{6+}	O 1s Peak2/peak 1	O_{total}/ (O+Na+W)	W_{total}/ (O+Na +W)	Na_{total}/ (O+Na+W)
Pure $W_{18}O_{49}$	0.102	0.19	0.790	0.21	-
Na/W = 1:16	0.160	0.22	0.747	0.221	0.032
Na/W = 1:12	0.182	0.24	0.723	0.237	0.04
Na/W = 1:8	0.241	0.25	0.699	0.24	0.061
Na/W = 1:4	0.227	0.21	0.681	0.251	0.068

Note: The O 1s peak 1 is located at the lower binding energy (529.95 - 530.79 eV), and the O 1s peak 2 is located at the higher binding energy (531.26 - 532.44 eV) of the O 1s regions.

The atomic concentrations of Na are measured as 6.8%, 6.1%, 4% and 3.2% for the 1:4, 1:8, 1:12 and 1:16 doped samples, respectively. The atomic ratios of W and O are increased first and then decreased, with increasing the concentration of Na^+ inside the structures. The increases of W^{5+}/W^{6+} and O 1s peak 1/peak 2 ratios are indirectly related to the increases of oxygen vacancy (V_o) inside the structure. The results suggest that the V_o could be increased with increasing the Na concentration.

As evidenced from Table 4.2, Na is incorporated into the WO_x framework. However, it would be difficult for the Na^+ to replace the W in the lattice of $W_{18}O_{49}$ nanowires, due to the larger ionic radii of Na^+ (0.098 nm) compared with those of W^{6+} (0.065 nm) and W^{5+} (0.068 nm) [302]. The Na cations might be inserted into the small tunnels of V_o on the surface area of the WO_x structure, whilst forming new V_o on other surfaces in the structure. Another possibility is that the Na cation is inserted into the hexagonal channels of the WO_x structure, based on the evidence from the XRD patterns of all doped samples and previous investigations which are presented in Chapter 2 of this thesis. Na^+ could improve the electron transfer and the oxygen mobility of the doped samples, as confirmed by the altered states in the XPS results. The noticeable peak shift of the W 4f and O 1s regions in doped samples could be another evidence of the increases of defects and weaker W-O bonding inside the structure, as a result of the lattice relaxation and structure modification in the doped samples.

4.3.2.3 Ce-doped WO_x

The XRD patterns of the un-doped and Ce-doped samples are all matched well with JCPDS No: 01-073-2177 (PDF standard pattern is presented in Appendix A), confirming the dominant base crystalline feature of the $W_{18}O_{49}$ monoclinic phase, with lattice constants of a = 0.1832, b = 0.379, c = 1.404 nm and β = 115.03°. Two main diffraction peaks at 2θ at about 23.2° and 47.5° can be assigned to the (010) and (020) respectively (Fig. 4.9). The strongest intensity of the (010) plane is indicative of the preferable growth direction of <010>. The

very weak intensities of other planes in the profiles, such as (100), indirectly confirm the 1-dimensional feature of the nanowires. The FWHM of the (010) plane also shows greater values with increased Ce:W molar ratios, as a result of the smaller nanowires. This result matches very well with the SEM observations that the doped nanowires became shorter and wider at higher Ce concentrations (Fig. 4.4). However, the XRD results have failed to show a strong evidence to distinguish the crystallinity changes between the doped and un-doped samples.

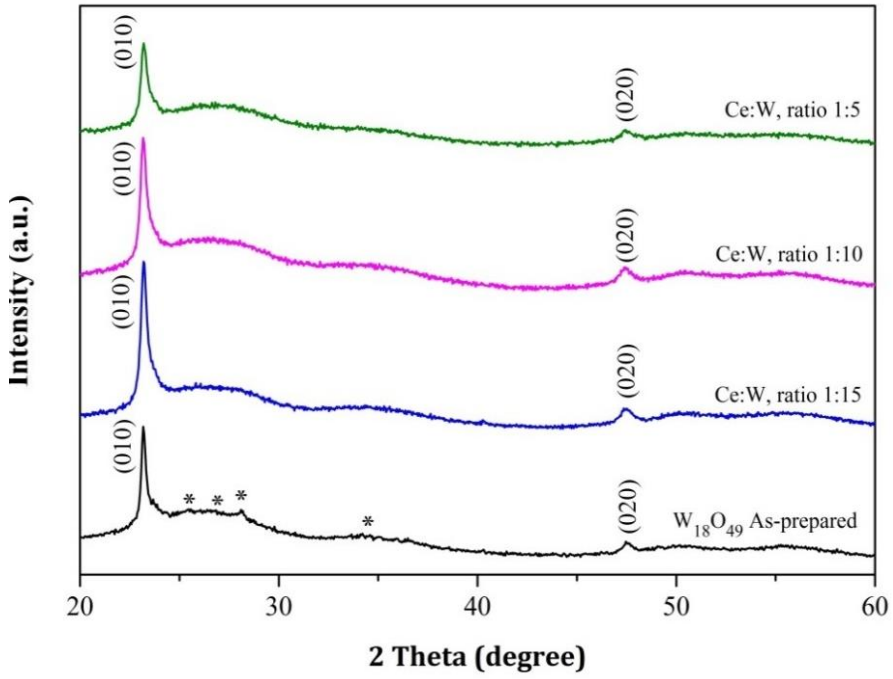

Fig. 4.9 XRD patterns of the as-synthesised nanomaterials of different Ce:W molar ratios.

The EDX element mapping confirms the homogeneous distribution of the constituent elements, and W and O are dominant within the nanowires (Fig. 4.10). Ce is visible and presented across the entire nanowire area, therefore it is most likely that Ce exists inside the parental WO_x. The atomic percentage of the 1:5 sample is 60.3, 34.1 and 5.6 for O, W and Ce respectively. For the 1:10 sample, the values are 74.8% for O, 22.2% for W and 3% for Ce. A ratio of 69 %, 29.1% and 1.95% for O, W and Ce, respectively, is obtained for the 1:15 sample.

Due to the small diameter nature of the nanowires, 2 - 5 nm, the surface composition characteristics obtained by the XPS which has a surface penetration of up to 2 nm, it is therefore believed that the XPS results are a logical reflection of the chemical composition of the nanowire body. The XPS results are presented in Fig. 4.11. The W 4f peak shifted toward the lower binding energy with the Ce doping into the structure.

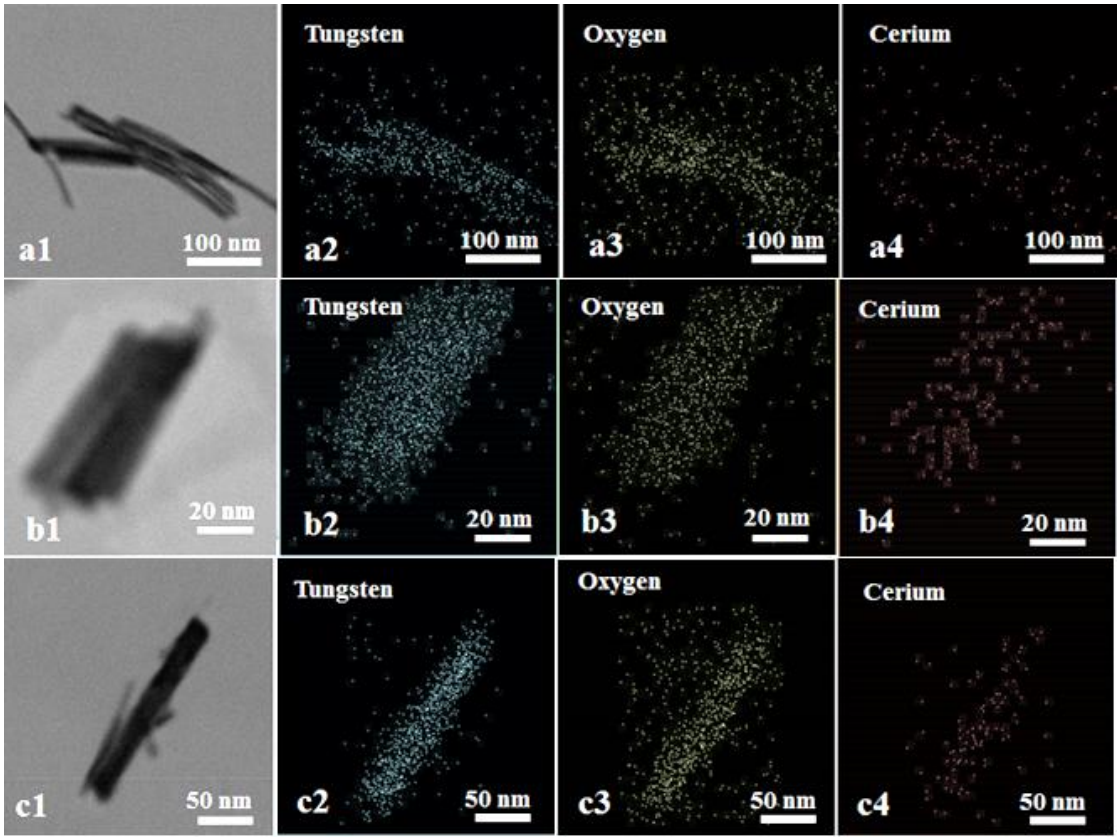

Fig. 4.10 Element mapping images of differently Ce-doped samples at various Ce:W ratios. (a1-4) 1:15, (b1-4) 1:10, and (c1-4) 1:5. The blue, yellow and red dots are representative of the distribution of W, O and Ce.

Fig. 4.11b shows the Ce 3d XPS spectra of samples with different molar ratios, and the spectra suggest that both oxidation states of Ce^{3+} and Ce^{4+} co-exist on the surface of doped samples. The main part of the ceria was Ce^{3+} which shows a higher intensity and larger area, compared with those of the Ce^{4+} oxidation state. At the lowest concentration of Ce:W = 1:15, the two peaks at ~905 and ~886 eV are assigned to Ce^{3+} $3d_{3/2}$ and $Ce^{3+}3d_{5/2}$, respectively. Moreover, those peaks at ~901 and ~882 eV are associated with the Ce^{4+} oxidation state. At the intermediate and higher molar ratios of 1:10 and 1:5, the peak positions of Ce^{3+}

$3d_{3/2}$ and Ce^{3+} $3d_{5/2}$ shift slightly toward the higher binding energy which are located at 905.39 and 886.35 eV for the 1:10 sample, and 904.65 and 885.95 for the 1:5 sample. In addition, the higher binding energy peaks of the Ce^{4+} oxidation state for the 1:10 and 1:5 samples are also detected at 901.49 and 882.54 eV for Ce^{4+} $3d_{3/2}$ and $3d_{5/2}$, respectively (1:10 sample), and at 901.44 and 882.44 eV for Ce^{4+} $3d_{3/2}$ and $3d_{5/2}$, respectively (1:5 sample).

To visualise the variation of W^{6+} content more clearly between the un-doped and the Ce-doped samples, the ratio of W^{5+}/W^{6+} which is an approximate to the ratio of fitting peak areas, is presented in Table 4.3.

Table 4.3 shows that the atomic ratios of W and O are decreased with increasing the concentration of Ce ions in the structures. Interestingly, the increases of the W^{5+}/W^{6+} ratios exhibit that the Ce^{3+} oxidation state of the Ce ions is reduced by way of charge transfer from the W ions, accompanying decreases of the W^{6+} oxidation state. As evidenced from Table 4.3, the Ce is indeed incorporated into the WO_x, rather than on the surface or physically mixed. Similar to that of the Na-doped WO_x samples, it would also be difficult for the Ce^{4+} and Ce^{3+} to directly replace the W in the lattice of $W_{18}O_{49}$ nanowires, due to the even larger ionic radii of Ce^{4+} (0.101 nm) and Ce^{3+} (0.103 nm), compared with those of W^{6+} (0.065 nm) and W^{5+} (0.068 nm) [302]. The Ce cations might be inserted into the small tunnels of V_o on the surface area or hexagon channel inside the $W_{18}O_{49}$ structure, while forming V_o elsewhere on the surface.

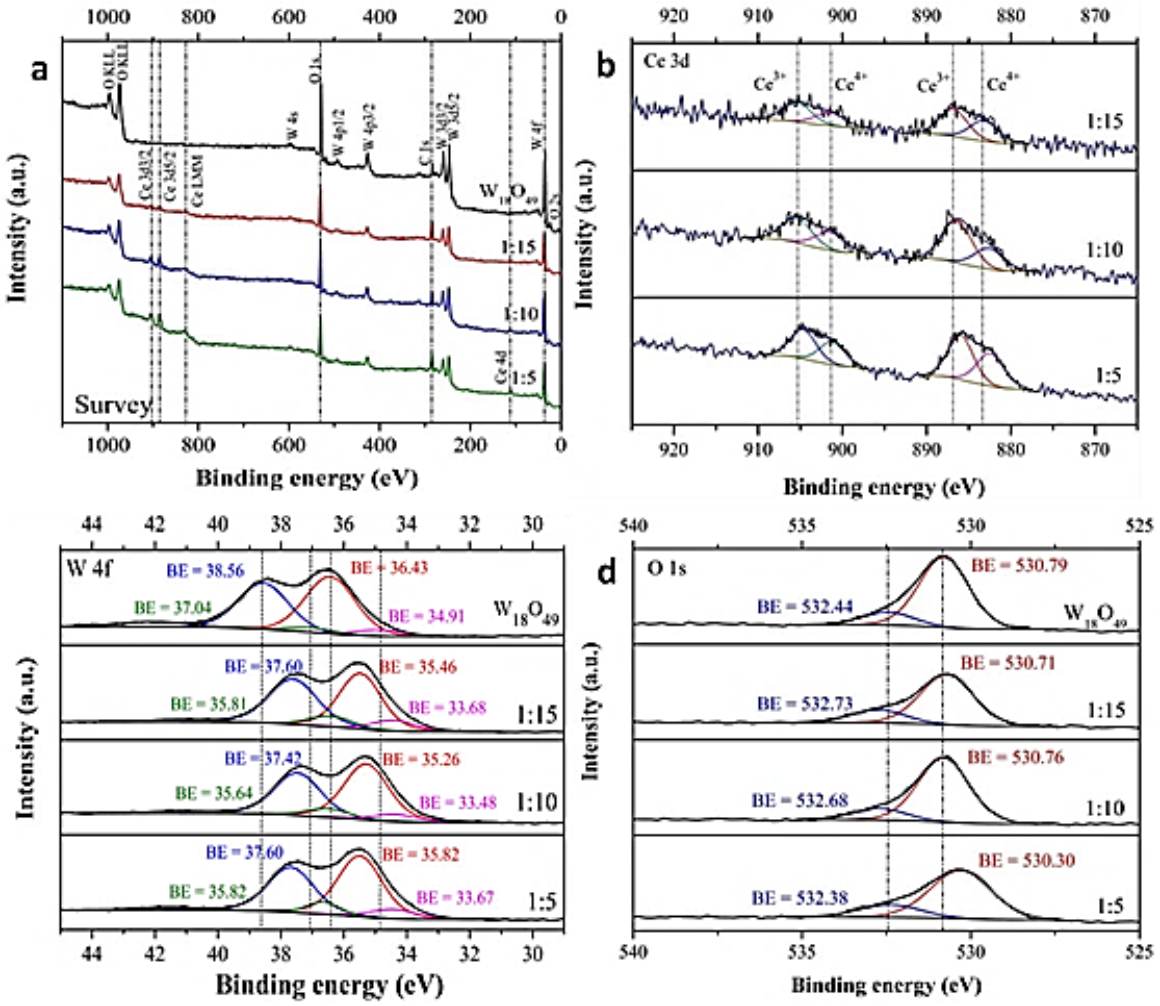

Fig. 4.11 XPS spectra. (a) survey spectra, (b) Ce 3d, (c) W 4f and (d) O 1s high resolution scan of the un-doped and doped samples.

Ce cations could improve the electron transfer and the oxygen mobility of the doped samples, as confirmed by the altered states in the XPS results. This suggestion is supported by the increase of W^{5+} oxidation state and the increased ratio between peak 1/peak 2 of the O 1s when they are compared with un-doped $W_{18}O_{49}$ samples. However, peak 1 of O 1s shifts toward lower binding energy in the Ce-doped samples, compared with the plain $W_{18}O_{49}$. This provides another evidence for the increases of defective and weak W-O bonding inside the structure. The noticeable peak shift in the doped samples could arise from the electronegativity of Ce which is lower than that of O.

Table 4.3 Surface characterisation results from XPS.

Samples	Surface composition (atomic ratio)				
	Ce^{4+}/Ce^{3+}	W^{5+}/W^{6+}	O_{total}/ (O+Ce+W)	W_{total}/ (O+Ce+W)	Ce_{total}/ (O+Ce+W)
Pure $W_{18}O_{49}$	-	0.102	0.790	0.21	-
Ce/W = 1:15	0.72	0.207	0.785	0.185	0.03
Ce/W = 1:10	0.57	0.157	0.761	0.196	0.043
Ce/W = 1:5	0.78	0.175	0.764	0.160	0.076

In summary, the decreased atomic contents of W and O, and the changes in the oxidation state from Ce^{4+} to Ce^{3+} of the Ce 3d spectra upon subsequent reduction offer further evidence for the release of free electrons inside the doped crystalline structures and the increases of V_o. These free electrons and V_o would benefit the electrochemical performance of these doped nanomaterials.

4.3.2.4 La-doped WO_x

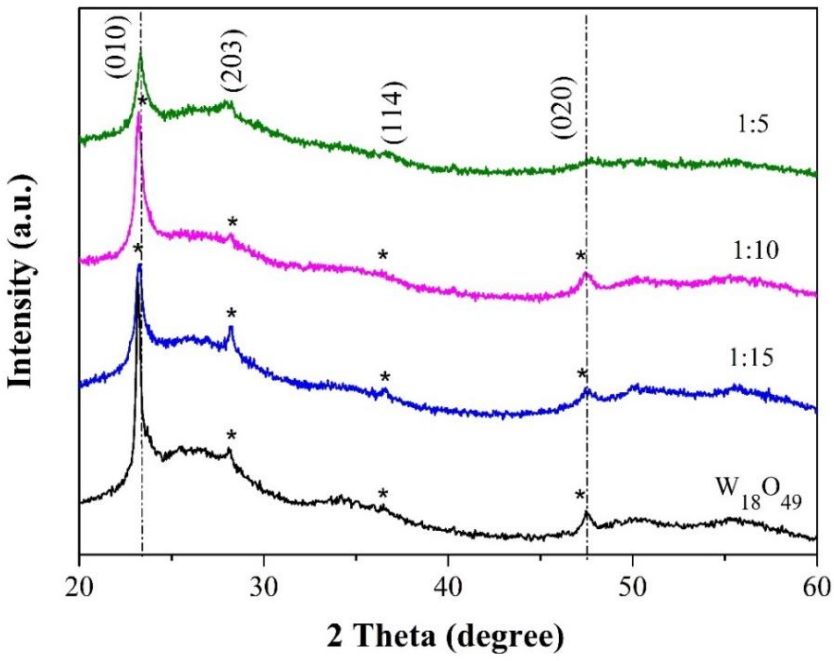

Fig. 4.12 XRD patterns of the as-synthesised nanomaterials of different La/W molar ratios.

The XRD patterns of La-doped nanowires are also assigned to the $W_{18}O_{49}$ monoclinic structure, according to JCPDS No: 01-073-2177, as shown in Fig. 4.12. The same findings of the (010) and (020) peaks remain unchanged for all La-doped samples, i.e. La does not affect the crystallinity of the original $W_{18}O_{49}$. Accordingly, the strongest intensity of (010) plane is indicative of the preferred nanowire growth direction of 010>, which matches with the observed results from HRTEM. The other planes of (203) and (114) can also be used to confirm the feature of nanowires.

For the La-doped sample, as shown in Table 4.4, the intensity ratios of (203)/(010) of all doped samples are bigger than that of the plain $W_{18}O_{49}$. This correlation suggests that the incorporation of La ions into the WO_x has changed the original plane stacking characteristics. The ratio reduction is a result of either the reduced number of (010) planes, i.e. shortened nanowires, or enhanced other planes growth, i.e. formed slightly thicker nanowires. Meanwhile, the FWHM of the (010) plane in the La-doped samples shows slightly increased values than in plain $W_{18}O_{49}$, which means smaller sizes of the nanowires, due to the single crystalline features of the nanowires. This new finding could not be visualised during SEM observations of the La-doped samples, owing to the bundled appearance.

Table 4.4 A summary of the main peaks (010) and (203) in each sample.

Samples	**Intensity (a.u.)**		**2 Theta (Degree)**		**Intensity Ratio**	**FWHM**	
	(010)	(203)	(010)	(203)	(203)/(010) peak	(010)	(020)
$W_{18}O_{49}$	8704	4175	23.18	28.09	0.48	0.43	0.29
La:W, ratio 1:15	6434	4720	23.29	28.28	0.73	0.44	0.33
La:W, ratio 1:10	7206	3884	23.22	28.21	0.54	0.42	0.19
La:W, ratio 1:5	5402	4098	23.32	27.88	0.76	0.52	0.31

The incorporation of La within the WO_x nanowires is further confirmed by EDX elemental mapping under the STEM mode, as shown in Fig. 4.13. The W and O distributions are clearly dominant, and the presence of La is also visible. These

element mapping results have shown that La is present across the entire nanowires and is most likely existing inside the parental WO_x. The elemental composition of the $LaWO_x$ sample with a La:W ratio of 1:15 is about 67.5, 30.8 and1.7 at% for O, W and La, respectively. For the La:W=1:10 sample, the values are 69.7 for O, 26.8 for W and 3.5 for La. For the La:W=1:5 sample, we have obtained values of 62.24% for O, 33.6% for W and 4.2% for La. All Ce- and La-doped samples obtained lower at.% of W and O compared with $W_{18}O_{49}$ (79.5 for W and 20.5 for O, at.%), as we have suggested that La and Ce ion could introduce more V_o inside the structure. The element mapping results have also confirmed that it is easier for Ce ion to get into the WO_x structure then for La ion. This may due to the smaller size of Ce ionic radii, compared with La ionic radii.

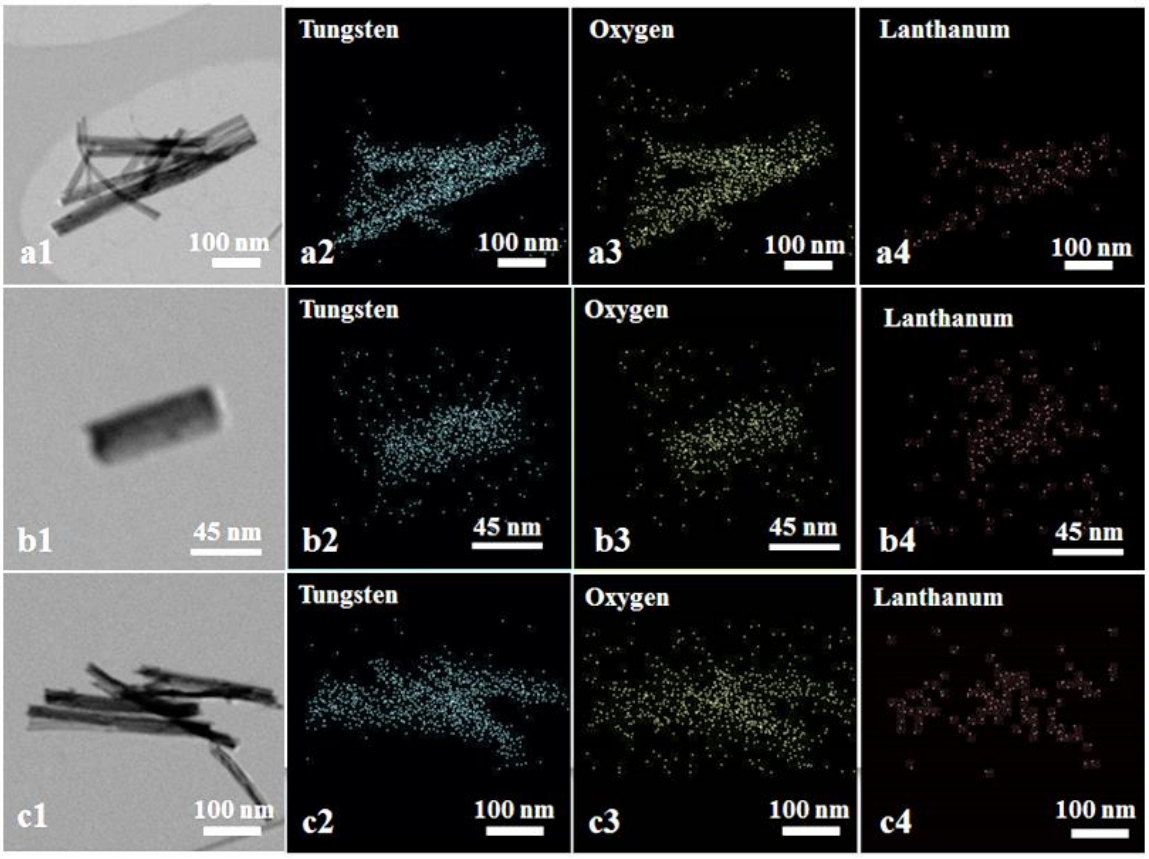

Fig. 4.13 EDX elemental mapping images of various La:W ratios. (a1-4), 1:15; (b1-4), 1:10; (c1-4), 1:5. Blue, yellow and red dots represent the distribution of W, O and La.

XPS chemical composition of the La-doped WO_x nanowires is presented in Fig 4.14a. The chemical state of core-level W 4f of La-doped samples (Fig. 4.14c)

is assigned to two different oxidation states of W, including W^{6+} and W^{5+}, similar to the un-doped and Ce-doped samples that we have discussed earlier. This peak is shifted toward lower binding energy in the presence of La doping in the WO_x structure. The La 3d spectra of all doped samples can be assigned to the $3d_{5/2}$ and $3d_{3/2}$ spin-orbit components, and each spin-orbit consists of double peak, therefore a total of four peaks for an ideal Lorentzian– Gaussian curve fitting at binding energies of about 855.57, 851.85, 838.88 and 835.62 eV. The energy loss peaks appearing on the high energy side of the $3d_{5/2}$ and $3d_{3/2}$ spin-orbit are satellite peaks, and the value of the spin-orbit splitting between major peaks (located at lower energy) of $3d_{5/2}$ and $3d_{3/2}$ is about 16.6 eV [303]. The appearance of those doublet peaks is due to the bonding and anti-bonding states between the $3d^94f^0$ (major peak) and 3d94f1L (satellite peak) configuration respectively, where L represents the O 2p hole [304]. It can be explained that the splitting of these lines occurs due to the transfer of an electron from oxygen ligands to the La-4f (initially empty) that is caused by the charge transfer shake up process [305]. All those peaks are attributed to the La^{3+} oxidation states.

At the intermediate molar ratio of 1:10, the peak positions of La 3d are shifted slightly toward the lower binding energy, which are located at 854.67, 851, 837.9 and 834.6 eV. The peak positions of the highest molar ratio (1:5) also shift slightly toward the higher binding energy, at 855.84, 852.40, 839 and 835.77 eV. In detail, the atomic percentage of satellite peaks of $3d_{3/2}$ are 25.9, 25.1 and 28.9 for the 1:5, 1:10 and 1:15 samples respectively, and the satellite peaks of $3d_{5/2}$ represented 12.9% for the 1:5 sample, 13.7% for the 1:10 sample and 14.5% for the 1:15 sample. The satellite peaks decrease with increasing the La concentration inside the structure, due to the decreases of the O 2p hole. These match well with the result of total O amounts inside the structure that decrease with increasing the La concentration, as presented in Table 4.5. Table 4.5 shows the variation of the W^{6+} content between the un-doped and La-doped samples, the ratios of W^{5+}/W^{6+} which are an approximate to the ratio of fitting peak areas.

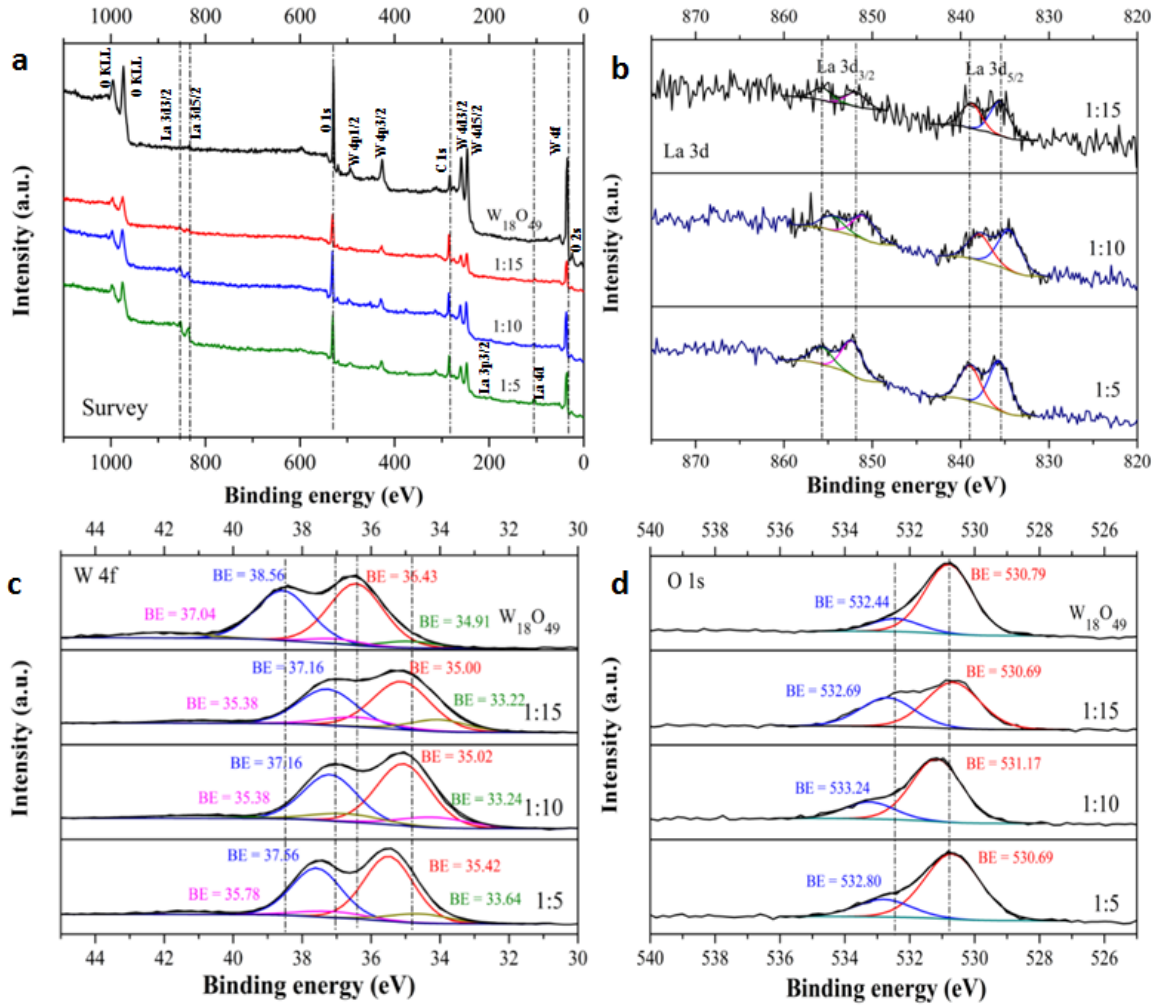

Fig. 4.14 XPS survey and high-resolution scan spectra of the un-doped and La-doped samples. (a) Survey spectra. (b) La 3d, (c) W 4f, and (d) O 1s.

Table 4.5 A summary of the XPS surface characterisation results.

Samples	**Surface composition (atomic ratio)**			
	W^{5+}/W^{6+}	O_{total}/(O+La+W)	W_{total}/(O+La+W)	La_{total}/(O+La+W)
Pure $W_{18}O_{49}$	0.102	0.790	0.21	-
La/W = 1:15	0.282	0.845	0.14	0.015
La/W = 1:10	0.228	0.792	0.175	0.034
La/W = 1:5	0.179	0.785	0.159	0.056

Table 4.5 also shows that the atomic ratio of W is decreased with the increase of La concentrations inside the structures, compared with the plain $W_{18}O_{49}$.

Interestingly, the atomic ratio of O at low and intermediate La concentrations becomes higher than that of the plain $W_{18}O_{49}$, whilst the highest La concentration sample has a lower amount of O inside the structure. The reduced O contents in the doped samples are indicative of an increased V_o in the structure. Further, the increase of W^{5+}/W^{6+} ratios has also revealed that adding La ion in the structure increases the W^{5+} oxidation state, which correlates well with the increased V_o. This effect is similar to that we have been observed earlier for Na- and Ce-doped WO_x nanowires.

O 1s spectra (Fig. 4.14d) can be deconvoluted into two main peaks, of which the lower binding energy peak (530.6 - 531.2 eV) is corresponded to the O in the lattice as O^{2-} (peak 1), and the higher binding energy peak (532.4 – 533.2 eV) is associated with O^{2-}, O^- and OH^- in the oxygen-deficient regions (peak 2) [10]. As in the case of Ce, it would be difficult for La to directly replace the W in the lattice of $W_{18}O_{49}$ nanowires, due to the larger ionic radii of La^{3+} (0.115 nm) than that of W^{6+} (0.065 nm) and W^{5+} (0.068 nm) [5]. As a consequence, La cations might be inserted into the small channels of V_o or hexagonal channels.

La cations can improve the electron transfer and the O mobility of the doped samples, as confirmed by the altered states in the XPS results. Further evidence is from the reduced W^{6+} oxidation state and increased number of bonding between La and O in the structure, as the increased O 1s peak 2 compared with un-doped $W_{18}O_{49}$ samples. Moreover, Peak 1 of O 1s shifts toward lower binding energy in the La:W=1:15 and 1:5 samples, against the plain $W_{18}O_{49}$ nanowires, which provides another evidence for the increased defective and weak O bonding in the structure.

In summary, the change atomic contents of W and O, and the changes in the atomic percentage of La^{3+} from the La 3d spectra offer new evidence for the release of free electrons inside the doped crystalline structures and for the increase of V_o.

4.3.2.5. X-ray absorption near edge spectroscopy (XANES) measurement

A sensitive X-ray absorption near edge spectroscopy (XANES) measurement was performed on the Soft X-ray Spectroscopy beamline at the Australian Synchrotron to precisely analyse the oxidation states and coordination chemistry of Ce and La in the doped nanowires. XANES spectra for the M edge of Ce and La dopants were recorded in both fluorescence yield (FLY) and total electron yield (TEY), which showed similar absorption features. All XANES signals were normalized by the photon flux.

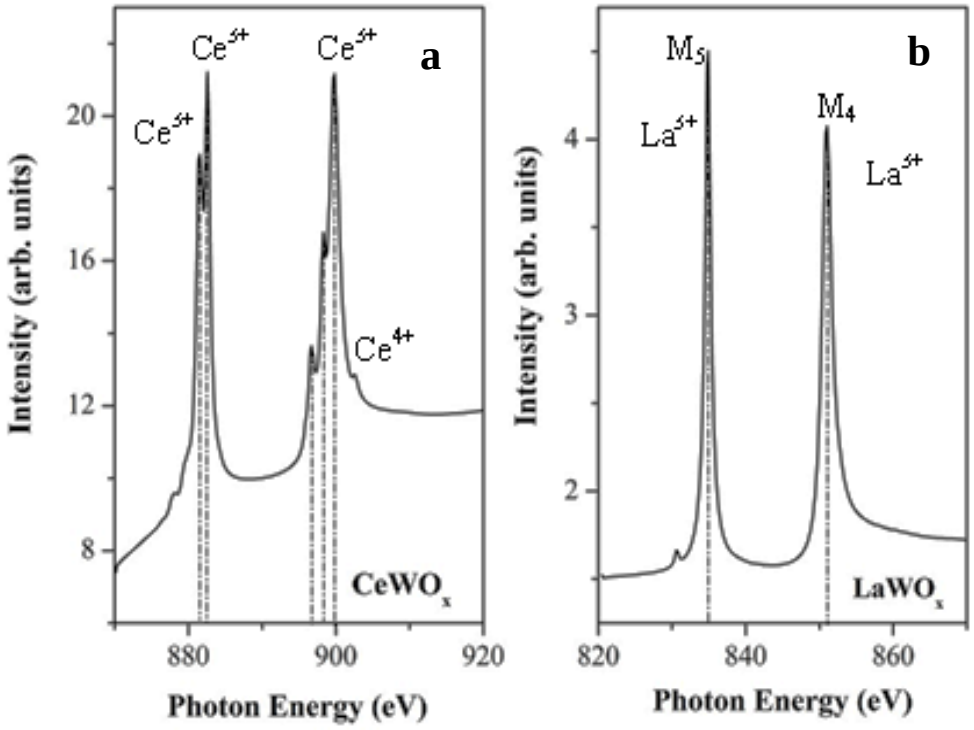

Fig. 4.15 (a) Ce $M_{4,5}$-edge XANES spectrum of Ce-doped WO_x and (b) La $M_{4,5}$-edge

The oxidation and valence states of both the Ce and La dopants in the nanowires were investigated by XANES (Fig. 4.15a and b). The Ce $M_{4,5}$-edges corresponds to the electronic transition from the 3*d* level to the unoccupied 4f state. The spin orbit coupling of the 3*d* hole splits the Ce $M_{4,5}$ spectrum in two edges: M_4 ~ 900 eV and M_5 ~ 882 eV. The multiplet effect due to the core-valence electron-electron interaction is manifested in multiple sharp peaks: 881.5 and 882.6 eV due to the $3d_{5/2} \rightarrow 4f$ transition of Ce^{3+}, 896.7, 898.3 and

899.7 eV due to the $3d_{3/2} \rightarrow 4f$ transition Ce^{3+}, whilst the $3d_{3/2} \rightarrow 4f$ transition of Ce^{4+} at 902.6 eV is very weak. Similarly, the $M_{4.5}$-edges of La dopants display a transition from the 3*d* level to the 4f state. The La M-edge spectrum consists of M_5 and M_4 edges at 834.8 and 851 eV of La^{3+}, respectively. Both spectra of the Ce- and La-doped samples match well with those reported in literature [29, 30]. XANES spectrum of La-doped WOx. The Ce dopants exist in mixed 3+ and 4+ oxidation states, while the La dopants are purely in 3+ state.

4.4 In-situ phase change investigations

4.4.1 WO_x thin films preparation

Plain $W_{18}O_{49}$ nanowires and commercial WO_3 nanoparticles were used in this investigation using thin film samples. To prepare the thin film, 0.1 g of the as-prepared $W_{18}O_{49}$ nanowires was dispersed in 2 ml of ethanol, and then was subject to an ultrasonic bath treatment for 30 min at room temperature. 0.6 ml of the well-mixed suspension was drop-cast onto a flat quartz substrate (or Si wafer) and dried at room temperature overnight, to form a thin film. WO_3 thin films were also preparation following the same procedures.

4.4.2 In-situ characterisation procedure

The in-situ hot stage XRD investigation was carried out using a Cu radiation generated at 40 kV and 40 mA, recorded in 50 °C intervals from room temperature up to 900 °C under low vacuum condition. The heating rate was 50 °C/min, with 10 min dwell time for each step to record the diffraction profile. The scanned 2θ range was 20 - 45° for the $W_{18}O_{49}$ and 20 - 40° for the WO_3 samples. The morphological changes of $W_{18}O_{49}$ and WO_3 nanostructures at selected temperatures were collected for further investigations using TEM, EDX, and XPS etc.

The in-situ Raman spectroscopy was conducted at The University of Nottingham, using a Horiba–Jobin–Yvon LabRAM HR spectrometer, with a 532 nm wavelength at variable power (0.01 to 100%, 0.00336 to 33.6 mW), a 50×

objective and a 300 µm confocal pinhole. A 600 lines/mm rotatable diffraction grating along a path length of 800 mm was utilised to simultaneously scan a range of Raman shifts. Spectra were recoded using a Synapse CCD detector (1024 pixels) thermoelectrically cooled to −60 °C. Before spectrum collection, the instrument was calibrated using the Rayleigh line at 0 cm^{-1} and a standard Si (100) reference band at 520.7 cm^{-1}. Samples were deposited onto Si (100) wafers, inserted into a Linkam LTS350 stage and the temperature profile modulated using a Linkam TMS94 temperature controller. The measurements were recorded in 25 ^{o}C intervals, from room temperature up to 350 ^{o}C in air, due to instrumentation limitation this could not go higher. The heating rate was 10 ^{o}C/min, with 5 min dwell time for each step to record the spectra.

4.4.3 Results and discussion

In Fig. 4.16a the XRD profile, from room temperature to 250 °C, the as-purchased WO_3 nanoparticles showed several main diffraction peaks at 23.1°, 23.6°, 24.3°, 26.6°, 28.8°, 33.4° and 34.1°, which were assigned to the (002), (020), (200), (120), (112), (022) and (202) planes of the monoclinic I (γ-WO_3) (COD 2106382), respectively. The orthorhombic phase (β-WO_3, COD 2107312) was detected at the temperature range from 300 to 700 °C. The main 2θ diffraction peaks appeared at 22.9°, 23.5°, 24.2°, 26.5°, 28.6°, 33.1°, 33.6° and 34.0° were indexed as the (002), (200), (020), (210), (112), (202), (022) and (220) planes, respectively. The β-WO_3 phase started to convert as a tetragonal phase (α-WO_3) at 750 °C, as the (202) peak started to merge with the (022) peak at ~24^{o} and the (200) peak also started to merge with the (020) peak at ~33^{o}. At 800 °C, only the α-WO_3 was identified with peaks at 22.6°, 23.8°, 28.3°, 33.0° and 33.9°, which can be indexed as the (002), (110), (102), (112) and (200) planes of α-WO_3, respectively (COD 1521532). All XRD PDF patterns were provided in Appendix A.

The results of the cooling process (Fig. 4.16b) clearly exhibited that WO_3 nanostructure completely transferred from the α-WO_3 to β-WO_3 phase at 700 °C, and from β-WO_3 to γ-WO_3 at 150 °C. The WO_3 nanoparticles presented reversible phase transitions at lower temperature during cooling, compared with

the heating process. Those mild shifts of transition temperature have been recognized which should be a result of the over cooling. The results from these experiments were also analysed and compared with other previous works. Boulova *et al.* and Lu *et al*. reported in-situ XRD results of the WO_3 nanoparticles in the lower temperature range [306, 307], and they found that the γ-WO_3 phase started to transit to the β-WO_3 phase at ~250 °C, similar to our findings. The α-WO_3 phase transformation was reported at ~670 °C by them, whilst was detected at ~750 °C in our case, which is much closer to the transition temperature of bulk WO_3 structure [308]. Moreover, the triclinic (δ-WO_3) and hexagonal (h-WO_3) phases could not be identified during our investigations.

The heating process of the as-prepared $W_{18}O_{49}$ nanowires (Fig 4.17a) has shown that the γ-$W_{18}O_{49}$ phase (COD 1528166) could be identified at room temperature and remained stable up to 500 °C. The typical diffraction peaks of the γ-$W_{18}O_{49}$ phase were detected at 23.5°, 26.2°, 28.1° and 43.6° at room temperature, which were indexed to the (010), (104), (004) and (413) planes, respectively. At 550 °C, new peaks that emerged in the profile were matched well with the orthorhombic phase (β-WO_3) (COD 2107312). The main diffraction peaks at 22.9°, 23.5°, 24.2°, 26.5°, 28.6°, 33.1°, 33.6° and 34.0° were identified as the (002), (200), (020), (210), (112), (202), (022) and (220) planes of the β-WO_3 phase, respectively. Similar to the WO_3 phase transition, the β-phase remained stable until 700 °C and then started to transfer to the tetragonal phase (α-WO_3) at 750 °C, as the 33.1° peak (202) started to merge with the 33.6° peak (022), and the 23.5° peak (200) started to combine with the 24.2° peak (020). The completely converted α-WO_3 appeared at 800 °C, with peaks at 22.6°, 23.8°, 28.3°, 33.0° and 33.9° being identified as the (002), (110), (102), (112) and (200) planes of the α-WO_3 phase (COD 1521532).

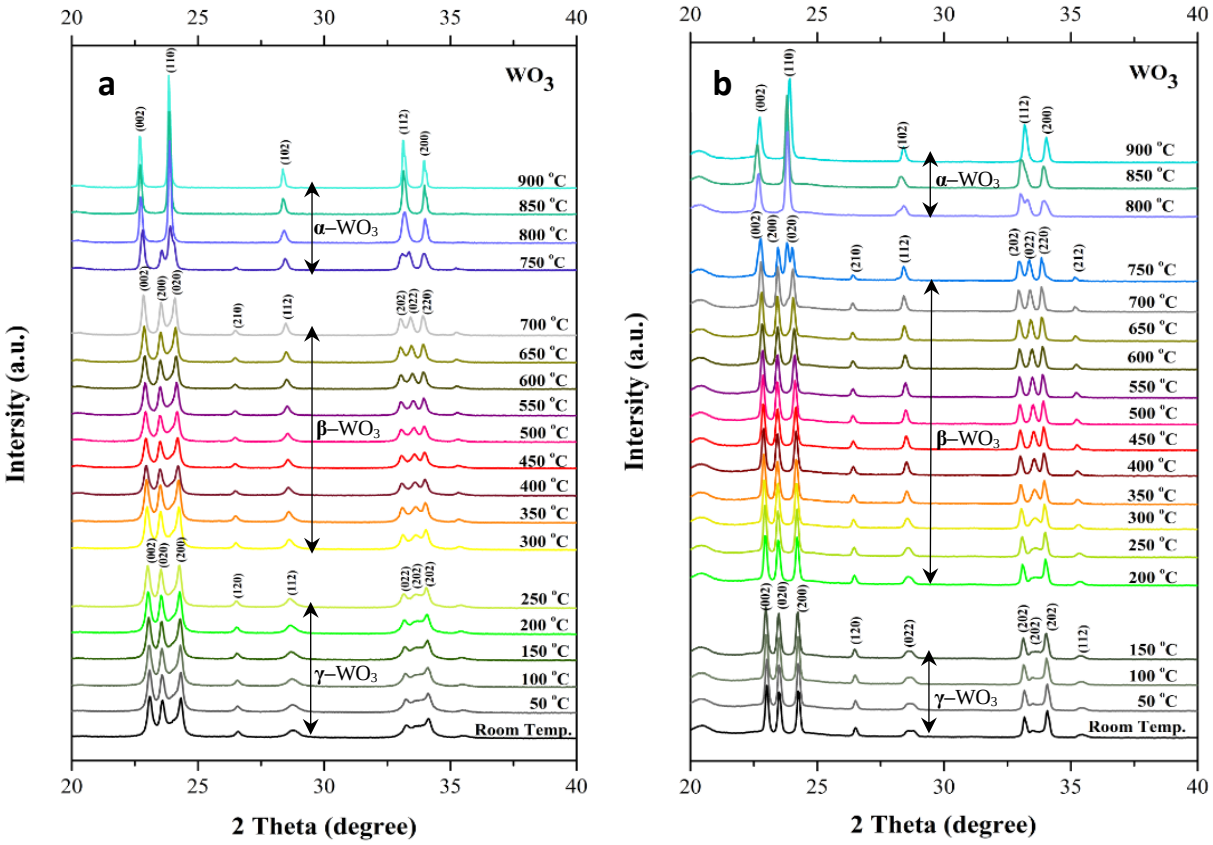

Fig. 4.16 In-situ XRD patterns of the WO_3 nanoparticles, (a) obtained during heating and (b) cooling stage, with 50 °C intervals from room temperature up to 900 °C under low vacuum condition.

For the reverse process, two key phase transitions are noticed from the XRD profiles: (1) from α-WO_3 to β-WO_3 at 800 °C and (2) from β-WO_3 to γ-WO_3 at 200 °C (Fig. 4.17b). Therefore, we can conclude that the $W_{18}O_{49}$ nanowires are stable only up to 500 °C, and that they will be fully oxidised, due to the minute residue oxygen in the low vacuum, to form β-WO_3 at 550 °C and change to different phases until 900 °C, as described earlier. However, the materials cannot be reversed back to $W_{18}O_{49}$ in terms of composition during the cooling process, even down to room temperature, because they have been converted to WO_3.

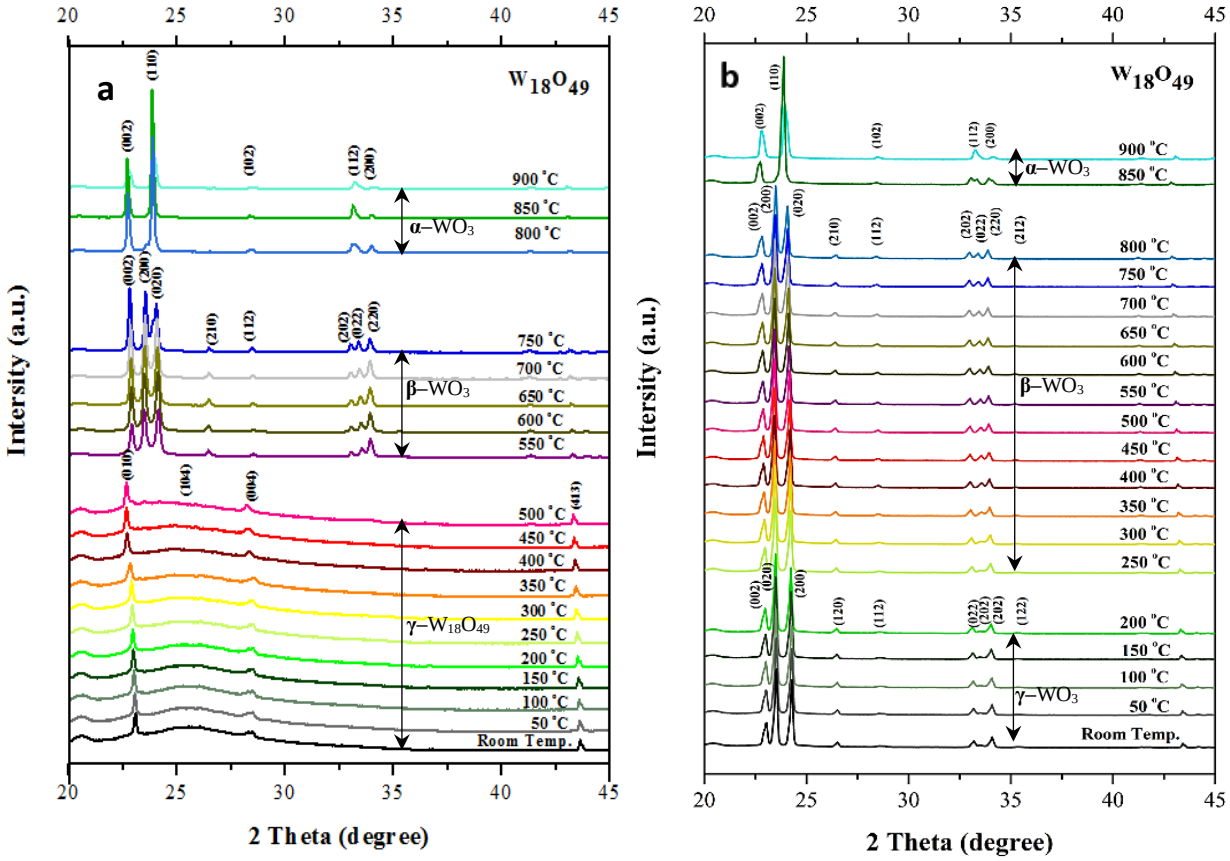

Fig. 4.17 In-situ XRD patterns of the W18O49 nanowires, (A) obtained during heating and (B) cooling, with 50 °C intervals from room temperature up to 900 °C under low vacuum condition.

The in-situ results of $W_{18}O_{49}$ confirmed the similar trends of previous ex-situ study of the same $W_{18}O_{49}$ nanowires reported by Sun *et al*. They have shown that the γ-$W_{18}O_{49}$ only remained stable at temperatures below 450 °C and completely transformed to the monoclinic β-WO_3 phase above 500 °C [300], whilst our results have showed that the γ-$W_{18}O_{49}$ remained stable at temperature below 500 °C, and was then converted to WO_3 after temperature reached 550 °C. These converted WO_3 nanoparticles remained stable up to 900 °C without further crystalline transitions, based on the XRD results.The phase change sequence of the $W_{18}O_{49}$ sample after 500 °C was similar to the original WO_3 sample, with the transition temperatures slightly higher (by 50 °C) than the commercial WO_3 nanoparticles. The result might be due to the difference in crystalline structures and geometry between the $W_{18}O_{49}$-converted WO_3 and the as-received commercial WO_3 (as explained in Chapter 2), since the transformation from $W_{18}O_{49}$ to WO_3 would naturally involve crystal lattice

rearrangement *via* atomic diffusion which will subsequently exaggerate the oxygen vacancy filling and morphology evolution [309]. Moreover, the $W_{18}O_{49}$-converted WO_3 sample did not reverse back to $W_{18}O_{49}$ during cooling at temperature below 500 °C, instead it remained as WO_3, in terms of both structure and phase transition behaviours (Fig. 4.17b). The phase transition temperature of $W_{18}O_{49}$-converted WO_3 at the cooling process was slightly higher by 50 °C compared with those of the original WO3. This might be due to the higher relaxation of the original $W_{18}O_{49}$ structure compared with the original WO_3.

Different phases of both samples were collected at cooling stage, to allow for their corresponding morphological features to be investigated, and the results are shown in Figs. 4.18 and 4.19.

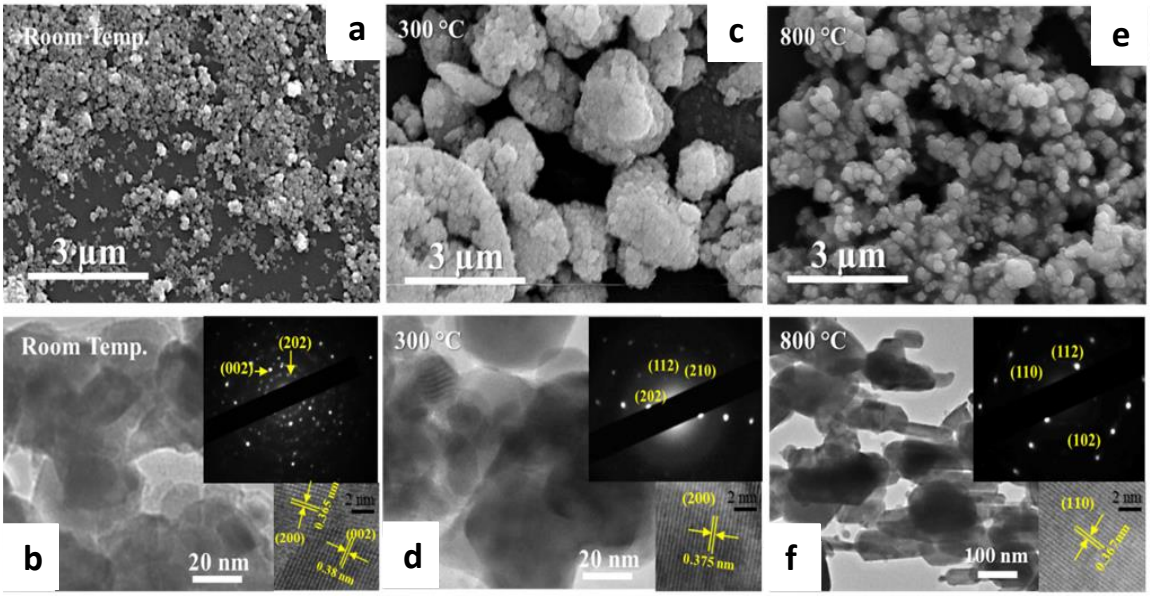

Fig. 4.17 Ex-situ SEM and HRTEM images of the WO_3 nanoparticles after treatment at various heating temperatures: (a and b) room temperature, (c and d) 300 °C, and (e and f) 800 °C. The insets show the diffraction patterns and lattice fringe images of the γ monoclinic, β orthorhombic, and α tetragonal phases of WO_3, respectively.

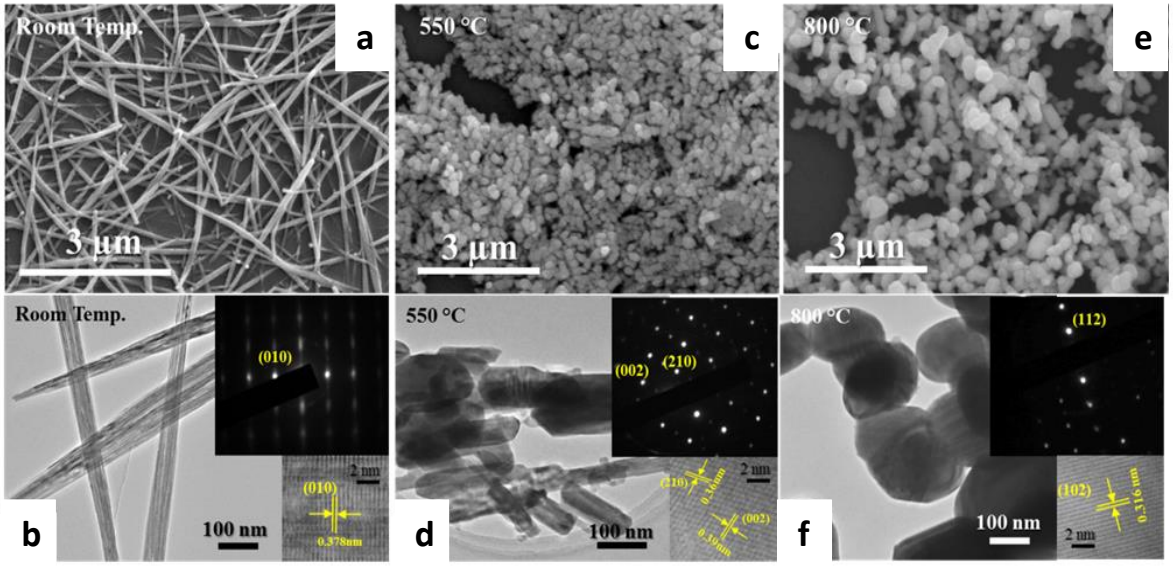

Fig. 4.18 SEM (a, c, e) and HRTEM (b, d, and f) images of bundled ultrathin $W_{18}O_{49}$ nanowires at room temperature, 550 and 800 °C, which were identified as the monoclinic γ-$W_{18}O_{49}$, orthorhombic β-WO_3 and tetragonal α-WO_3 phases, respectively. The samples were collected during heating process.

Fig. 4.18 shows the sequence changes of the γ-, β- and α- phase of the original WO_3 nanoparticles, accompanied with size and morphological modifications. The average size of original γ-WO_3 nanoparticles was about 40 nm in diameter, then it became bigger (about 1-4 μm) due to the agglomeration after 300 °C heating treatment. A clear change of the morphology was occurred at 800 °C for the heated sample, where the α-WO_3 became short nanorods with an average size of 100-150 nm in diameter. The HRTEM lattice fringes and the SAED patterns of each phase, shown as insets, matched very well with our XRD results for these corresponding phases.

In the case of as-prepared $W_{18}O_{49}$ nanowires, the SEM and TEM images confirmed that the bundles with an average size of *ca.* 3 μm in length and 50 nm in diameter (Fig. 4.19a) consisted of ultrathin nanowires of only *ca*. 2-5 nm in diameters and up to 2 μm in length (Fig. 4.19b) [300]. The insets in Fig. 4.18B showing a lattice spacing of 0.378 nm as indicated in the image, corresponded to the (010) plane of γ-$W_{18}O_{49}$, which is in good agreement with the XRD result

of the γ-$W_{18}O_{49}$. More details about the morphology as-prepared $W_{18}O_{49}$ nanowires have been discussed in 4.3.1.1.

The short nanobricks (about 100 nm in diameter and up to 200 nm in length) of the as-converted WO_3 (β-phase) were observed after the temperature reached 550 °C (Fig. 4.19d), which were then completely changed to larger nanoparticles of about 200 nm in diameter after the temperature reached 800 °C (α-phase) (Fig. 4.19f). The SAED and HRTEM results also showed that both the β-phase and α-phase of the as-converted WO_3 samples matched well with our XRD results. At this stage, the $W_{18}O_{49}$ was completely converted to β-WO_3 at 550 °C, due to the minute ambient oxygen residue, as evidenced by the blue thin film turning to yellow during this stage. Meanwhile, the long and thin bundles were broken and re-assembled into short and fat nanorods, and eventually became much larger particles. These results confirmed that different morphologies and phases of WO_x can be variously created due to the temperature and original structure of the raw material. These could be used as a guidance for future structure and morphological design and modification of the WO_x-based nanomaterials.

Effort to understand the phase transitions of WO_3 has been attempted earlier by using XRD and Raman techniques. For revealing the complex structural transitions of the WO_x system, Raman spectroscopy is a more effective technique than XRD, owing to its higher sensitivity to changes in the positions and bonding of the W and O atoms. On the contrary, due to the compositional similarity and structural complexity, XRD is difficult to distinguish the similar and often over-crowded and over-lapped diffraction peaks. Chen *et al*. using Raman spectroscopy studied the phase transformation of WO_3 nanowires under different hydrostatic pressure conditions, ranging from atmospheric to 42.5 GPa [310]. The results showed that bulk WO_3 nanocrystals had lower phase transition pressures than WO_3 nanowires. Cazzanelli *et al*., used both XRD and Raman spectroscopy to investigate WO_3 and H-doped WO_3 powders. Their results confirmed a sequence of phase change from γ- phase → β- phase → α-phase, achieved by increasing temperatures from room temperature to 800 °C [311]. Lai *et al.* also investigated the structural change of WO_3 nanoplatelet

films containing different amounts of NH_4F using Raman technique, and had related it to the photocatalytic behaviour [312]. Lu *et al*. reported the phase transition and oxidation of $W_{18}O_{49}$ nanowires using intrinsic Raman spectroscopy by changing the input laser power [307]. Our study using in-situ Raman had focused on the temperature change, and was aiming to provide more insight into the bonding structures of the two nanomaterials in question.

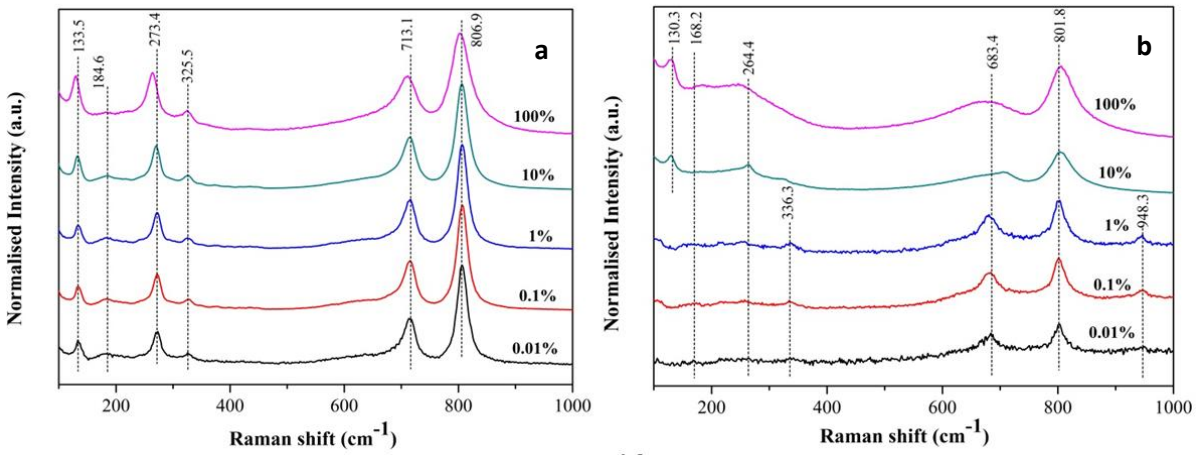

Fig. 4.19 Raman spectra of (a) the WO_3 nanoparticles, and (b) the $W_{18}O_{49}$ nanowires, irradiated with various laser power.

Lu *et al.* reported the laser power effect on the phase transition of the sample, as it generated heat during the process. They reported that the $W_{18}O_{49}$ nanowires were oxidized to form WO_3 when the laser power was increased to 2.3 mW. Moreover, phase transitions of WO_3 from γ- to β- phase were observed at 15 mW laser power. To clarify the effect of laser power on the thermal phase transition, our in-situ Raman experiments were carried out at different laser power, varying from 0.01% to 100% (0.0336 – 33.6 mW), which could lead to temperature raises of the samples from room temperature equivalent to 350 °C (0.01% to 100%), by measuring the surrounding environment close to the sample. The spectra of the WO_3 sample presented in Fig. 4.20a showed that most of the peaks shifted slightly toward lower wavenumbers with increased laser power. However, two peaks at 133.5 and 806.9 cm^{-1} remained at the same positions until 10% laser power (3.36 mW) being applied, and then shifted to lower wavenumber of 129.8 and 801.8 cm^{-1} at 100% laser power (33.6 mW).

These could be the fingerprint wavenumbers of the phase transition from γ- to β of WO_3 nanoparticles.

It has clearly seen that the 130.3 and 168.2 and 264.5 cm^{-1} bands appeared when the laser power was increased for the $W_{18}O_{49}$ nanowires (Fig 4.20b). The W=O stretching vibration mode disappeared as the laser power was raised to 10%, the 801.8 and 683.4 cm^{-1} of asymmetric and symmetric stretching vibration mode of O-W-O remarkably shifted towards higher and lower wavenumber, respectively. These peaks shifted, occurred or disappeared must be corresponding to the points when the $W_{18}O_{49}$ was oxidised to WO_3 between the laser power increase from 10% and 100%. However, it is difficult to precisely correlate the phase transition to the laser power, due to the challenge of accurately measuring the exact sample temperature. We believe that the peak shift could be an indicator of the relaxation of the channels inside the WO_3 and $W_{18}O_{49}$ structures or the elimination of the impurity inside the structures [16]. Based on the above laser power results, 1% laser power was selected for further thermal experiments for both samples.

The in-situ Raman spectra of the WO_3 nanoparticles and bundled $W_{18}O_{49}$ nanowires from room temperature up to 350 °C are presented in Fig. 4.21a and b. The structure of γ-WO_3 crystal at room temperature comprised of corner-shared octahedral with the W atoms displaced from the centres, to form zig-zag chains with alternating short and long W-O bond lengths (As explained more detail in chapter 2). The 718 and 809 cm-1 bands were therefore allocated to O-W-O stretches, with the shorter bonds (1.82 Å) giving rise to the 809 cm-1 bands and the longer (1.88 Å) to the 718 cm-1 bands (Fig 4.20A). The 329 and 275 cm-1 bands were assigned to the O-W-O deformation and bending mode, respectively. The other two peaks detected at 187.5 and 137.1 cm^{-1} belonged to the lattice vibration modes [115].

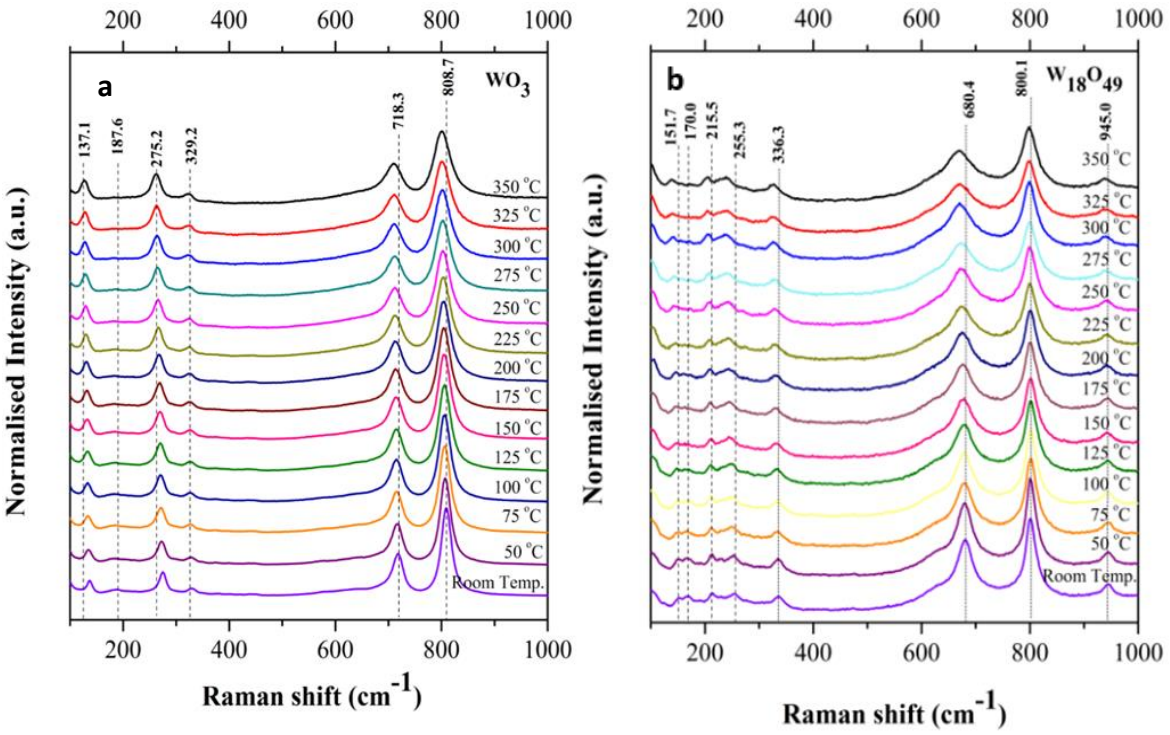

Fig. 4.20 Raman spectra of (a) the WO_3 nanoparticles, and (b) bundled $W_{18}O_{49}$ nanowires, under different annealing temperatures ranging from room temperature up to 350 °C, increasing at 25 °C for each stage, acquired with 1% laser power (3.36 mW).

As the $W_{18}O_{49}$ nanowires structure could be derived from that of WO_3 by introducing V_o compensated by a pair of pentagonal columns of edge-sharing octahedral to produce hexagonal channels which run through the structure. This complex structure was expected to contain a range of O-W-O bond lengths, resulting in a broad band. Raman spectra of the bundled $W_{18}O_{49}$ nanowires showed three main regions (Fig. 4.21b). Two high wavenumber bands at 680 and 800 cm^{-1} were assigned to asymmetric and symmetric stretching vibration mode of O-W-O, respectively. The 255 and 336 cm^{-1} band could be assigned to the O-W-O bending mode of bridging oxygen and deformation mode, respectively [313]. In addition, the weak band at 921-1000 cm^{-1} could be used as the characteristic shifts for $W_{18}O_{49}$ nanowires, which was ascribed to the W=O stretching vibration mode of a terminal oxygen. A moiety did not exist in the WO_3 structure, but was expected in WO_{3-x} channels. This peak intensity remained intact during the testing range, representing good stability of the nanowires. The Raman peak positions are summarised in Table 4.6. It is clearly

shown that the spectra shifted towards lower wavenumber of the stretching and bending modes with increasing temperature, related to an increase in the O-W-O bond length for both structures.

Both the WO_3 and $W_{18}O_{49}$ Raman spectra did not clearly provide the exact characteristic wavenumbers of β-WO_3, although the wavenumber downshifts of both samples with increased heating temperatures appeared to agree well with both works by Boulova *et al*. and Lu *et al*. [32, 306]. Boulova *et al*. reported the structural transitions of WO_3 nanoparticles (average ~35 nm in diameter) by using in-situ Raman spectroscopy, from room temperature to 677 °C. Their result showed that the WO_3 transferred from γ-WO_3 to β-WO_3 phase at temperature about 227 °C, and then to α-WO_3 at about 577 °C. Similar phase transition results of larger WO_3 nanowires about 40-80 nm in diameter and 1 μm in length were also reported by Lu *et al*., which transited from γ- to β-WO_3 at 230 °C. The downshifting to lower wavenumbers in the stretching and bending shift positions could be a result of enlarged W-O bond lengths in the lattice, as being verified in our ex-situ HRTEM examination that the lattice distance of (200) plane increased from 0.365 to 0.375 nm (Fig. 4.18b and d). This enlargement remained after the temperature dropping back to room temperature during the cooling process.

The in-situ XRD results show that the transition from γ- to β-WO_3 phase occurred at around 300 °C for the WO_3 particles and at 550 °C for the $W_{18}O_{49}$ nanowires. This γ- to β phase transformation point is in line with the in-situ Raman result of 275 °C observed here. The disappearance of the 187.6 cm^{-1} band of WO_3 can therefore be considered as the fingerprint shift of the transition from γ- to β-WO_3 (Table 4.6). The Raman peaks of the β-WO_3 phase 129 cm^{-1} can be assigned to the lattice mode; 323.4 and 265 cm^{-1} for the bending mode; and 802.9 and 712.1 cm^{-1} for the major stretching vibrational modes. The $W_{18}O_{49}$ nanowires remain as the monoclinic γ-phase at 350 °C, based on the two in-situ observations, whereas downshift with increases of temperature in the Raman spectra has been verified.

Table 4.6 Raman shifts of $W_{18}O_{49}$ nanowires and WO_3 nanoparticles in the range from 100 to 1000 cm^{-1}. δ is the deformation/in-plane bending, and υ refers to stretching.

	Temperature (°C)	Band positions (cm^{-1})						
		Peak 1	Peak 2	Peak 3	Peak 4	Peak 5	Peak 6	Peak 7
		Lattice modes		δ (O-W-O)		υ (O-W-O)		υ (W=O)
WO_3 nano-particles	Room Temp.	137.1	187.6	275.2	329.2	718.3	808.7	-
	50	134.7	184.8	272.5	327.6	716.6	807	-
	75	134.2	183.2	272.2	326.9	715.6	806.4	-
	100	133.5	184.9	270.0	325.6	714.9	805.8	-
	125	133.3	184.1	269.5	325.8	714.3	805.3	-
	150	132.6	183.9	269.3	325.5	714.1	804.9	-
	175	131.3	183.0	269.5	325.1	713.8	804.9	-
	200	131.3	184.2	266.9	325.1	713	803.8	-
	225	129.8	186.8	266.2	325.3	712.6	802.5	-
	250	129.1	181.8	265.6	324.6	711.8	802.5	-
	275	129.0	-	265.0	323.4	712.1	802.9	-
	300	127.9	-	263.6	323.5	710.6	801.8	-
	325	128.7	-	262.6	323.4	711	800.2	-
	350	127.1	-	262.1	322.6	709.8	800	-
	Reverse at room temp.	129.3	181.4	267.3	322.3	711.8	802.3	-
Bundled $W_{18}O_{49}$ Nano-wires	Room Temp.	151.7	170.0	255.3	336.3	680.4	800.1	945.0
	50	150.1	166.4	253.5	334.5	678.7	800.1	945.0
	75	153.6	166.4	248.1	334.5	680.4	801.8	948.3
	100	148.1	170.0	248.1	334.5	680.4	801.8	945.0
	125	148.1	170.0	246.3	332.7	678.7	800.1	943.3
	150	151.7	-	244.5	329.1	678.7	801.8	941.6
	175	146.3	-	244.5	330.9	675.3	801.8	945.0
	200	146.5	-	244.5	332.7	675.3	801.8	941.6
	225	146.3	-	240.9	330.9	675.3	798.4	943.3
	250	140.8	-	244.5	329.1	670.1	798.4	941.6
	275	144.4	-	239.1	325.5	671.8	800.1	938.3
	300	142.6	-	235.4	325.5	670.1	798.4	940.0
	325	138.9	-	240.7	325.5	671.8	798.4	936.6
	350	138.9	-	239.1	327.3	670.1	798.4	938.3
	Reverse at room temp.	144.4	-	246.3	327.3	673.6	795.1	938.3

In summary, the hot stage XRD results have confirmed that, different from the γ-WO_3 nanoparticles that converted to β-WO_3 just below 300 °C, the γ-$W_{18}O_{49}$ nanowires remained stable up to 500 °C, then were completely oxidized and transferred to β-WO_3 at 550 °C. The ex-situ HRTEM images and SAED patterns of all phases of both samples are in good agreement with the in-situ XRD analyses. The in-situ Raman spectroscopy investigations have confirmed the shift of peak position toward lower wavenumber in both structures, which can be attributed to the increased length of the W-O chemical bonds inside the lattice. Furthermore, we have identified the 187.6cm^{-1} fingerprint band as a means of identifying the phase transition from γ- to β- of the WO_3 nanoparticle structures at 275 °C, which is about 75 °C lower than the relaxation temperature of above 350 °C for the monoclinic γ-$W_{18}O_{49}$ nanowires. This finding suggests the better thermal stability and often higher performance of the ultrathin $W_{18}O_{49}$ nanowires than those of the WO_3 nanoparticles. These properties are highly desirable for engineering applications where elevated temperature is involved.

4.5 Effect of cathodoluminescence properties on WO_x nanostructures

4.5.1 Background of cathodoluminescence (CL) property

A number of studies have been focused on its luminescence properties of the WO_x [314-317]. In contrast, the emission properties of WO_3 have received less attention since it is an indirect bandgap semiconductor with low emission efficiencies. However, non-stoichiometric WO_x with oxygen deficiency has recently attracted much attention in light emission due to its unique structural and electronic features. Two strong luminescence bands from the non-stoichiometric WO_x in the ultraviolet-visible and blue regions have been reported by Lee and Feng [318, 319]. Niederberger *et al.* have suggested that the blue emission is attributed to the band-to-band emission [320], while the ultraviolet-visible emission is ascribed to the states of V_o in the conduction band of WO_x nano-networks [317]. Recently, rare-earth doped semiconductor host, such as $EuWO_6$ [321], TiO_2:Eu [322], ZnO:(La, Eu)Cl [323], $BaTiO_3$:Er [324], WO_3-CeO_2-TiO_2 [325], $LaNiO_3$ [326], etc. has been recognized as an efficient way to develop light emitting devices, because these doped semiconducting

oxides exhibit narrow emission bands in the visible to near-infrared spectral range, which is of importance for applications in light emitting nanodevice.

In this section, we will investigate the CL properties of the Ce- and La-doped WO_x nanowires, benchmarked against the plain $W_{18}O_{49}$ nanowires. The CL microanalysis of the nanowires was conducted in University of Technology of Sydney (Australia), on a FEI Quanta 200 Environmental SEM equipped with a diamond machined parabolic light collector and a Hamamatsu S7011-1007 CCD spectrometer.

4.5.2 Results and discussions of cathodoluminescence properties on WO_x nanostructures

Fig. 4.22(a) shows the CL emission of the un-doped and the two Ce- and La-doped nanowires recorded at 80 K. All the nanowires exhibit a broad asymmetrical emission with a long emission tail extending to the red region. The un-doped $W_{18}O_{49}$ nanowires exhibit a UV peak centred at 3.21 eV (386 nm); this peak is red shifted to 3.0 eV upon doping with La or Ce. The UV emission has been attributed to the band-to-band transition of $W_{18}O_{49}$, whilst the blue emission at ~ 2.5 eV has been attributed to radiative recombination involving defect states, namely V_o [302].

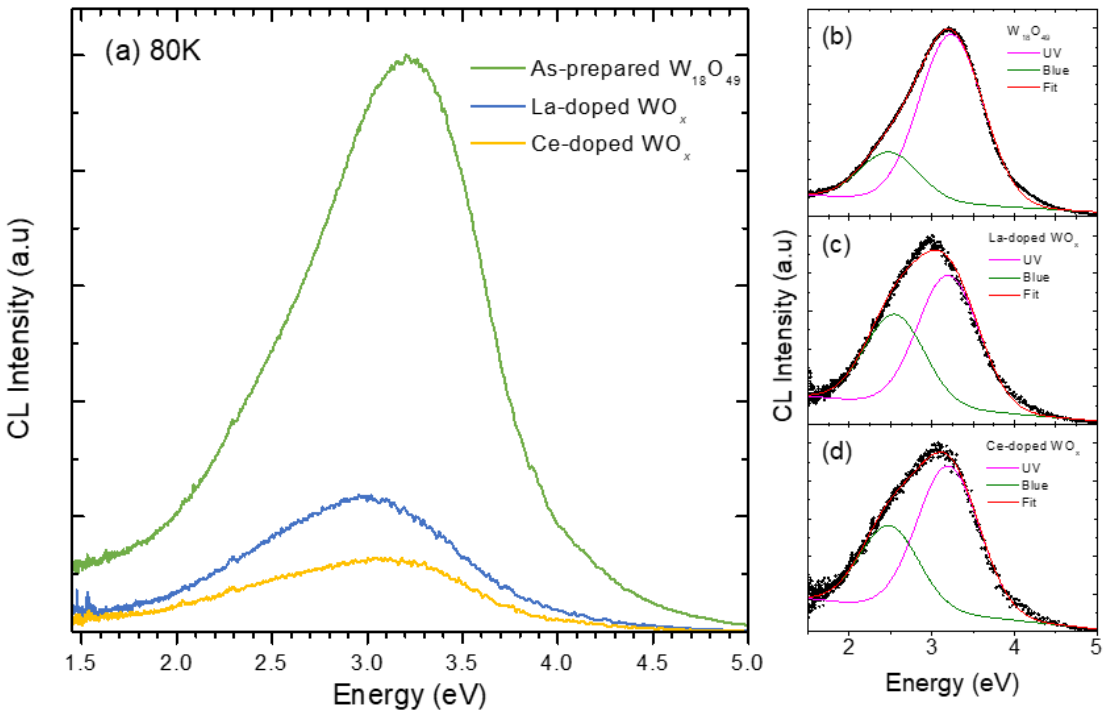

Fig. 4.21 (a) CL spectra of the as-prepared $W_{18}O_{49}$ and Ce- and La-doped WO_x nanowires. The spectra were acquired at 80 K with a beam energy of 10 keV and beam current of 15 nA. (b-d) CL spectra deconvoluted into two UV and blue components, corresponding to the band-to-band transition and radiative recombination involving V_o defects.

To identify the effects of Ce/La incorporation on the luminescence properties of the nanowires, the CL spectra were deconvoluted into two Gaussian functions centred at 3.2 and 2.5 eV (Figs 5b-d). The V_o-related emission is significantly stronger in the doped nanowires with the intensity ratio I(blue)/I(UV) = 0.2, 0.6 and 0.5 for the as-prepared, La- and Ce-doped nanowires, respectively. This result indicates that the introduction of Ce or La ions in the $W_{18}O_{49}$ increases the concentration of V_o defects, which dominate the luminescence mechanism in Ce- and La-doped nanowires. The UV emission intensities of the doped nanowires are significantly weaker than that the un-doped nanowires due to the competitive V_o recombination centres.

Ce and La ions played a role in the evolution of the morphology of the final products as demonstrated in earlier sections, which could modify the growth habit of WO_x and introduced V_o into the structure. This could result in an interesting red-shift in the luminescence emission from the nanowires doped with Ce or La, as had been observed, due to the abundance of V_o in the doped nanowires. Moreover, the La-doped WO_x luminescence spectra of blue emission peak shifted towards green region which presented lower energy and lower intensity compared with that of the plain $W_{18}O_{49}$ nanowires. The UV emission of La-doped sample also moved towards the lower photon energy, which was closer to the violet region with very sharp intensity.

4.6 Summary

In this Chapter, all the resulting nanomaterials including the plain $W_{18}O_{49}$, Na-, Ce- and La- doped WO_x nanostructures have been thoroughly characterised, to determine their morphology, structure, composition, and state of the doping

cations by using combined techniques. These extensive investigations have led to the following findings:

- The changes in morphology and distortion of the framework after doping with different cations (Na, Ce and La) have been confirmed, and the formation of shorter and slightly thicker nanowires has been considered as a result of the growth habit modification by the dopants.
- The addition cations (Na, Ce and La) could be located in the V_o or hexagonal channel of the WO_x structure, based on evidences of various characterisation techniques.
- The results of structure relaxation inside the doped samples and increased W^{5+} compared with plain $W_{18}O_{49}$ could be related to the increase of V_o inside the WO_x framework.
- A complete relationship of geometry-composition-structure-property of both $W_{18}O_{49}$ nanowires and WO_3 nanoparticles have been investigated. The results have shown that temperature could be an important factor for structural relaxation and phase transition.
- An interesting red-shift in the luminescence emission from the nanowires doped with Ce or La has been observed due to the abundance of V_o in the doped nanowires.

Understanding of the structures from both plain and modified WO_x are essentially helpful in the design and development of WO_x-based nanomaterials and their chromic devices by defining their allowed operating conditions and ways for structure modifications.

In the next Chapter, further studies of the electrochromic properties of plain $W_{18}O_{49}$, Ce- and La-doped samples will be investigated and analysed via different essential parameters including diffusion coefficient, response time and stability, to show our findings associated with the structures and compositions.

Chapter 5 Electrochemical properties of WO_x-based nanostructures

5.1 Introduction

In this Chapter, the previously synthesised products, including plain $W_{18}O_{49}$ nanowires, and Ce- and La doped WO_x nanowires, will be further investigated to assess their electrochromic properties via 3-electrode cell using an electrochemistry potentiostat technique (as presented in Chapter 3). The results of Cyclic Voltammetric (CV) will be used to calculate the effective diffusion coefficient (D) for the Li^+ interacalation/de-intercalation during the process. Chronoamperometry (CA) measurements will be used to estimate the switching time of the colouration and bleaching process for each sample.

This Chapter consists of 3 main parts. Firstly, the general electrochromic behaviour differences between the as-synthesized $W_{18}O_{49}$ sub-stoichiometric bundled nanowires and the commercial WO_3 nanoparticles will be discussed, and then extend to the Ce- and La- doped nanowires. Secondly, the effect of low temperature annealing of the WO_x thin film samples on the electrochromic performance will be investigated, to understand the fundamental aspects in the heat treatment-structure-performance relationship. Finally, the mechanisms of coloration and bleaching in both un-doped and doped samples will also be discussed, mainly based on surface chemical composition measurements.

5.2 Electrochemistry measurement

5.2.1 General electrochemical performance of the as-prepared WO_x nanowires *vs* commercial WO_3 nanoparticles

The electrochemistry testing can record the cyclic current changes that are originating from the intercalation/de-intercalation of Li^+ from electrolyte and electron transfer between W^{6+} and W^{5+} during a charge-discharge cycle. This is accompanied by a typical reversible colour change, from blue to transparent (the coloration and bleached states) during each scan cycle. More details will be presented in the mechanism of colouration and bleaching section.

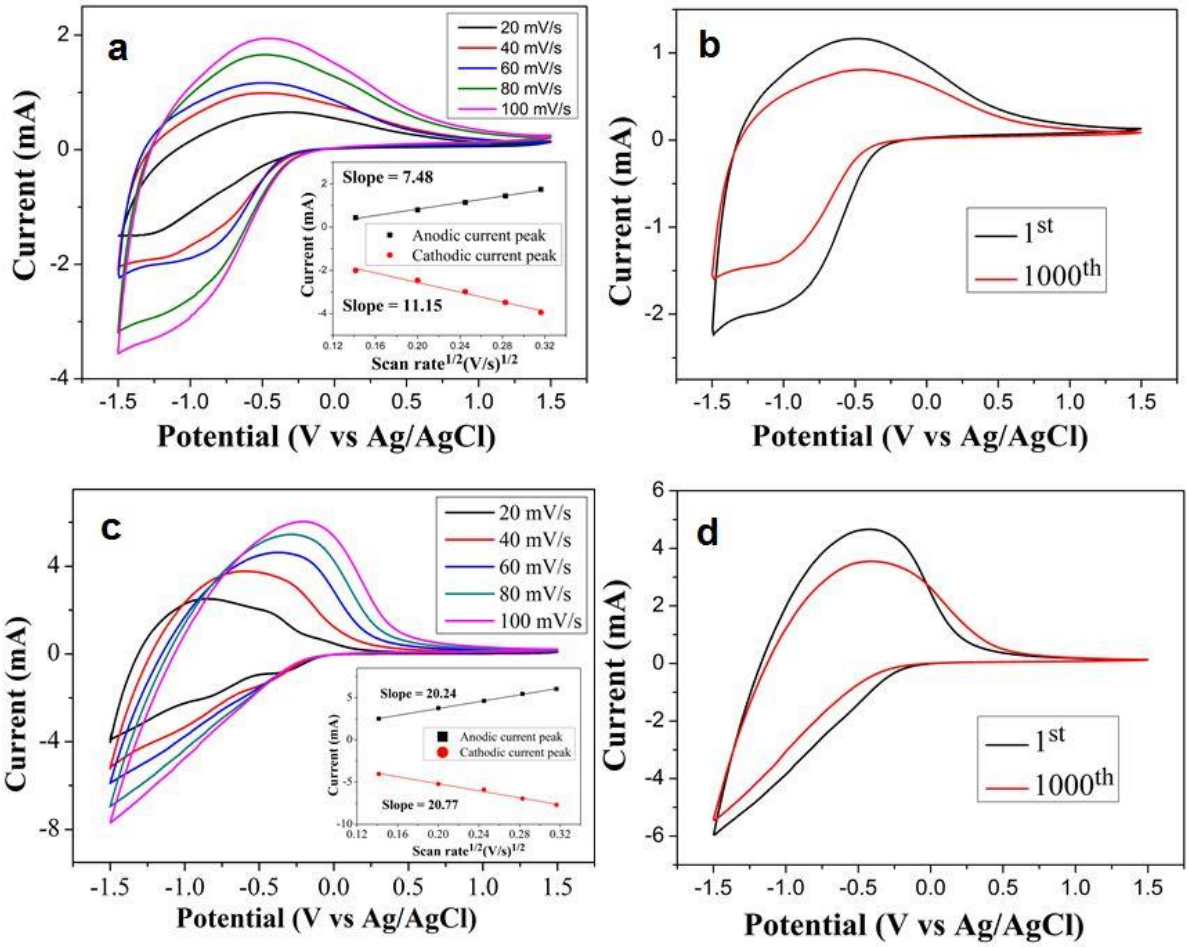

Fig. 5.1 Cyclic voltammetric (CV) results of: (a, b) as-purchased WO_3 nanoparticles, and (c, d) as-prepared $W_{18}O_{49}$ nanowires. Measured at room temperature using propylene carbonate (PC) with 0.5 M $LiClO_4$ and 4 w/v% PPC as the gel electrolyte. Scanned with an applied voltage between -1.5 - 1.5 V, at different scan rate of 20, 40, 60, 80 and 100 mV/s, respectively. Inset: the anodic and cathodic peak current density as a function of the square root of the scan rate. The 1st and 1000th cycles of (b) WO_3 nanoparticles and (d) the as-prepared $W_{18}O_{49}$ nanowires thin films were carried out at a scan rate of 60 mV/s.

Based on the switching time of potential device applications, high scan rates ranging from 20 to 100 mV/s were selected in this study, which led to the overlapping peak in the oxidation from CV profile. From Fig. 5.1, the $W_{18}O_{49}$ nanobundles showed 3 times bigger in charge-insertion density than that of the WO_3 nanoparticles, which means that $W_{18}O_{49}$ can provide faster Li^+ intercalation/de-intercalation kinetics compared with the WO_3 nanoparticles thin films. The inside peak current *vs*. $v^{1/2}$ graph (Fig. 5.1a and c) has been plotted using the maximum and minimum current values. The anodic and cathodic peak

current density plots exhibit an approximate linear relationship, which implies a diffusion-controlled process [246]. The effective diffusion coefficient D of Li^+ intercalation/de-intercalation with units of cm^2/s can be estimated from the anodic and cathodic peak current density dependence on the square root of the potential scan rate $v^{1/2}$, by assuming a simple solid-state diffusion-controlled process [2, 187] (Eq. 2.4):

$$D^{1/2} = \frac{i_p}{2.69 \times 10^5 \times n^{3/2} \times A \times C_o \times v^{1/2}} \qquad \text{(Randles-Sevick's Eq.)}$$

where i_p is the peak current density, n is the number of electrons transferred in unit reaction (electron stoichiometry), A is the surface area of both WO_3 and $W_{18}O_{49}$ electrode film (6.25 cm^2), C_o is the concentration of the diffusion species Li^+ (0.5 mol/cm^3) and v is the scan rate (V/s). By using the slopes of anodic and cathodic peak current density, the estimated diffusion coefficient (D) of the Li^+ for the thin film samples in $LiClO_4$ + PC + PPC electrolyte are $6.1 \times 10^{-10}/5.8 \times 10^{-10}$ and $1.8 \times 10^{-10}/7.9 \times 10^{-11}$ cm^2/s for intercalation/de-intercalation of $W_{18}O_{49}$ and WO_3, respectively. The bigger charge-insertion density of $W_{18}O_{49}$ compared with WO_3 could be related to the structural differences between $W_{18}O_{49}$ and WO_3 (as explained in Chapters 2 and 4). $W_{18}O_{49}$ contains hexagonal channels and oxygen vacancies in its structure framework; whilst monoclinic WO_3 comprises fully the WO_6-octahedra, almost without any oxygen vacancy. Therefore, the $W_{18}O_{49}$ structure could allow Li^+ get into their framework much easier than into the WO_3 structure. These results have shown that the $W_{18}O_{49}$ nanowires will response much faster during the coloration cycle than WO_3 nanoparticles.

Both samples showed a higher intercalation than de-intercalation in the D_{Li}^+ values, which might be due to the trapping of charge carriers inside the lattice structures [327]. To further analysis the stability of both samples, the scan rate of 60 mV/s had been chosen and 1000 cycles of test had been carried out, and the CV results are shown in Fig. 5.1b and d. The maximum specific anodic and cathodic peak currents obtained at the middle scan rate of 60 mV/s were used to calculate the D_{Li}^+ values for intercalation/de-intercalation of both samples,

and the results were $8.4\times10^{-10}/5.1 \times 10^{-10}$ for the 1st cycle and $7 \times 10^{-10}/ 3 \times 10^{-10}$ cm^2/s for the 1000th cycle for $W_{18}O_{49}$, and $1.2 \times 10^{-10}/3.2 \times 10^{-11}$ cm^2/s for the 1st cycle and $6 \times 10^{-11}/1.5 \times 10^{-11}$ cm^2/s for the 1000th for WO_3. The difference between the 1st and the 1000th of D_{Li}^+ intercalation was 17% and 50% for the $W_{18}O_{49}$ and WO_3 respectively. Meanwhile, the difference between the 1st and the 1000th of D_{Li}^+ de-intercalation was 41% and 53% for $W_{18}O_{49}$ and WO_3 respectively. These results have revealed that $W_{18}O_{49}$ nanowires have a better stability, by 33% for intercalation and 12% for de-interaction, compared with the WO_3 nanoparticles.

5.2.2 Effect of electrochromic properties on rare-earth doped nanostructures compared with $W_{18}O_{49}$ nanowires

5.2.2.1 Electrochromic properties of Ce-doped WO_x analysis

The electrochromic properties of the Ce-doped thin film samples were also estimated by the CV technique, using the same gel electrolyte of propylene carbonate (PC) with 0.5 M $LiClO_4$ and 4 w/v% PPC, with comparison to the plain bundled $W_{18}O_{49}$ nanowire thin films, and the results are shown in Fig. 5.2.

Fig. 5.2 shows that the area of the Voltammogram increased and anodic peak current values shifted toward higher potentials at higher scan rates. The D_{Li}^+ was calculated according to Randles-Sevick's equation (Eq. 2.5). The slopes of anodic and cathodic current density (inset in Fig. 5.2) have been used to estimate the average D_{Li}^+ of all sample. The estimated D_{Li}^+ values of 1:15, 1:10 and 1:5 Ce-doped samples intercalation/de-intercalation are $1.5 \times 10^{-9}/1.23 \times 10^{-9}$ cm^2/s, $1.74 \times 10^{-9}/7.9 \times 10^{-10}$ cm^2/s and $4.8 \times 10^{-10}/5.8 \times 10^{-10}$ cm^2/s, respectively. The 1:15 and 1:10 samples present higher D_{Li}^+ values than the plain $W_{18}O_{49}$ ($6.1 \times 10^{-10}/5.8 \times 10^{-10}$ cm^2/s for intercalation/de-intercalation). In addition, the intercalation values of all doped samples also exhibit higher values than those of the de-intercalation, and this might be caused by the trapping of charge carriers inside the lattice structure, as explained in the case for the plain $W_{18}O_{49}$ and WO_3 in previous section [327]. For the stability of doped samples, the 1st and 1000th cycle of CV results for all doped samples are presented in

Fig. 5.3, obtained at the scan rate of 60 mV/s. We have also used the maximum specific anodic and cathodic peak values to calculate the D_{Li}^+ values for intercalation and de-intercalation, and the results are summarised in Table 5.1.

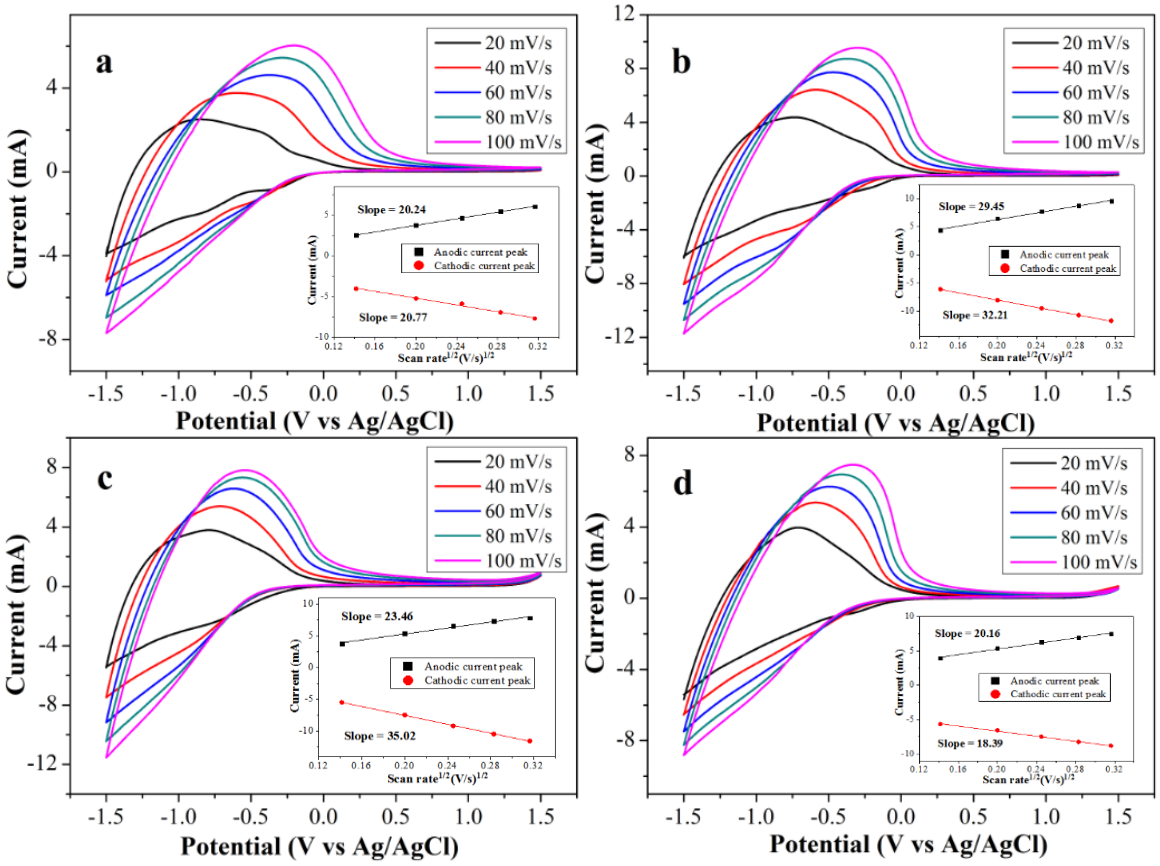

Fig. 5.2 CV curves of different nanowire thin films: (a) Pure $W_{18}O_{49}$, (b) Ce/W = 1:15, (c) Ce/W = 1:10, and (d) Ce/W = 1:5. All results were recorded between -1.5 and 1.5 V at different scan rates of 20, 40, 60, 80 and 100 mV/s. Insets: the anodic peak current density as a function of the square root of the scan rate.

Table 5.1 shows that all doped samples exhibited better ion diffusion kinetics than the plain $W_{18}O_{49}$ nanowires. The D_{Li}^+ was 8.2×10^{-10} cm^2/s for the intercalation of plain $W_{18}O_{49}$ nanowires, whereas this was increased to 2.1×10^{-9}, 1.99×10^{-9}, and 1.32×10^{-9} cm^2/s for the 1:15, 1:10 and 1:5 samples, respectively, at 60 mV/s scan rate. The D_{Li}^+ value decreased with increasing of Ce ion concentrations. Similar trend was observed for the D_{Li}^+ of de-intercalation. Intercalation of the doped samples were much higher than that of the plain $W_{18}O_{49}$ nanowires, by 177%, 102% and 84% for the 1:15, 1:10 and 1:5

samples respectively. The difference in D_{Li}^+ values between the 1st and 1000th cycle showed that Ce dopant reduced the stability in intercalation for the thin films, by 4%, 10% and 12% for Ce/W = 1:15, 1:10 and 1:5, respectively, compared with the plain $W_{18}O_{49}$. The stability in de-intercalation for 1:10 and 1:5 obtained similar trend as in the intercalation which decreased by 6% and 1% respectively, however the improvement of 20% (against the plain $W_{18}O_{49}$) was observed from the film with the lowest Ce concentration (Ce/W = 1:15).

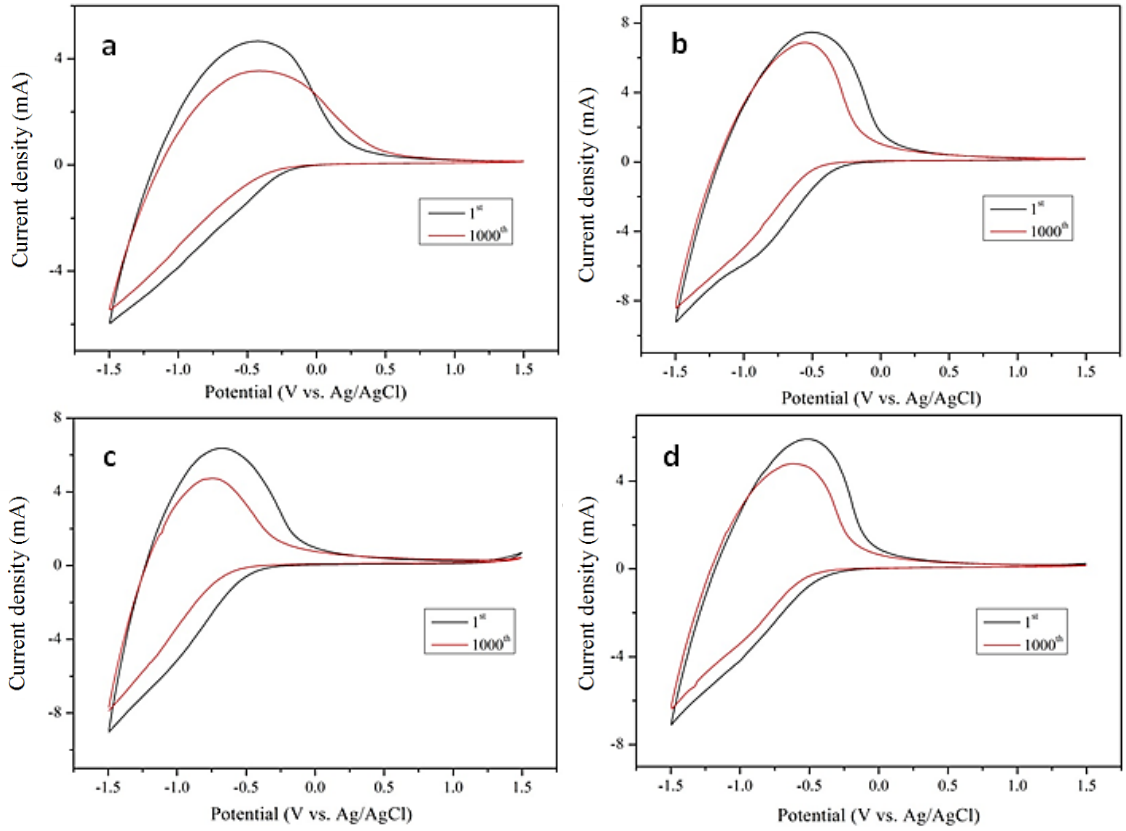

Fig. 5.3 CV curves of different nanowire samples: (a) Plain $W_{18}O_{49}$, (b) Ce/W = 1:15, (c) Ce/W = 1:10, and (d) Ce/W = 1:5, after the 1st and the 1000th cycle, recorded between -1.5 and 1.5 V at a scan rate of 60 mV/s for all samples.

The Ce/W = 1:15 sample offered the fastest ion diffusion kinetics and best stability compared with other doped samples. This might be due to the decreased dimensions of the sample, which resulted in an increase of the surface area, and reduction of the ion diffusion path length, whilst still preserved enough room between the lattice for Li^+ intercalation and de-intercalation to take place (The morphologies and structures were presented in Chapter 4). On the

contrary, both Ce/W = 1:10 and 1:5 samples suffered from agglomeration, and their structures became bigger, thus resulted in a longer diffusion path (measured by the radius of the nanostructures). Meanwhile, too many Ce ions in the lattice would be more difficult for the Li^+ to get into/out the structure during cycles. Moreover, larger D_{Li}^+ means a greater mobility of Li^+, translating to a shorter switch time between the colouration/bleaching process. Fig. 5.4 shows the different intensities of the 1st cycle of the coloured stage for each thin film sample.

Table 5.1 A summary of the intercalation D_{Li}^+ values for the doped and plain $W_{18}O_{49}$ thin film samples.

Samples	**D_{Li}^+ of Intercalation (cm^2/s)**			**D_{Li}^+ of De-intercalation (cm^2/s)**		
	1st cycle	1000th cycle	Difference between 1st and 1000th cycle (%)	1st cycle	1000th cycle	Difference between 1st and 1000th cycle (%)
Pure $W_{18}O_{49}$	8.2×10^{-10}	7×10^{-10}	15	5.05×10^{-10}	3×10^{-10}	41
Ce/W = 1:15	2.1×10^{-9}	1.7×10^{-9}	19	1.4×10^{-9}	1.1×10^{-9}	21
Ce/W = 1:10	1.99×10^{-9}	1.5×10^{-9}	25	1.02×10^{-9}	5.3×10^{-10}	47
Ce/W = 1:5	1.32×10^{-9}	9.6×10^{-10}	27	9.3×10^{-10}	5.4×10^{-10}	42

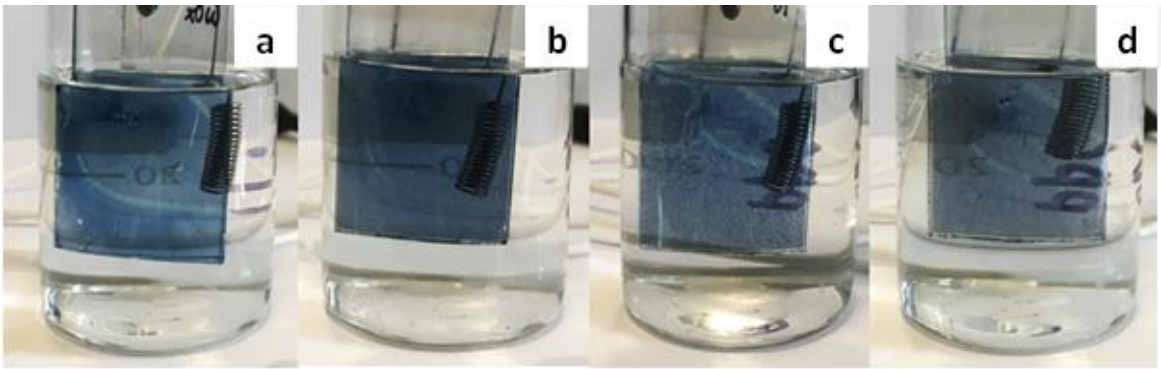

Fig. 5.4 The coloured stage of various thin films. (a) Plain $W_{18}O_{49}$ nanowires, (b) Ce/W = 1:15, (c) Ce/W = 1:10, and (d) Ce/W = 1:5. The pictures were taken after the 1st cycle of the CV testing between -1.5 and 1.5 V at a scan rate of 60 mV/s.

The switching responses for the reversible process (colouration and bleaching) of all thin films were measured from the CA (Fig. 5.5), as the time required for excess current to reduce to 10% of its absolute maximum value [189, 328]. The plain $W_{18}O_{49}$ sample was estimated about 7.5 s for bleaching and 13.5 s for colouration, compared with 10.5 s for bleaching and 14.9 s for colouration for the Ce/W = 1:15 sample. The response time of 1:10 was slightly faster, being 9.2 s/14.2 s for the bleaching/colouration, whilst the 1:5 sample was slower at 11.2 s/ 16.9 s for the bleaching/colouration, compared with the 1:15 sample.

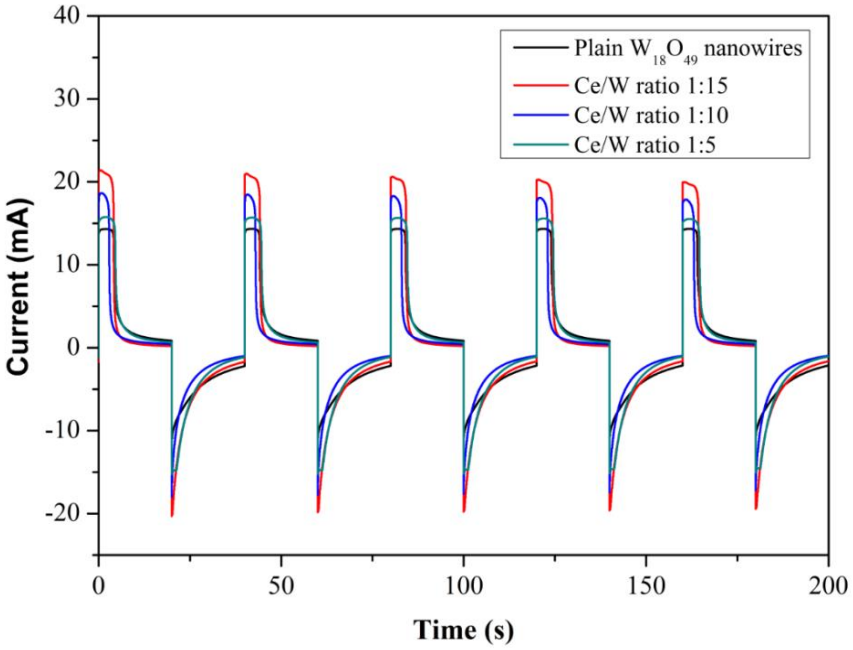

Fig. 5.5 Chronoamperometry (CA) measurements of all un-doped and doped samples for voltage steps between +1.5 V and -1.5 V for 20 s in the same gel electrolyte.

5.2.2.2. Electrochromic properties of La-doped WO_x analysis

The CV results of the La-doped thin films, performed in the same potentiostat system using similar propylene carbonate (PC) with 0.5 M LiClO4 and 4 w/v% PPC electrolytes, is presented with comparison to the plain bundled W18O49 nanowires in Fig. 5.6. By applying a cathodic potential from +1.5 to -1.5 V, a cathodic current raised, and the colour of the film turned to dark blue as the Li+ and electrons were intercalated into the film. Reversing the direction from -1.5

to +1.5 V, the anodic current was recorded, and the film turned colourless, subjecting to the Li+ and electron being de-intercalated from the film.

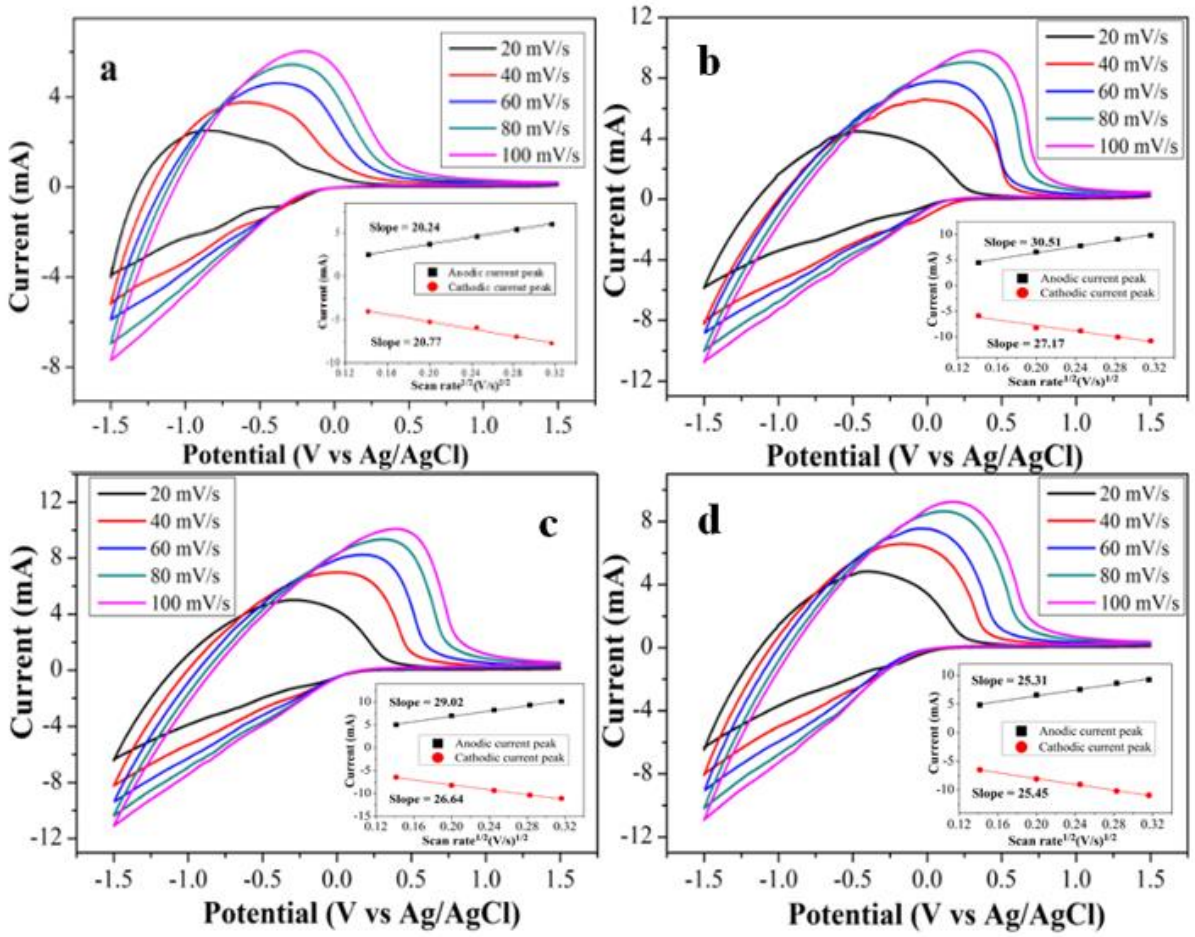

Fig. 5.6 CV curves of different nanowire thin films: (a) Plain $W_{18}O_{49}$, (b) La/W = 1:15, (c) La/W = 1:10, and (d) La/W = 1:5. All results were recorded between -1.5 and 1.5 V at different scan rates of 20, 40, 60, 80 and 100 mV/s. Insets: the anodic peak current density as a function of the square root of scan rates.

Fig. 5.6 shows that the area of the voltammogram increased and anodic peak current values shifted toward higher potentials with increasing the scan rate. D_{Li}^+ was estimated according to Randles-Sevick's equation (Eq. 2.5). The average D_{Li}^+ of all La-doped thin films were optimised by using the slope value in the current *vs.* $v^{1/2}$ graph. The estimated D_{Li}^+ values of the 1:15, 1:10 and 1:5 samples for intercalation/de-intercalation were $1.05 \times 10^{-9}/1.32 \times 10^{-9}$ cm^2/s, $1 \times 10^{-9}/1.19 \times 10^{-9}$ cm^2/s and $9.17 \times 10^{-10}/9.07 \times 10^{-10}$ cm^2/s, respectively. The doped samples have shown better D_{Li}^+ values, compared with the plain $W_{18}O_{49}$

(6.1×10^{-10}/5.8×10^{-10} cm^2/s). Interestingly, the de-intercalation values of 1:10 and 1:15 samples were higher than those of the intercalation, and this might be due to degradation of the sample. More details of this analysis will be discussed in next section, 'mechanism of the colouration and bleaching state'.

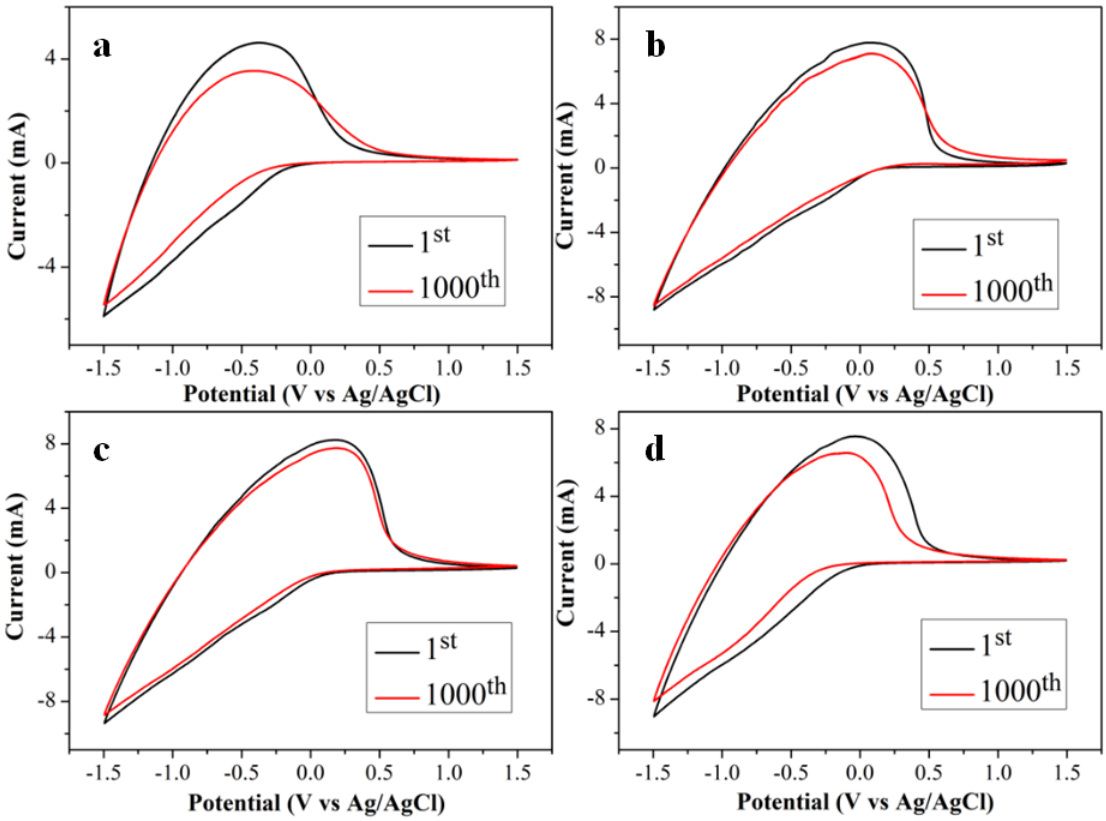

Fig. 5.7 CV curves of different nanowire samples: (a) Pure $W_{18}O_{49}$, (b) Ce/W = 1:15, (c) Ce/W = 1:10 and (d) Ce/W = 1:5, after the 1st and the 1000th cycle, recorded between -1.5 and 1.5 V at 60 mV/s scan rate for all samples.

The stability of these samples, the 1st and 1000th cycle of CV for all samples had been evaluated (as shown in Fig. 5.7) at the scan rate of 60 mV/s. Using the maximum specific anodic and cathodic peak we calculated the D_{Li}^+ values for intercalation/de-intercalation, and the results are summarised in Table 5.2. For the first CV cycle, the cathodic current density value was 5.89, 8.81, 9.36 and 9.04 mA for the plain $W_{18}O_{49}$, 1:15, 1:10 and 1:5 samples, respectively. And the lower value of the anodic current density was obtained at 7.79 mA for the 1:15 sample, 8.24 mA for the 1:10 sample, and 7.54 mA for the 1:5 sample for the 1st cycle. At the 1000th cycle, all La-doped samples displayed decreased

current density values when compared with the 1st cycle of CV. The cathodic current density for the 1:15, 1:10 and 1:5 samples at 1000th cycle was recorded as 8.53, 8.85 and 8.13 mA, respectively. The anodic current density at the 1000th was 7.12 mA for the 1:15 sample, 7.74 mA for 1:10 and 6.56 mA for the 1:5 sample.

Table 5.2 A summary of the intercalation D_{Li}^+ values for the doped and pure $W_{18}O_{49}$ thin film samples.

Samples	**D_{Li}^+ of Intercalation (cm^2/s)**			**D_{Li}^+ of De-intercalation (cm^2/s)**		
	1st cycle	1000th cycle	Difference between 1st and 1000th cycle (%)	1st cycle	1000th cycle	Difference between 1st and 1000th cycle (%)
Pure $W_{18}O_{49}$	8.2×10^{-10}	7×10^{-10}	15	5.05×10^{-10}	3×10^{-10}	41
La/W = 1:15	1.83×10^{-9}	1.72×10^{-9}	6	1.43×10^{-9}	1.2×10^{-9}	16
La/W = 1:10	2.07×10^{-9}	1.85×10^{-9}	11	1.6×10^{-9}	1.31×10^{-9}	18
La/W = 1:5	1.93×10^{-9}	1.56×10^{-9}	19	1.34×10^{-9}	1.01×10^{-9}	25

From Table 5.2, both intercalation and de-intercalation D_{Li}^+ values of all La-doped samples were over 100% higher than those of the plain $W_{18}O_{49}$. The La-doped samples also had better D_{Li}^+ values than the Ce-doped samples (as shown in Table 5.1). The D_{Li}^+ of plain $W_{18}O_{49}$ was 8.2×10^{-10} cm^2/s for the intercalation, which increased to 1.83×10^{-9}, 2.07×10^{-9}, and 1.93×10^{-9} cm^2/s for the 1:15, 1:10 and 1:5 doped samples, respectively. The difference in D_{Li}^+ values between the 1st and 1000th cycle indicated that La dopant increased the stability in intercalation for the thin films, by 9%, 4% for La/W = 1:15 and 1:10 samples, respectively; whilst reduced the stability by 4% for the 1:5 sample, when compared with the plain $W_{18}O_{49}$. The stability in de-intercalation for all doped samples improved by 25, 23 and 16% for the 1:15, 1:10 and 1:5 samples respectively (against the plain $W_{18}O_{49}$). To compare with the Ce-doped samples, it was clearly shown that La-doped samples offered better stability performance with slightly higher D_{Li}^+ values for films with intermediated and lower dopant concentrations (1:10 and 1:15).

La-doped with ratio 1:10 offered the fastest ion diffusion kinetics and best stability compared with the other La-doped samples; whilst the Ce-doped samples exhibited the best D_{Li}^+ value and stability for the lowest concentration sample (1:15). Fig. 5.8 represented different intensities of the 1st cycle of the coloured stage for each La-doped thin film sample.

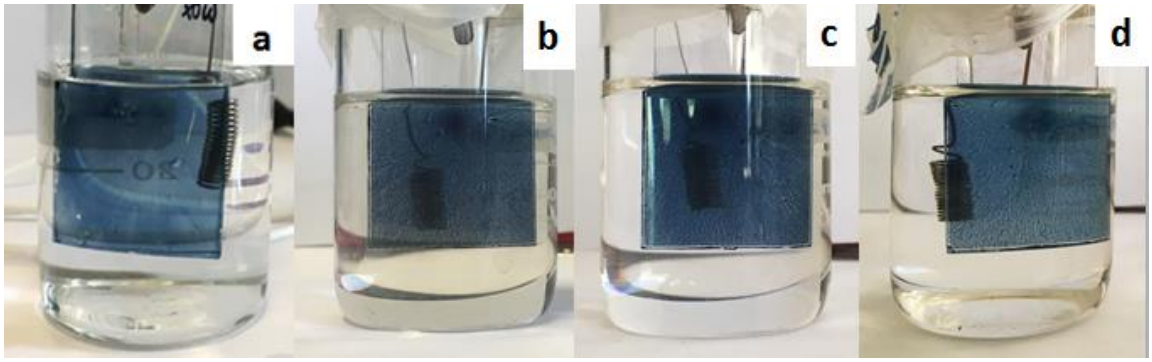

Fig. 5.8 The coloured stage of various thin films. (a) Pure $W_{18}O_{49}$, (b) La:W = 1:15, (c) La:W = 1:10, and (d) Ce/W = 1:5. The pictures were taken after the 1st cycle of the CV testing between -1.5 and 1.5 V at a scan rate of 60 mV/s.

Larger D_{Li}^+ means a greater mobility of Li^+, which can be regarded as equivalent to a shorter switch time of the colouration/bleaching process. The switching responses for reversible process of all La-doped samples were also estimated from the CA measurement (Fig. 5.9), as the time required for excess current to reduce to 10% of its absolute maximum value. As we mentioned in previous section, the response time of plain $W_{18}O_{49}$ was estimated to be 13.5 s and 7.5 s for the colouration and bleaching stage, respectively. For La-doped samples, the switch time of the bleaching process was 6.6, 7.7 and 7.6 s for the 1:15, 1:10 and 1:5 samples, separately. Longer response time was detected during the colouration process, which was 12.8 s for 1:15 sample, 13.9 s for the 1:10 sample and 13.5 s for the 1:5 sample. Those response time and DLi+ value results have proven that the doped samples (both Ce- and La-doped) offered a greater mobility of Li+ and faster switch time compared with the plain W18O49, if we assumed that the similar amount of DLi+ value was obtained in each sample.

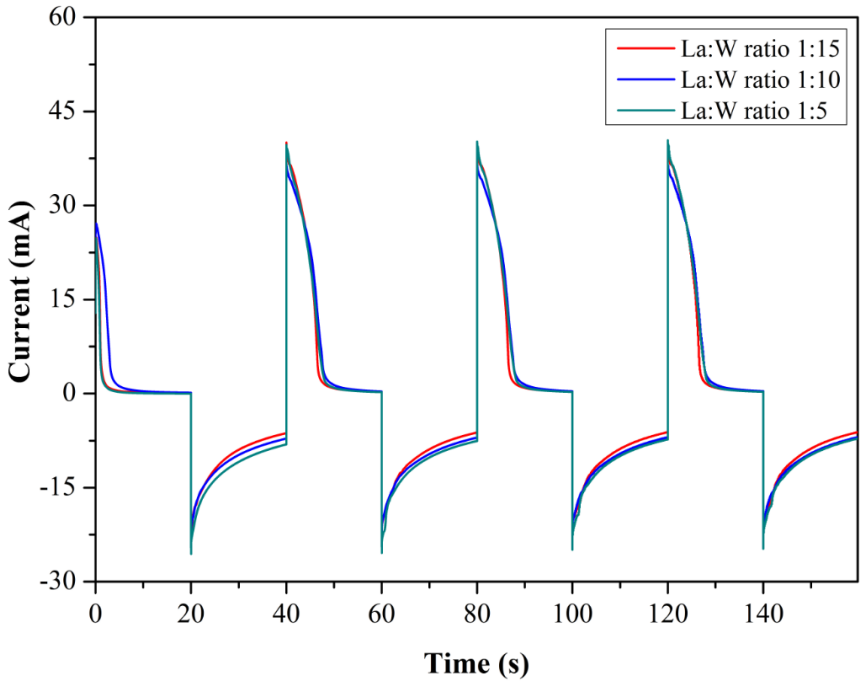

Fig. 5.9 Chronoamperometry (CA) measurements of all un-doped and doped samples for voltage steps between +1.5 V and -1.5 V for 20 s in the gel electrolyte.

5.3 Effect of annealing treatment on colouration

The stability and degradation of these electrochromic materials are interested issues that affecting the performance of chromic devices. Fewer studies have been paid attentions to the cause for, and solutions to, these issues [6-8]. A simple low temperature annealing treatment is one possible solution to deal with the degradation issue in the chromic and others energy related applications of these WO_x nanomaterials [329]. Annealing treatment affects the structure homogeneity, eliminates the defects and improves crystallinity of transition metal films. As provided in results of previous Chapters, temperature could affect the crystalline structure of both $W_{18}O_{49}$ nanowires and WO_3 nanoparticles. This section will focus on the fundamental aspects of annealing treatment effects on the electrochromic performance of both thin films of the as-synthesised $W_{18}O_{49}$ bundled nanowires and commercial WO_3 nanoparticles. The set-up used for the low temperature annealing in this Chapter has been described in Chapter 4 (in-situ investigation). The experimental design is aimed to not change the original phase of the material, whilst endeavour to improve

the relaxation of the structure *via* annealing. This study is trying to link detailed structural analyses with the kinetic behaviour of the intercalation compounds (*via* the electrochromic measurement results), and aiming to establish the fundamental relationship of the heat treatment-structure-performance.

5.3.1 WO_x thin films preparation

Thin films of the as-prepared $W_{18}O_{49}$ nanowires and as-purchased WO_3 nanoparticles were prepared using the spin coating technique, as explained in Chapter 3. As-dried thin films were further heat-treated under a rich Ar atmosphere (100 sccm flow rate) in a tube furnace for 2 h. The treatment temperature ranging from 250 to 350 °C was selected based on results from pervious Chapter, because the thin films started to crack at 400 °C.

5.3.2 Results and discussion of annealing treatment on WO_x thin films

5.3.2.1 Effect of annealing treatment on morphology and structure of WO_x

Fig. 5.10A and B presented the XRD crystalline structures of the as-prepared and heat-treated WO_3 nanoparticles and bundled $W_{18}O_{49}$ nanowires, respectively. The $W_{18}O_{49}$ film exhibited main diffraction peaks at 23.1, 28.6 and 47.2°, which were assigned to the (010), (310) and (020) planes, corresponding to a monoclinic phase structure, with lattice constants of a = 18.32, b = 3.79, c = 14.04 Å and β = 115.03° (reference: JCPDS No: 01-073-2177). The increased relative intensities and narrowed feature of the peaks of (010) and (310) indicated that the crystal planes of the nanowires preferably grew along the <010> direction. For comparison, the main diffraction peaks at 23.1°, 23.6° and 24.4° were assigned as the (002), (020) and (200) plane of the γ-WO_3 nanoparticles. The measured lattice constants of the commercial WO_3 were: a = 7.33, b = 7.54, c = 7.68 Å and β = 90.884° (reference: JCPDS No. 83-0951). It is noted that the intensities of the three main peaks for WO_3 did not show any changes before and after the heat-treatments under various conditions.

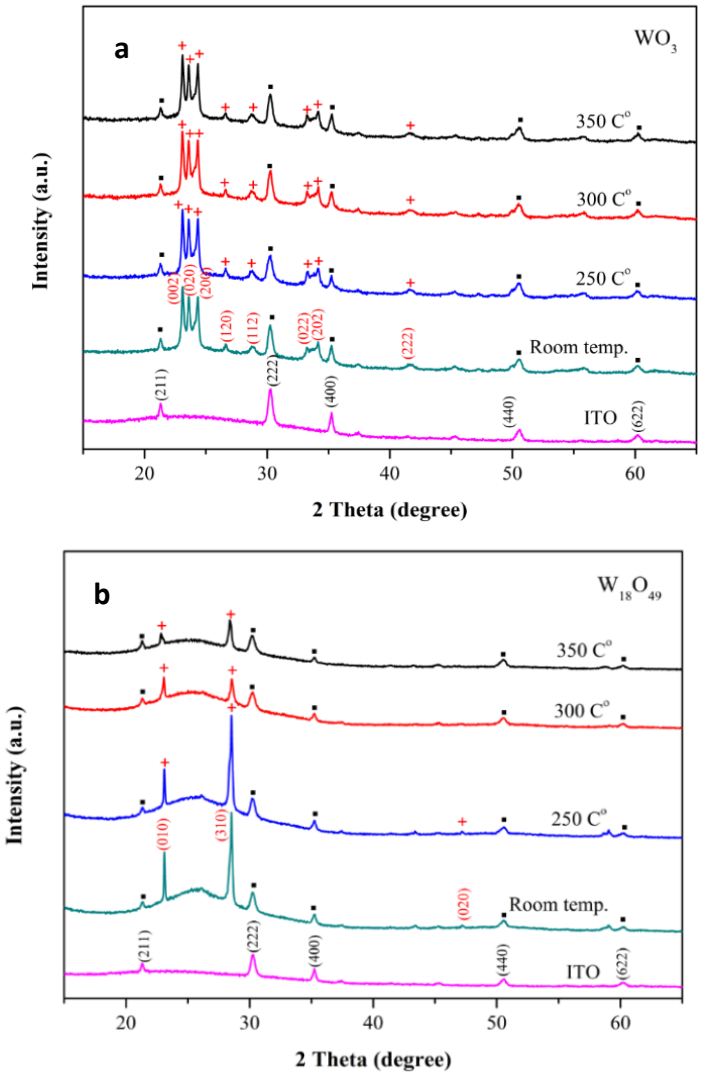

Fig. 5.10 XRD patterns. (a) Thin film of WO_3 nanoparticles with and without heat treatment (reference: JCPDF No. 83-0951). (b) Thin films of bundled $W_{18}O_{49}$ nanowires with and without heat treatment (reference: JCPDS No: 01-073-2177). The dot (▪) indicates the peaks from the ITO substrate following JCPDS No. 06-0416, and the plus (+) represents peaks of WO_x.

The morphology of the WO_3 thin films did not show any differences or signs of agglomeration before (Fig. 5.11a) and after the annealing (Fig. 5.11c, e and g). The particles appeared to remain their average diameter of 40 nm. Similarly, the bundled $W_{18}O_{49}$ nanowires also showed no signs of morphological change before (Fig. 5.11b) and after the annealing (Fig. 5.11d, f and h). The bundles kept their originally random distribution and orientation intact after the annealing. The only difference between the two types of thin film was that the WO_3 nanoparticles exhibited isolated distributions whilst the bundled nanowires

easily formed networks. In localised areas, the nanowire bundles appeared to be quasi-aligned, originating from the spin coating process, which could be beneficial for the films to have better mechanical stability and higher conductivity than those of nanoparticle films.

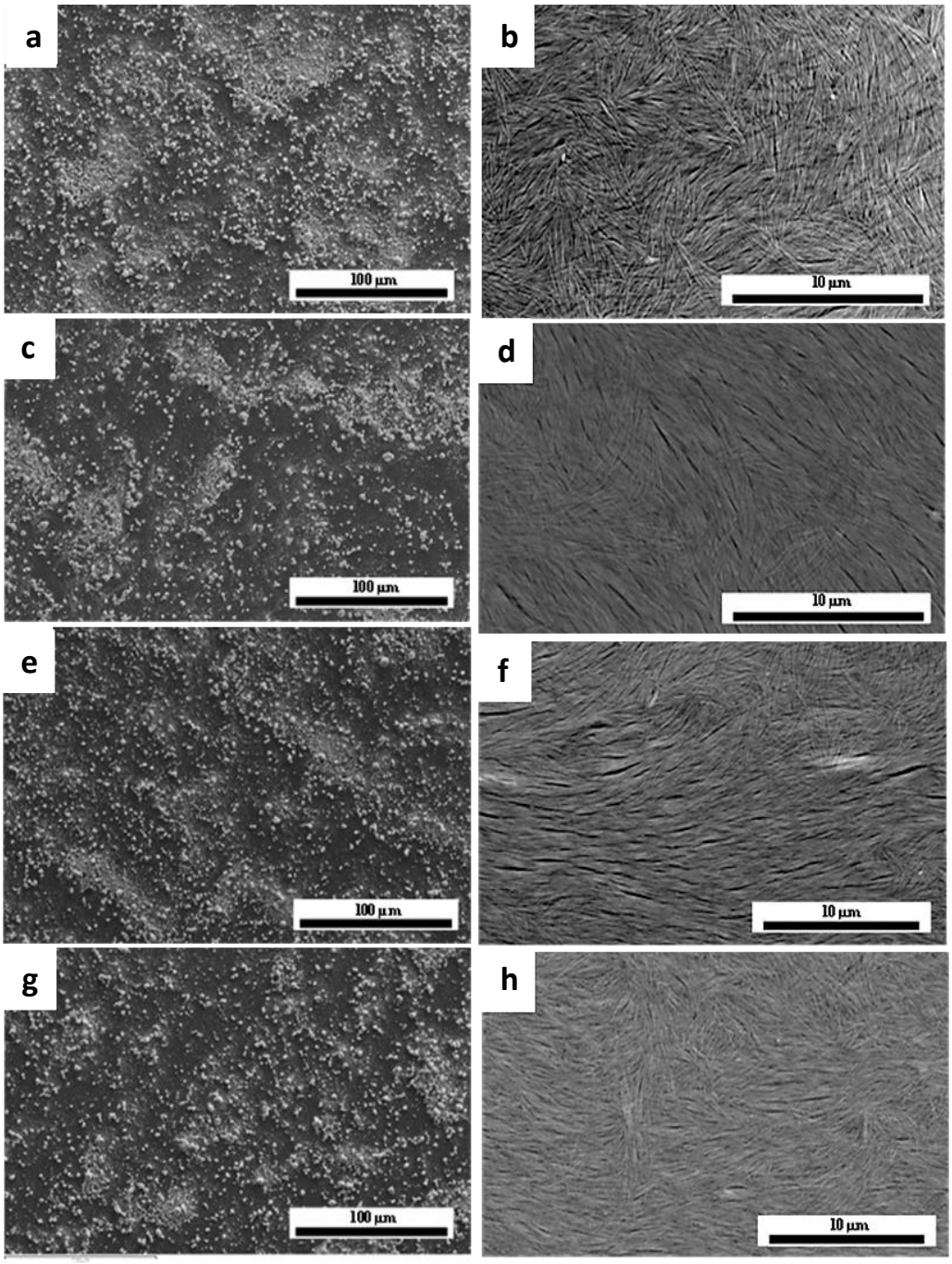

Fig. 5.11 SEM images of thin films before and after annealing at different temperatures of 250, 300 and 350 °C, for the WO3 nanoparticles (a, c, e and g), and bundled W18O49 nanowires (b, d, f and h), respectively.

According to the in-situ XRD hot stage study from previous Chapter, we have reported that the WO_3 nanoparticles completely changed from γ- to β-WO_3 at 300 °C in vacuum atmosphere with structure about ~1-4 μm in diameter, whereas the ex-situ XRD and SEM results of the 300 and 350 °C Ar heat-treatment thin film samples did not detect any phase transition signal, and presented the same morphology to the room temperature thin film sample. This suggests that the Ar atmosphere could be an important factor for the difference in phase change temperature point from γ- to β-WO_3, which shifted toward the higher temperature (above 350 °C).

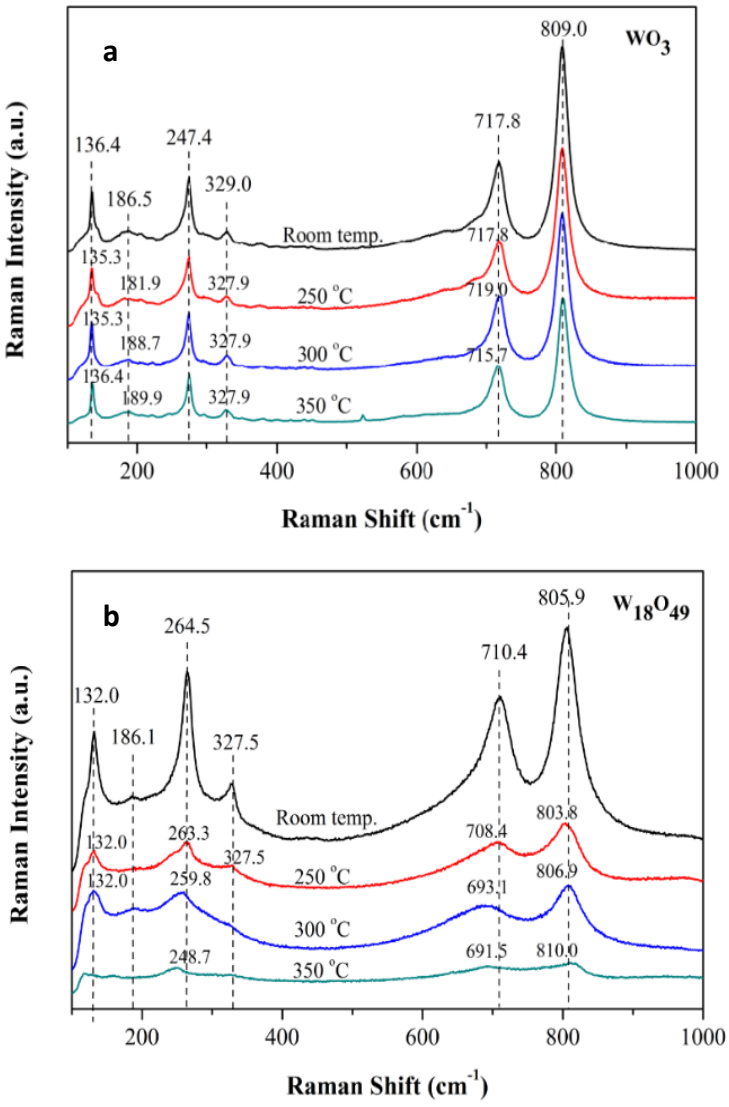

Fig. 5.11 Raman spectra of different heat treatment samples of both WO_3 nanoparticles (a) and $W_{18}O_{49}$ nanowires (b) irradiated at 10% laser power.

Prior to annealing, the Raman spectra of WO_3 nanoparticles clearly showed 3 main spectral regions which were referred to the stretching and bending vibration mode. Two strongest Raman shifts at about 809 and 717.8 cm^{-1} can be assigned to the O-W-O stretching vibration modes, whilst the 329 and 247.4 cm^{-1} belong to the O-W-O bending vibration modes of monoclinic WO_3 (Fig. 5.12a). Moreover, the peaks below 200 cm^{-1} are attributed to the lattice vibration modes. Raman shift regions of $W_{18}O_{49}$ show some new features, the peaks are slightly shifted towards lower wavenumbers for the stretching and lattice modes (Fig. 5.12b), whilst towards higher wavenumbers for the bending modes, benchmarked against the spectra of WO_3. Two main peaks in the highest region at 805.9 and 710.4 cm^{-1} can be assigned to the O-W-O stretching mode. The bands at 327.5 and 264.5 cm^{-1} belong to the O-W-O bending mode, 186 and 132 cm^{-1} belong to the lattice mode.

After heat treatment, the Raman bands of both WO_3 and $W_{18}O_{49}$ are shifted towards lower and higher wavenumbers in different regions, and the overall intensities of each region are decreased, and some peaks are disappeared. All samples showed no sign of the W=O bond, which means that any trace of water or other impurities were eliminated. These Raman spectra have confirmed that the chemical bonds within WO_3 and $W_{18}O_{49}$ have been reinforced *via* lattice relaxation (*i.e*. defect elimination) after the low temperature heat treatment.

The slightly changed lattice distance for both WO_3 and $W_{18}O_{49}$ after annealing was also supported by our HRTEM observations, as shown in Figs. 5.13 and 5.14 (a, c, e and g). The lattice spacing of WO_3 nanoparticles was affected by the heat treatment under Ar, and a small reduction of the d spacing was recognised with increased temperatures, from 0.39 nm to 0.37 nm from room temperature up to 350 °C. A similar trend was observed in the (010) plane space for all $W_{18}O_{49}$ nanowire samples, being slightly smaller than that of the as-prepared sample, from 0.38 nm down to 0.37 nm. A closer plane indeed originated from less structural defects and a stronger bonding between atoms. The thin nanowires have a diameter of less than 5 nm, hence during the annealing process it is easier for their internal structural defects to move out of

the structures and dissipate on the surface than for larger particles. Therefore, prior to annealing at room temperature, the nanowires exhibited smaller (010) plane spacing than the 10 times larger WO_3 nanoparticles that are more likely to contain lattice defects internally.

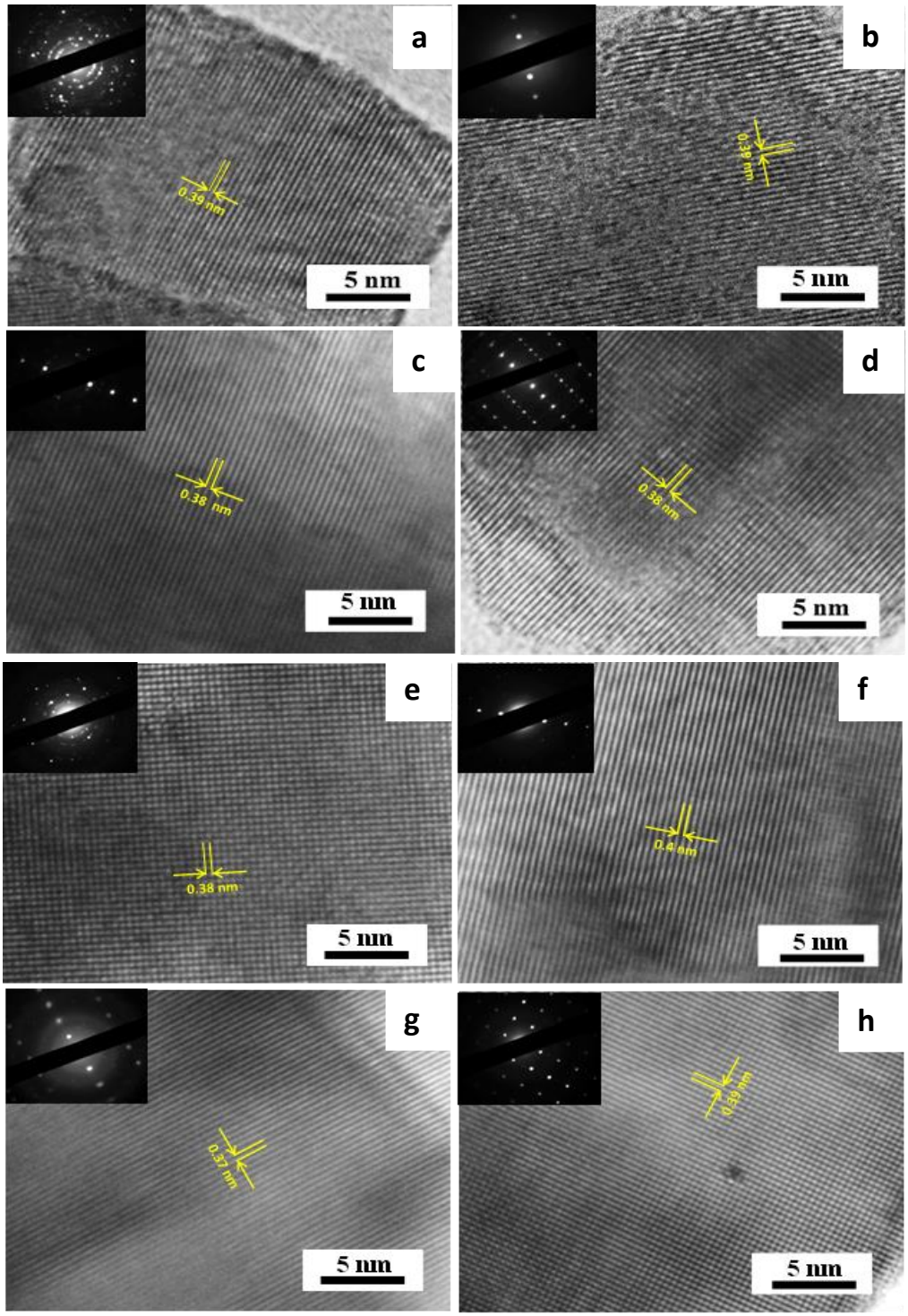

Fig. 5.12 HRTEM images of thin films of WO_3 nanoparticles treated at different annealing temperatures, before (a, c, e and g) and after (b, d, f and h) the electrochemical testing. (a) and

(b), as-prepared; (c) and (d), 250 °C; (e) and (f), 300 °C; (g) and (h), 350 °C. All insets are the corresponding diffraction pattern of each sample.

Figs. 5.13 and 5.14 (b, d, f and h) also presented the lattice changes of both WO_3 and $W_{18}O_{49}$ thin films respectively, with and without annealing, after the 1000th of cyclic voltammetric (CV) testing, to assess the annealing effects on the Li^+ retaining characteristics for the two types of oxide. The WO_3 did not detect any change in the lattice spaces between the as-purchased and the 250 °C annealed samples, however a slightly increased lattice space for the 300 and 350 °C annealed samples were observed, compared with those before the CV testing (Fig. 5.13b, d, f and h). The d space value of (010) plane for the nanowires after the 1000th electrochemistry testing was slightly increased for all annealed samples (Fig. 5.14b, d, f and h), whilst no changes occurred to the as-prepared thin films, possibly due to the apparent earlier reduction in the d values after annealing. The enlarged d value of the oxides after the CV tests could be attributed to the Li^+ trapped (left behind) within the oxide lattice which could not be detected using the TEM technique. It has been proposed that the Li^+ inserted into the oxide lattice during the colouration process cannot be completely extracted during the de-trapping process [7].

It has been discussed that the Li^+ might be located close to the W^{5+} colour centres, binding to the O coordination shells of W^{5+} sites. The more Li^+ remained within the lattice, the larger the d value of the (010) would be observed after the CV testing. A highly efficient chromic process not only demands more Li^+ to enter the oxide lattice to promote an intense coloration, but also requires the Li^+ to be able to come out of the lattice smoothly during the bleaching stage, to achieve high stability and cyclic performance. It is interesting to find out the annealing effect on these properties.

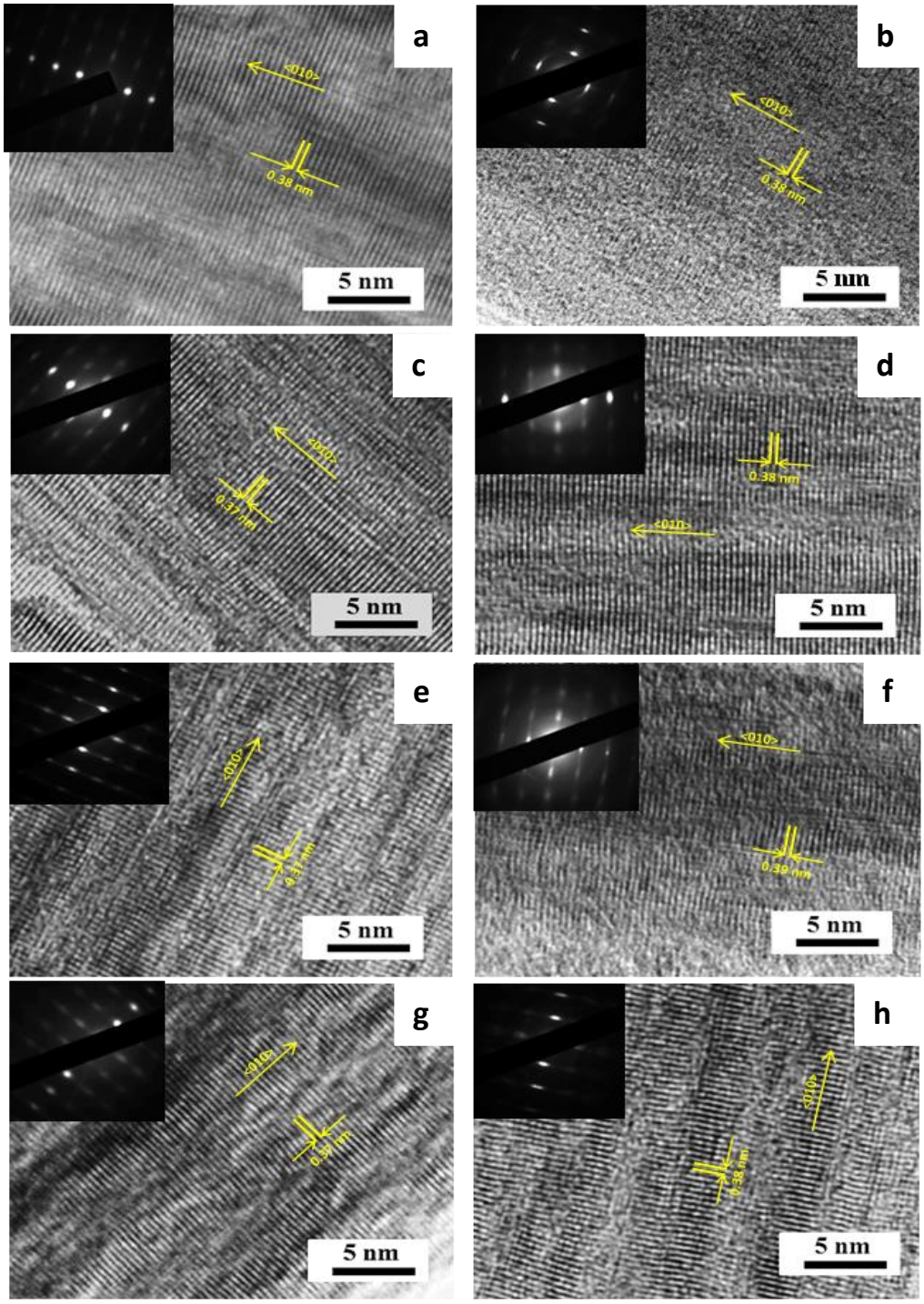

Fig. 5.13 HRTEM images of thin films of bundled $W_{18}O_{49}$ nanowires heat-treated at different temperatures before (a, c, e and g for room temperature, 250, 300, 350 °C, respectively) and after the electrochemical testing (b, d, f and h for room temperature, 250, 300, 350 °C, separately). Inset is the diffraction pattern of the bundles.

5.3.2.2 Electrochemistry testing of un-annealed and annealed WO_x thin films

An easy and smooth path for the Li^+ to pass through both ways was of importance for the diffusion kinetics, whilst different levels of defects within the crystalline structures would therefore have an impact on such diffusion path, thus on the efficiency, when other parameters in question were kept constant, except annealing. The effective diffusion coefficient (D) for both intercalation and de-intercalation processes was obtained to evaluate the effectiveness of diffusion path in various annealed oxide structures.

The average D_{Li}^+ value for oxidation and reduction has been estimated again by using those slopes from the linear relationship between current and $v^{1/2}$ graph (indicated as a diffusion-controlled process) with Eq. 2.5. The result of Li^+ diffusion for the intercalation/de-intercalation of WO_3 nanoparticles are $1.62 \times 10^{-10}/7.7 \times 10^{-11}$, $1.5 \times 10^{-10}/5.8 \times 10^{-11}$, $1.8 \times 10^{-10}/7.6 \times 10^{-11}$ and $1.9 \times 10^{-10}/8.2 \times 10^{-11}$ cm^2/s for room temperature, 250, 300 and 350 °C samples, respectively. The intercalation values for $W_{18}O_{49}$ nanowires are 6.54×10^{-10}, 1.73×10^{-9}, 1.22×10^{-9} and 8.24×10^{-10} cm^2/s for room temperature, 250, 300 and 350 °C samples, respectively. Moreover, the Li^+ diffusion for de-intercalation of $W_{18}O_{49}$ are 5.8×10^{-10}, 4.3×10^{-10}, 1.01×10^{-9} and 7.56×10^{-10} cm^2/s for room temperature, 250, 300 and 350 °C samples, respectively. WO_3 nanoparticle thin films generally obtained lower charge-insertion than that of $W_{18}O_{49}$ nanowire thin films even after annealing treatment, which means that the WO_3 nanoparticle provide slower Li^+ intercalation/de-intercalation kinetics than the $W_{18}O_{49}$ nanowires.

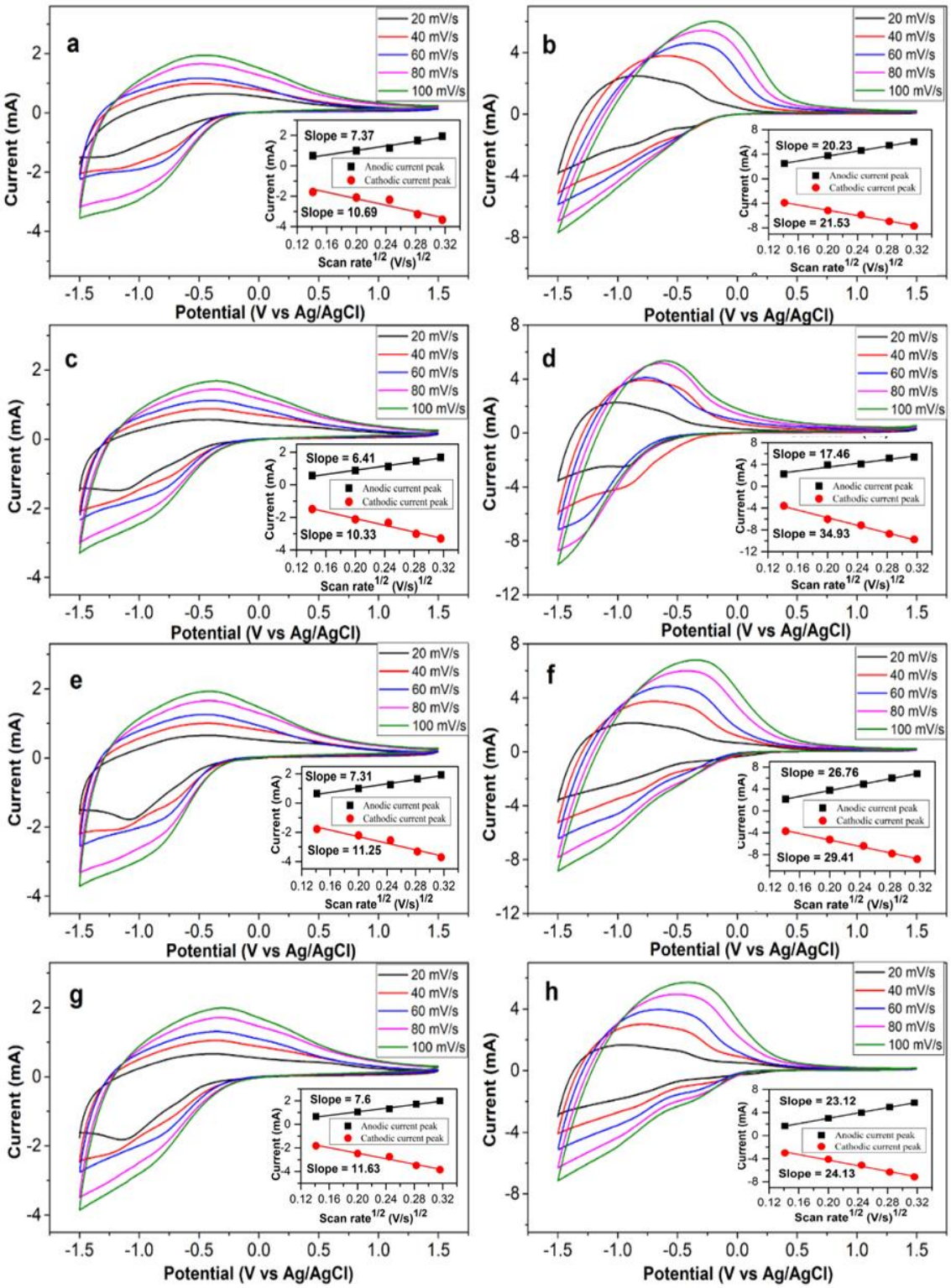

Fig. 5.14 CV profiles of the WO_3 without heat treatment, and annealed at 250, 300 and 350 °C (a, c, e and g, respectively); and CV curves of the $W_{18}O_{49}$ without heat treatment, and heat-treated at 250, 300 and 350 °C (b, d, f and h, respectively). The CV experiments were conducted at room temperature, scanned between -1.5 V and 1.5 V at different scan rates of

20, 40, 60, 80 and 100 mV/s, respectively. Inset shows the anodic peak current density as a function of the square root of the scan rate.

The improvement in the electrochromic behaviour of these WO_x thin films, especially the stability for both the coloration and bleaching stages of differently annealed oxides was also analysed by comparing the coefficient changes between the 1st and the 1000th CV cycle (Fig 5.16). These tests were run at a selected scan rate of 60 mV/s for each sample, and the resulting D_{Li}^+ values are represented in Table 5.3.

Table 5.3 A summary of the D_{Li}^+ values of different thin films.

Samples	**Diffusion coefficients D_{Li}^+ (cm^2/s)**					
	Intercalation (anodic peak)		**Different (%)**	**De-intercalation (cathodic peak)**		**Different (%)**
	1st cycle	**1000th cycle**		**1st cycle**	**1000th cycle**	
WO_3 As-purchased	1.2×10^{-10}	6.04×10^{-11}	50	3.2×10^{-11}	1.5×10^{-11}	53
WO_3, 250 °C	1.3×10^{-10}	5.9×10^{-11}	55	3×10^{-11}	1.6×10^{-11}	46
WO_3, 300 °C	1.53×10^{-10}	7.31×10^{-11}	52	3.7×10^{-11}	1.8×10^{-11}	52
WO_3, 350 °C	1.8×10^{-10}	9.3×10^{-11}	48	4×10^{-11}	2.34×10^{-11}	42
$W_{18}O_{49}$ As-prepared	8.4×10^{-10}	7×10^{-10}	17	5.1×10^{-10}	3×10^{-10}	41
$W_{18}O_{49}$ 250 °C	1.21×10^{-9}	7.5×10^{-10}	38	4×10^{-10}	2×10^{-10}	50
$W_{18}O_{49}$ 300 °C	9.8×10^{-10}	7×10^{-10}	29	5.6×10^{-10}	3.4×10^{-10}	39
$W_{18}O_{49}$ 350 °C	6×10^{-10}	5.1×10^{-10}	15	3.7×10^{-10}	3.32×10^{-10}	10

As summarised in Table 5.3, annealed WO_3 thin films exhibited a slightly higher D_{Li}^+ values for both intercalation (1.3×10^{-10}, 1.53×10^{-10} and 1.8×10^{-10} cm^2/s for 250, 300 and 350 °C samples, respectively) and de-intercalation stage (3.7×10^{-11} cm^2/s for 300 °C sample and 4×10^{-11} cm^2/s for 350 °C samples), compared with 1.2×10^{-10} cm^2/s for intercalation and 3.2×10^{-11} cm^2/s de-intercalation of WO_3 samples without treatment. However, the de-intercalation of the 250 °C annealed sample showed a slightly lower D_{Li}^+ value of 3×10^{-11} cm^2/s than the as-purchased WO_3. The magnitude of the diffusion coefficient for Li^+ intercalation at these selected scan rate of 60 mV/s was greater than that of

the de-intercalation for all samples ($D_{intercalation} > D_{de\text{-}intercalation}$). It clearly indicated the presence of the charge trapping phenomenon. The trapped Li^+ must remain inside the WO_x structures, therefore resulting in the increased lattice distance after 1000 cycles, as verified by the HRTEM results.

The stability of annealed WO_3 samples exhibited slightly better values than the original WO_3 thin film, by 7% and 11% of the de-intercalation for the 250 and 350 °C annealed samples respectively, whereas only improved by 2% of intercalation stability for 350 °C annealed samples. For the $W_{18}O_{49}$ samples, the 250 and 300 °C annealing resulted in a noticeable improvement in the diffusion, achieving D_{Li}^+ values for intercalation (1.21×10^{-9} and 9.8×10^{-10} cm^2/s, respectively), compared with the un-treated $W_{18}O_{49}$ sample (8.14×10^{-10} cm^2/s for intercalation). Only de-intercalation of $W_{18}O_{49}$ sample annealed at 300 °C obtained a slightly better D_{Li}^+ value of 5.6×10^{-10} cm^2/s than the value of 5.1×10^{-10} cm^2/s from the original $W_{18}O_{49}$. Stabilities in both chromic reactions of annealed $W_{18}O_{49}$ samples were increased by 2% and 31% for the intercalation and de-intercalation for the 350 °C treatment, respectively, against the un-annealed $W_{18}O_{49}$ sample. However, the improvement trend of both D_{Li}^+ could be related to the decrease of stability for the 250 and 300 °C treated samples, and the reason remains unclear, though the developments due to annealing were reported.

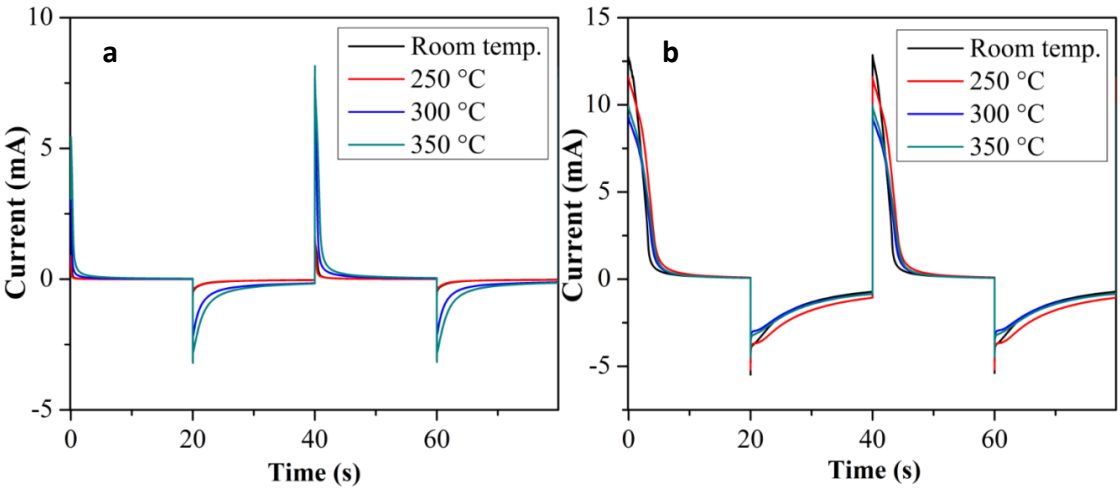

Fig. 5.15 Chronoamperometry (CA) measurements for voltage steps between +1.5 V and -1.5 V for 20 s in 0.5 M $LiClO_4$ electrolyte: (A) WO_3 nanoparticle thin films with and without annealing treatment, and (B) $W_{18}O_{49}$ nanowire thin films with and without annealing treatment.

The switching response for coloration and bleaching of all thin film samples can be determined by the chronoamperometry scan (CA) (Fig. 5.16), as the time needed for excess current to reduce to 10% of its absolute maximum value. The WO_3 thin film showed a response time of 5 s for colouration and 1 s for bleaching, compared with the 350 °C annealed sample of 8.4 and 1.5 s for the coloration and bleaching time, respectively. The as-prepared $W_{18}O_{49}$ obtained 13.5 s for coloration and 7.5 s for bleaching time, against the 13.3 and 4.4 s (for coloured and bleached time) for 300 °C annealed sample. These slower values of both the annealed samples and the nanowires against the pristine samples and nanoparticles, respectively, are rather surprising. However, these values did not reflect the total amounts of Li^+ intercalated into or de-intercalated out of the lattice, i.e. the intensity of the coloration/bleaching processes. To achieve the similar $D_{Li}{}^+$ values and higher intensity, more Li^+ transportation could be involved during the process, hence a longer time would be required.

5.4 Mechanism of coloration and bleaching process

It is commonly accepted that a reduction of W^{6+} to W^{5+} through the insertion of electron and alkaline metal cation will cause optical absorption (colouration and bleaching stage of the tungsten oxide thin film) in the near infrared and visible spectral region by means of intervalence charge transfer (IVCT) and small polaron absorption (the model was mentioned in chapter 2). The intercalation and de-intercalation of electrons from the electrode and Li^+ from the electrolyte result in an optically coloured and bleached state of the WO_x thin films [14]. The electrochromic mechanism of $W_{18}O_{49}$ in Li^+ electrolyte can be expressed as:

$$\underbrace{W_{18}O_{49} + xLi^+ + xe^-}_{Bleaching} \quad \leftrightarrow \quad \underbrace{Li_xW_{18}O_{49}}_{Colouration} \qquad \text{Eq 5.1}$$

However, this model suggests that the optical absorption of the ion-doped WO_x could be caused by small polaron transitions exchange between the W^{5+} and W^{6+} sites. The inserted electrons are located in W^{5+} sites and polarise their surroundings to form small polarons. Incident photons are absorbed by these small polarons that hop from one site to another, following Eq. 5.2:

$$h\nu + W^{5+}(A) + W^{6+}(B) \rightarrow W^{6+}(A) + W^{5+}(B) \qquad \text{Eq 5.2}$$

Based on this model, it however could not explain the transparent appearance in the WO_x thin film with V_o up to 0.3 whilst the film obtained a better CE. Lee *et al*. have proposed another model that the as-deposited WO_x films could contain mainly W^{6+} and W^{4+} states [215]. During a Li^+ insertion, the W^{6+} was reduced to W^{5+}, while W^{4+} was not affected. The coloured films contained W^{5+}, W^{4+}, and W^{6+} stages, and the optical absorption was caused by the small polarons between the W^{6+}, W^{4+} stage and the W^{5+} stage, as illustrated in Eq. 5.3.

$$h\nu + W^{4+}(A) + W^{5+}(B) \rightarrow W^{5+}(A) + W^{4+}(B) \qquad \text{Eq. 5.3}$$

To provide evidence for the colouration and bleaching mechanism of the plain and doped $W_{18}O_{49}$ samples, we rely on our XPS results, by comparing differences in the chemical component before and after electrochromic testing. The XPS results of bleaching and colouration stages of the thin films were collected after 500th cycle of electrochemistry testing.

The XPS spectra have shown that the W 4f of the as-prepared thin film contains two typical peaks, which exhibit the characteristics of spin-orbit split for W($4f_{7/2}$) and W($4f_{5/2}$) of a tungsten ion (Fig. 5.17a, d and g). W $4f_{7/2}$ consists of two doublets, located at the range from 35 to 36.4 eV and 33.2 to 34.9 eV, which can be associated to the W^{6+} and W^{5+} oxidation stage, respectively. The other two peaks are attributed to the W $4f_{5/2}$ spin-orbit split which locate at the range from 37.2 to 38.6 eV and 35.4 to 37 eV, and are assigned to W^{6+} and W^{5+} respectively. At the colouration and bleaching stage, the experimental XPS data presented that the composite W 4f spectra were not only fitted with two doublets (corresponding to W^{5+} and W^{6+} oxidation stage), but also include the third doublet relating to the W^{4+} oxidation stage (Fig. 5.17b, c, e, f, h and i). More details of peak position and each oxidation stage during the colouration and bleaching stage are summarised in Table 5.4.

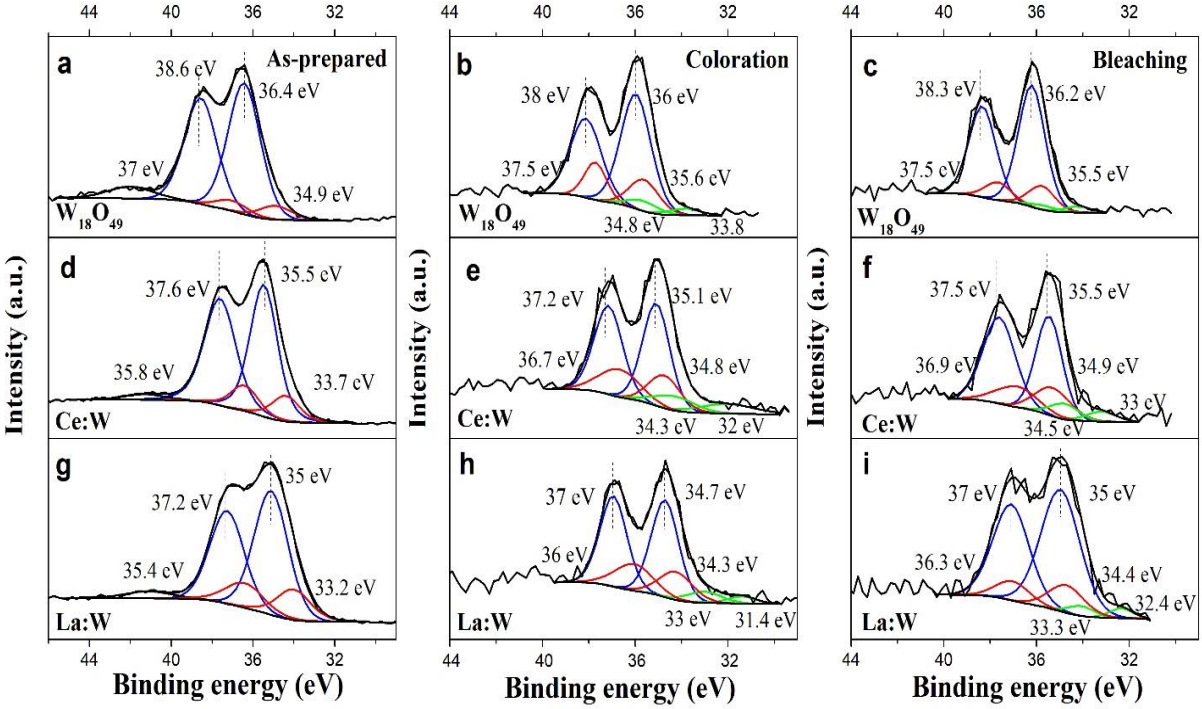

Fig. 5.16 W 4f XPS spectra of the as-prepared stage (a, d, g), colouration (b, e, h) stage and bleaching stage (c, f, i) for plain $W_{18}O_{49}$, Ce-doped (1:15) and La-doped (1:15) samples.

From Table 5.4, the amount of W^{6+} has been reduced during the colouration stage, whilst the W^{5+} and W^{4+} have increased and occurred, respectively. The amount of W^{6+} from bleached films was increased compared with the coloured thin film, while was still slightly lower than those of the as-prepared thin films. The results could imply that the colouration mechanism of the electrochromic is related to two transition sites between W^{6+} and W^{5+} or W^{5+} and W^{4+}, as the intervalence transitions can be described by following both Eqs. 5.2 and 5.3. Moreover, the amount of W^{6+}, W^{5+}, and W^{4+} at the bleached stage could not be regained to the same level to the original stage. This could be an indirect evidence for the Li^+ trapping inside the structure, causing the thin film degradation.

Table 5.4 A summary of the binding energy and atomic ratio of the W 4f region of un-doped and doped samples at coloration and bleaching stage.

		$W_{18}O_{49}$			**Ce doped WO_x**			**La doped WO_x**		
		As-prepared	Coloured	Bleached	As-prepared	Coloured	Bleached	As-prepared	Coloured	Bleached
Peak Position (B.E.)	W 4f $4f_{7/2}(W^{6+})$	36.43	35.89	36.2	35.46	35.00	35.5	35.00	34.73	35.05
	W 4f $_{5/2}(W^{6+})$	38.56	37.97	38.32	37.59	37.14	37.5	37.16	36.87	37.00
	W $4f_{7/2}(W^{5+})$	34.91	34.78	35.5	33.68	34.27	34.9	33.24	34.25	34.4
	W $4f_{5/2}(W^{5+})$	37.04	37.36	37.5	35.81	36.64	36.9	35.38	36.87	36.3
	W $4f_{7/2}(W^{4+})$	-	33.78	33.2	-	32.00	33.02	-	31.38	32.4
	W $4f_{5/2}(W^{4+})$	-	34.79	34.5	-	34.30	34.5	-	33.01	33.3
Atomic %	W^{6+}	90.5	73.9	80.99	82.78	67.05	81.07	81.4	65.82	79.45
	W^{5+}	9.5	20.2	15.17	17.22	23.66	13.09	18.6	25.41	14.83
	W^{4+}	-	5.93	3.85	-	9.29	5.84	-	8.77	5.72
	$(W^{5+}+W^{4+})/W^{6+}$	0.102	0.353	0.235	0.207	0.491	0.234	0.229	0.519	0.259

The O 1s of all stages (as-prepared, coloured and bleached) from all samples were also presented in Fig. 5.18. The O 1s XPS region spectra were deconvoluted to two overlapping peaks, with the major peak located at lower binding energy (about 529.0 to 530-79 eV) and the shadow peak located at range between 532.14 and 532.73 eV that were assigned to the lattice oxygen of oxide (peak 1) and the absorbed oxygen on the surface (peak 2), such as hydroxide, oxygen vacancy, oxygen ions, or other bounded oxygen-related species, respectively. During the coloration stage, the concentration percentage of peak 2 from all samples was higher than the original stage thin films, as the atomic percentages are presented in Table 5.5. The increased result of peak 2 could confirm that the Li^+ intercalation/de-intercalation was through adsorption of O^{2-}.

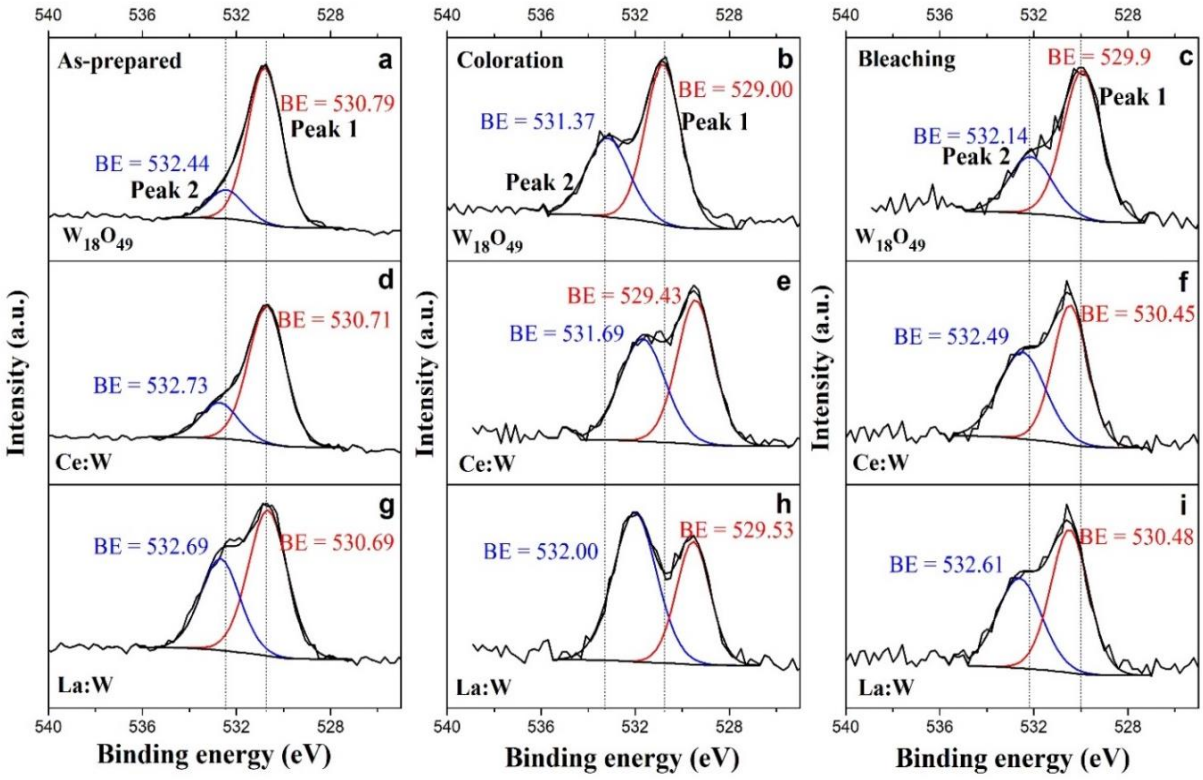

Fig. 5.17 O 1s XPS spectra of the as-prepared stage (a, d, g), colouration (b, e, h) stage and bleaching stage (c, f, i), for plain $W_{18}O_{49}$, Ce-doped (1:15) and La-doped (1:15) samples.

As we have discussed earlier that peak 2 could be related to V_o which co-related to the occurred W^{5+} oxidation stage inside the as-prepared structure. From Fig. 5.18c, f and i, the percentage of peak 2 was decreased, compared

with the results of the colouration stage; whilst remained higher than the original stage. There might be two possible reasons: 1) the different concentration between peak 2 of the as-prepared and bleached stage could be due to Li^+ trapping phenomena; and 2) due to the increased V_o or lose of the oxygen inside the structure. These analyses are also supported by the number of W^{5+} and W^{4+} in the W 4f region, remaining inside the bleaching thin films.

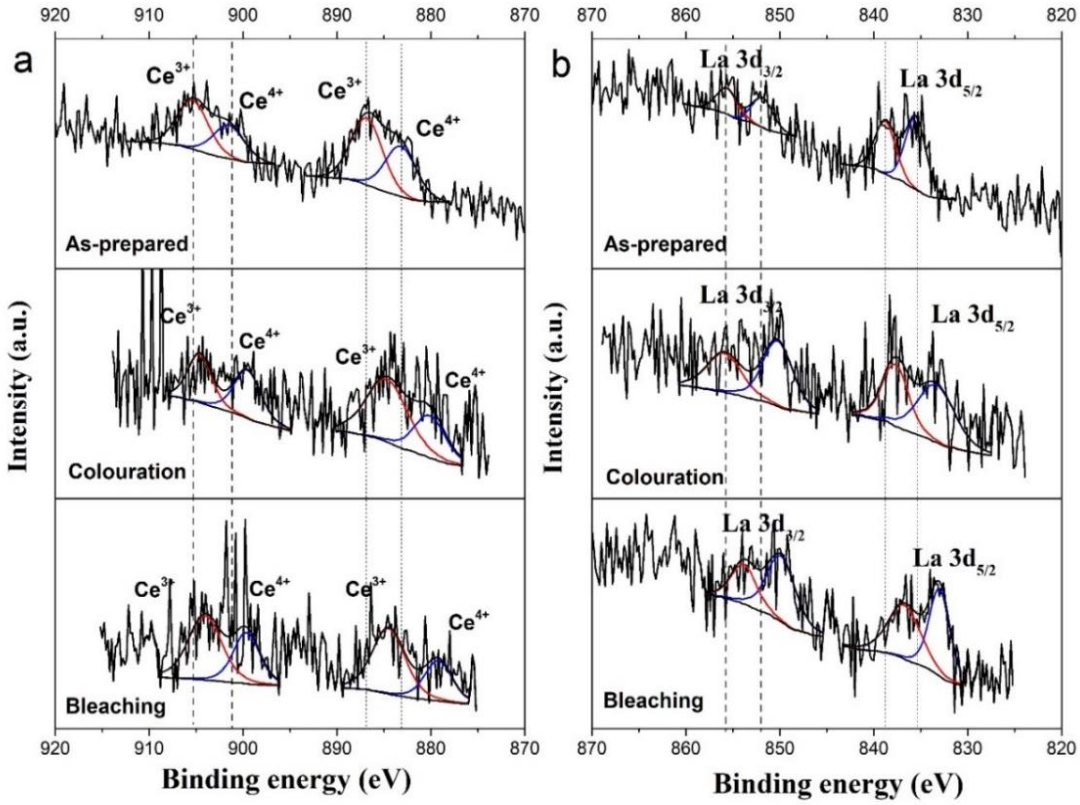

Fig. 5.18 (a) Ce 3d and (b) La 3d XPS spectra of the as-prepared, colouration and bleaching stage for Ce-doped (1:15) and La-doped (1:15) samples.

The Ce 3d spectra have revealed that Ce ions could possibly take place in term of ion transition, which provided evident for the existence of V_o during the colouration and bleaching stage based on the increased Ce^{3+} concentrations (Table 5.6). Moreover, the increasing of Ce^{3+} at the bleaching stage could be used to explain and support the ion-trapping idea inside the structure. Furthermore, we could not analyse based on La 3d region in the La-doped sample, which only contained La^{3+}, however the evidence from the W 4f and O

1s of La-doped samples is enough to support that colouration mechanism of La-doped sample may behave as the same as the Ce-doped sample.

Table 5.5 A summary of the binding energy and atomic ratio of the O 1s region of un-doped and doped samples at the coloration and bleaching stage.

	Samples	**Peak position (B.E.)**		**Atomic percentage**	
		Main peak (peak 1) eV	Shadow peak (peak 2) eV	Main peak (peal 1)	Shadow peak (peak 2)
As-prepared	$W_{18}O_{49}$	530.79	532.44	84	16
	Ce-doped WO_x	530.80	532.68	68.29	31.71
	La-doped WO_x	530.67	532.69	62	39
Coloration stage	$W_{18}O_{49}$	529	531.37	63.27	36.73
	Ce-doped WO_x	529.43	531.69	53.41	46.59
	La-doped WO_x	529.53	532.00	39.15	60.85
Bleaching stage	$W_{18}O_{49}$	529.9	532.14	72.82	27.18
	Ce-doped WO_x	530.45	532.49	59.56	40.44
	La-doped WO_x	530.48	532.61	61.47	38.53

Table 5.6 A summary of the binding energy and atomic ratio of Ce 3d and La 3d region of un-doped and doped samples at the coloration and bleaching stage.

Samples		**Peak position (B.E.)**				**Atomic %**		
		$3d_{3/2}$ Ce^{3+} (eV)	$3d_{5/2}$ Ce^{3+} (eV)	$3d_{3/2}$ Ce^{4+} (eV)	$3d_{5/2}$ Ce^{4+} (eV)	Ce^{3+}	Ce^{4+}	Ce^{4+}/Ce^{3+}
Ce-doped WO_x	**As-prepared**	905.36	886.81	901.52	883.20	58.1	41.9	0.72
	Coloured stage	904.62	884.67	899.53	880.1	60.8	39.2	0.65
	Bleached stage	904.05	884.49	899.64	879.21	63.4	36.6	0.58
		$3d_{3/2}$ (major peak*) (eV)	$3d_{3/2}$ (satellite peak*) (eV)	$3d_{5/2}$ (major peak*) (eV)	$3d_{5/2}$ (satellite peak*) (eV)			
La-doped WO_x	**As-prepared**	851.82	855.62	835.53	838.77	-	-	-
	Coloured stage	850.22	855.9	833.32	837.68	-	-	-
	Bleached stage	849.86	853.82	832.99	836.72			

* the major peaks are located at lower binding energy in both $3d_{3/2}$ and $3d_{5/2}$ regions, thus the satellite peak is located at higher binding energy.

5.5 Effect of different electrolytes on WO_x thin films

5.5.1 Introduction

As the prime ionic conduction medium, electrolytes play an important role in various electrochemical devices. Various types of polymer electrolyte, including solid, gel or liquid forms, have attracted a wide attention. This section will summarise the study of effects of different gel polymer electrolytes on the electrochemical performance of $W_{18}O_{49}$, by analysing the electrochemistry results.

5.5.2 Materials and measurement

This $W_{18}O_{49}$ films were prepared as described earlier, on 1.5 × 2.5 cm^2 ITO glasses, to achieve a thinness of 300 nm. Propylene carbonate (PC) and Polypropylene carbonate (PPC) were applied as the basic solvent and polymer for different electrolytes. The homogeneous electrolyte solutions were obtained after overnight magnetic stirring at the room temperature. The component details of different electrolytes are presented in Table 5.7. The ionic conductivity was measured on a Potentiostat (CHI 760D) with a standard three-electrode. The CV curve was obtained from -1.5 to +1.5 V. The three-electrode test cell consisted of the $W_{18}O_{49}$ thin film, electrolyte of a fixed amount (15 ml), and working electrode with fixed reactive area (1.5 × 1.5 cm^2). The Pt courter and Ag/AgCl reference electrode was dipped into the electrolyte with a 1.2 cm depth for all testing. The 3 electrodes were also separated by a fixed distance of 1.5 cm during all electrochemistry scan.

Table 5.7 Component details of the electrolytes.

Electrolytes	Alkaline salt	Solvent (ml)	Matrix polymer
1	0.5M $LiClO_4$	15 ml PC	-
2	0.5M $LiClO_4$	15 ml PC	1 g PPC
3	0.5M $LiClO_4$	15 ml PC	2 g PPC
4	0.5M $LiClO_4$	7.5 ml PC + 7.5 ml $BMIMBF_4$	-
5	0.5M $LiClO_4$	15 ml $BMIMBF_4$	-

5.5.3 CV and CA results and discussion of $W_{18}O_{49}$ in different gel electrolytes

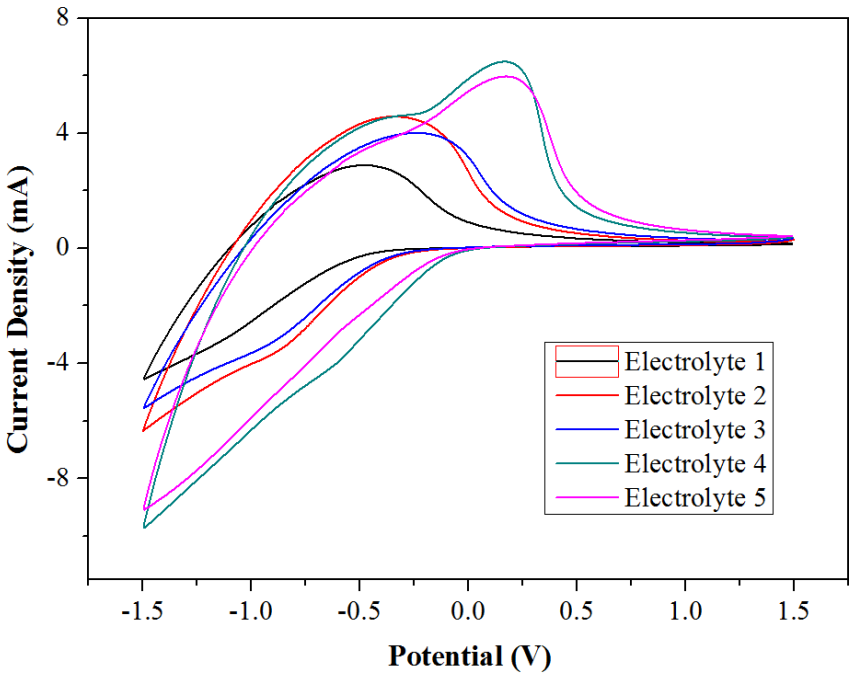

Fig. 5.19 Cyclic voltammetric (CV) profiles of the $W_{18}O_{49}$ in different gel electrolytes, scanned with 60 mV/s.

The D_{Li}^+ of $W_{18}O_{49}$ thin films in different electrolytes was calculated according to Randles-Sevick's equation (Eq. 2.5), and the values for both cathodic and anodic processes are presented in Table 5.8.

Table 5.8 Summary of the CV and CA testing of different type of electrolytes.

Electrolytes	Cathodic Peak (mA)	Anodic Peak (mA)	Diffusion coefficient (D), cm^2/s	
			De-intercalation (Cathodic)	Intercalation (Anodic)
1	2.91	4.54	1.54×10^{-9}	3.75×10^{-9}
2	4.58	6.33	3.82×10^{-9}	7.29×10^{-9}
3	4.02	5.55	2.94×10^{-9}	5.61×10^{-9}
4	6.49	9.71	7.67×10^{-9}	1.72×10^{-8}
5	5.97	9.10	6.49×10^{-9}	1.51×10^{-8}

As shown in Table 5.8, electrolyte 2 has obtained higher values for both the intercalation and de-intercalation than those of electrolytes 1 and 3. It has been

recommended that the flexibility and segmental motion of the host polymer chains are improved due to the plasticization effect of the PC, which in turn enhances the ion kinetics of the gel electrolytes [223]. However, the mixed IL with PC presented the best D_{Li}^{+} value of 7.67×10^{-9} for the de-intercalation and 1.72×10^{-8} for the intercalation.

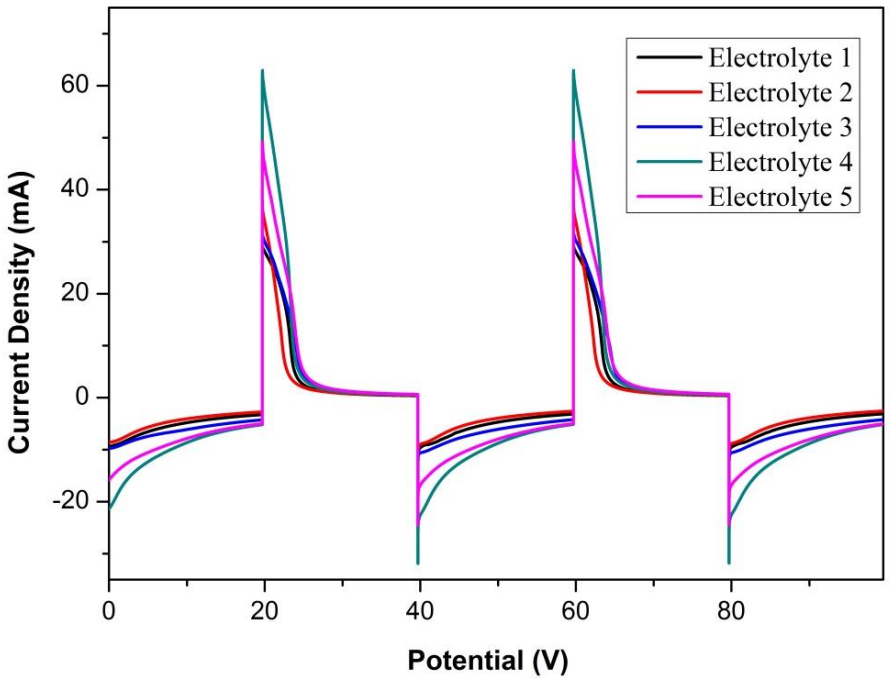

Fig. 5.20 Chronoamperometry (CA) profiles of the $W_{18}O_{49}$ samples, for voltage steps between +1.5 V and -1.5 V for 20 s in the different gel electrolytes.

The switching responses for coloration and bleaching of thin films in different electrolytes can be determined by the chronoamperometry scan (CA) (Fig. 5.21). By using electrolyte 1, the $W_{18}O_{49}$ thin film showed a response time of 15.6 s for colouration and 4.4 s for bleaching; whilst electrolyte 2 presented a shorter response time of 10.9 and 3.2 s for the coloration and bleaching, respectively. The higher concentrate of the polymer, the slightly longer switching response. Benchmarked against the lower concentrate electrolytes, they were longer by 2.4 s for colouration and 2.1 s for bleaching. However, the faster switching time was obtained by adding IL in the electrolyte, which was about 11.6s/3.9s and 12.59s/4.7s for colouration/bleaching for electrolytes 4 and 5, respectively.

From the CV and CA results, we believe that the electrolytes have affected the performance of $W_{18}O_{49}$ thin films, which could be another interesting subject for future electrochromic device development. The chain of polymer matrix inside the electrolyte could be the main enhancement factor of the ion mobility, thus affecting the switching time of $W_{18}O_{49}$ thin film. However, the optimal structure of electrolyte and role of a polymer inside the electrolyte are still unclear and need further investigations.

5.6 Summary

This Chapter reported detailed electrochromic performance of the plain $W_{18}O_{49}$, Ce- and La- doped samples, investigated the effects of annealing treatment, and analysed the mechanisms for both the colouration and bleaching stages. The essential factors including D_{Li}^+, stability, and response time have been presented and are used to assess and optimise the electrochromic performance of different samples. The improvements of the electrochromic property from the annealing treated samples have also been discussed based on evidence of their structure analyses. Moreover, the colouration and bleaching mechanism have been investigated and analysed by using the surface chemical component results. The findings are summarised as following:

- The $W_{18}O_{49}$ nanowires exhibit faster Li^+ kinetics than that of WO_3 nanoparticles. The D_{Li}^+ of $W_{18}O_{49}$ sample is about 7 times for intercalation and 12 times for de-intercalation higher than those of WO_3. Moreover, $W_{18}O_{49}$ nanowires also show a better stability by 33% for intercalation and 12% for de-intercalation compared with those of WO_3.
- The electrochromic properties of $W_{18}O_{49}$ nanowires have been further improved *via* Ce- and La-doping. The best doped samples of Ce:W = 1:15 exhibit better ion diffusion kinetics than the plain $W_{18}O_{49}$ nanowires, about 2.5 times faster for both intercalation and de-intercalation, and their stability for de-intercalation has been improved by 20% against the plain $W_{18}O_{49}$ nanowires. The La-doped samples with La/W =1:10 offer the fastest diffusion kinetics and best stability compared with other La-

doped samples. The D_{Li}^+ is about 2.5 times for intercalation and 3 times for de-intercalation higher than those of the plain $W_{18}O_{49}$.

- Annealing has successfully increased the kinetics of the Li^+ and enhanced the electrochromic stability of both forms of WO_x nanomaterials. The best stability improvement for the WO_3 nanoparticles has been found in samples annealed at 350 °C, with 11% improvement for intercalation and 23.5% for de-intercalation, compared with the un-treated WO_3 samples. For the $W_{18}O_{49}$ nanowire thin films, the best improvements are 36% for intercalation and 60% for de-intercalation for samples annealed at 350 °C, against the un-treated $W_{18}O_{49}$ thin film. We have shown that the degradation of thin films is related to Li^+ trapping inside the structures, based on the enlarged d values found in both post-testing samples after 1000 cycles.
- The colouration mechanism of thin films has been related to both transitions from W^{6+} to W^{5+} state and from W^{4+} to W^{5+} state. Our XPS spectrum analyses based on W 4f and O 1s have revealed that degradation of the thin film samples is caused by either Li^+ trapping or loss of V_o in the structures after long cycles of electrochemistry testing.
- The mixed polymer electrolyte can help to improve the D_{Li}^+ values and shorten the switching time of $W_{18}O_{49}$ nanowire thin films.

Chapter 6 The rational design and exploration of WO_x electrochromic devices

6.1 Introduction

In the previous chapter, the fundamental electrochromic performance has been characterised by using the 3-electrode technique, and the performance of different samples was discussed and compared using 3 main parameters: D_{Li}^+, stability and response time. At a device level, Colouration Efficiency (CE) is the key parameter, which will be analysed. In this Chapter, we first construct device prototypes of each sample, based on previous findings, and then we will conduct *in-situ* absorbance studies on these prototypes, to evaluate the actual electrochromic performance.

6.2 Prototype performance and optical transmittance

6.2.1 Preparation and measurement of WO_x thin films

The details of thin films and electrochromic device preparation have been presented in Chapter 3, sections 3.2.3 and 3.2.4. We used a 0.5 M $LiClO_4$ and 4 w/v% of Polypropylene (PPC) in propylene carbonate (PC) as the gel electrolyte for all device construction.

The optical transmittance values of all devices were recorded ranging from 430 to 750 nm for the intercalated (coloured) or de-intercalated (bleached) stages, using a custom-build UV-Vis spectroscopy machine, by acquiring the transmission spectra [330]. Light sourced from an incandescent bulb was focused onto the sample *via* a condenser lens which was collected by a 20× microscopy objective (Olympus MPLFLN, NA 0.45). After travelling though, the sample, the light was recorded on a spectrometer (Princeton Instruments Acton SP2500) when it reached the entrance slit. The spectrometer was equipped with a 1200 g/mm grating and a CCD camera (Princeton instruments PIXIS400). We used a Princeton Instruments IntelliCal system to calibrate and

obtain the efficiencies of optics and gratings at different wavelengths. A Keithley 2400 Source Meter was used to generate the bias voltage to the device.

6.2.2 The electrochromic prototypes constructed using Ce-doped WO_x

The transmittance values of both the bleached and coloured states of Ce-doped samples, against the $W_{18}O_{49}$, were presented in Fig. 6.1. These values at a given specific wavelength of 630 nm (which is sensitive to human eyes) were used for the optical contrast (ΔT) calculation based on Eq. 2.5, as presented in chapter 2 [187]:

$$\Delta T = [T_{bleched} - T_{coloued}]_{\lambda = 630\ nm} \qquad \text{Eq. 2.5}$$

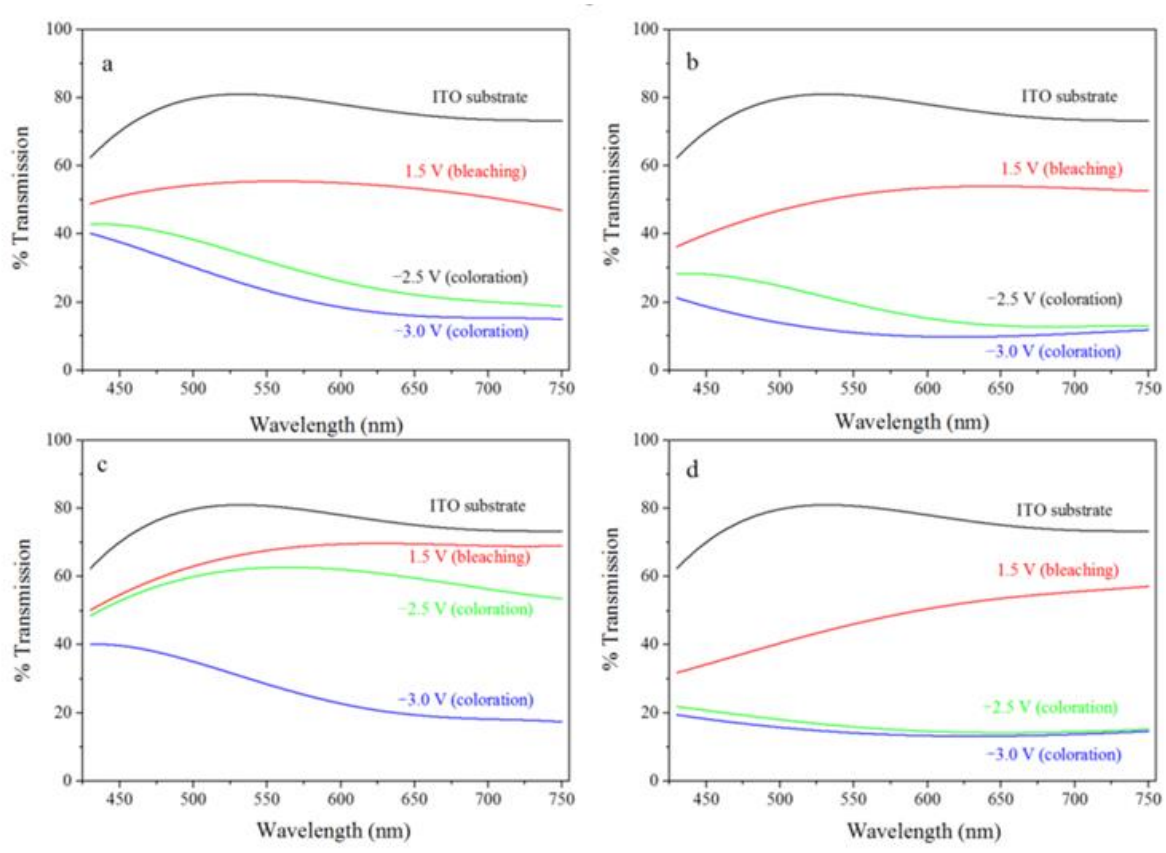

Fig. 6.1 Prototype transmission spectra: (a) pure $W_{18}O_{49}$ nanowires, (b) Ce/W = 1:15, (c) Ce/W = 1:10, and (d) Ce/W = 1:5 thin films, in their coloured and bleached states, subjecting to different potentials ranging from +1.5 to -3.0V.

The CE, which represents the change in optical density (ΔOD) per the total charge passed across a unit area of the thin film (Q_d, C/cm^2), can be calculated based on Eqs. 2.7 and 2.8 (as were also presented in chapter 2).

$$CE(\lambda) = \frac{\Delta(OD)}{Q_d} \qquad \text{Eq. 2.7}$$

where $$(\Delta OD)(\lambda) = \log[T_b(\lambda)/T_c(\lambda)] \qquad \text{Eq. 2.8}$$

Q_d is the amount of charge intercalated into the thin film samples, which can be estimated by integrating the area under the curve of current density *vs*. time.

Table 6.1 Optical performance of the electrochromic prototypes constructed by using Ce-doped WO_x and pure bundled $W_{18}O_{49}$ nanowires, evaluated at 630 nm.

Sample	$T_{coloured}$ (%)	$T_{bleached}$ (%)	ΔT(%)	Q(C)	Q_d(C/cm^2)	ΔOD	CE (Colouration Efficiency, cm^2/C)
Pure $W_{18}O_{49}$	16.8	54.2	37.4	0.051	0.0083	0.51	61.9
Ce/W = 1:15	9.8	54.1	44.3	0.072	0.011	0.74	67.3
Ce/W = 1:10	20.4	70.1	49.7	0.05	0.008	0.53	66.3
Ce/W = 1:5	13.1	52.3	39.4	0.07	0.011	0.60	54.6

Table 6.1 lists the optical contrast (ΔT), change of the optical density (ΔOD), charge density (Q_d) and colouration efficiency (CE) values for both the doped and un-doped samples. The ΔT value is found to be increased by 6.9, 12.3 and 2% for Ce/W = 1:15, 1:10 and 1:5, respectively, compared with the plain $W_{18}O_{49}$ thin film. The percentages of optical contrast (%ΔT) of the doped samples are all greater than the plain $W_{18}O_{49}$, which was 39.4%, 49.7%, 44.3% and 37.4% for Ce/W = 1:5, 1:10, 1:15 and plain $W_{18}O_{49}$, respectively. The Ce/W = 1:15 thin film sample presents the highest ΔOD value of 0.74, compared with plain $W_{18}O_{49}$ thin films (about 0.51). The CE corresponding to Ce/W = 1:5, 1:10, 1:15 and pure $W_{18}O_{49}$ is 61.9, 67.3, 66.3 and 54.6 cm^2/C, respectively. The sample with the lowest doping amount (1:15) shows the highest CE value than the other two samples (1:10 and 1:5).

Table 6.2 Optical performance for the electrochromic prototypes constructed using La-doped WO_x and pure bundled $W_{18}O_{49}$ nanowires, evaluated at 630 nm.

Sample	$T_{coloured}$ - (%)	$T_{bleached}$ (%)	ΔT(%)	Q(C)	Q_d(C/cm^2)	ΔOD	CE (Colouration Efficiency, cm^2/C)
Pure $W_{18}O_{49}$	16.8	54.2	37.4	0.051	0.0083	0.51	61.9
La/W = 1:15	10.9	64.3	53.4	0.066	0.01	0.77	77
La/W = 1:10	15	69.2	54.2	0.068	0.011	0.66	60
La/W = 1:5	28.7	49.6	20.9	0.071	0.011	0.24	21.8

6.3.3 The electrochromic prototypes constructed using La-doped WO_x

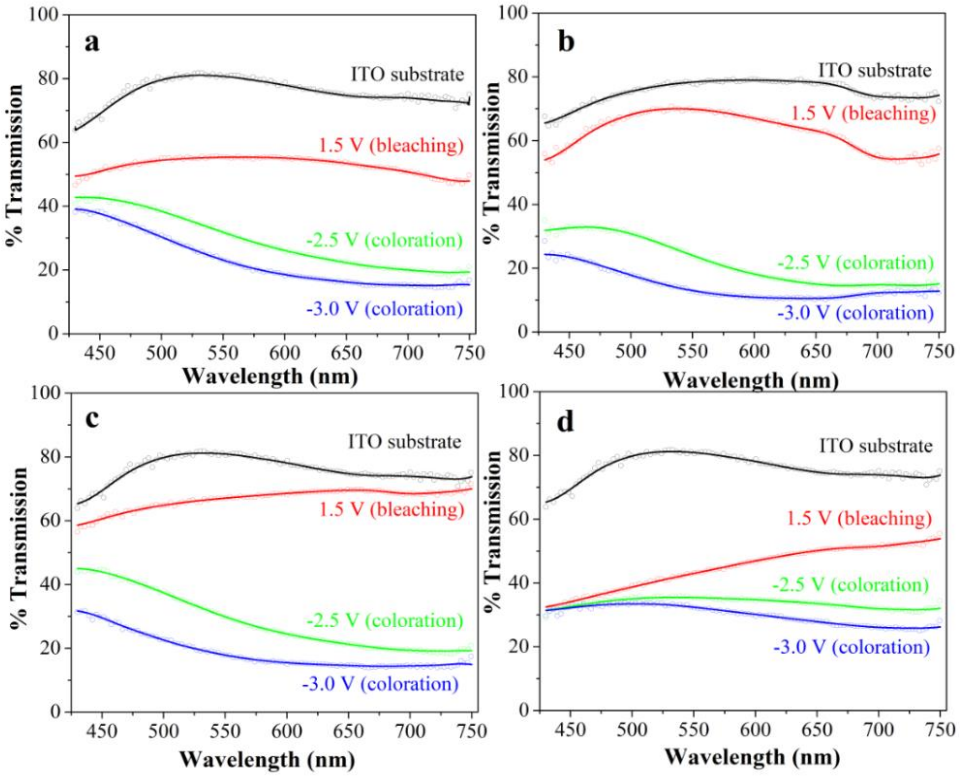

Fig. 6.2 Transmission spectra of thin films: (a) pure bundled $W_{18}O_{49}$ nanowires, (b) La:W = 1:15, (c) La:W = 1:10, and (d) La:W = 1:5, in their coloured and bleached states, measured at applied potentials ranging from +1.5 to -3.0V.

The Optical density (ΔOD) and colouration efficiency (CE) of La-doped samples are also calculated using Eqs. 2.6, 2.7 and 2.8, and the results are presented in Table 6.2. The ΔT value was found to be increased by 16% and 16.8% for La/W

= 1:15, 1:10 respectively, compared with the plain $W_{18}O_{49}$ thin film. The ΔT value of the 1:5 film samples was only 20.9%, due to the film was destroyed after a large -2.5 V voltage was applied (which cannot be reversed back to the bleaching stage).

In contrast to the Ce-doped samples, the La-doped samples displayed a better optical contrast percentage than the Ce-doped samples, by 9.1% and 4.5% for ratios of 1:15 and 1:10, respectively. The OD value of La-doped 1:15, 1:10 and 1:5 samples was 0.77, 0.66 and 0.24, respectively, exhibiting a similar trend to the Ce dopants. The highest OD value was obtained at the lowest amount of La dopant (1:15), which was also much higher than that of the plain $W_{18}O_{49}$ nanowire samples, by 0.26. The CE values of La-doped 1:15, 1:10 and 1:5 samples were 77, 60 and 21.8 cm^2/C respectively, and the 1:15 sample exhibited an improvement of 24.4% against the plain $W_{18}O_{49}$. Except that the 1:10 sample was slightly decreased by 3.1%, compared with the plain $W_{18}O_{49}$, the other two samples exhibited a better OD value than the plain $W_{18}O_{49}$. The OD values of La/W = 1:5, 1:10, 1:15 and pure $W_{18}O_{49}$ were 72, 59, 74 and 63 cm^2/C, respectively.

6.4 Further extension and future investigation to smart window device on soft substrates

In recently year, there have been great interest in developing flexible to stretchable and foldable device for various application such as wearable electrochromic device, soft electronic, optoelectronic device, implantable display, robotic skin and others energy related device [331, 332]. The development of flexible, light weight, cost efficiency, and low-power consumption deformable electronics is instantly needed to realize those applications. The flexible electorochromic device generally consist multiple layer as same as original glass electrochromic device, while theirs using the soft conductive substrate such as polyethylene naphthalate (PEN) [333], Polyethylene terephthalate (PET) [334] etc. to replace the glass conductive substrate.

Many recent progresses have been focussing on different design and fabrication of those smart device while based on the same objective, making a new generation of the devices in term of flexibility, stretchability, foldability, implantability and wearability. Liang *et al.* have successfully prepared $WO_3{\cdot}2H_2O$ ultrathin nanosheet/ITO/PET flexible electrochromic device with impressive result of 120.9 cm^2C^{-1} coloration efficiency and up to 400 switching time stability [335]. Park *et al.* reported on a stretchable, transparent and skin-attachable strain sensor with colour changing system [336]. The thin layer of polyaniline nanofibers and V_2O_5 were coated on ITO-PET substrate to make of electrochromic device. The strain sensor was successfully integrated on skin via an Arduino circuit for an interactive colour change with the variation of the applied strain which allows real-time visual display of body motion. Alesanco *et al*. studied viologen-modified TiO_2 nanostructure films for flexible ITO-PET electrochromic devices [334]. The flexible device offered transmittance change above 60% and 6-8 s for switching speeds. This section will summarise the study on our flexible electrochromic device of $W_{18}O_{49}$, by analysing the electrochemistry and transmittance results.

6.4.1 Thin film preparation on soft substrates

The well mixed solution of 0.1 g $W_{18}O_{49}$ with 3 ml of 1% nafion mixed ethanol was used for thin film preparation. Nafion porous polymer could help to prevent a degradation issue and easier to form thin films on soft substrate. The solution was deposited on Indium oxide coated PET soft substrate (purchased from Sigma, resistivity about 60Ω/sq), 3.8 × 2.5 cm in size, by using spin coater technique at 1500 rpm for 15 s. 6 layers were deposited altogether to achieve about 300 nm thickness thin film.

6.4.2 Characterisations

As similar as previous chapter 5, the electrochromic performance of thin film was characterised using both 3 electrode electrochemistry potential stat and Uv-vis techniques. All essential value of electrochromic performance such as $D_{Li}+$, stability and CE were presented and discussed. The submerged area of

thin film on PET substrate during electrochemistry measurement is 2.5 × 2.5 cm^2. The CV curve of these thin films were recorded between -1 V and 1.8 V at difference scan rates of 20, 40, 60, 80 and 100 mV/s. 0.5M $LiClO_4$ with PC mixed 4% w/v of PPC polymer are sued as gel electrolyte for this set of experiment. To obtain the transmittance spectra, the ultraviolet-visible (UV-Vis) spectrophotometry was used and the Instrument used was the MSV-5300.

6.4.3 Result of electrochemistry on $W_{18}O_{49}$/ PET thin film

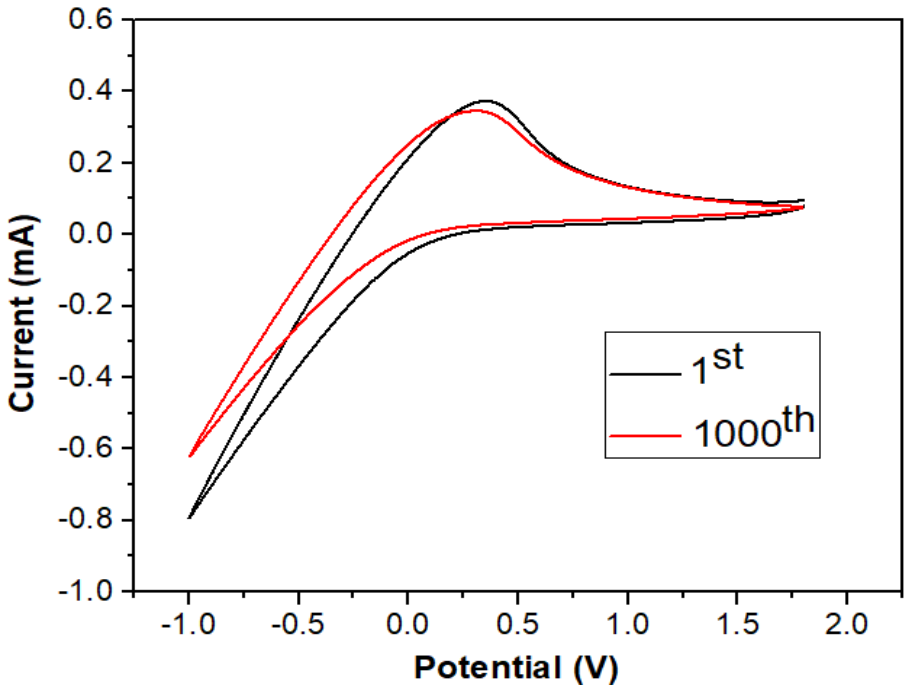

Fig. 6.3 CV curves of $W_{18}O_{49}$/nafion thin film on the PET substrate after the 1st and the 1000th cycle, recorded between -1.5 and 1.5 V at 60 mV/s.

According to Randles-Sevick's equation (Eq 2.5), the D_{Li}+ are 1.48 ×10^{-11} cm^2/s for intercalation and 3.29 ×10^{-12} cm^2/s for de-intercalation at the first cycle. After 1000th cycle, the D_{Li}+ slightly dropped by 38% for intercalation (9.07 ×10^{-12} cm^2/s) and 14% for de-intercalation (2.83 ×10^{-12} cm^2/s) compare with that of 1st cycle. The stability of de-intercalation improves by 27% compare with the film without nafion (as presented in section 5.2), however the stability of intercalation of $W_{18}O_{49}$/nafion thin film was slightly decreased by 21% compare with the film without nafion. It could be suggested that nafion might be an

alternative conductive polymer for degradation issue of the electrochromic thin films.

Fig.6.4 shows the transmission spectra measured in the range from 350 to 750 nm in the coloured and bleached state, whilst intercalated and de-intercalated with Li^+ ions. With the transmittance values from the graph, the optical contrast or variation (ΔT) for each sample at a specific wavelength of 630 nm could be also calculated using Eq 2.6. The optical density change is defined as the light absorption ability of the electrochromic film and can be calculated using Eq. 2.8. The transmission percentage of coloured and bleached stage at wavelength 630 nm are 30.73 and 81.41 %, respectively. The optical contrast is 50.7 % with optical density change of 0.42.

6.4.4 Result of transmittance measurement on $W_{18}O_{49}$/PET thin film

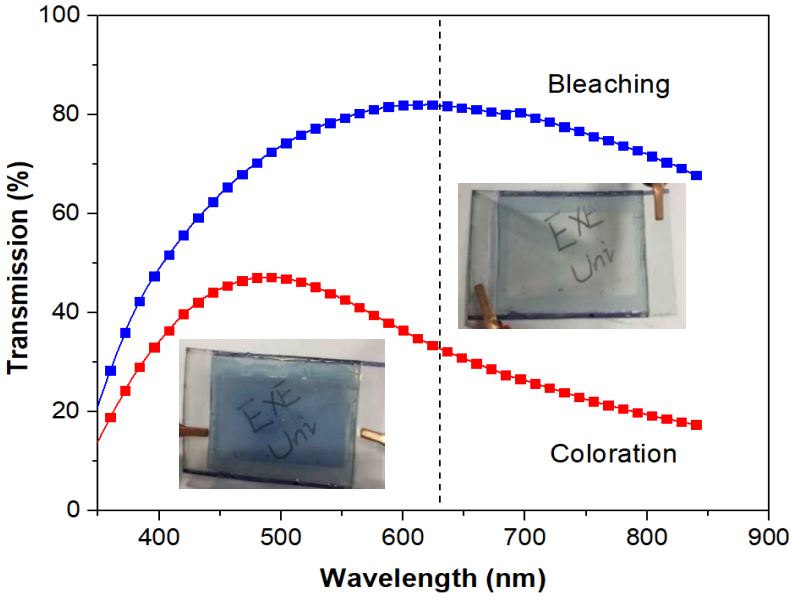

Fig. 6.4 Transmission spectra (from 350 nm to 750 nm) for $W_{18}O_{49}$/Nafion thin film sample in their bleached and coloured states.

6.5 Summary

This chapter has introduced optical property of doped samples compare with plain $W_{18}O_{49}$ structure. An importance parameter includes optical contrast (ΔT),

Optical density (ΔOD) and colouration efficiency (CE) have been calculated and discussed. All findings are summarised as following:

- The best improvement of the optical contrast (ΔT) can be obtained from the lowest doped samples which slightly increased by 6.9% for Ce-doped sample and 16% for La doped sample compare with plain $W_{18}O_{49}$.
- Increasing of optical density (ΔOD) by 0.23 and 0.26 for lowest Ce- and La-doped sample respectively compare with plain $W_{18}O_{49}$.
- 5.4% and 15.1% CE improvement of lowest Ce- and La-doped sample compare with plain $W_{18}O_{49}$.
- Successfully prepared a soft substrate device which can be obtained 1.48 $\times 10^{-11}$ cm^2/s for intercalation and 3.29 $\times 10^{-12}$ cm^2/s for de-intercalation. Moreover, the result of 31 % and 81% transmission of coloured and bleached stage have also been reported.

Chapter 7 Conclusions and future work

7.1 Conclusions

The present work, the tungsten oxide ($W_{18}O_{49}$) nanowires and doped WO_x nanostructure samples (including Na-, Ce-, La- dopants) were prepared by using simple solvothermal technique. Their morphologies, crystals structures and electrochromic properties were investigated and analysed in detail.

In chapter 4, Well-crystallised bundles $W_{18}O_{49}$ nanowires and Na-, Ce, and La-doped samples nanostructure were successfully synthesised by solvothermal technique. A pure 1-D bundles $W_{18}O_{49}$ with ultrathin nanowires of only *ca*. 2-5 nm in diameters and up to 2 µm in length have been reported. The results also show that the growth habit of WO_x framework was modified by the different types of dopant, resulting of shorter and slightly thicker nanowires morphology compare with plain $W_{18}O_{49}$. Based on evidences, Na-, Ce- and La- cation was located in the hexagonal channel or V_o position of the WO_x framework leading to structure relaxation and increase of V_o inside WO_x structure. From a complete relationship of geometry-composition-structure-property result was showed that temperature could be an important factor for structural relaxation and phase transition of the WO_x structure. An interesting red-shift in the luminescence emission from the nanowires doped with Ce or La has been reports which cause by the abundance of V_o in the doped nanowires.

In chapter 5, The $W_{18}O_{49}$ nanowires exhibit 7 times faster Li^+ kinetic and better stability by 33% for intercalation and 12% for de-intercalation than that of WO_3 nanoparticles. The improvement of WO_x electrochromic performance has been achieved by using Ce- and La-doped nanostructure. Ce:W = 1:15 doped sample exhibits 2.5 times faster ion diffusion kinetics and 20% better stability for de-intercalation against the plain $W_{18}O_{49}$ nanowires. La-doped samples with ratio 1:10 also offer about 3 times faster diffusion kinetics compared with plain $W_{18}O_{49}$ samples. The kinetics of the Li^+ and electrochromic stability of both $W_{18}O_{49}$ nanowires and WO_3 nanoparticles can be improved by annealing treatment. The WO_3 samples annealed at 350 °C obtained the best stability,

about 11% improvement for intercalation and 23.5% the for de-intercalation, compared with the un-treated WO_3. 350 °C annealed $W_{18}O_{49}$ nanowire thin films also presented better improvements by 36% for intercalation and 60% for de-intercalation against the un-treated $W_{18}O_{49}$ thin film. It is suggested that the degradation of the thin films is related to Li^+ trapping or loss of V_o inside the structures, based on the enlarged d values found in both post-testing samples after the 1000th cycle and XPS spectrum results. The colouration mechanism of thin films has been related to both transitions from W^{6+} to W^{5+} state, and from W^{4+} to W^{5+} state.

In chapter 6, the optical result from Ce-doped with ratio 1:15 sample shows an improvement of the optical contrast (ΔT) by 6.9% compared with plain $W_{18}O_{49.}$ Similar trend for La:W 1:15 sample, the optical contrast (ΔT) increases by 16% compared with plain $W_{18}O_{49}$. Moreover, the optical density (ΔOD) improves by 0.23 and 0.26 for lowest Ce- and La-doped sample respectively compared with plain $W_{18}O_{49}$. The higher colouration efficiency for both lowest ratio La and Ce doped samples also presented which increases by 5.4% for Ce- doped sample and 15.1% for La-doped sample compared with plain $W_{18}O_{49}$. Successfully prepared a soft substrate device which can obtain D_{Li}^+ value of 1.48 $\times 10^{-11}$ cm^2/s for intercalation and 3.29 $\times 10^{-12}$ cm^2/s for de-intercalation. The result of 31 % and 81% transmission of coloured and bleached stage have also reported.

In summary, we have achieved to improve an electrochromic behaviour of WO_x structure by using annealing treatment and doping with different elements into the WO_x structure. The result of W-O relaxation and increase of V_o have been found from those developed WO_x framework compared with original framework. Relaxation and V_o could be an important key for an improvement of electrochromic behaviour.

7.2 Future work

Based on the obtained results in this thesis, some suggestions are recommended for further work as follows: Some of suggestion have not presented in thesis due to equipment and time limit.

- Synthesised and structural analysed of the different non-stoichiometry structures of tungsten oxide and also their electrochromic performance could be a further recommended topic. As we found out that the V_o could play an important role during the colouration and bleaching process of WO_x. Thus, it would be of interest, if we could find out a condition to control each non-stoichiometry synthesis and also compare their electrochromic performance, hence that the temperature could be the main factor to control each non-stoichiometry synthesis.
- The investigation of electrochromic performance from Na-doped samples.
- The low temperature electrochromic performance (work at -40 degree) could be an interesting topic to investigate. The limit of working temperature of smart electrochromic device has being an issue in current laboratory. Most investigations were only presented at the room temperature working stage. Few reported suggested that the electrochromic performance is reduced (very slower switching time, lower CE etc.) after the temperature dropped from the room temperature and then stop working at some point after temperature reach to minus degree Celsius due to the frozen electrolyte. We believe that the gel electrolyte could be an important key, not only to enhance the Li^+ intercalation/de-intercalation but also to unsolved the temperature limitation of the electrochromic and other energy related-devices.
- It will be interesting to further investigate on soft substrate electrochromic device. This could open-up an opportunity to support more wide range of future applications.

References

1. A. C. Dillon, A. H. Mahan, R. Deshpande, P. A. Parilla, K. M. Jones and S. H. Lee, *Thin Solid Films*, 2008, **516**, 794-797.
2. Z. Jiao, J. Wang, L. Ke, X. Liu, H. V. Demir and M. F. Yang, *Electrochim. Acta*, 2012, **63**, 153-160.
3. S. H. Lee, R. Deshpande, P. A. Parilla, K. M. Jones, B. To, A. H. Mahan and A. C. Dillon, *Adv. Mater.*, 2006, **18**, 763-766.
4. Y. T. Park, Y. K. Hong and K. T. Lee, *J. Ceram. Process. Res.*, 2013, **14**, 337-341.
5. M. Weil and W. D. Schubert, *International Tungsten Industry Association*, 2013, 1-12.
6. S. Hashimoto, H. Matsuoka, H. Kagechika, M. Susa and K. S. Goto, *J. Electrochem. Soc*., 1990, **137**, 1300-1304.
7. R. T. Wen, C. G.Granqvist and G. A. Niklasson, *Nature Mater*., 2015, **14**, 994-1002.
8. R. T. Wen, G. A. Niklasson and C. G. Granqvist, *ACS Appl. Mater. Interfaces*, 2015, **7**, 28100-28104.
9. R. Deshpande, S. H. Lee, A. H. Mahan, P. A. Parilla, K. M. Jones, A. G. Norman, B. To, J. L. Blackburn, S. Mitra and A. C. Dillon, *Solid State Ionics*, 2007, **178**, 895-900.
10. H. Zheng, J. Z. Ou, M. S Strano, R. B. Kaner, A. Mitchell and K. K. Zadeh, *Adv. Funct. Mater.*, 2011, **21**, 2175-2196.
11. Y. Djaoued, S. Balaji and R. Bruning, *J. Nanomater*., 2012, **2012**, 1-9.
12. Y. C. Nah, A. Ghicov, D. Kim and P. Schmuki, *Electrochem. Commun.*, 2008, **10**, 1777-1780.
13. L. Meda, R. C. Breitkopf, T. E. Haas and R. U. Kirss, *Thin Solid Films*, 2001. **402**, 126-130.
14. A. I. Inamdar, Y. S. Kim, B. U. Jang, H. Im, W. Jung, D. Y. Kim and H. Kim, *Thin Solid Films*, 2012, **520**, 5367-5371.
15. M. H. Kim, T. Y. Kang, Y. S. Jung and K. H. Kim, *J. Appl. Phys.*, 2013, **52**, 05EC03.
16. K. Vijayalakshmi and V. V. Pillay, *Philos. Mag. Lett.*, 2011, **91**, 682-689.

17. A. Romanyuk, L. Marot, R. Steiner and P. Oelhafen, *SCV*, 2007, 36-38
18. M. Ahila, J. Dhanalakshmi, J. C. Selvakumari, and D. P. Padoyan, *Mater. Res. Express*, 2016, **3**, 105025.
19. H. Wei, X. Yan, Q. Wang, S. Wu, Y. Mao, Z. Luo, H. Chen, L. Sun, S. Wei and Z. Guo, *Energy Environ. Focus*, 2013, **2**, 112-120.
20. A. Abareshi and H. Haratizadeh, *Iranian J. Phys. Res.*, 2016, **16**, 47-54.
21. C. Y. Kim and S. Park, *Asian J. Chem.*, 2013, **23**, 5874-5878.
22. A. M. Datir, V. S. Ghole and S. D. Chakane, *IMCS – The 14th International Meeting on Chemical Sensors*, 2012, 1688-1691.
23. S. F. Chen, A. Aldalbahi and P. X. Feng, *Sensors (Basel)*, 2015, **15**, 27035-27046.
24. Y. Qin, X. Li, F. Wang and M. Hu, *J. Alloys Comp*., 2011, **509**, 8401-8406.
25. Y. Wicaksana, S. Liu, J. Scott and R. Amal, *Molecules*, 2014, **19**, 17747-17762.
26. S. H. N. Lim, J. Isidorsson, L. Sun, B. L. Kwak and A. Anders, *Sol. Energy Mater. Sol. Cells*, 2013, **108**, 129-135.
27. D. K. Nandi and S.K. Sarkar, *4 International Conference on Advances in Energy Research (Icaer 2013)*, 2014, **54**, 782-788.
28. J. Yin, H. Cao, J. Zhang, M. Qu and Z. Zhou, *Cryst. Growth Des.*, 2013, **13**, 759-769.
29. S. Pal and K. K. Chattopadhyay, *Inter. J. Res. Eng. Technol*., 2016, **5**, 97-101.
30. T. Vogt, P. M. Woodward and B. A. Hunter, *J. Solid State Chem.*, 1999, **144**, 209-215.
31. E. Cazzanellia, C. Vinegonib, G. Mariottob, A. Kuzminc and J. Puransc, *Solid State Ionics*, 1999, **123**, 67-74.
32. D. Y. Lu, J. Chen, H. J. Chen, L. Gong, S. Z. Deng, N. S. Xu and Y. L. Liu, *Appl. Phys. Lett.,* 2007, **90**, 041919.
33. H. N. Cui, Doctor of Philosophy, School of Science, University of Minho, 2005, 1-200.
34. M. D. Bhatt and J. S. Lee, *J. Mater. Chem.* A, 2015, **3**, 10632-10659.
35. Z. F. Huang, J. Song, L. Pan, X. Zhang, L. Wang and J. J. Zou, *Adv. Mater.*, 2015, **27**, 1-19.

36. D. B. Migas, V. L. Shaposhnikov and V. E. Borisenko, *J. Appl. Phys.*, 2010, **108**, 093714.
37. R. Satyabrata, S. Takafumi, S. Seigo and T. Takashi, *Modern Phys. Lett. B*, 2009, **23**, 2819-2846.
38. F. J. Castro, F. Tonus, J. L. Bobet and G. Urretavizcaya, *J. Alloys Compd*., 2010, **495**, 537-540.
39. P. J. Wiseman and P. G. Dickens, *J. Solid State Chem.*, 1973, **6**, 374-377.
40. D. Yoon and A. Manthiram, *Energy Environ. Sci.*, 2014, **7**, 3069-3076.
41. C. Guo, S. Yin, Q. Dong and T. Sato, *Cryst. Eng. Comm*., 2012, **14**, 7727.
42. A. M. E. Sayed and S. M. A. Mousa, *Indian J. Chem. Technol.*, 2005, **12**, 304-308.
43. K. C. Kim, M. H. Kwak, S. B. Kang, S. Kim, M. C. Paek, K. Y. Kang, H. Y. Kim, J. H. Jang, C. K. Kim, H. S. Kye and L. S. Cheong, *Ferroelectrics*, 2011, **422**, 14-18.
44. K. R. Dey, C. H. Ruscher, T. M. Gesing and A. Hussain, *Mater. Res. Bull.*, 2007, **42**, 591-599.
45. C. Delmas, A. Nadiri, G. L. Flem, S. H. Chang, J. P. Chaminade and M. Menetrier, *MRS Proceedings*, 1988. **135**. 489-494.
46. P. Roussel, O. Perez and P. Labbe, Acta Crystallogr. B, 2001, 57, 603-632.
47. H. Qi, C. Wang and J. Liu, *Adv. Mater.*, 2003, **15**, 411-414.
48. S. A. Ivanov, J. R. Sahu, V. I. Voronkova, R. Mathieu and P. Nodblad, *Solid State Sci*., 2015, **40**, 44-49.
49. A. Magneli, *Acta Chem. Scandinavica*, 1953, **7**, 315-324.
50. T. Gao, B. P. Jelle and A. Gustavsen, IEEE International Conference on Nanotechnology, 2013, 1093-1096.
51. J. Wang, E. Khoo, P. S. Lee and J. Ma, *J. Phys. Chem. C,* 2009, **113**, 9655–9658.
52. J. Wang, E.Khoo, P. S. Lee and J. Ma, *J. Phys. Chem. C*, 2008, **112,** 14306–14312.
53. B. Ingham, S. Hendy, S. V. Chong and J. L. Tallon, *Adv. Mater. Nanotechnol*., 2008, 72, 1-12.

54. N. D. Zakharov, P. Werner, I. P. Zibrov, V. P. Filonenko and M. Sundberg, *J. Solid State Chem*., 1999, **147**, 536-544.
55. X. Zeng, Y. Zhou, S. Ji, H. Luo, H. Yao, X. Hauge and P. Jin, *J. Mater. Chem. C*, 2015, **3**, 8050-8060.
56. L. S. Leonova, N. G. Bukun, L. O. Atovmyan, A. V. Levchenko, N. S. Tkacheva and Y. A. Dobrovol'skii, *Russ. J. Electrochem.*, 2007, **43**, 462-469.
57. J. Guo, C. Dong, L. Yang and G. Fu, *J. Solid State Chem.*, 2005, **178**, 58-63.
58. I. C. Lekshmi and M. S. Hegde, *Mater. Res. Bull.*, 2005, **40**, 1443-1450.
59. J. Wang, G. Liu, and Y. Du, Mater. Lett., 2003, **57**, 3648-3652.
60. S. Reich, G. Leitus, Y. Tssaba, Y. Levi, A. Sharoni and O. Millo, *J. Supercond. Nov. Magn.*, 2000, **13**, 855-861.
61. S. Reich, and Y. Tsabba, *Eur. Phys. J. B*, 1999, **9**, 1-4.
62. R. Azimirad, M. Goudarzi, O, Akhavan and A. Z. Moshfegh, *Vacuum*, 2008, **82**, 821-826.
63. R. Azimirad, O. Akhavan and A. Z. Moshfegh, *J. Phys. Chem.*, 2009, **113**, 13098–13102.
64. K. B. Lee, S. W. Lee and S. B. Park, *J. Cryst. Growth*, 2009, **311**, 4365-4370.
65. N. T. Garavand, S. M. Mahdavi, A. Lrajizad and K. Ahadi, *Mater. Lett*., 2012, **82**, 214-216.
66. T. Sheng, P. P. Chavvakula, B. Cao, N. Yue, Y. Zhang and H. Zhang. *J. Cryst. Growth*, 2014, **395**, 61-67.
67. C. Genin, A. Driouiche, B. Grand and M. Figlarz, *Solid State Ionics*, 1992, **53-56**, 315-323.
68. J. Purans, A. Kuzmin, P. Parent and C. Laffone, *Ionics*, 1998, **4**, 101-105.
69. L. Hernan, M. Macias, J. Morales, L. Sfinchez and J. L. Tirado, *Solid State Ionics*, 1991, **47**, 75-79.
70. A. Watanabe and M. Goto, *J. Less-Common Metals*, 1978, **61**, 265 - 272.
71. M. Figlarz, *Prog. Solid State Chem.*, 1989, **19**, 1-46.
72. T. Nanba, Y. Nishiyama and I. Yasui, *Mater. Res. Soc.*, 1991, **6**, 1324-1333.

73. G. A. D. Wijs and R. A. D. Groot, *Phys. Rev. B*, 1999, **60**, 16463-16474.
74. A. Hjelm and C. G. Granqvist, *Phys. Rev. B*, 1996, **54**, 2436-2445.
75. D. B. Migas, V. L. Shaposhnikov, V. N. Robin and V. E. Borisanko, *J. Appl. Phys.*, 2010, **108**, 093713.
76. M. Johansson, Doctor of Philosophy, Department of Engineering Sciences, Uppsala University: Acta Universitatis Upsaliensis, 2014, 1-129.
77. F. Cora, M. G. Stachiotti and C. R. A. Catlow, *J. Phys. Chem. B*, 1997, **101**, 9345-3952.
78. Y. Ping, D. Rocca and G. Galli, *Phys. Rev. B*, 2013, **87**, 165203.
79. L. Berggren, J. C. Jonsson and G. A. Niklasson, *J. Appl. Phys.*, 2007, **102**, 083538.
80. L. Berggren and G. A. Niklasson, *Sol. Energy Mater. Sol. Cells*, 2005, **85**, 573-586.
81. I. C. Hurtado, T. Tavera, P. Yurrita, N. Perez, A. Rodriguez, C. G. Mandayo, E. Castano, *Appl. Surf. Sci.*, 2013, **276**, 229-235.
82. C. L. Mauriat and V. Oison, *J. Phys. Condens. Matter*, 2006, **18**, 7361-7371.
83. G. A. D. Wijs, P. K. D. Boer and R. A. D. Groot, *Phys. Rev. B*, 1999, **59**, 2684-2693.
84. M. R. Field, D. G. Mcculloch, S. N. H. Lim, A. Anders, V. J. Keast and R. W. Burgess, *J. Phys. Condens. Matter*, 2008, **20**, 175216.
85. M. G. Stachiotti, F. Cora, C. R. A. Catlow and C. O. Rodriguez, *Phys. Rev. B*, 1997, **55,** 7508-7514.
86. R. Chatten, A. V. Chadwich, A. Rougier and P. J. D. Lindan, *J. Phys. Chem. B,* 2005, **109**, 3146-3156.
87. M. B. Johansson, G. Baldissera, L. Valyukh, C. Persson, H. Arwin, G. A. Niklasson, *J. Phys Condens Matter*, 2013, **25**, 205502.
88. M. N. Huda, Y. Yan, C. Y. Moon, S. H. Wei and M. M. A. Jassim, Phys. Rev. B, 2008, **77,** 1-13.
89. P. P. G. Borrero, F. Sato, A. N. Medina, M. L. Baesso, A. C. Bento, G. Baldissera, C. Persson, G. A. Niklasson, C. G. Granqvist and A. F. D. Siliva. *Appl. Phys. Lett*., 2010, **96,** 061909.
90. O. Y. Khyzhun, *J. Alloys Comp*., 2000, **305**, 1-6.

91. G. A. Niklasson, *Phys. Scripta*, 2015, **90, 1-5**.
92. J. Purans, A. Kuzmin, P. Parent and C. Laffon, *Electrochim. Acta*, 2001, **46,** 1973-1976.
93. H. Hochst, R. D. Bringans and H. R. Shanks, *Phys. Rev. B*, 1982, **26,** 1702-1712.
94. D. Meng, N. M. Shaalan, T. Yamazaki and T. Kikula, *Sens. Act. B: Chem.*, 2012, **169**, 113-120.
95. T. Tokunaga, T. Kawamoto, K. Tanaka, N. Nakamura, Y. Hayashi, K. Sasaki, K. Kurodu and T. Yamamoto. *Nanoscale Res Lett*, 2012, **7**, 1-7.
96. Y. T. Hsieha, U. S. Chena, S. H. Hsueha, M. W. Huangb and H. C. Shih, *Appl. Surf. Sci.*, 2011, **257,** 3504-3509.
97. C. H. Chen, S. J. Wang, R. M. Ko, Y. C. Kuo, K. M. Uang, T. M. Chen, B. W. Liou and H. Y. Tsai, *Nanotechnology*, 2006, **17,** 217-223.
98. J. Wang, P. S. Lee and J. Ma, *Cryst. Growth Des.,* 2009, 2293-2299.
99. S. Sun, Z. Zou and G. Mina, *Mater. Charact.*, 2009, **60**, 437-440.
100. T. Yang, Y. Zhang, and C. Li, *J. Alloys Comp.*, 2014, **584**, 546-552.
101. S. Yoon, S. G. Woo, K. N. Jung and H. Song, *J. Alloys Comp.*, 2014, **613**, 187-192.
102. C. H. Lu, M. H. Hon, C. Y. Kuan and I. C. Leu, *Jpn. J. Appl. Phys.*, 2014, **53**, 06JG08.
103. K. Huang, Q. Pan, F. Yang, S. Ni, X. Wei and D. He, *J. Phys. D: Appl. Phys.*, 2008, **41**, 155417.
104. P. J. Wojcik, L. Santos, L. Pereira, R. Martins and E. Fortunato, *Nanoscale*, 2015, **7**, 1696-708.
105. S. Adhikari and D. Sarkar, *J. Nanomater.*, 2015, **2015**, 269019.
106. J. Sungpanich, T. Thongtem and S. Thongtem, J. Nanomater., 2014, **2014**, 739251.
107. W. Mu, X. Xie, X. Li, R. Zhang, Q. Yu, K. Lv, H. Weia and Y. Jian. *RSC Adv.*, 2014, **4**, 36064.
108. H. Li, J. Chen, M. Cui, G. Cai, A. L. S. Eh, P. S. Lee, H. Wang, Q. Zhangc and Y. Li, *J. Mater. Chem. C*, 2016, **4**, 33-38.
109. Y. Song, J. Zhao, Y. Zhaoa and Z. Huanga, *RSC Adv.*, 2016, **6**, 99898-99904.

110. W. Shan, Y. Geng, X. Chen, N. Huang, F. Liub and S. Yanga, *Catal. Sci. Technol.*, 2016, **6**, 1195-1200.
111. Y. Shen, P. Yan, Y. Yang, F. Hu, Y. Xiao, L. Pan, Z. Li, *J. Alloys Comp.*, 2015, **629**, 27-31.
112. W. Xu, Z. Meng, N. Yu, Z. Chen, B. Sun, X. Jianga and M. Zhu, *RSC Adv.*, 2015, **5**, 7074-7082.
113. Y. X. Qin, C. Y. Liu, and Y. Liu, *Chin. Phys. B*, 2015, **24**, 027304.
114. Y. M. Zhao, W. B. Hu, Y. D. Xia, E. F. Smith, Y. Q. Zhu, C. W. Dunnill and D. H. Gregory, J. Mater. Chem., 2007, **17**, 4436-4440.
115. S. Rajagopal, D. Nataraj, D. Mangalaraj, Y. Djaoued, J. Robichaud and O. Y. Khyzhun, *Nanoscale Res. Lett.*, 2009, **4**, 1335-1342.
116. V. V. Kondalkar, S. S. Mali, R. R. Kharade, K. V. Khot, P. B. Patil, R. M. Mane, S. Choudhury, P. S. Patil, C. K. Hong, J. H. Kim, P. N. Bhosale, *Dalton Trans.*, 2014, **6**, 2788-2800.
117. H. Zhou, Y. Shi, Q. Dong, Y. Wang, C. Zhu, L. Wang, N. Wang, Y. Wei, S. Taoa and T. Ma, *J. Mater. Chem. A*, 2014, **2**, 4347-4354.
118. J. X. Liu, X. L. Dong, X. W. Liu, F. Shi, S. Yin and T. Sato, *J. Alloys Comp.*, 2011, **509**, 1482-1488.
119. F. Li, H. Gong, Y. Wang, H. Zhang, Y. Wang, S. Liu, S. Wang and C. Sun, *J. Mater. Chem. A*, 2014, **2**, 20154-20163.
120. C. W. Lai, *Sci. World J.*, 2014, **2014**, 843587.
121. S. V. Pol, V. G. Pol, V. G. Kessler, G. A. Seisenbaeva, L. A. Solovyov and A. Gedanken, *Inorg. Chem.*, 2005, **44**, 9938-9945.
122. M. Zumer, V. Nemanic, B. Zajec, M. Wang, J. Wang, Y. Liu and L. M. Peng, *J. Phys. Chem. C*, 2008, **112**, 5250-5253.
123. M. C. Rao and O. M. Hussain, Res. J. Chem. Sci., 2011, **1**, 76-80.
124. A. Lusis, J. Kleperis and E. Pentjuss, *J. Solid State Electrochem.*, 2003, **7**, 106-112.
125. E. Ozkan, S. H. Lee, C. E. Tracy, J. R. Pitts, S. K. Deb, *Sol. Energy Mater. Sol. Cells*, 2003, **79**, 439-448.
126. C. C. Liao, F. R. Chen and J. J. Kai, *Sol. Energy Mater. Sol. Cells*, 2006, **90,** 1147-1155.
127. G. Beydaghyan, G. Bader and P. V. Ashrit, *Thin Solid Films*, 2008, **516,** 1646-1650.

128. Y. F. Lu and H. Qiu, J. Appl. Phys., 2000, **88,** 1082-1087.
129. M. G. Hur, T. Masaki and D. H. Yoon, *J. Nanosci. Nanotechnol.*, 2014, **14**, 8941-8945.
130. R. S. Vemuri, M. H. Engelhard and C. V. Ramana, *ACS Appl. Mater. Interfaces*, 2012, **4**, 1371-7.
131. M. Acosta, D. González and I. Riech, *Thin Solid Films*, 2009, **517**, 5442-5445.
132. R. Sato, N. Kawamura and H. Tokumaru, *Appl. Surf. Sci.*, 2008, **254**, 7676-7678.
133. E. Washizu, A. Yamamoto, Y. Abe, M. Kawamura and K. Sasaki, *Solid State Ionics*, 2003, **165**, 175-180.
134. C. Charles, N. Martin, M. Devel, J. Ollitrault, A. Billard, *Thin Solid Films*, 2013, **534**, 275-281.
135. H. H. Lu, *J. Alloys Comp*., 2008, **465**, 429-435.
136. S. K. Deb, *Sol. Energy Mater. Sol. Cells*, 2008, **92**, 245–258.
137. W. Cheng, E. Baudrin, B. Dunna and J. I. Zinkb, *J. Mater. Chem.* 2001, **11**, 92-97.
138. J. H. Cho, Y. J. Byun, J. H. Kim, Y. J.Lee, Y. H. Jeong, M. P. Chun, J. H. Paik and T. H. Sung, *Ceram. Int.*, 2012, **38**, S589-S593.
139. E. Widenkvist, R. A. Quinlan, B. C. Holloway, H. Grennberg and U. Jansson, *Cryst. Growth Des.*, 2008, **8**, 3750-3753.
140. I. Riech, M. Acosta, M. A. Z. Arjona, F. Penunuri, M. R. Mendoza, E. Marin, P. R. Fragoso and J. G. M. Alvarez, *Int. J. Photoenergy*, 2013, **2013**, 1-8.
141. S. Zanarini, N. Garino, J. R. Nair, C. Francia, P. J. Wojcik, L. Pereira, E. Fortunato, R. Martins, S. Bodoardo and N. Penazzi, *J. Electrochem.* Sci. .China Ser. B: Chem., 2014, **9**, 1650-1662.
142. S. J. Yoo, J. W. Lim and Y. E. Sung, Appl. Phys. Lett., 2007, **90**, 173126.
143. S. J. Yoo, Y. H. Jung, J. W. Lim, H. G. Choi, D. K. Kim, Y. E. Sung, *Sol. Energy Mater. Sol. Cells*, 2008, **92**, 179-183.
144. M. Deepa, A. K. Srivastava, K. N. Sood and S. A. Agnhotry, *Nanotechnology*, 2006, **17**, 2625-30.
145. A. J. More, R. S. Patil, D. S. Dalavi, S. S. Mali, C. K. Hong, M. G. Gang, J. H. Kim, and P. S. Patil, *Mater. Lett.*, 2014, **134**, 298-301.

146. M. Ahsan, Doctor of Philosophy, School of Engineering Systems Faculty of Built M. Ahsan, Environment and Engineering, Queensland University of Technology, Australia, 2012.
147. M. C. Rao and O. M. Hussain, Res. J. Chem. Sci., 2011, **1**, 92-95.
148. D. A. Jameel, *Int. J. Mod. Phys. Appl.,* 2015, **1**, 193-199.
149. M. D. Giulio, D. Manno, G. Micocci, A. Serra and A Tepore, *J. Phys. D*, 1997, **30**, 3211–3215.
150. C. K. Wangati, W.K.Njoroge, J. Okumu, *East Afr. J. Phys. Sci.*, 2008, **8**, 55-74.
151. K. I. Hiroharu, T. Mastsunaga, W. Guan, T. Ohshima, Y. Yagyu and Y. Suda, *J. Plasma Fusion Res*., 2009, **8**, 1431-1434.
152. A. K. Chawla, S. Singhal, H. O. Gupta and R. Chandra, *Thin Solid Films*, 2008, **517**, 1042-1046.
153. M. Kitao, S. Yamada, S. Yoshida, H. Akram and K. Urabe, *Sol. Energy Mater. Sol. Cells*, 1992, **25**, 241-255.
154. A. C. Jones and M. L. Hitchman, *in Chemical Vapour Deposition: Precursors, Processes and Applications*, Royal Society of Chemistry, 2009, DOI: 10.1039/9781847558794, pp.1-35
155. K. Bange, *J. Sol. Energy Mater. Sol. Cells*, 1999, **58**, 1-131.
156. S. Badilescu, *Solid State Ionics*, 2003, **158**, 187-197.
157. A. Novinrooz, M.Sharbatdaran and H. Noorkojouri, *Cent. Eur. J. Phys.*, 2005, **3**, 456-466.
158. V. V. Abramova, A. S. Sinitskii, E. A. Goodilina and Y. D. Tretyakov, *Mendeleev Commun.*, 2005, **15**, 178-180.
159. S. A. Hussain*, J. Sci. Dev. Env. Res.*, 2005, **8**, 1-8.
160. KSV NIMA, *What and why: Langmuir-Blodgett films*, Biolin Scientifin, 2013, https://www.biolinscientific.com/measurements/langmuir-and-langmuir-blodgett#langmuir-film-characterization, p. 1-2.
161. A. Mallik and B. C. Ray, *Int. J. Electrochem.,* 2011. **2011**, 1-16.
162. M. Z. Najdoski and T. Todorovski, *Mater. Chem. Phys*., 2007, **104**, 483-487.
163. S. H. Baeck, T. Jaramillo, G. D. Stucky, and E. W. McFarland, *Nano. Lett.*, 2002, **2**, 831-834.

164. O. Gurcuoglu, D. Evecan and E. O. Zayim, *J. Solid State Electrochem.*, 2014, **19***,* 403-413.
165. O. Gurcuoglu, D. Evecan and E. O. Zayim, *Microelectron. Eng.,* 2014, **128**, 42-47.
166. W. L. Kwong, H. Qiu, A. Nakaruk, P. Koshy and C.C. Sorrell, *Energy Procedia*, 2013, **34**, 617-626.
167. N. Sahu, B. Parija and S. Panigrahi, *Indian J. Phys.*, 2009, **83**, 493-502.
168. K. Paipitaka, C. Kahatthaa, W. Techitdheera, S. Porntheeraphatd and W. Pecharapa, *Energy Procedia*, 2011, **9**, 446 – 451.
169. W. Y. Chung, G. Sakai, K. Shimanoe, N. Miura, D, D. Lee and N. Yamazoe, *Sensor. Actuat. B Chem*., 1998, **46**, 139-145.
170. N. B.Patil, A. R. Nimbalkar and M. G.Patil, *Mater. Sci. Eng. B*, 2017, **227**, 53-60.
171. D. Channei, A. Nakaruk, S. Phanichphant, P. Koshy and C. C. Sorrell, *J. Chem.*, 2013, **2013**, 579284.
172. D. S. C. Halin, I. A. Talib, A. R. Daud and M. A. A. Hamid, *Int. J. Photoenergy*, 2014, **2014**, 352156.
173. T. Tasaki, S. Takase and Y. Shimizu, *J. Sensor Technol*., 2012. **2**: p. 75-81.
174. S. K. Deb, Philos. Mag., 1973, **27**, 801-822.
175. S. Arman, *J. New Mat. Electrochem. Syst.*, 2001, **3**, 173-179.
176. R. Chatten, A. V. Chadwick, A. Rougier and P. J. D. Lindan, *J. Phys. Chem. B*, 2005, **109**, 3146-3156.
177. B.W. Faughnan, R. S. Crandall and P. M. Heyman, *RCA Rev.,* 1975, **36**, 177-197.
178. O. F. Schirmer, V. Wittwer, G. Baur and G. Brand, *Solid State Sci. Technol.*, 1977, **124**, 749-753.
179. D. Langhammer, Doctor of Philosophy, Department of Chemistry-Ångström, Uppsala University, Sweden, 2015.
180. J. V. Gabrusenoks, P. D. Cikmach, A. R. Lusis, J. J. Kleperis and G. M. Ramans, *Solid State Ionics*, 1983, **14**, 25-30.
181. P. Gerard, A. Deneuville and R. Courths, *Thin Solid Films*, 1980, **71**, 221-236.

182. C. Bechinger, J. G. Zhang, D. K. Benson, C. E. Tracy, S. K. Deb and A. W. Czanderna, *J. Electrochem. Soc.*, 1997, **144**, 2022-2026.
183. S. H. Lee, M. J. Seong, H. M. Cheong, E. Ozkan, E. C. Tracy, S. K. Deb, *Solid Sstate lonics*, 2003, **156**, 447-452.
184. S. H. Lee, H. M. Cheong, J. G. Zhang, A. Mascarenhas, D. K. Benson and S. K. Deb, *Appl. Phys. Lett.*, 1999, **74**, 242-244.
185. T. Kubo and Y. Nishikitani, *J. Electrochem. Soc.*, 1998, **145**, 1729-1734.
186. V. V. Kondalkar, S. S. Mali, R. R. Kharade, R. M. Mane, P. S. Patil, C. K. Hong, J. H. Kim, S. Choudhury and P. N. Bhosale*, RSC Adv.*, 2015, **5**, 26923-26931.
187. S. S. Kalagia, S. S. Malib, D. S. Dalavib, A. I. Inamdarc, H. Im and P. S. Patil, *Electrochim. Acta*, 2012, **85**, 501-508.
188. C. H. Lu, M. H. Hon, C. Y. Kuan and I. C. Leu, *RSC Adv.*, 2016, **6**, 1913-1918.
189. M. Panagopoulou, D. Vernardou, E. Koudoumas, N. Katsarakis, D. Tsoukalas and Y. S. Raptis, *J. Phys. Chem. C*, 2017, **121**, 70-79.
190. P. R. Somani and S. Radhakrishnan, *Mater. Chem. Phys*., 2002, **77**, 117-133.
191. AIST, *Light-control glass using nanoparticles with gel electrolyte*, Press release*,* 2010, http://www.aist.go.jp/aist_e/list/latest_research/2010/20100520/20100520.html.
192. K. C. Ho, *Elecrrochim. Acta*, 1999, **44**, 3227-3235.
193. R. Sivakumar, K. Shanthakumari, A. Thayumanavan, M. Jayachandran and C. Sanjeeviraja. *Surf. Eng.*, 2007, **23**, 373-379.
194. K. D. Lee, *Thin Solid Films*, 1997, **302**, 84-8.
195. A. Subrahmanyam, C. S. Kumar and K. M. Karuppasamy, *Sol. Energy Mate. Sol. Cells*, 2007, **91**, 62-66.
196. K. W. Park, H. S. Shim, T. Y. Seong and Y. E. Sung, *Appl. Phys. Lett.*, 2006, **88**, 211107.
197. W. T. Wu, W. P. Liao, J. S. Chen and J. J. Wu, *ChemPhysChem*, 2010, **11**, 3306-3312.
198. A. Mohammed, T. Tuquabo, I. Mehail, B. M. John, and M. Nunzi*. Sens. Actuator. B: Chem.*, 2012, **162,** 14-21.

199. I. Kostis, M. Vasilopoulou, A. Soultati, P. Argitis, N. Konofaos, A. M. Douvas, N. Vourdas, G. Papadimitropoulos and D. Davazoglou, *Microelectron. Eng.*, 2013, **111**, 149-153.
200. C. P. Li, C. A.Wolden, A. C. Dillon and R. C.Tenent, *Sol. Energy Mater. Sol. Cells*, 2012, **99**, 50-55.
201. Y. Djaoued, S. Priya and S. Balaji, *J. Non-Cryst. Solids*, 2008, **354**, 673-679.
202. Y. Djaoued, P. V. Ashrit, S. Badilescu and R. Bruning, *J. Sol-Gel Sci.Technol*., 2003, **28**, 235-244.
203. S. Balaji, Y. Djaoued, A. S. Albert, R. Z. Ferguson and R. Bruning, *Chem. Mater.*, 2009, **21**, 1381-1389.
204. L. Yang, D. Ge, J. Zhao, Y. Ding, X. Kong and Y. Li, *Sol. Energy Mater. Sol. Cells*, 2012, **100**, 251-257.
205. C. C. Liao, F. R. Chen and J. J. Kai, *Sol. Energy Mater. Sol. Cells*, 2007, **91**, 1258-1266.
206. K. M. Karuppasamy and A. Subrahmanyam, *J. Phys. D: Appl. Phys.*, 2008, **41**, 035302.
207. N. N. Dinh, D. H. Ninh, T. T. Thao and T. V. Van, *J. Nanomater*., 2012, **2012**, 781236.
208. Y. C. Nah, A. Ghicov, D. Kim, S. Berger and P. Schmuki, *J. Am. Chem. Soc.*, 2008, **130**, 16154-16155.
209. Y. Nah, *Solid State Ionics*, 2003, **165**, 229-233.
210. A. Pennisi, F.Simone and C. M. Lampert, *Sol. Energy Mater. Sol Cells*, 1992, **28**, 233-247.
211. I. C. Lekshmi, A. Gayen, V. Prasad, S. V. Subramanyan and M. S. Hegde, *Mater. Res. Bull*., 2002, **37**, 1815-1823.
212. Y. S. Lin, Y. C. Chen and P. S. Shie, *Sol. Energy Mater. Sol. Cells*, 2014, **122**, 59-69.
213. M. Alsawafta, Y. M. Golestania, T. Phonemac, S. Badilescu, V. Stancovski and V. V. Truong, *J. Electrochem. Soc.*, 2014, **161**, H276-H283.
214. G. A. Niklasson, A. Norling, G. Possnert and L. Berggren*. J. Phys. Conf. Ser.,* 2008, **100**, 082023.

215. S. H. Lee, H. M. Cheong, C. E. Tracy, A. Mascarenhas, A. W. Czanderna and S. K. Deb, *Appl. Phys. Lett.*, 1999, **75**, 1541-1543.
216. A. Subrahmanyam and A. Karuppasamy, *Sol. Energy Mater. Sol. Cells*, 2007, **91,** 266-274.
217. K. D. Lee, *J. Korean Phys. Soc.*, 2001, **38**, 33-37.
218. E. M. Girotto and M. A. D. Paoli, *J. Braz. Chem. Soc.*, 1999, **10**, 394-400.
219. M. Morita, *J. Polym. Sci. B*, 1994, **32**, 231-242.
220. S. J. Yoo, J. W. Lim and Y. E. Sung, *Sol. Energy Mater. Sol. Cells*, 2006, **90**, 477-484.
221. T. Y. Wu, W. B. Li, C. W. Kuo, C. F. Chou, J. W. Liao, H. R. Chen and C. G. Tseng, *Electrochem. Sci.*, 2013, **8**, 10720-10732.
222. D. R. MacFarlane, J. Sun, M. Forsyth, J. M. Bell, L. A. Evans and I. L. Skyrabin, *Solid State Ionics*, 1996, **86-88**, 959-964.
223. Y. Zhu, M. T.Otley, F. A. Alamer, A. Kumar, X. Zhang, D. M. D. Mamangun, M. Li, B. G. Arden and G. A. Sotzing, *Org. Electron.*, 2014, **15**, 1378-1386.
224. A. Brazier, G. B. Appetecchi, S. Passerini, A. S. Vuk, B. Orel, F. Donsanti and F. Decker, *Electrochim. Acta*, 2007, **52**, 4792-4797.
225. M. Kucharski, T. Lukaszewicz and P. Mrozek, *Opto-Electron. Rev*., 2004, **12**, 175-180.
226. C. A. Nguyen, S. Xiong, J. Ma, X. Lu and P. S. Lee, *J. Phys. Chem. B*, 2009, **113**, 8006–8010.
227. J. A. Duffy, M. D.Ingram and P. M. S. Monk, *Solid State Ionics*, 1992, **58**, 109-114.
228. B. P. Ilknur, Doctor of Philosophy, Department of Science and Technology, Uppsala University, Sweden, 2013.
229. L. Astratine, Doctor of Philosophy, Dublin Institute of Technology, Republic of Ireland, 2012, DOI: 10.21427/D73G67.
230. A. Hofmann, M. Schulz and T. Hanemann, *Int. J. Electrochem. Sci.*, 2013, **8**, 10170-10189.
231. M. Sriyudthsak and S. Supothina, *Sens. Actuator. B: Chem*., 2006, **113**, 265-271.
232. P. Vijayakumar, M. S. Pandian, S. Mukhopadhyay and P. Ramasamy, *J. Sol-Gel Sci. Technol.*, 2015, **75**, 487-494.

233. K. Adachi, M. Tokushige, K. Omata, S. Yamazaki and Y. Iwadate. *ACS Appl. Mater. Interfaces*, 2016, **8**, 14019-14028.
234. M. E. A. Warwick, I. Ridley and R. Binions, *Open J. Energy Efficiency*, 2013, **2**, 75-88.
235. J. H. Youn, S. J. Baek, H. P. Kim, D. H. Nam, Y. Lee, J. G. Leeb and J. Jang, *J. Mater. Chem. C*, 2013, **1**, 3250-3254.
236. T. Y. Tsai, P. R. Yan and S. H. Yang, *Nanoscale Res Lett*, 2016, **11**, 1-9.
237. J. Song, Z. F. Huang, L. Pan, J. J. Zou, X. Zhang and L. Wang. *ACS Catal*, 2015, **5**, 6594-6599.
238. B. A. Wasmi, A. A. A. Amiery, A. A. H. Kadhum and A. B. Mohamad, *J. Nanomater*., 2014, **2014**, 715457.
239. W. Zhang, L. Yue, F. Zhang, Q. Zhang, X. Gui, R. Guan, G. Houa and N. Xu, *J. Mater. Chem. A*, 2015, **3**, 6102-6109.
240. J. Lee, C. Jo, B. Park, W. Hwang, H. I. Lee, S. Yoon, and J. Lee, *Nanoscale*, 2014, **6**, 10147-10155.
241. T. D. Senguttuvan, *Sens. Actuators B: Chem.*, 2010, **150**, 384-388.
242. S. Ashraf, C. S. Blackman, S. C. Naisbitt and I. P Parkin, *Meas. Sci. Technol*., 2008, **19**, 025203.
243. J. Krainer, M. Deluca, E. Lackner, R. W. Teubenbacher, F. Sosada, C. Gspan, K. Rohrcher, E. Wachmann and A. Koeck, *IEEE Int. Conf. Nanotechnol.*, 2016, DOI: 10.1109/ICSENS.2016.7808634.
244. C. Wongchoosuk, A. Wisitsoraat, D. Phokharatkul, A. Tuantranont and T. Kerdcharoen, *Sensors*, 2010, **10**, 7705-7715.
245. R. Ghosh, M. B. Baker and R. Lopez, *Thin Solid Films*, 2010, **518**, 2247-2249.
246. A. Georg , W. Graf and V. Wittwer, *Electrochim. Acta*, 2001, **46**, 2001-2005.
247. M. H. Yaacob, M. Breedon, K. K. Zadeh and W. Wlodarski, *Sens. Actuator B: Chem.*, 2009, **137**, 115-120.
248. A. A.Tomchenko, V. V. Khatko and I. L.Emelianov, *Sens. Actuator. B Chem.*, 1998, **46**. 8-14.
249. S. Luo, G. Lu, H.Chen and Y. Zhang, *Mater. Chem. Phys*., 2008, **109**, 541-546.

250. E. Rossinyol, A. Prim, E. Pellicer, J. Arbiol, F. H. Ramírez, F. Peiro, A. Cornet, J. R. Morante, L. A. Solovyov, B. Tian, T. Bo and D. Zhao*. Adv. Func. Mater.*, 2007, **17**, 1801-1806.

251. E. Rossinyol, A. Prim, E. Pellicer, J. Arbiol, F. H. Ramírez, F. Peiro, A. Cornet, J. R. Morante, B. Tian, T. Bo and D. Zhao*. Sens. Actuator. B: Chem.,* 2007, **126**, 18-23.

252. A. Hoel, L. F. Reyes, P. Heszler, V. Lantto and C. G. Granqvist, *Curr. Appl. Phys*., 2004, **4**, 547-553.

253. E. Comini, L. Pandolfi, S. Kaciulis, G. Faglia and G. Sberveglieri, *Sens, Actuator. B: Chem*., 2007, **127**, 22-28.

254. H. Kawasaki, T. Ueda, Y. Suda and T. Ohshima, *Sens. Actuator. B: Chem.*, 2004, **100**, 266-269.

255. M. Ranjbar, S. M. Mahdavi and A. I. zad, *Sol. Energy Mater. Sol. Cells*, 2008, **92**, 878-883.

256. S. G. Zamharir, M. Ranjbar and H. Salamati, *Sol. Energy Mater. Sol. Cells*, 2014, **130**, 27-35.

257. S. Chen, J. Luo, H. Tan, J. Chen, S. Deng and N. Xu, *Sens. Actuator. B: Chem.*, 2012, **173**, 824-832.

258. J. Y. Luoa, W. Li, F. Chen, X. X. Chen, W. D. Li, H. Y. Wu, Y. J. Gao and Q. G. Zeng*. Sens. Actuator. B: Chem.*, 2014, **197**, 81-86.

259. L. F. Zhua, J. C. Shea, J. Y. Luoa, S. Z. Denga, J. Chena, X. W. Ji and N. S. Xu, *Sens, Actuator, B: Chem,* 2011, **153**, 354-360.

260. C. O. Avellaneda and L. O.S. Bulhoes*, Solid State Ionics*, 2003, **165,** 117-121.

261. C. Bechinger, E. Wirth and P. Leiderer, *Appl. Phys. Lett.*, 1996, **68**, 2834-2836.

262. He, T. and J. Yao, *Prog. Mater. Sci.*, 2006, **51**, 810-879.

263. H. M. F. Ahmed and N. S. Begum, *Mater. Sci.*, 2013, **36**, 45-49.

264. S. Y. Lee, J. Y. Kim, J. Y. Lee, H. J. Song, S. Lee, K. H. Choi and G. Shin, *Nano. Res. Lett.*, 2014, **9**, 1-8.

265. G. Poirier, M. Nalin, Y. Messadddeq and S. J. L. Ribeiro, *Solid State Ionics*, 2007, **178***,* 871-875.

266. M. Ahlawat, G. V. Vazquez, M. Nalin, Y. Messaddeq and S. Ribeiro, *J. Non-Cryst. Solids*, 2010, **356**, 2360-2362.

267. N. I. Fernandes, G. Poirier and M. Nalin, *Solid State Ionics*, 2010, **181**, 1125-1130.
268. A. Paone, M. Geiger, R. Sanjines and A. Schuler*. Sol. Energy*, 2014, **110**, 151-159.
269. A. Paone, R. Sanjines, P. Jeanneret,H. J. Whitlow, E. Guibert, G. Guibert, F. Bussy, J. L. Scartezzini and A. Schuler, *J. Alloys Comp.*, 2015, **621**, 206-211.
270. K. P. Sibin, S. John And H. C. Barshilia, *Sol. Energy Mater. Sol. Cells*, 2015, **133**, 1-7.
271. P. Jin, S. Nakao and S. Tanemura, *Thin Solid Films*, 1997, **324**, 151-158.
272. M. A. Sobhan, R. T. Kivaisi, B. Stjerna and C.G. Granqvist, *Sol. Energy Mater. Sol. Cells*, 1995, **44**, 451-455.
273. C.Tao, S. Ruan, G. Xie, X. Kong, L. Shen, F. Meng, C. Liu, X. Zhang, W. Donga and W. Chen, *Appl, Phys, Lett*, 2009, **94**, 043311.
274. Z. Tan, L. Li, C. Cui, Y. Ding, Q. Xu, S. Li, D. Qian and Y. Li, *J. Phys. Chem. C*, 2012, **116**, 18626-18632.
275. X. Yang, E. Mutlugun, Y. Zhao, Y. Gao, K. S. Leck, Y. Ma, L. Ke, S. T. Tan, H. V. Demir and X. W. Sun, *Nanomicro Small*, 2014, **10**, 247-252.
276. J. Meyer, T. Winkler, S. Hamwi, S. Schmale, H. H. Johannes, T. Weimann, P. Hinze, W. Kowalsky and T. Riedl, *Adv. Mater.*, 2008, **20**, 3839-3843.
277. G. F. Li, Q. Zhang, F. Yu, C. Liu and H. R. Wu, *Electron. Lett*., 2008, **44**, 818-819.
278. W. L. Dai, J. Ding, Q. Zhu, R. Gao and X. Yang, *RSC Catal.*, 2016, **28**, 1-27.
279. A. J. Roosmalen and J. C. Mol, *J. Catal.*, 1982, **78**, 17-23.
280. S. Lwin and I. E. Wachs, *ACS Catal.*, 2014, **4**, 2505-2520.
281. H. Liu, L. Zhang, X. Li, S. Huang, S. Liu, W. Xin, S. Xie, L. Xu, *J. Nat. Gas Chem.*, 2009, **18**, 331-336.
282. A. E. A. A. Said, M. M. M. A. E. Wahab and M. A. E. Aal, *Chem. Mater. Eng.*, 2016, **4**, 17-25.
283. H. Wang, Z. Liu, Y. Wu, Z. Yao, W. Zhao, W. Duan and K. Guo, *Arab. J. Chem.*, 2016, **9**, 18-24.
284. Y. Bi, D. Li and H. Nie, *Mater. Chem. Phys*., 2010, **123**, 225-230.

285. A. S. Ivanova, E. V. Korneeva, G. A. Bukhtiyarova, A. L. Nuzhdin, A. A. Budneva, I. P. Prosvirin, V. I. Zaikovskii and A. S. Noskov, *Kinet. Catal.*, 2011, **52**, 446-458.
286. E. J. V. D. Ham, K. Elen, I. Kokal, B. Yagci, N. Peys, G. Bonneux, F. Ulu, W. Marchal, M. K. V. Baela and A. Hardy*. RSC Adv.*, 2016, **6**, 51747-51756.
287. J. B. Mitchell, W. C. Lo, A. Genc, J. LeBeau and V. Augustyn, *Chem. Mater.*, 2017, **29**, 3928-3937.
288. N. Soultanidis, W. Zhou, C. J. Kiely and M. S. Wong, *Langmuir*, 2012, **28**, 17771-17777.
289. Kshitij Education India, *Diffraction of xirays by crytals,* 2011-2016, http://www.kshitij-iitjee.com/diffraction-of-x-rays-by-crystals.
290. T. Ida, *in Crystal Structure Analysis: Bragg's Law*, Nagoya Institute of Technology, Japan, 2013.
291. Anton Paar, *X-ray diffraction (XRD)*, 2016, http://wiki.anton-paar.com/x-ray-diffraction-xrd/.
292. I. Guwahati, *Catalyst characterization - XRD analysis*, NPTEL, 2017, http://nptel.ac.in/courses/103103026/module2/lec12/1.html.
293. D. Leadley, *Transmission Electron Microscopy (TEM)*, 2010, https://www2.warwick.ac.uk/fac/sci/physics/current/postgraduate/regs/mpags/ex5/techniques/structural/tem/.
294. D. Fields, *What is Transmission Electron Microscopy,* 2017, http://www.news-medical.net/life-sciences/What-is-Transmission-Electron-Microscopy.aspx.
295. A. Aryal, *Differences between light microscopy and electron microscopy* 2015, https://microbiologyinfo.com/differences-between-light-microscope-and-electron-microscope/.
296. A. A. Lueje, M. Perez and C. Zapata, *in Topic on drug metabolism - Electrochemical Methods for the In Vitro Assessment of Drug Metabolism*, Intech, Chile, 2012, DOI: 10.5772/28647.
297. D. K. Green, *Cyclic Voltammetry (CV)*, 2017, https://www.jove.com/science-education/5502/cyclic-voltammetry-cv.
298. A. W. Bott and W. R. Heineman, *Current Separations*, 2004, **20**, 121-126.

299. K. Vo, *Spectrophotometry*, 2015, https://chem.libretexts.org/Core/Physical_and_Theoretical_Chemistry/Kinetics/Reaction_Rates/Experimental_Determination_of_Kinetcs/Spectrophotometry.
300. S. Sun, Y. Zhao, Y. Xia, Z. Zou, G. Min and Y. Q. Zhu*. Nanotechnol.*, 2008, **19**, 305709.
301. L. Jiang , H. Zhub, R. Razzaq, M. Zhua, C. Li and Z. Li, *Int. J. Hydrog. Energy*, 2012, **37**, 15914-15924.
302. X. Chang, S. Sun, Y. Zhou, L. Dong and Y. Yin, *Nanotechnol*., 2011, **22***,* 265603.
303. L. Xu, D. Gu, X. Chang, L. Chai, Z. Li, X. Jin and S. Sun, *Ceram. Int.*, 2017, **43**, 10263-10269.
304. A. Nashim, S. Martha and K. M. Parida, *RSC Adv.*, 2014, **4**, 14633-14643
305. I. Bhat, S. Husain And S.I. Patil, *Mater. Res. Bull.*, 2014, **57**, 72-78.
306. M. Boulova and G. Lucazeau, *J. Solid State Chem.*, 2002, **167**, 425-434.
307. D. Y. Lu, J. Chen, J. Zhou, S. Z. Deng, N. S. Xu, and J. B. Xu. *J. Raman Spectrosc*., 2007, **38**, 176-180.
308. P. M. Woodward, A. W. Sleight, and T. Vogt, *J. Solid State Chem*., 1997, **131**, 9-17.
309. M. H. Cho, S. A. Park, K. D. Yang, I. W. Lyo, K. Jeong, S. K. Kang, D. H. Ko, K. W. Kwonm J. H. Ku, S. Y. Choi and H. J. Shin, *J. Vac. Sci.Technol. B: Microelectron. Nanometer Struct.*, 2004, **22**, 1084-1087.
310. J. Chen, S. Chen, D. Lu, W. Zhang, F. Xie, W. Xie, L. Gong and C. Wang, *Chemphyschem*, 2010, **11***,* 2546-2549.
311. E. Cazzanelli, C. Vinegoni, G. Mariotto, A. Kuzmin and J. Purans, *Solid State lonics*, 1999, **123**, 67-74.
312. C. W. Lai, *J. Nanomater.*, 2015, **2015**, 563587.
313. Z. Ma, D. Weng, X. Wu and Z. Si, *J. Environ. Sci.,* 2012, **24**, 1305-1316.
314. M. B. Johansson, B. Zietz, G. A. Niklasson and L. Osterlund, J.Appl. Phys., 2014, **115**, 213510.
315. A. Karuppasamy and A. Subrahmanyam, *J. Appl. Phys.*, 2007, **101**, 113522.

316. V. Madhavi, P. Kondaiah, O. M. Hussain and S. Uthanna, *ISRN Optics*, 2012, **2012**, 1-8.
317. S. Park, H. Kim, C. Jin and C. Lee, *Nanoscale Res Lett*, 2011, **6**, 1-6.
318. K. Lee, W. S. Seo and J. T. Park, *J. Am. Chem. Soc.*, 2003, **125**, 3408-3409.
319. M. Feng, A. L. Pan, H. R. Zhang, Z. A. Li, F. Liu, H. W. Liu, D. X. Shi, B. S. Zou and H. J. Gao, *Appl. Phys. Lett.*, 2005, **86**, 141901.
320. M. Niederberger, M. H. Bartl and G. D. Stucky, *J. Am. Chem. Soc*, 2002, **124**, 13642-13643.
321. C. Qin, Y. Huang, G. Chen, L. Shi, X. Qiao, J. Gan and H. J. Seo, *Mater. Lett.*, 2009, **63**, 1162-1164.
322. M. Pal, U. Pal, J. M. G. Y. Jiménez and F. P. Rodríguez*, Nanoscale Res. Lett.*, 2012, **7**, 1-12.
323. Z. Liu and Y. Li, *Thin Solid Films*, 2008, **516**, 5557-5561.
324. Y. Zhang, J. Hao, C. L. Mak and X. Wei*. Opt. Express*, 2011, **19,** 1824-1829.
325. L. Chena, D. Wenga, Z. Sib and X. Wu, *Prog. Nat. Sci.: Mater. Int.*, 2012, **22**, 265-272.
326. Y. Kumar, A. P. Singh, S. K. Sharma, R. J. Choudhary and P. Thakur*, Appl. Phys. Lett.*, 2012, **101**, 112103.
327. B. E. Francisco, C. R. Stoldt and J. C. M'Peko, *Chem. Mater.*, 2014, **26**, 4741-4749.
328. V. V. Kondalkar, P. B. Patil, R. M. Mane, P. S. Patil, S. Choudhury, P. N. Bhosal*. Macromol. Symp.*, 2016, **361**, 47-50.
329. F. F. Santiago, G. G. Belmonte, J. Bisquert, N. S. Ferriols, P. R. Bueno, E. Longo, J. S. Anton and S. C. Garcia, *J. Electrochem. Soc.*, 2001, **148**, E302-E309.
330. A. D. Sanctis, G. F. Jones, N. J. Townsend, M. F. Craciun and S. Russo, *Rev. Sci. Instrum.*, 2017, **88**, 1-29.
331. A. L. S. Eh, A. W. M. Tan, X. Cheng, S. Magdassi and P. S. Lee, *Energy Technol.*, 2018, **6**, 33-45.
332. G. Cai, J. Wang and P. S. Lee, *Acc. Chem, Res.*, 2016, **49**, 1469−1476.
333. P. Cossari, A. Cannavale, S. Gambinoa and G. Gigli, *Sol. Energy Mater. Sol. Cells*, 2016, **155**, 411–420.

334. Y. Alesanco, J. Palenzuela, R. T. Zaera, G. Cabanero, H. Grandea, B. Herbig, A. Schmitt, M. Schott, U. Posset, A. Guerfic, M. Dontigny, K. Zaghib and A. Vinuales, Sol. *Energy Mater. Sol. Cells*, 2016, **157**, 624-635.

335. L. Liang, J. Zhang, Y. Zhou, J. Xie, X. Zhang, M. Guan, B. Pan and Y. Xie, *Sci. Rep.*, 2013, **3**. 1-8.

336. H. Park, D. S. Kim, S. Y. Hong, C. Kim, J. Y. Yun, S. J. S. Y. Oh, Y. R. Jeong, G. T. Kim and J. S. Ha, *Nanoscale*, 2017, **9**, 7631–7640.

Appendix A

Pattern: COD 2106382 Radiation: 1.54060 Quality: Quality Unknown

Formula O3 W
Name
Name (mineral)
Name (common)

Lattice: Monoclinic
S.G.: P 1 21/n 1 (14)

a = 7.30600
b = 7.54000
c = 7.69200
a/b = 0.96897
c/b = 1.02016

beta = 90.881
Z = 8

Mol. weight =
Volume [CD] = 423.68
Dx =
Dm =
I/Icor = 7.400

Primary Reference
Loopstra B.O., Rietveld H.M., "Further refinement of the structure of W O3", Acta Crystallographica B (24,1968-38,1982) 25 (1969) 1420-1421.

Wavelength SS/FOM 1.54060

Filter Not specified
d-spacing

d	2θ	I fix	h	k	l	d	2θ	I fix	h	k	l
5.38420	16.451	1	0	-1	-1	2.17830	41.418	158	-2	-2	2
3.84550	23.110	973	0	0	-2	2.15600	41.867	166	-2	-2	-2
3.77000	23.580	944	0	-2	0	2.12000	42.612	1	0	-2	-3
3.65260	24.349	999	-2	0	0	2.10380	42.956	13	0	-3	-2
3.42570	25.989	9	0	-1	-2	2.04550	44.244	49	-3	-2	0
3.38520	26.306	4	0	-2	-1	2.03530	44.478	2	-2	-1	3
3.35020	26.585	203	-1	-2	0	2.02620	44.688	36	-1	-3	2
3.11810	28.605	172	-1	-1	2	2.01720	44.899	37	-1	-3	-2
3.08540	28.915	173	-1	-1	-2	2.00370	45.218	1	-2	-3	1
3.03790	29.377	5	-2	-1	1	1.99770	45.361	49	-3	-1	2
2.69210	33.253	426	0	-2	-2	1.98310	45.714	1	-3	-2	1
2.66890	33.551	262	-2	0	2	1.97200	45.986	49	-3	-1	-2
2.62820	34.086	236	-2	0	-2	1.97040	46.025	4	-3	-2	-1
2.62330	34.152	499	-2	-2	0	1.92280	47.233	102	0	0	-4
2.53490	35.381	70	-1	-2	2	1.88500	48.240	103	0	-4	0
2.51730	35.637	68	-1	-2	-2	1.86310	48.844	5	0	-1	-4
2.51600	35.656	7	-2	-1	2	1.83080	49.763	1	0	-4	-1
2.49130	36.022	2	-2	-2	1	1.82970	49.795	14	-2	-3	2
2.48180	36.164	4	-2	-1	-2	1.82630	49.894	160	-4	0	0
2.47450	36.275	1	-2	-2	-1	1.82520	49.926	126	-1	-4	0
2.40750	37.321	4	-1	0	-3	1.81650	50.182	13	-2	-3	-2
2.33180	38.580	2	-3	0	1	1.81560	50.209	25	-3	-2	2
2.31350	38.897	1	-1	-1	3	1.81180	50.321	121	-1	-1	4
2.31130	38.935	2	-3	0	-1	1.79890	50.708	121	-1	-1	-4
2.29340	39.252	1	-1	-1	-3	1.79630	50.786	25	-3	-2	-2
2.26750	39.719	10	-1	-3	-1	1.77440	51.458	1	-1	-4	-1
2.22770	40.459	2	-3	-1	1	1.73860	52.598	1	-1	-3	-3
2.20980	40.801	1	-3	-1	-1	1.73520	52.709	2	-4	-1	1

Appendix A

d	2θ	I fix	h	k	l	d	2θ	I fix	h	k	l	d	2θ	I fix	h	k	l	d	2θ	I fix	h	k	l
1.71290	53.450	84	0	-2	-4	1.49120	62.204	45	-1	-3	-4	1.31160	71.931	46	-4	-4	0	1.21360	78.799	2	0	-2	-6
1.71230	53.470	54	-2	0	4	1.49060	62.232	59	-3	-4	0	1.30960	72.058	2	-3	0	5	1.21330	78.822	4	-3	-5	-2
1.70130	53.843	1	-3	-3	-1	1.49050	62.237	61	-3	-1	4	1.30800	72.160	8	-2	-5	-2	1.20480	79.488	5	-5	-3	2
1.69260	54.143	88	0	-4	-2	1.46960	63.223	1	-4	-1	3	1.30090	72.616	27	-3	-3	4	1.20380	79.567	2	-2	0	-6
1.69070	54.208	47	-2	0	-4	1.46920	63.242	59	-3	-1	-4	1.29460	73.027	1	-4	-1	-4	1.19990	79.878	2	-2	-1	6
1.67510	54.755	104	-2	-4	0	1.46080	63.648	2	-3	-4	-1	1.28990	73.336	8	-5	-2	2	1.19530	80.248	7	-5	-3	-2
1.67270	54.840	13	-1	-2	4	1.44950	64.204	1	-1	-5	-1	1.28840	73.435	1	-1	-3	-5	1.19450	80.312	4	0	-6	-2
1.66980	54.944	5	-2	-1	4	1.41510	65.960	16	-2	-3	4	1.28670	73.548	25	-3	-3	-4	1.19030	80.654	1	-6	-1	1
1.66260	55.202	11	-1	-2	-4	1.41010	66.223	7	-3	-2	4	1.28180	73.876	4	0	0	-6	1.18870	80.785	2	-2	-1	-6
1.65960	55.310	81	-4	0	2	1.40390	66.554	9	0	-5	-2	1.27840	74.106	7	-5	-2	-2	1.18830	80.818	7	-2	-6	0
1.65140	55.609	68	-1	-4	2	1.40290	66.607	18	-2	-3	-4	1.26750	74.851	18	-2	-4	4	1.18660	80.957	16	0	-5	-4
1.64980	55.667	5	-2	-1	-4	1.39420	67.078	36	-3	-4	2	1.26370	75.115	2	0	-1	-6	1.18350	81.214	13	-3	-4	4
1.64650	55.788	66	-1	-4	-2	1.39200	67.198	7	-3	-2	-4	1.25860	75.473	16	-2	-4	-4	1.17970	81.531	32	-1	-6	2
1.64360	55.896	157	-4	-2	0	1.38540	67.561	35	-3	-4	-2	1.25800	75.515	23	-4	-2	4	1.17860	81.623	5	-4	-3	4
1.64000	56.029	72	-4	0	-2	1.38490	67.589	4	-4	-3	2	1.25670	75.607	4	0	-6	0	1.17800	81.673	31	-1	-6	-2
1.63910	56.062	1	-2	-4	1	1.38010	67.856	4	-1	-5	2	1.24840	76.199	49	-1	-1	6	1.17300	82.096	8	-1	-5	4
1.62080	56.752	1	-4	-1	2	1.37730	68.012	4	-1	-5	-2	1.24560	76.401	28	-4	-4	2	1.17270	82.122	11	-3	-4	-4
1.61770	56.871	1	-2	-3	3	1.37340	68.232	4	-4	-3	-2	1.24380	76.532	2	-5	-3	-1	1.16950	82.395	8	-1	-5	-4
1.59860	57.614	16	-3	-3	2	1.36230	68.866	13	-5	-2	0	1.24210	76.656	49	-1	-1	-6	1.16590	82.705	17	-6	0	2
1.58540	58.139	17	-3	-3	-2	1.35060	69.548	13	-5	-1	2	1.24090	76.743	27	-4	-2	-4	1.16450	82.827	7	-4	-3	-4
1.55900	59.221	43	-2	-2	4	1.34610	69.814	27	0	-4	-4	1.23850	76.919	46	-1	-6	0	1.15860	83.342	34	-6	-2	0
1.54270	59.910	49	-2	-2	-4	1.33730	70.341	13	-5	-1	-2	1.23730	77.007	25	-4	-4	-2	1.15810	83.386	23	-5	-1	4
1.53970	60.039	49	-2	-4	2	1.33450	70.510	25	-4	0	4	1.23710	77.022	2	-3	-2	5	1.15680	83.501	1	-2	-2	6
1.53180	60.380	46	-2	-4	-2	1.32630	71.012	18	-1	-4	4	1.22320	78.062	1	-1	-6	1	1.15560	83.607	16	-6	0	-2
1.52710	60.586	16	0	-3	-4	1.32120	71.328	17	-1	-4	-4	1.22220	78.138	1	-1	-6	-1	1.15480	83.678	22	-5	-4	0
1.51900	60.943	78	-4	-2	2	1.31410	71.773	20	-4	0	-4	1.21920	78.367	4	-3	-5	2	1.14670	84.405	2	-2	-2	-6
1.50380	61.626	81	-4	-2	-2	1.31400	71.779	1	-4	-1	4	1.21750	78.498	25	-6	0	0	1.14190	84.843	10	0	-3	-6
1.49850	61.868	45	-1	-3	4	1.31290	71.849	10	-2	-5	2	1.21540	78.660	2	-2	0	6	1.14150	84.879	23	-5	-1	-4

Appendix A

d	2θ	I fix	h	k	l	d	2θ	I fix	h	k	l
1.13690	85.304	4	-2	-6	2	1.06000	93.221	1	0	-4	-6
1.13370	85.602	4	-2	-6	-2	1.05760	93.496	2	-6	-3	2
1.13170	85.790	17	-2	-5	4	1.05690	93.577	2	-4	0	6
1.13060	85.894	25	-1	-3	6	1.05190	94.158	2	0	-6	-4
1.12870	86.073	34	-3	-1	6	1.05090	94.275	2	-1	-4	6
1.12590	86.340	25	-1	-3	-6	1.05000	94.381	2	-6	-3	-2
1.12540	86.388	18	-2	-5	-4	1.04930	94.464	13	-5	-3	-4
1.11920	86.985	4	-5	-2	4	1.04710	94.724	2	-1	-4	-6
1.11670	87.229	32	-3	-6	0	1.04660	94.784	1	-4	-1	6
1.11610	87.287	4	-4	-5	2	1.04240	95.287	13	-1	-6	4
1.11480	87.415	33	-3	-1	-6	1.04170	95.372	1	-4	0	-6
1.11390	87.503	22	-6	-2	2	1.04000	95.578	13	-1	-6	-4
1.11000	87.889	4	-4	-5	-2	1.03940	95.651	20	-3	-3	6
1.10970	87.919	16	-5	-4	2	1.03720	95.919	4	0	-7	-2
1.10490	88.400	25	-6	-2	-2	1.03590	96.079	7	-6	0	4
1.10410	88.481	2	-5	-2	-4	1.03530	96.153	5	-4	-6	0
1.10400	88.491	1	-3	-6	-1	1.02850	97.000	19	-3	-3	-6
1.10230	88.663	16	-5	-4	-2	1.02270	97.737	16	-6	-4	0
1.09470	89.443	1	-6	-1	3	1.02160	97.878	7	-6	0	-4
1.09420	89.495	11	-2	-3	6	1.02150	97.891	1	-2	-4	6
1.08920	90.018	11	-4	-4	4	1.01760	98.397	1	-4	-2	6
1.08570	90.388	11	-2	-3	-6	1.01520	98.711	1	-5	-5	2
1.07800	91.215	10	-4	-4	-4	1.01310	98.988	1	-2	-6	4
1.07450	91.597	22	-3	-6	2	1.00950	99.468	2	-5	-5	-2
1.07070	92.016	7	-3	-5	4						
1.07040	92.049	23	-3	-6	-2						
1.06270	92.913	7	-3	-5	-4						
1.06220	92.970	13	-5	-3	4						

Pattern: COD 2107312 Radiation: 1.54060 Quality: Quality Unknown

Formula O3 W
Name
Name (mineral)
Name (common)

Lattice: Orthorhombic
S.G.: P n m a (62)

a = 7.57000
b = 7.34100
c = 7.75400
a/b 1.03119
c/b 1.05626

Z = 8

Mol. weight =
Volume [CD] = 430.9
Dx =
Dm =
I/Icor = 7.650

Primary Reference
Salje E., "The orthorhombic phase of W O3", Acta Crystallographica B (24,1968-38,1982) 33 (1977) 574-577.

Wavelengt 1.54060
h
SS/FOM

Filter Not specified
d-spacing

d	2θ	I fix	h	k	l	d	2θ	I fix	h	k	l
3.87700	22.920	986	0	0	-2	1.68210	54.508	106	-4	-2	0
3.78500	23.485	958	-2	0	0	1.67960	54.596	20	-2	-1	-4
3.67050	24.229	1000	0	-2	0	1.67180	54.872	7	-1	-2	-4
3.45080	25.797	8	-1	0	-2	1.65880	55.339	158	0	-4	-2
3.36420	26.473	158	-2	-1	0	1.65680	55.412	132	-4	-1	-2
3.12290	28.560	279	-1	-1	-2	1.65140	55.609	160	-2	-4	0
2.70830	33.049	452	-2	0	-2	1.62030	56.772	1	-1	-4	-2
2.66540	33.596	487	0	-2	-2	1.60010	57.555	27	-3	-3	-2
2.63500	33.995	489	-2	-2	0	1.56150	59.116	91	-2	-2	-4
2.54090	35.295	112	-2	-1	-2	1.54310	59.893	89	-4	-2	-2
2.51420	35.682	7	-1	-2	-2	1.53720	60.146	19	-3	0	-4
2.17930	41.398	300	-2	-2	-2	1.51930	60.930	149	-2	-4	-2
2.11490	42.720	15	-3	0	-2	1.50460	61.589	89	-3	-1	-4
2.05500	44.029	40	-2	-3	0	1.49700	61.936	59	-4	-3	0
2.04960	44.151	2	-2	-1	-3	1.48980	62.269	115	-1	-3	-4
2.03220	44.549	60	-3	-1	-2	1.41790	65.813	26	-3	-2	-4
1.99610	45.400	77	-1	-3	-2	1.41030	66.213	8	-5	0	-2
1.93850	46.828	113	0	0	-4	1.41010	66.223	12	-2	-3	-4
1.89250	48.037	115	-4	0	0	1.39650	66.953	71	-4	-3	-2
1.87790	48.434	4	-1	0	-4	1.38610	67.522	8	-3	-4	-2
1.83530	49.633	173	0	-4	0	1.38500	67.583	8	-5	-1	-2
1.83260	49.711	123	-4	-1	0	1.36880	68.493	10	-2	-5	0
1.83240	49.717	19	-3	-2	-2	1.35420	69.336	35	-4	0	-4
1.81930	50.099	238	-1	-1	-4	1.35100	69.524	20	-1	-5	-2
1.81570	50.206	40	-2	-3	-2	1.33270	70.620	54	0	-4	-4
1.72540	53.032	101	-2	0	-4	1.33170	70.681	38	-4	-1	-4
1.71410	53.409	101	0	-2	-4	1.31750	71.559	58	-4	-4	0
1.70070	53.864	97	-4	0	-2	1.31650	71.622	13	-5	-2	-2

Appendix A

d	2θ	I fix	h	k	l	d	2θ	I fix	h	k	l	d	2θ	I fix	h	k	l
1.31250	71.874	2	-1	-4	-4	1.16000	83.219	23	-4	-5	0	1.03470	96.227	18	0	-6	-4
1.30170	72.565	51	-3	-3	-4	1.15670	83.510	46	-1	-5	-4	1.02750	97.126	19	-4	-6	0
1.29230	73.178	7	0	0	-6	1.15030	84.080	10	-3	0	-6	1.02510	97.430	1	-1	-6	-4
1.29070	73.283	13	-2	-5	-2	1.14040	84.980	7	-6	-2	-2	1.02480	97.469	4	-4	-2	-6
1.27390	74.411	2	-1	0	-6	1.13640	85.351	45	-3	-1	-6	1.01770	98.384	8	-2	-4	-6
1.27050	74.644	36	-4	-2	-4	1.13480	85.500	27	-5	-2	-4	1.01710	98.462	4	-5	-5	-2
1.26170	75.255	8	-6	0	0	1.13000	85.950	61	-1	-3	-6	1.01610	98.593	4	-6	-2	-4
1.25710	75.579	61	-2	-4	-4	1.12140	86.772	30	-6	-3	0	1.01080	99.321	4	-2	-7	0
1.25510	75.720	87	-1	-1	-6	1.11820	87.082	8	-5	-4	-2						
1.24740	76.271	60	-4	-4	-2	1.11820	87.082	5	-2	-5	-4						
1.24340	76.561	42	-6	-1	0	1.11500	87.395	37	-2	-6	-2						
1.22350	78.039	30	0	-6	0	1.11140	87.750	31	-4	-5	-2						
1.22300	78.077	7	-2	0	-6	1.09760	89.144	18	-3	-2	-6						
1.22190	78.161	5	-5	-3	-2	1.09400	89.516	1	-2	-3	-6						
1.21900	78.383	5	0	-2	-6	1.08960	89.976	31	-4	-4	-4						
1.20640	79.362	1	-2	-1	-6	1.07720	91.302	40	-6	-3	-2						
1.20610	79.385	10	-3	-5	-2	1.07250	91.817	15	-5	-3	-4						
1.20350	79.591	4	-1	-2	-6	1.06720	92.406	4	-4	0	-6						
1.19970	79.894	8	-6	0	-2	1.06170	93.027	26	-3	-5	-4						
1.19320	80.418	16	-5	0	-4	1.05900	93.335	4	-3	-6	-2						
1.19310	80.426	8	-6	-2	0	1.05740	93.519	5	-6	0	-4						
1.18480	81.106	25	-4	-3	-4	1.05660	93.611	7	0	-4	-6						
1.18400	81.172	54	-6	-1	-2	1.05610	93.669	4	-4	-1	-6						
1.17850	81.631	13	-3	-4	-4	1.04660	94.784	25	-6	-1	-4						
1.17770	81.699	19	-5	-1	-4	1.04650	94.796	2	-1	-4	-6						
1.16680	82.627	32	0	-6	-2	1.04170	95.372	4	-7	0	-2						
1.16420	82.853	33	-2	-6	0	1.04100	95.456	36	-3	-3	-6						
1.16030	83.193	4	-2	-2	-6	1.03970	95.614	8	-6	-4	0						

Pattern: COD 1521532 Radiation: 1.54060 Quality: Quality Unknown

Formula O3 W
Name
Name (mineral)
Name (common)

Lattice: Tetragonal
S.G.: P 4/n c c (130)

a = 5.28850
c = 7.86260
a/b = 1.00000
c/b = 1.48674

Z = 4

Mol. weight =
Volume [CD] = 219.9
Dx =
Dm =
I/Icor = 15.580

Primary Reference
Locherer K.R., Swainson I.P., Salje E.K.H., "Transition to a new tetragonal phase of W O3 : crystal structure and distortion parameters", Journal of Physics: Condensed Matter 11 (1999) 4143-4156.

Wavelength 1.54060
SS/FOM

Filter Not specified
d-spacing

d	2θ	I fix	h	k	l
3.93130	22.599	486	0	0	-2
3.73950	23.775	999	-1	-1	0
3.15510	28.263	174	-1	0	-2
2.70950	33.034	477	-1	-1	-2
2.64420	33.874	281	-2	0	0
2.26480	39.768	2	-2	-1	-1
2.19410	41.107	171	-2	0	-2
2.02660	44.679	97	-2	-1	-2
1.96560	46.144	57	0	0	-4
1.86980	48.657	173	-2	-2	0
1.84250	49.426	124	-1	0	-4
1.73990	52.556	101	-1	-1	-4
1.68850	54.285	155	-2	-2	-2
1.67240	54.851	185	-3	-1	0
1.60850	57.226	23	-3	0	-2
1.57750	58.458	47	-2	0	-4
1.53890	60.073	171	-3	-1	-2
1.51170	61.269	123	-2	-1	-4
1.37420	68.187	26	-3	-2	-2
1.35480	69.301	54	-2	-2	-4
1.32210	71.272	46	-4	0	0
1.31240	71.880	36	-3	0	-4
1.31040	72.007	2	0	0	-6
1.27370	74.425	64	-3	-1	-4
1.27200	74.541	52	-1	0	-6
1.25320	75.855	50	-4	0	-2
1.24650	76.336	29	-3	-3	0
1.23670	77.052	4	-1	-1	-6
1.21940	78.352	16	-4	-1	-2
1.18820	80.826	31	-3	-3	-2
1.18250	81.297	41	-4	-2	0
1.17560	81.876	49	-3	-2	-4
1.14620	84.450	71	-2	-1	-6
1.13240	85.724	46	-4	-2	-2
1.09710	89.195	23	-4	0	-4
1.07420	91.630	36	-4	-1	-4
1.07310	91.751	4	-2	-2	-6
1.05270	94.064	16	-3	-3	-4
1.05170	94.182	27	-3	0	-6
1.03720	95.919	32	-5	-1	0
1.03150	96.624	4	-3	-1	-6
1.02140	97.904	6	-5	0	-2
1.02140	97.904	9	-4	-3	-2
1.01330	98.962	23	-4	-2	-4

Pattern: PDF 01-073-2177 Radiation: 1.54060 Quality: Indexed

Formula	W O2.72
Name	Tungsten Oxide
Name (mineral)	
Name (common)	γ-W O2.72

Lattice:	Monoclinic	Mol. weight =	227.37
S.G.	P2/m (10)	Volume [CD] =	883.29
		Dx =	7.69
		Dm =	
		I/Icor =	6.650

a =	18.31999	alpha =	
b =	3.79000	beta =	115.030
c =	14.04000	gamma =	
a/b =	4.83377	Z =	18
c/b =	3.70449		

ANX: A18X49
Analysis: O2.72 W1
Formula from original source: W O2.72
ICSD Collection Code: 24731
Minor Warning: No e.s.d reported/abstracted on the cell dimension. No R factors reported/abstracted
Wyckoff Sequence: n24 m9 h(P12/M1)
Unit Cell Data Source: Single Crystal

Structure
Publication: Ark. Kemi
Detail: volume 1, page 223 (1949)
Authors: Magneli, A.
Primary Reference
Publication: Calculated from ICSD using POWD-12++

Radiation:	CuKα1	Filter	Not specified
Wavelength:	1.54060	d-spacing	
SS/FOM:	152.7 (0.0052,38)		

d	2θ	I fix	h	k	l	d	2θ	I fix	h	k	l
16.59950	5.320	2	1	0	0	3.52948	25.212	9	4	0	1
13.12930	6.727	77	-1	0	1	3.50452	25.395	21	-2	0	4
12.72150	6.943	308	0	0	1	3.50452	25.395	21	3	0	2
8.87999	9.953	2	-2	0	1	3.46202	25.712	9	1	1	1
8.50780	10.389	30	1	0	1	3.46202	25.712	9	-3	0	4
8.29975	10.651	44	2	0	0	3.44756	25.822	12	2	1	0
7.01320	12.612	6	-1	0	2	3.40076	26.183	309	-1	0	4
6.56465	13.477	10	-2	0	2	3.40076	26.183	309	-5	0	3
6.36073	13.911	2	0	0	2	3.31990	26.833	15	5	0	0
6.10614	14.495	34	-3	0	1	3.28233	27.146	9	-4	0	4
5.90177	14.999	9	2	0	1	3.28233	27.146	9	-2	1	2
5.53316	16.005	4	3	0	0	3.25867	27.347	49	0	1	2
5.47697	16.170	2	-3	0	2	3.25867	27.347	49	2	0	3
5.24431	16.893	29	1	0	2	3.22014	27.680	11	-3	1	1
4.65817	19.037	4	-2	0	3	3.18036	28.033	73	0	0	4
4.60190	19.272	39	-1	0	3	3.12682	28.524	3	3	1	0
4.55404	19.476	36	-4	0	1	3.11657	28.619	2	-3	1	2
4.43999	19.982	63	3	0	1	3.07180	29.046	11	1	1	2
4.43999	19.982	63	-4	0	2	3.05307	29.228	37	-6	0	2
4.37644	20.275	21	-3	0	3	3.02264	29.529	30	-5	0	4
4.25390	20.865	4	0	0	3	2.97762	29.985	29	-6	0	1
4.25390	20.865	4	2	0	2	2.96000	30.168	78	-6	0	3
4.14987	21.395	5	4	0	0	2.95088	30.264	95	4	0	2
3.90454	22.756	26	-4	0	3	2.92422	30.546	150	5	0	1
3.79000	23.454	1000	0	1	0	2.92422	30.546	150	-1	1	3
3.74601	23.733	394	1	0	3	2.91314	30.665	98	-4	1	1
3.64239	24.418	297	-5	0	2	2.88262	30.998	28	-4	1	2
3.64239	24.418	297	0	1	1	2.88262	30.998	28	3	1	1
3.60672	24.664	29	-5	0	1	2.86500	31.194	11	-3	1	3

Appendix A

d	2θ	I tix	h	k	l	d	2θ	I tix	h	k	l	d	2θ	I tix	h	k	l	d	2θ	I tix	h	k	l
2.82979	31.592	4	2	1	2	2.36313	38.048	20	3	0	4	2.12024	42.607	2	0	0	6	1.91365	47.473	6	-8	1	4
2.80570	31.870	48	-3	0	5	2.34143	38.415	21	-6	1	1	2.11243	42.772	4	0	1	5	1.89500	47.969	156	2	1	5
2.79853	31.954	32	4	1	0	2.33283	38.562	55	-6	1	3	2.10548	42.920	3	-7	1	1	1.89500	47.969	156	0	2	0
2.78506	32.113	15	-2	0	5	2.32836	38.639	64	-4	0	6	2.10548	42.920	3	5	1	2	1.88419	48.262	14	1	2	0
2.76658	32.333	87	6	0	0	2.32836	38.639	64	4	1	2	2.10137	43.009	2	-8	0	5	1.88419	48.262	14	7	1	1
2.74822	32.555	123	-4	0	5	2.31520	38.867	89	5	1	1	2.07623	43.556	11	-7	0	6	1.87301	48.568	53	2	0	6
2.73849	32.674	86	-6	0	4	2.30546	39.038	51	1	1	4	2.07623	43.556	11	8	0	0	1.87301	48.568	53	0	2	1
2.71953	32.908	15	-4	1	3	2.28183	39.459	8	-8	0	3	2.06490	43.807	2	-6	1	5	1.85483	49.076	2	-2	2	1
2.69121	33.265	6	-1	0	5	2.28183	39.459	8	-7	0	5	2.03538	44.476	2	-9	0	3	1.85483	49.076	2	4	1	4
2.66425	33.611	183	1	1	3	2.27702	39.546	6	-8	0	2	2.01393	44.976	7	-9	0	2	1.84841	49.257	6	2	2	0
2.62619	34.113	144	2	0	4	2.27702	39.546	6	-5	0	6	2.00573	45.170	32	-9	0	4	1.84841	49.257	6	4	0	5
2.62619	34.113	144	-5	1	2	2.25502	39.948	33	-3	1	5	2.00573	45.170	32	-4	0	7	1.84439	49.372	4	9	0	0
2.58291	34.703	7	4	1	1	2.24427	40.148	12	-2	1	5	1.99952	45.318	29	1	0	6	1.83779	49.561	2	-8	1	5
2.57308	34.839	12	-2	1	4	2.23457	40.329	60	6	1	0	1.99486	45.429	16	-3	0	7	1.83088	49.761	7	-1	2	2
2.57308	34.839	12	3	1	2	2.22486	40.513	86	-4	1	5	1.98710	45.617	6	-5	0	7	1.83088	49.761	7	-10	0	3
2.53116	35.435	173	-5	1	3	2.22486	40.513	86	-1	0	6	1.98710	45.617	6	-3	1	6	1.82566	49.913	6	-9	0	6
2.53116	35.435	173	-1	1	4	2.21968	40.612	64	-6	1	4	1.96628	46.127	15	7	0	2	1.82090	50.052	16	8	1	0
2.49729	35.932	12	5	1	0	2.21968	40.612	64	6	0	2	1.96628	46.127	15	-2	1	6	1.82090	50.052	16	-7	1	6
2.49321	35.993	11	6	0	1	2.20087	40.974	4	5	0	3	1.95487	46.412	8	-7	1	5	1.81735	50.157	42	0	2	2
2.48633	36.096	13	4	0	3	2.20087	40.974	4	-8	0	1	1.95487	46.412	8	-8	1	3	1.81735	50.157	42	0	0	7
2.48118	36.174	10	-4	1	4	2.19428	41.103	4	-1	1	5	1.95227	46.478	8	-8	1	2	1.80336	50.573	6	-10	0	2
2.47091	36.329	29	2	1	3	2.18822	41.222	3	2	0	5	1.95227	46.478	8	-8	0	6	1.80336	50.573	6	2	2	1
2.46246	36.458	18	-7	0	4	2.18822	41.222	3	-6	0	6	1.94595	46.638	20	-9	0	1	1.79419	50.850	14	3	2	0
2.46246	36.458	18	-6	0	5	2.17156	41.553	9	7	0	1	1.94210	46.736	29	-6	0	7	1.79419	50.850	14	-8	0	7
2.43624	36.865	42	0	1	4	2.15637	41.859	6	2	1	4	1.93123	47.014	8	-9	0	5	1.79084	50.952	9	-3	2	2
2.37759	37.808	23	-6	1	2	2.15637	41.859	6	-5	1	5	1.92543	47.165	23	8	0	1	1.77600	51.409	56	7	0	3
2.37136	37.911	15	1	0	5	2.15133	41.962	5	-7	1	2	1.92543	47.165	23	5	0	4	1.77600	51.409	56	-10	0	5
2.37136	37.911	15	7	0	0	2.13730	42.251	2	-7	1	3	1.91864	47.342	13	-1	1	6	1.77278	51.509	52	-4	1	7
2.36313	38.048	20	-5	1	4	2.12695	42.466	2	4	0	4	1.91365	47.473	6	6	1	2	1.77278	51.509	52	-9	1	4

d	2θ	I fix	h	k	l
1.76849	51.643	36	1	1	6
1.76526	51.745	16	8	0	2
1.76526	51.745	16	-3	1	7
1.75988	51.914	8	-5	1	7
1.75226	52.157	40	-1	2	3
1.75226	52.157	40	6	0	4
1.74957	52.243	29	3	0	6
1.74957	52.243	29	-4	2	1
1.74335	52.444	57	3	2	1
1.74335	52.444	57	-10	0	1
1.73898	52.586	35	-2	1	7
1.73898	52.586	35	-3	2	3
1.73564	52.695	29	-8	1	6
1.73564	52.695	29	-3	0	8
1.73110	52.844	41	-6	0	8
1.73110	52.844	41	-9	1	1
1.72839	52.933	31	-6	1	7
1.72378	53.086	16	4	2	0
1.72378	53.086	16	9	0	1
1.72072	53.187	10	-9	1	5
1.71661	53.325	22	8	1	1
1.71661	53.325	22	5	1	4
1.70426	53.742	15	-10	0	6
1.70426	53.742	15	-9	0	7